Properties of Early X-Ray Afterglows of Gamma-Ray Bursts

Rie Sato

Department of Physics, Graduate School of Science,
Tokyo Institute of Technology, Tokyo, Japan

December 2006

Abstract

With the successful launch and operation of the *Swift* mission, it has been revealed that the early X-ray afterglows show a "canonical behavior", where the light curve generally consists of three distinct power-law segments: (1) an initial very steep decay, (2) a very shallow decay and finally (3) a somewhat steeper decay.

In this thesis, we studied the prompt emissions and the early X-ray afterglows observed by *Swift* during the period January 2005 until the end of September 2006. For our analysis we used 160 prompt GRBs and 127 X-ray afterglows.

From the systematic study of X-ray flares, we found that the temporal property of an individual X-ray flare is a FRED (fast-rise exponential decay) similar to that of the most prompt emission pulses. Furthermore, we found that (1) the tails of X-ray flares follow the power-law decay expected for emission from relativistic shells with curvature, where the zero epochs of the power-law agree with the beginning of flares, and (2) time scales of X-ray flares, obtained from the comparison between the observed variability timescale Δt and the time t, are very short ($\Delta t/t \ll 1$). These properties are inconsistent with those of external shock emission, and therefore the X-ray flares are due to central engine activity, after the early prompt emission is over.

We found negative correlation between the break time at the shallow-to-normal decay transition in the X-ray light curve ($T_{\rm brk}$) and the isotropic equivalent energy $E_{\gamma,{\rm iso}}$. We discuss the implication of this observational results on the theoretical models for the shallow decay light curve. We argue that the shallow decay is not consistent with the "time-dependent microphysics model".

Contents

Chapter 1

Gamma-ray Bursts

1.1 Observational History of GRBs

A series of U.S. Vela satellites were run from 1960's to 1970's jointly by the Advanced Research Projects of the U.S. Department of Defense and the U..S Atomic Energy Commission, managed by the U.S. Air Force. Although their primary task was to look for violations of the Nuclear Test Ban Treaty during the Cold War, they provided much useful astronomical data. On July 2, 1967, a large increase of gamma-ray emission was detected by their CsI scintillation detectors. Timing the burst arrival times between different satellites, Vela 4A, B and 3, suggested that the gamma-rays came not from the vicinity of Earth but from a region in outer space (Klebsadel, Strong & Olson 1973). This was the first detection of a gamma-ray burst recorded in history. The later four satellites (5A, B and 6A, B) recorded 73 gamma-ray bursts in the ten year interval July 1969 - April 1979. The distribution in the sky appeared to come from all directions, unlike galactic objects which cluster near the plane or center of the galaxy. This suggested three possible scenarios: the bursts were faint and close (within a few hundred light years); they were associated with the halo of the galaxy; they were bright and very far away. Over 100 hypotheses for their origin had been suggested by 1992 such as asteroids or comets falling onto neutron stars, neutron starquakes, neutron star novae, stellar flares, black holes, white holes, active galactic nuclei, collisions of cosmic strings, strange matter, supernovae, etc. (Nemiroff 1994)

1.1.1 BATSE

Entering in the Compton Gamma-Ray Observatory (CGRO, 1991-2000) era, the isotropic distribution in the sky was completely established. The Burst And Transient Source

Experiment (BATSE) onboard the CGRO satellite recorded 2704 bursts with the NaI(Tl) scintillation detectors. It had a moderate angular resolution (5-10 degrees) and an energy range of approximately 20-600 keV. Figure 1.1 shows the locations all bursts and statistical tests confirmed that the bursts are located at cosmological distances, and the energy requirement faced a serious difficulty. Therefore, the interpretation still needed to have direct measurements of the distances.

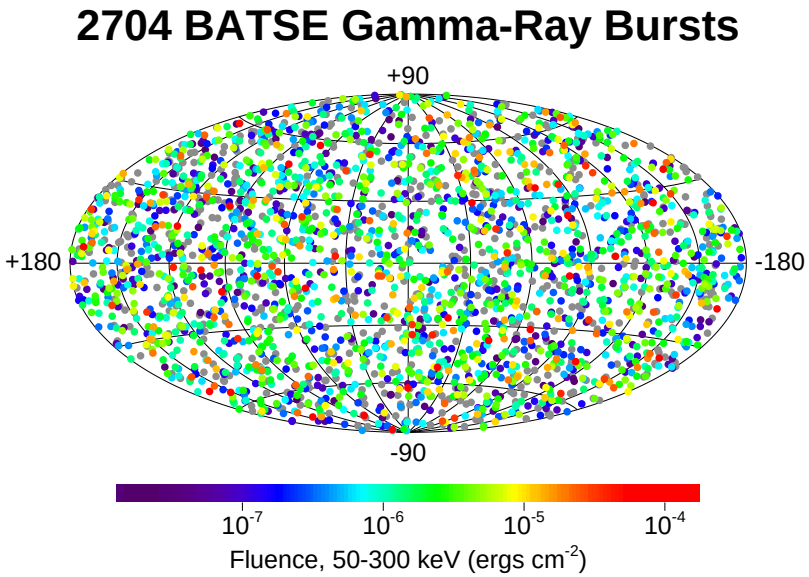

Figure 1.1: All sky map of 2704 GRBs detected with the BATSE instrument during the nine year mission. No clustering along the galactic plane was found, but showing their isotropic distribution in the sky. The burst locations are color-coded based on the fluence, which is the energy flux of the burst integrated over the total duration of the event. From http://www.batse.msfc.nasa.gov/batse/grb/skymap/.

1.1.2 HETE-2

Entering in the High Energy Transient Explore ($HETE-2$) era, GRB-SN connection was dramatically confirmed (Figure 1.2). $HETE-2$ firmly established that the long GRBs, whose durations are more than 2 s, are associated with Type Ic core collapse supernovae (see also section 1.2.3). Furthermore, accurate, rapid $HETE-2$ localizations sent to ground-based robotic telescopes have made it possible to explore the previously unknown behavior of optical afterglows. (see also section 1.2.2)

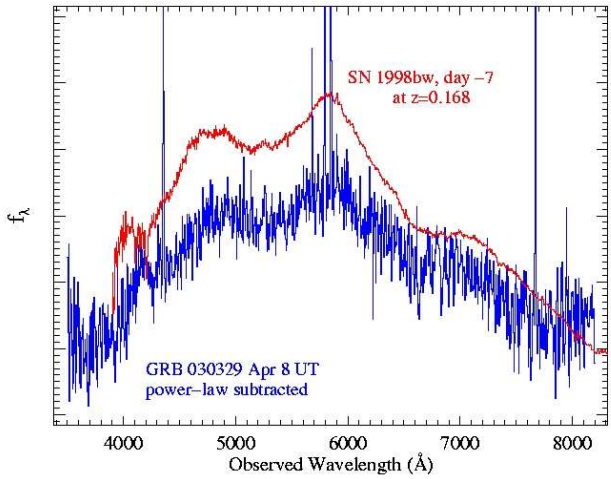

Figure 1.2: Observed spectrum of GRB 030329/SN 2003dh afterglow at 9 days after the burst (Matheson et al. 2003). This spectrum reveals an energy distribution remarkably similar to that of the SN 1998bw.

1.2 Observational Properties of GRBs

A GRB afterglow is thought to be produced by the interaction of an ultra-relativistic blastwave with the interstellar or intergalactic medium. The afterglow model predicts a series of stages as the wave slows down. A key prediction is a break in the spectrum that moves from the gamma to the radio band, and is responsible for the power-law decay of the source flux. This spectral break moves though the X-ray band in a few seconds but takes up to 1000s to reach the optical. Thus, observations within the first 1000s in the optical are crucial to see this early phase. While it now seems likely that all the GRBs have X-ray afterglow, not all have bright optical afterglow (at least after several hours). This may be due to optical extinction, but it is also possible that in some cases the optical afterglow is present but decays much more rapidly and is a function of the density of the local environment. Prompt high quality X-ray, UV, and optical observations over the first minutes to hours of the afterglow are crucial to resolve this question. Continuous monitoring for hours and days is then important since model-constraining temporal variation (e.g. jet break) or flares can occur in the decaying emission.

1.2.1 Prompt Emission

Temporal Characteristic

Let us review and summarize the properties of gamma-ray emissions observed in the BATSE gamma-ray bursts (Fishman et al. 1994; Fishman & Meegan 1995). A unique feature of gamma-ray bursts is the diversity of their light curves. Some are erratic, spiky, while some others are smooth with one or a few components. On the other hand, the burst has distinct, well-separated emission. Widths of individual pulses are asymmetric, with sharper leading edges than trailing edges. The duration of gamma-ray burst is usually denoted as T_{90}, which is the time interval during which 90% of the total observed counts have been detected. Figure 1.3 shows the distribution of the T_{90} observed by BATSE. They distributes in a rather wide range from $\sim 10^{-2}$ to ~ 1000 seconds. Interestingly it exhibits a bimodal distribution: long bursts peaking at ~ 50 seconds; short bursts peaking at ~ 0.3 seconds. Furthermore, these two groups may have different spectral hardness as shown in Figure 1.4. This is why they are sometimes called "short hard GRBs" and "long soft GRBs". It is possible that the two groups have different origins: a collapse of massive star for long bursts, and a merger of compact objects for short bursts. Intensive discussions have been made on this topic and now this interpretation has increasing supports by the recent observations for host galaxies of GRBs (Gehrels et al. 2005; Villasenor et al. 2005), though there are still large uncertainties.

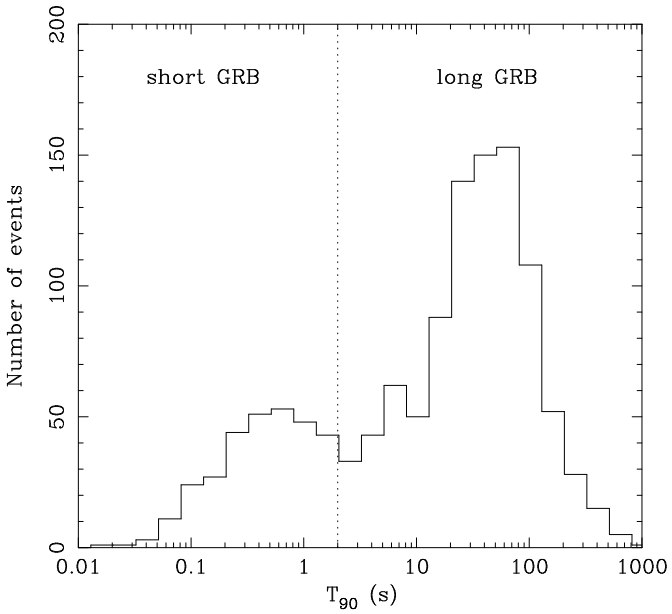

Figure 1.3: Distribution of the burst duration of the 4B catalog GRBs recorded with BATSE.

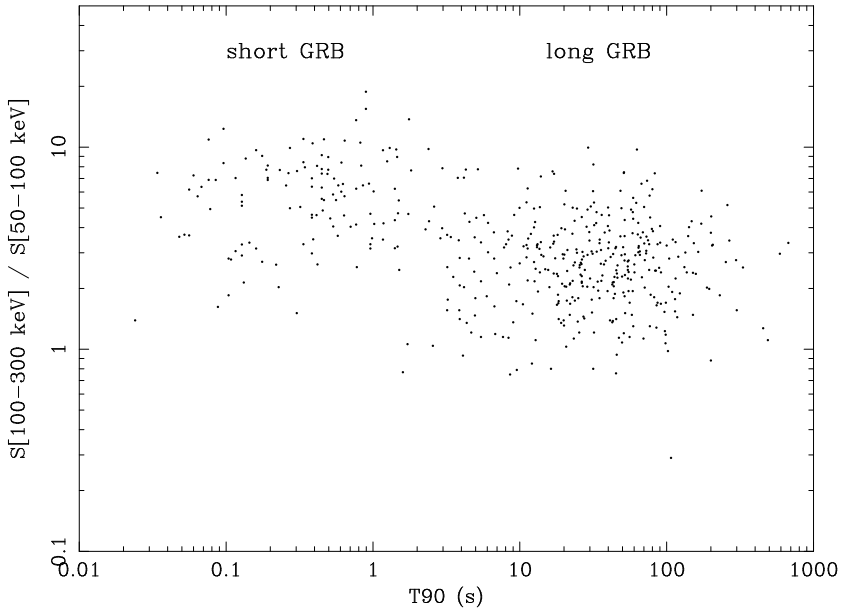

Figure 1.4: Distribution of the burst duration (T_{90}) and Hardness ratio.

Spectral Characteristics

Another feature of GRB is their high energy emission. The spectrum is usually represented by a continuum with a νF_ν peak at a few hundreds keV. Figure 1.5 shows typical νF_ν spectra of GRBs observed with CGRO multi-instruments. The spectrum can be phenomenologically characterized with smoothly-joint broken power-law function, known as Band function (Band et al. 1993):

$$N(E) = \begin{cases} A\left(\frac{E}{100\text{keV}}\right)^{\alpha} \exp\left(-\frac{E}{E_0}\right) & \text{for} \quad E \leq (\alpha-\beta)E_0, \\ A\left(\frac{E}{100\text{keV}}\right)^{\beta} \left(\frac{(\alpha-\beta)E_0}{100keV}\right)^{\alpha-\beta} \exp(\beta-\alpha) & \text{for} \quad E \geq (\alpha-\beta)E_0, \end{cases} \tag{1.1}$$

where νF_ν peaks at $E^{\text{obs}}_{\text{peak}} = E^2 N(E) = (\alpha+2)E_0$. The function has a photon index of α for the lower energy part, and flattening out smoothly to a high energy tail described with a photon index of β. The values for α, β, E_0 all vary between bursts, and some time evolutions have been reported even within a single burst. The distributions of the BATSE spectral parameters in the Band function are shown in Fig. 1.6, respectively. As seen in figure 1.6, E_0 is concentrated around ~ 250 keV. The photon indices α and β are clustered around ~ -1 and ~ -2.2, respectively.

$E^{\text{src}}_{\text{peak}} - E_{\gamma,\text{iso}}$ Relation (Amati's Relation)

Amati et al. (2002) studied the spectral and energetics properties of Beppo-SAX GRBs with known redshifts. They investigated the time-integrated spectra using the Band

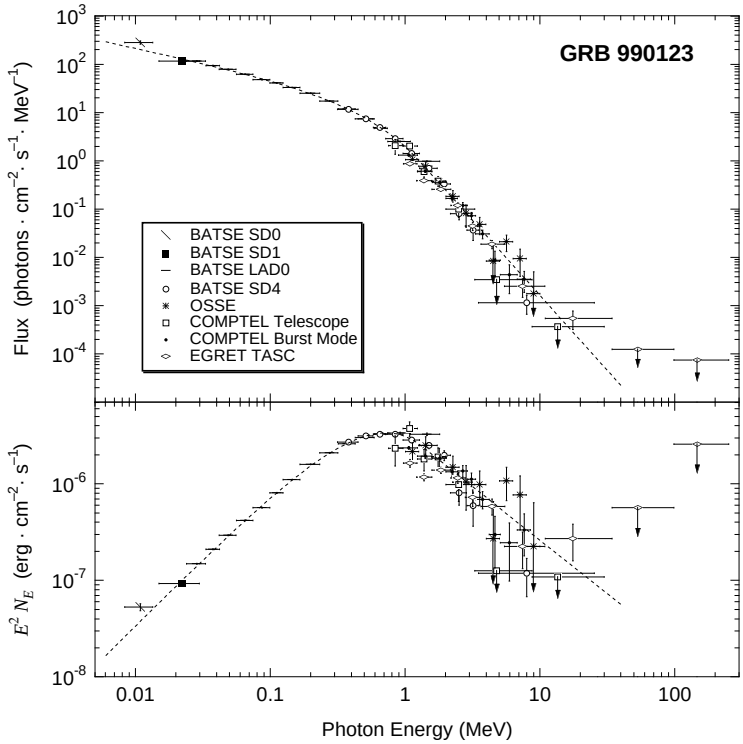

Figure 1.5: Example of a GRB spectrum (GRB 990123) observed by the CGRO (Briggs et al. 1999). This spectrum is constructed by combining the BATSE, OSSE, COMPTEL and EGRET detectors. The horizontal axis denotes the energy at the GRB rest frame. The upper panel is a photon spectrum in units of photons/cm^2/s/MeV and the lower panel is the νF_ν spectrum in units of erg/cm^2/s. This GRB spectrum can be fitted by a Band function.

function, and found a positive correlation between the total energy and the peak energy in the source frame. The total energy is calculated in 1-10,000 keV assuming an z by $E^{\rm src}_{\rm peak} = (1+z)E^{\rm obs}_{\rm peak}$. They found that more luminous GRBs are characterized also by large peak energies following the relation: $E^{\rm src}_{\rm peak} \propto E^{0.5}_{\gamma,{\rm iso}}$ (Figure 1.7).

$E^{\rm src}_{\rm peak} - L_{\rm peak}$ Relation (Yonetoku's Relation)

Yonetoku et al. (2004) found a positive correlation between the spectral peak energy in the source frame ($E^{\rm src}_{\rm peak}$) and the isotropic peak luminosity ($L_{\rm peak}$). The peak luminosity is calculated in 30-10,000 keV. With a sample of 12 GRBs of known redshift they found that: $L_{\rm peak} \propto {E^{\rm src}_{\rm peak}}^{2.0}$ (Figure 1.8).

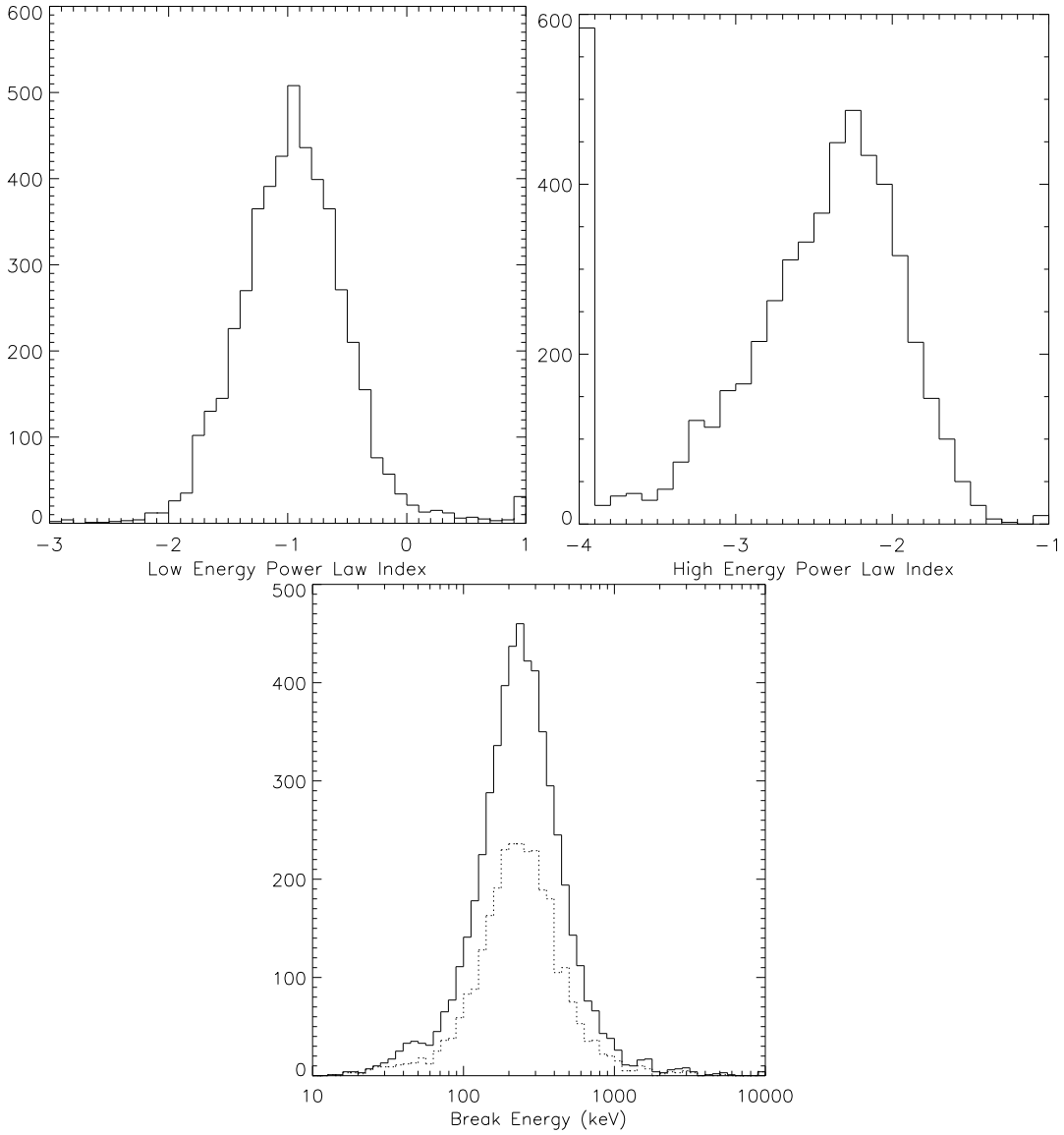

Figure 1.6: Distributions of low-energy power-law index ($left$), high-energy power-law index (*center*) and break energy (*bottom*) of bright BATSE GRBs (Preece et al. 2000)

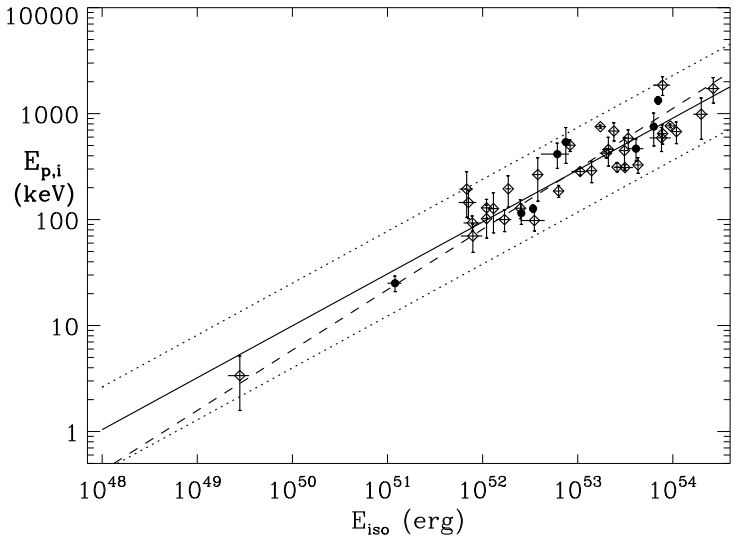

Figure 1.7: Redshift corrected peak energy and total energy values for 41 GRBs/XRFs with firm redshift and peak energy estimate. The solid line is the best fit power-law $E_{\rm peak}^{\rm src} = 95 \times E_{\gamma,{\rm iso}}^{0.49}$.

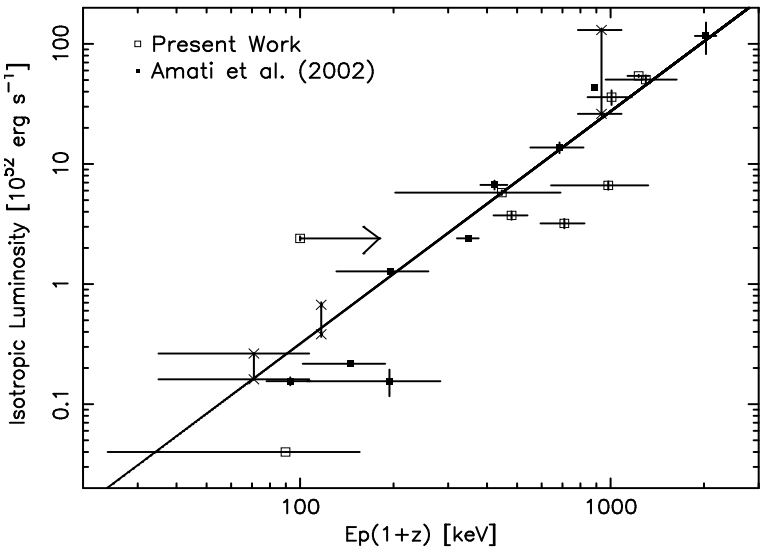

Figure 1.8: $E_{\rm p}$-luminosity relation. The open squares are our present results with BATSE. The results of BeppoSAX (Amati et al. 2002) are also shown as the filled squares. Both results are plotted as $E_{\rm peak}^{\rm src}$ at the rest frame of the GRBs and the peak luminosity between 30 and 10,000 keV derived by the 1 s peak flux. The points shown with two crosses indicate the results of GRBs with ambiguous redshifts (GRB 980326, GRB 980329 and GRB 000214). The solid line is the best-fit power-law model for the data: $(L/10^{52}$ ergs/s$) = 2.34 \times 10^{-5} \times {E_{\rm peak}^{\rm src}}^{2.0}$.

1.2.2 Afterglow

On February 28, 1997, there was a breakthrough to solve the GRB distance mystery. The Beppo-SAX satellite detected a historical gamma-ray burst, GRB 970228 with its Wide Field Camera (WFC). The WFC had a wide field of view (FOV) of 20 degrees×20 degrees as well as a precise localization with ∼5 arcmin accuracy. It allowed the satellite to point the X-ray telescopes onboard the same satellite ∼8 hours later, resulting in discover of a fading X-ray source - an X-ray afterglow, as shown in Figure 1.9 (Costa et al. 1997). The rapid localization also enabled a multi-wavelength observational campaign which allowed the discovery of the optical afterglow (van Paradijs et al. 1997) and the host galaxy (HST observation shown in Figure 1.10) leading to measurement of the redshift of GRB 970228 at 0.695. Thus, it is finally revealed that GRBs are cosmological sources.

Before the *Swift* era, redshifts are determined well for 41 GRBs. Figure 1.12 shows the redshift distribution, where the average is ∼1.3 with the highest 4.5 (Andersen et al. 2000).

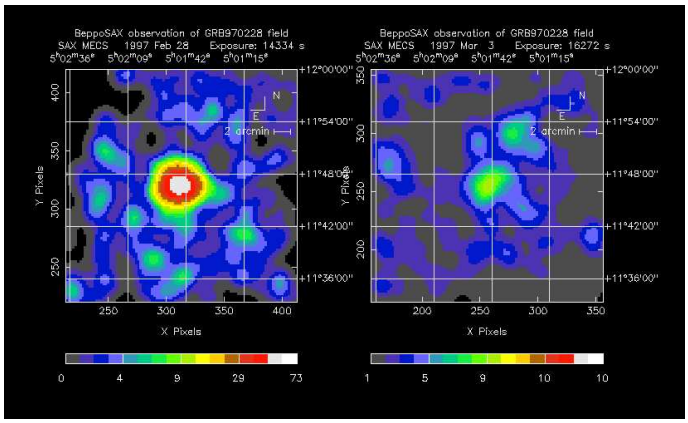

Figure 1.9: Images of the fading X-ray afterglow of GRB 970228 detected by BeppoSAX satellite (Costa et al. 1997)

The afterglow light curve of most GRBs show a smooth power-law decay with the time. This is consistent with the prediction of the simplest model of a spherical blast wave propagating into a uniform medium, where the spectrum consists of several power-law segments in which $F_\nu \propto \nu^{-\beta} t^{-\alpha}$ (Sari, Piran & Narayan 1998), and remains valid for an external density that drops as r^{-2} as expected for a stellar wind environment of massive star progenitor (Chevalier & Li 2000) and for jetted outflow (Rhoads 1999; Sari, Piran & Halpern 1999).

However, entering in the High Energy Transient Explore ($HETE-2$) era, accurate, rapid $HETE-2$ localizations sent to ground-based telescopes made it possible to observe

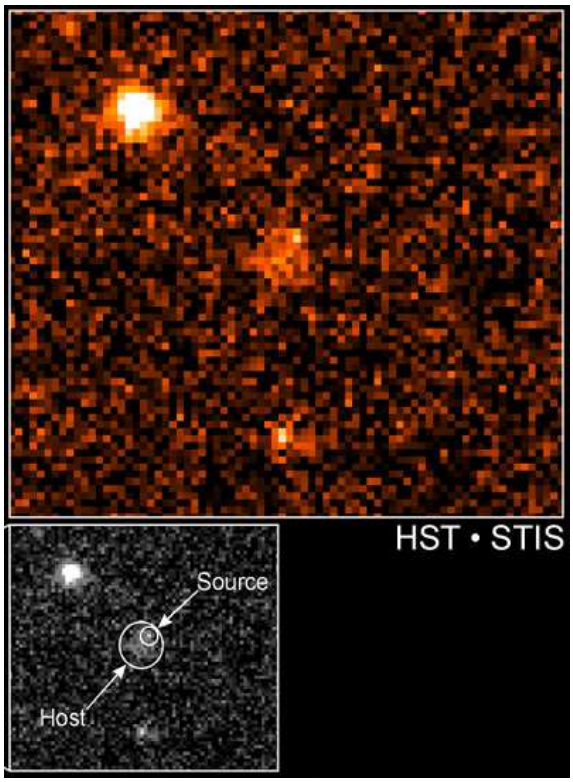

Figure 1.10: Hubble image of the optical afterglow of GRB 970228. Black and white images indicate the locations of the GRB source and the extended emission from the host galaxy. (Fruchter et al. 1999)

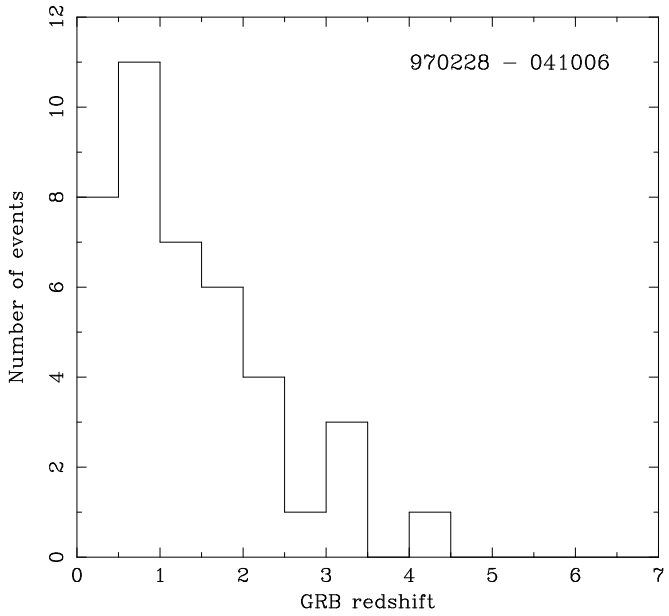

Figure 1.11: Redshift distribution before the *Swift* era.

the early afterglows and have revealed that some GRBs show deviations from a smooth power-law light curve. For example, GRB 021004 localized by $HETE-2$ showed a highly variable light curve, with several bumps and wiggles from a simple power-law (e.g., Fox et al. 2002, and Mirabal et al. 2002). GRB 030329 localized by $HETE-2$ (Vanderspek et al. 2003) also showed such a short time variability (Uemura et al. 2003, Sato et al. 2003). Light curve variability, i.e., bumps and wiggles, may be associated with the forward/reverse shock structures along the afterglow emitting regions (Kobayashi & Zhang 2003), fluctuation in the density of the interstellar medium (Nakar, Piran & Granot 2003), or repeated energy injection from the central engine (Granot, Nakar & Piran 2003). The early slow decay of GRB 021004 was interpreted by Fox et al. (2003) as arising from delayed shocks and continuous energy ejection from the central engine (Rees & Meszaros 1998; Kumar & Piran 2000; Sari & Meszaros 2000).

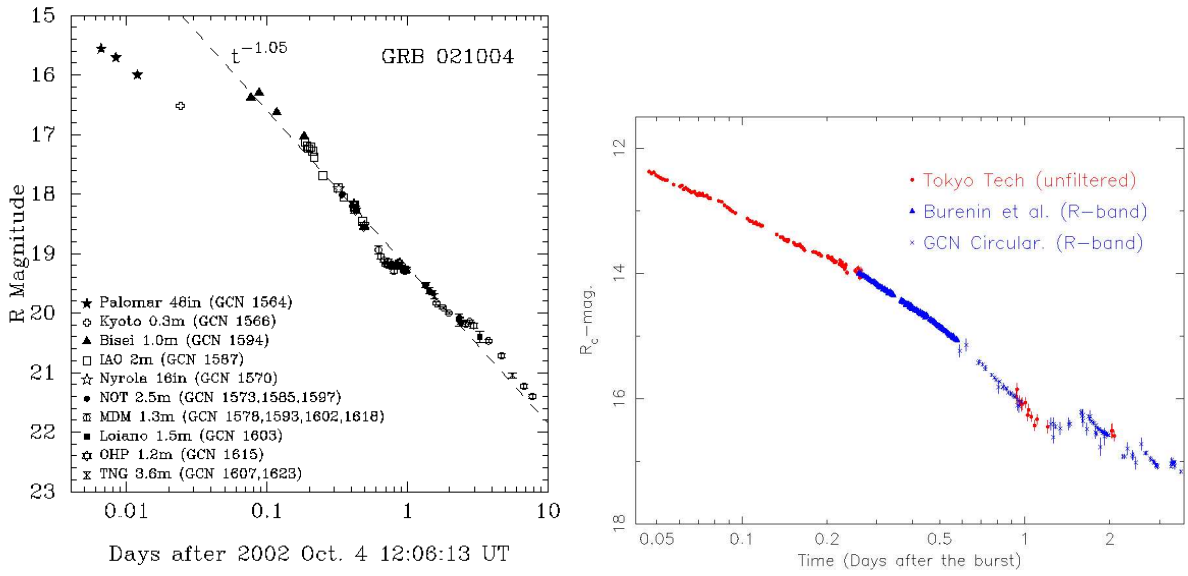

Figure 1.12: Light curve of the optical afterglow GRB 021004 (*left*; Mirabal et al. 2002) and GRB 030329 (*right*). These light curves show deviations from a smooth power-law light curve.

1.2.3 Supernova - GRB Connection

Evidence that at least some GRBs are connected to supernovae (SNe) is mounting. After the serendipitous discovery of SN 1998bw in coincidence with GRB 980425 (Galama et al. 1998), several other cases of possible SNe in GRBs have been reported (e.g., Bloom et al. 2002; Garnavich et al. 2003). All of these were, however, based only on the detection

of "bump" in the light curves of GRB afterglows, which could be decomposed to look like the light curve of SN 1998bw.

SN 1998bw was no ordinary SN. Its broad spectral features were explained as indicating a very energetic Type Ic SN (arising from the collapse of the bare CO core of a massive star). Because of its high explosion kinetic energy ($\sim 5 \times 10^{52}$ ergs in spherical symmetry), and the consequently very broad spectral lines, SN 1998bw was called a "hypernova" (Iwamoto et al. 1998). Other hypernovae have been discovered and analyzed (e.g., SNe 1997ef (Iwamoto et al. 2000; Mazzali , Iwamoto, & Nomoto 2000)) and SN 2002ap (Mazzali et al. 2002), but none were associated with GRB. This may be related to the fact that none of these SNe were either as bright or as powerful as SN 1998bw. So far, the only other positive detection of a SN spectrum in a GRB afterglow was the case of GRB 021203/SN 2002lw (Della Valle et al. 2003).

However, the situation has been dramatically improved by detection of GRB 030329. GRB 030329 was detected by the $HETE-2$ satellite on 2003 March 29. Its optical afterglow was 12.4 mag at 67 minutes after the burst (Sato et al. 2003). Optical spectroscopic observations have determined Its redshift was determined $z = 0.1685$ with optical spectroscopic observations (Greiner et al. 2003). which is one of the closest ever known and is possibly related to the exceptional brightness of this afterglow. A spectral signature very similar to SN 1998bw began to emerge in the spectrum of GRB 030329 $\sim$ 7 days after the burst (Stanek et al. 2003, Matheson et al. 2003), and became more prominent in the following days (Figure 1.13). This provides the best evidence so far for the association of GRBs with core collapse supernovae of the type of SN 1998bw.

1.3 Jet

It is widely believed that the GRB outflows are collimated like jets. When the emitting material has a highly relativistic speed, the radiations emitted isotropically in the rest frame of the emitting material, i.e. co-moving frame, are concentrated in the forward direction in the observer frame (relativistic beaming effect). Half of the radiations lie within a cone of half-angle $1/\Gamma$, and very few photons will be emitted with the off-axis angle $\theta \gg \Gamma$. Therefore, even if the radiations are emitted from a collimated shell-like jet, they are observed as long as the observer is located with in the radiation cone. It is considered that the material expands with the velocity $\sim c$ in the co-moving frame, and this may change the result. Let us assume that the shell expands to the radius R within time $t \sim R/c$ as shown in Fig 1.14, where h and $\theta_{\rm j}$ are the lateral size and the initial angular size, respectively.

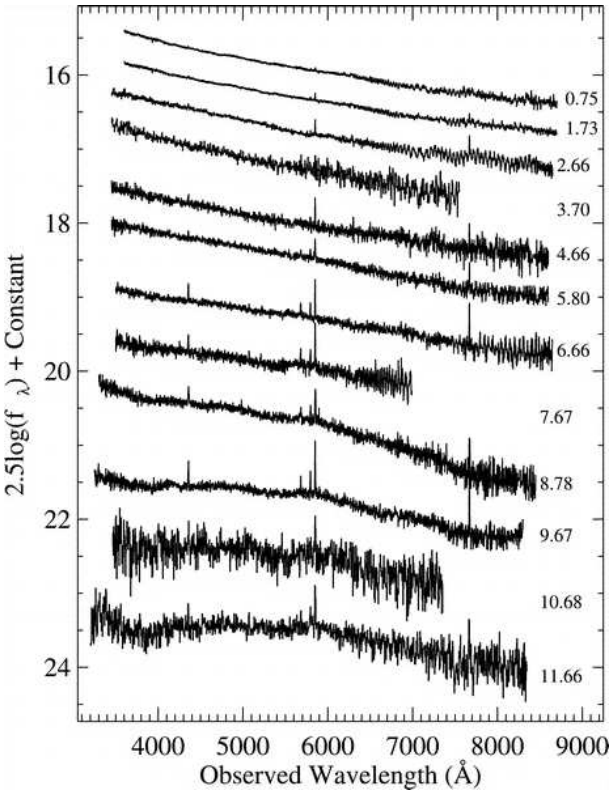

Figure 1.13: Evolution of the GRB 030329/SN 2003dh spectrum, from 0.75 days to 11.66 days after the burst. The early spectra consistent of a power-law continuum with narrow emission lines originating from HII regions in the host galaxy at $z = 0.1685$. Spectra taken after 6.66 days after the burst show the development of broad peaks characteristic of a supernova (Matheson et al. 2003).

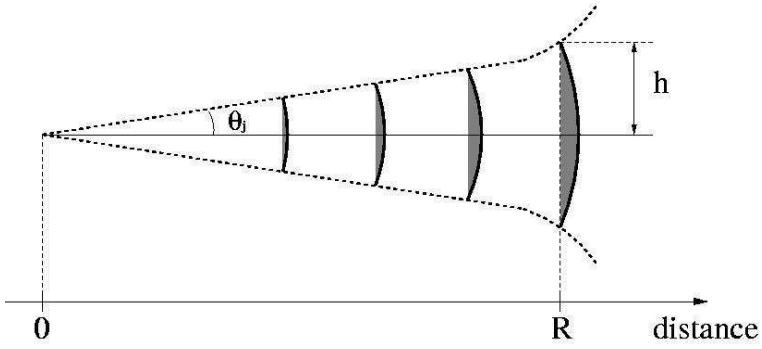

Figure 1.14:

Due to the Lorentz time dilation, only the time $t_{\rm com} \sim R/c\Gamma$ is elapsed in the shell co-moving frame. The total angular size is hence given by

$$h \simeq R\Big(\theta_{\rm j} + \frac{1}{\Gamma}\Big). \tag{1.2}$$

As long as $\Gamma \ll 1/\theta_{\rm j}$, the opening angle is almost constant and $\sim \theta_{\rm j}$. When the shell is decelerated to $\Gamma \sim 1/\theta_{\rm j}$, it begins to spread sideways. The shell sweeps more and more materials, and is more rapidly decelerated after that. This transition can be observed as a steeping break in a light curve, which is called the "jet break". The temporal scalings are expected as $F_\nu \propto t^{-1/3}$ and $F_\nu \propto t^{-p}$ below and above the frequency of $\nu_{\rm m}$ (see Section 2.1), where p is the index of the electron distribution.

Harrison et al. (1999) reported that the optical light curve of GRB 990510 exhibits a steeping break at ~ 1 day changing from $t^{-0.82}$ to $t^{-2.18}$. They also reported that the radio light curve is consistent with that having a break at the same time (~ 1 day). Since the jet break is being due to hydrodynamical transition, the break should be wave-length independent, and therefore the observations support the jet break scenario.

It is possible to calculate a jet opening angle by finding $\theta_{\rm j} \sim 1/\Gamma$:

$$\theta_{\rm j} = 0.161\Big(\frac{t_{\rm j,d}}{1+z}\Big)^{3/8}\Big(\frac{n\eta_\gamma}{E_{\rm iso,52}}\Big)^{1/8}, \tag{1.3}$$

where $t_{\rm j,d}$ is the break time in days, and $E_{\rm iso,52}$ is the isotropic energy in gamma-rays. It is also assumed that the fireball emits a fraction of η_γ of its kinetic energy in the prompt GRB phase. Frail et al. (2001) collected jet break times for 15 GRBs with known redshifts. A wide range of jet opening angles were inferred from those of samples from $\sim 3^\circ$ to more than $\sim 25^\circ$. The true radiated energy is calculated by correcting the opening angle as $E_\gamma \equiv (1 - cos\theta_\gamma)E_{\rm iso}$. Although the $E_{\rm iso}$ ranges from $\sim 5 \times 10^{51}$ to 1.4×10^{54} erg, the geometry-corrected energy E_γ appear narrowly clustered around the "standard" energy of 5×10^{50} erg as shown in Fig 1.15 (*left*). Bloom et al. (2003) calculated the E_γ for a sample of 24 GRBs using more reliable values of the ambient densities. They confirmed the tight E_γ distribution and refined the standard energy at $1.33 \pm 0.07 \times 10^{51}$ erg as shown in Fig 1.15 (*right*).

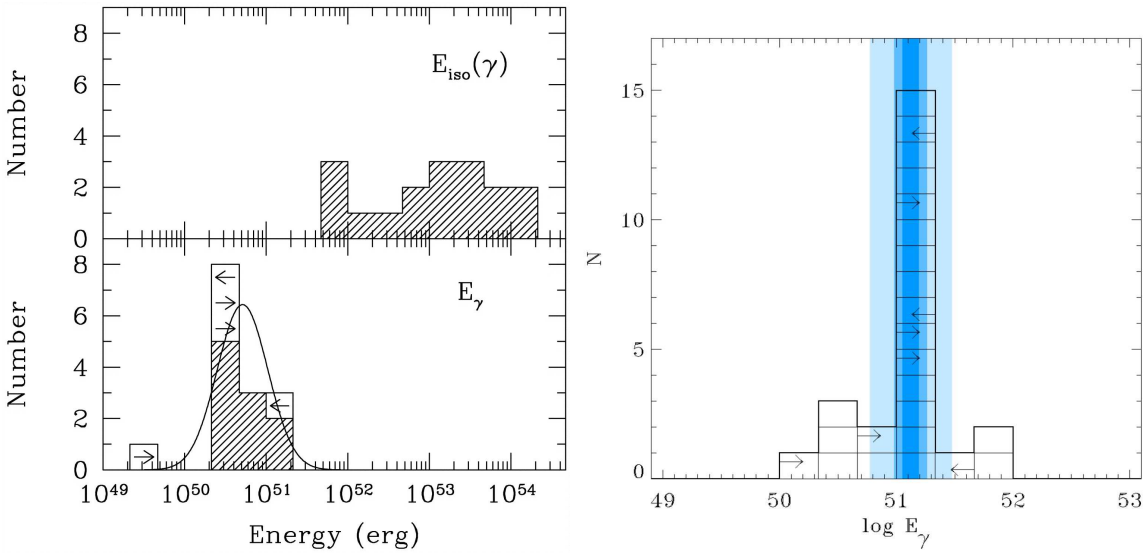

Figure 1.15: *Left*: Distribution of the apparent $E_{\rm iso}$ of GRBs with known redshifts (*top*) and the geometry corrected energy E_γ (*bottom*) (Frail et al. 2001). $E_{\rm iso}$ ranges in ~ 3 orders of magnitudes, but $E_{\rm gamma} = (1 - cos\theta_{\rm j})E_{\rm iso}$ has a narrow distribution around the standard energy of $\sim 5 \times 10^{50}$ erg. *Right*: Distribution of the geometry corrected energy $E_{\rm gamma}$ reported by Bloom et al. (2003).

Chapter 2

Cosmological Fireball Model

In this section, we follow the discussions which led to the development of the standard cosmological GRB model, which is well described in e.g. Piran (1999). Let us start from tracing the enormous amount of gamma-ray photons back to the GRB emitting site. The size of the emitting region can be estimated by the pulse width of the light curve, which gives the lower limit of the light travel time of the source (Rybicki & Lightman 1979). Since the pulse as short as $\delta t = 10$ ms is detected in the GRB emission, the emitting region is very compact with the size,

$$\begin{aligned} R &\leq \delta t \times c \\ &\simeq 3 \times 10^8 \left(\frac{\delta t}{10 \text{ ms}} \right) \text{ cm} \\ &= 3000 \left(\frac{\delta t}{10 \text{ ms}} \right) \text{ km}. \end{aligned}$$

The luminosity is also calculated from the observed energy flux F:

$$\begin{aligned} L &= 4\pi d^2 F \\ &\simeq 10^{50} \left(\frac{d}{3 \text{ Gpc}} \right)^2 \left(\frac{F}{10^{-7} \text{ erg cm}^{-2}} \right) \text{ erg s}^{-2} \end{aligned}$$

where d is a distance between the source and the observer. Then, the number density of gamma-rays n_γ is given as follows:

$$n_\gamma = \frac{L}{4\pi R^2 \epsilon c}$$

$$\simeq \ 2\times 10^{27}\Big(\frac{d}{3\ \mathrm{Gpc}}\Big)^2\Big(\frac{F}{10^{-7}\ \mathrm{erg\ cm^{-2}}}\Big)\Big(\frac{\delta t}{10\ \mathrm{ms}}\Big)^{-2}\mathrm{cm^{-3}}$$

where ϵ is a typical energy of the gamma-ray photons. Here we assumed $\epsilon \sim 1$ MeV. What if there is a sudden release of a large quantity of gamma-ray photons into a compact region? The electron-positron pair production $\gamma\gamma \longrightarrow \mathrm{e^+e^-}$ occurs if $\sqrt{(E_1E_2)} > m_\mathrm{e}c^2$, where E_1 and E_2 are energy of interacting photons. The optical depth $\tau_{\gamma\gamma}$ along the region size R is obtained as

$$\begin{aligned}\tau_{\gamma\gamma} &\simeq \sigma_\mathrm{T} n_\gamma R \\ &\simeq 4\times 10^{11}\Big(\frac{d}{3\ \mathrm{Gpc}}\Big)^2\Big(\frac{F}{10^{-7}\ \mathrm{erg\ cm^{-2}}}\Big)\Big(\frac{\delta t}{10\ \mathrm{ms}}\Big)^{-1}\mathrm{cm^{-3}}\end{aligned}$$

where σ_T is the Thomson cross section. We can realize an emerge of the opaque photon-lepton "fireball". However, since gamma-rays cannot survive in the fireball, the radiation cannot escape. This is known as the "compactness problem" (Epstein 1986 , Paczynski 1986).

A way to avoid this problem is to introduce a relativistic motion. Let us assume that the emitting source moves with the velocity of $v = \beta c$, where the Lorentz factor is defined as $\Gamma = 1/\sqrt{1-\beta^2}$. The energy of the photons received by the observer in the direction of θ is affected by the factor of $\delta = 1/\Gamma(1-\beta cos\theta)$, which is called "beaming effect" (Rybicki & Lightman 1979). When the angle $\cos\theta \sim \beta$, the photon is blue-shifted by $\delta \sim \Gamma$, and hence the energy can be lower than the sufficient energy for pair production. According to the detailed calculation, the cross-section becomes lower by a factor of $\Gamma^{-2\alpha}$ assuming a power-law distribution with the high-energy spectral index of α. In addition, when the emitting region moves toward the observer, the observed time scale is shorter by a factor of $1/2\Gamma^2$. The emitting region therefore can be larger by the same factor. Thus, the optical depth can be decreased by the relativistic motion as follows:

$$\tau_{\gamma\gamma} \propto \Gamma^{-2\alpha-2}. \tag{2.1}$$

The spectral index α is typically $\sim 2-3$. In order to obtain an optically thin fireball, approximately $\Gamma > 100$ is required.

This relativistic motion can be understood as a natural attribute of the time evolution of a pure radiation fireball. Because of the opacity of pair production, the fireball becomes photon-lepton plasma, which behaves like a perfect fluid. The local temperature drops

with $T \propto 1/R$ with a free expansion, where R is a radius. Energy conservation requires $E\Gamma =$ const., and hence $\Gamma \propto E^{-1} \propto T^{-1} \propto R$. Thus the fireball is accelerated and expands relativistically outwards. After the temperature drops low enough that pair annihilation dominates, gamma-rays can escape from the region and become detectable by the observer. However, the spectrum thus obtained is thermal with the temperature $T\Gamma$, which is equal to the initial temperature. This difficulty is solved by a contamination of baryonic matters. The baryonic load increases the opacity even after $\tau_{\gamma\gamma}$ becomes negligible, and convert the part of received energy into the bulk kinetic energy. As a result, the matter coast asymptotically with a constant Lorentz factor. The baryonic mass as small as $\sim 10^{-6} M_*$ is required so that the fireball becomes relativistic, otherwise the fireball cannot be accelerated enough, and the expansion becomes Newtonian.

2.1 The Internal-External Shock Scenario

The energy carried by the matter-dominated outflow should be somehow converted into radiation again to produce the gamma-ray burst emissions. The shock dissipation is the most likely mechanism to provide such energy transfers. Figure 2.1 illustrates the standard GRB fireball model. Let us assume a several of tens of blobs are ejected from the central engine of the gamma-ray burst. Due to Lorentz contractions, each blob looks like a thin "shell" for the observer in the rest frame. Collisions take place between the shells with different velocities. The collision distance is estimated as $\sim 10^{14}$cm. This is called "internal shock". This scenario is the most favored because it can explain the variability in the prompt emissions. The shells (or a merged blob after the collisions) continue to expand and collide with the inter-stellar medium (ISM). This collisions is considers to take place at $\sim 10^{16}$cm and gradually decelerated by the ambient gas. The emission will therefore show more smooth changes, which is the afterglow. This is called "external shock".

2.1.1 Internal Shock

Here, we follow the calculations in Kobayashi, Piran & Sari (1997). We assume that a relatively slow shell with the mass of $M_{\rm s}$ and the Lorentz factor of $\Gamma_{\rm s}$ is ejected, and then another relatively rapid shell can catch up the slow one, and two merge to form a single one. Energy and momentum conservation gives a bulk Lorentz factor of merged shell as:

$$\Gamma_{\rm m} \simeq \sqrt{\frac{M_{\rm r}\Gamma_{\rm m} + M_{\rm s}\Gamma_{\rm s}}{M_{\rm r}/\Gamma_{\rm m} + M_{\rm s}/\Gamma_{\rm s}}}. \tag{2.2}$$

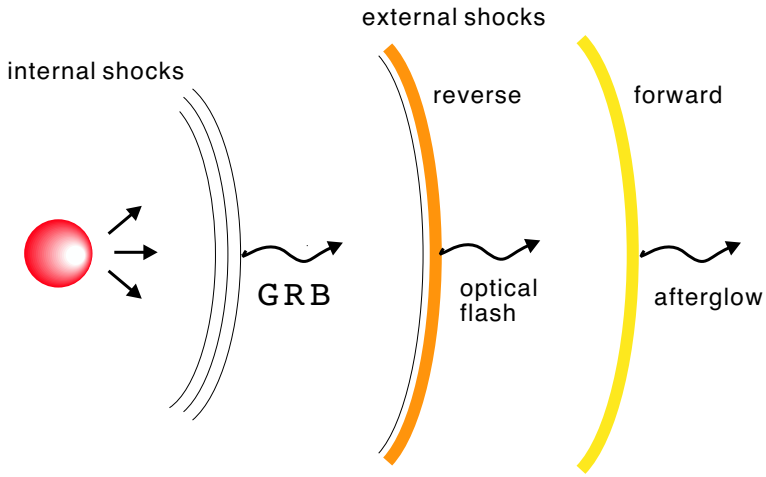

Figure 2.1: Outline of a fireball model. A large amount of shells with variable Lorentz factor is emitted from the central engine, and they interact with each other by the internal shocks, then prompt GRBs are generated. A merged shell propagates into the ISM, and the following afterglow is produced.

Using the difference of the bulk kinetic energy before and after the merging, the generated internal energy can be estimated as follows:

$$E_{\rm int} = M_{\rm r}c^2(\Gamma_{\rm r} - \Gamma_{\rm m}) + M_{\rm s}c^2(\Gamma_{\rm s} - \Gamma_m). \tag{2.3}$$

The conversion efficiency of the kinetic energy into the internal energy is given as

$$\eta = 1 - \frac{(M_{\rm r} + M_{\rm s})\Gamma_{\rm m}}{M_{\rm r}\Gamma_{\rm r} + M_{\rm s}\Gamma_{\rm s}} \simeq 1 - \frac{2\sqrt{\Gamma_{\rm r}/\Gamma_{\rm s}}}{1 + \Gamma_{\rm r}/\Gamma_{\rm s}}. \tag{2.4}$$

The approximation in the above formula is made for the case that the colliding two shells have similar mass. As the difference in velocity is larger, the efficiency becomes higher. If the Lorentz factor of the shells distributes from 100 to 1000, the efficiency can be reached to $\sim 20\%$ on average.

2.1.2 External Shock

For simplicity, the expansion of the ejecta into ISM is assumed as iterative interactions of the shell characterized by the velocity β, Lorentz factor Γ and the mass M with a small fraction of ISM with the velocity of 0, the Lorentz factor of 1 and the mass $\mathrm{d}m$. The merged shell obtains $\Gamma + \mathrm{d}\Gamma$, $M + \mathrm{d}m + \mathrm{d}E$, $\beta + \mathrm{d}\beta$, where $\mathrm{d}E$ is a newly generated internal energy. Energy momentum conversion for each interaction is written as

$$\begin{cases} M\Gamma + \mathrm{d}m = (M + \mathrm{d}m + \mathrm{d}E)(\Gamma + \mathrm{d}\Gamma), \\ M\beta\Gamma = (M + \mathrm{d}m + \mathrm{d}E)(\beta + \mathrm{d}\beta)(\Gamma + \mathrm{d}\Gamma), \end{cases} \tag{2.5}$$

The obtained internal energy is partly converted into radiation. Here we define the fraction as ϵ. Equation yields a relation between the swept-up mass m and the Lorentz factor:

$$\frac{m}{M_0} = \frac{1}{(2-\epsilon)\Gamma_0}\left(\frac{\Gamma}{\Gamma_0}\right)^{-2+\epsilon}, \tag{2.6}$$

where the parameters denoted with 0 are the initial values, and $\Gamma_0 \gg \Gamma \gg 1$ is assumed here. This implies that only a mass $m \sim M_0/\Gamma_0$ is required to decelerate the ejecta to $\Gamma_0/2$ regardless of the parameter ϵ. The swept-up mass inside the radius of R is given as $\frac{4}{3}\pi R^3 n m_\mathrm{p}$ assuming a uniform density n for ISM. Equating this with Eq. 2.6, we obtain the Lorentz factor as the function of radius:

$$\Gamma \propto R^{-\frac{3}{2-\epsilon}}. \tag{2.7}$$

If we assume an extreme case of $\epsilon = 0$, which means an adiabatic expansion, the Lorentz factor evolve as $\Gamma \propto R^{-3/2}$. In the other limit of $\epsilon = 1$, where the internal energy is fully converted into radiation, the Lorentz factor evolves as

$$\Gamma \propto R^{-3}. \tag{2.8}$$

In the mean time, due to the relativistic motion, the time interval is shortened for the observer. The observed time delay $\mathrm{d}t_\mathrm{obs}$ between the emissions at the radius R and at $R + \mathrm{d}R$ is calculated as

$$\mathrm{d}t_\mathrm{obs} = \frac{\mathrm{d}R}{2\Gamma^2 c}. \tag{2.9}$$

The observed time t_obs has the same dependence $t_\mathrm{obs} \propto R/\Gamma^2$. Thus, we can rewrite the evolution as a function of observed time: $R \propto t^{1/4}$ and $\Gamma \propto t^{-3/8}$ for the adiabatic case, and $R \propto t^{1/7}$ and $\Gamma \propto t^{-3/7}$ for the radiative case. Blandford & McKee (1976) discovered a self-similar solution that describes the adiabatic slowing down of an extremely relativistic shell propagating into the ISM, It yields more precise results:

$$R(t) = \left(\frac{17E_0 t}{\pi n m_\mathrm{p} c}\right)^{1/4} = 3.2 \times 10^{16} E_{52}^{1/4} n^{-1/4} t_\mathrm{obs}^{1/4} \text{ cm}, \tag{2.10}$$

$$\Gamma(t) = \frac{1}{4}\left(\frac{17E_0}{\pi n m_\mathrm{p} c^5 t^3}\right)^{1/8} = 260 \times E_{52}^{1/8} n^{-1/8} t_\mathrm{obs}^{3/8}, \tag{2.11}$$

where E_{52} is the initial energy of ejecta in the unit of 10^{52} erg.

2.1.3 Energy Transfer & Radiation Mechanism

The conversion from the internal energy to radiation is considered as follows (Sari et al. 1998). The collision within shells or between a shell and ISM produces shocks, which can be relativistic depending on the shock condition determined by the two quantities: the Lorentz factor describing the relative motion of the two shells, and the ratio of densities between the two materials. The shock accelerates electrons to have very high energies, and also forms an extremely strong magnetic field. The most likely process to radiate gamma-ray photons is synchrotron emission. An available energy through shock-heating is calculated as

$$U \sim \Gamma_{\rm sh} n m_{\rm p} c^2, \tag{2.12}$$

where $\Gamma_{\rm sh}$ is the relative Lorentz factor, n is the density of shocked materials, and $m_{\rm p}$ is the proton mass. We assume that the energy is given to electrons in part with a fraction of $\epsilon_{\rm e}$, and that a power-law distribution of electrons is formed in some acceleration mechanisms such as Fermi acceleration:

$$N(\gamma_{\rm e}) \propto \gamma_{\rm e}^{-p} \qquad \text{for} \quad \gamma_{\rm e} > \gamma_{\rm e,m}, \tag{2.13}$$

where $\gamma_{\rm e}$ and $\gamma_{\rm e,m}$ are the Lorentz factor of electrons and that of electrons with minimum energy, respectively. This Lorentz factor represents the random motion of electrons, i.e. the Lorentz factor in co-moving frame of the outflow. We write it in a small letter while we write the Lorentz factor of bulk motion of the outflow in a capital letter, Γ. The total energy of the electrons is given by

$$\int_{\gamma_{\rm e,m}} m_{\rm e} c^2 \gamma_{\rm e} N(\Gamma_{\rm e}) {\rm d}\gamma_{\rm e} = n m_{\rm e} c^2 \gamma_{\rm e,m} \frac{p-1}{p-2} \tag{2.14}$$

in the case that the index p is larger than 2. Equating the above formula and the energy given to electrons ($\epsilon_{\rm e}$), we obtain

$$\gamma_{\rm e,m} = \frac{m_{\rm p}}{m_{\rm e}} \frac{p-2}{p-1} \epsilon_{\rm e} \Gamma_{\rm sh} \sim 610 \epsilon_{\rm e} \Gamma_{\rm sh}. \tag{2.15}$$

The approximation in the above formula is made assuming $p \sim 2.5$. The minimum energy of electrons are thus determined mainly by the shock strength represented by $\Gamma_{\rm sh}$. Because it is measured as a relative velocity of colliding materials, $\Gamma_{\rm sh}$ is a few for internal shocks. On the other hand, since the un-shocked material, ISM, is at rest for external shock, $\Gamma_{\rm sh}$ is equal to that of ejecta, and therefore first higher and decreases as the ejecta expands into ISM.

Synchrotron emission from a single particle has a fairly broad spectrum with a power-law with $F_\nu \propto \nu^{1/3}$ up to the characteristic energy

$$(h\nu)_{\rm obs} = \frac{\hbar e B}{m_{\rm e} c} \gamma_{\rm e}^2 \Gamma, \tag{2.16}$$

and an exponential decay above it. The Lorentz factor of bulk motion, Γ, is multiplied because of the beaming effect. In order to calculate the overall spectrum we need to integrate it over $\gamma_{\rm e}$. Moreover, if the electron is energetic, it will cool rapidly until it will reach $\gamma_{\rm e,c}$, which is the Lorentz factor of an electron that cools on a hydrodynamic time scale. Two cases are considered by comparing $\gamma_{\rm e,c}$ to the minimum Lorentz factor, $\gamma_{\rm e,m}$. If $\gamma_{\rm e,c} < \gamma_{\rm e,m}$, all the electrons cool rapidly and distribution of electrons effectively extends down to $\gamma_{\rm e,c}$, which is called "fast cooling" regime. If $\gamma_{\rm e,c} > \gamma_{\rm e,m}$, only the electrons above $\gamma_{\rm e,c}$ cool and the system is in the "slow cooling" regime. Fig 2.2 shows expected spectra for two regimes given by Sari et al. (1998). The spectrum consists of four segments separated by $\nu_{\rm m}$, $\nu_{\rm c}$, $\nu_{\rm a}$; $\nu_{\rm a}$ is the synchrotron self absorption frequency, $\nu_{\rm m}$ is the synchrotron critical frequency for electrons with the minimum Lorentz factor, and $\nu_{\rm c}$ is the synchrotron cooling frequency, respectively. There is an effect of synchrotron self-absorption below $\nu_{\rm a}$.

Using the scalings on the radius R and the bulk Lorentz factor Γ derived in the previous section, the variation of the frequencies with time are calculated. The transitions between the two regimes occurs when $\nu_{\rm c} = \nu_{\rm m} \equiv \nu_0$. The expected light curves are shown in Fig 2.2. If the observation is made in relatively high frequency ($\nu > \nu_0$), the characteristic frequency $\nu_{\rm c}$ and $\nu_{\rm m}$ passes the observation is made in relatively low frequency ($\nu < \nu_0$), we experience the regime transition first, and followed by $\nu_{\rm m}$ and $\nu_{\rm c}$ in this order.

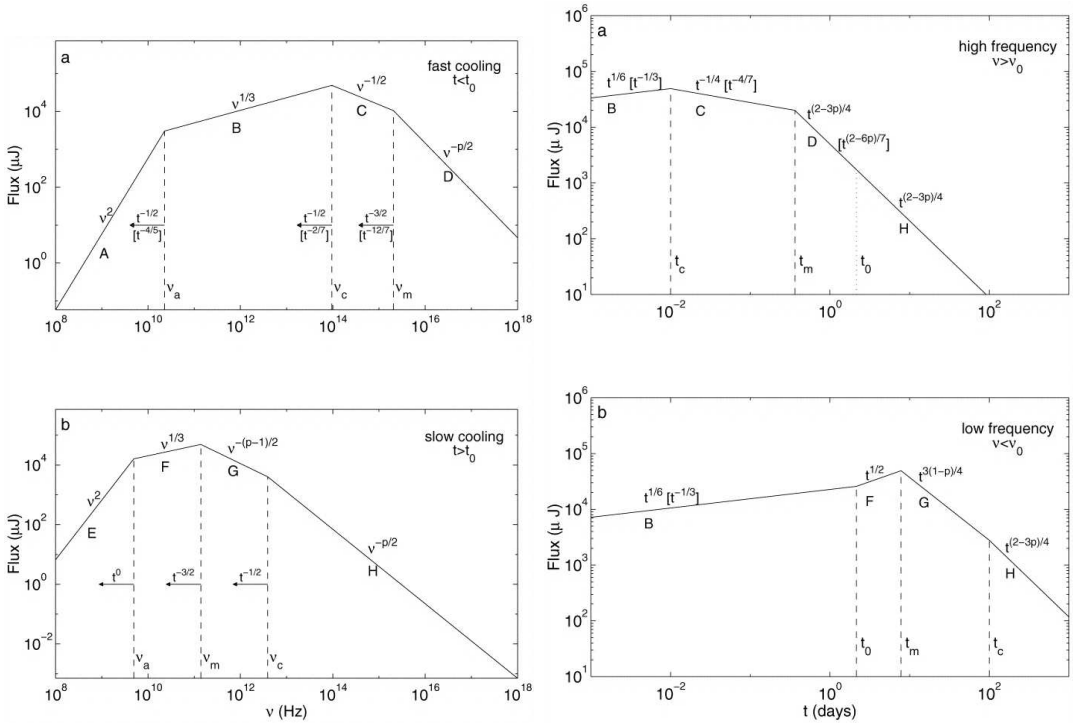

Figure 2.2: *Left*: Expected spectra in the fast cooling regime in the *top* panel and in the slow cooling regime *bottom* panel. The spectrum consists of four segments identified by A,B,C,D and E,F,G,H, respectively. The frequencies $\nu_{\rm m}$, $\nu_{\rm c}$ and $\nu_{\rm a}$ decreased with time. *Right*: Expected light curves for high frequency case, $\nu > \nu_0$, in the *top* panel and for low frequency case, $\nu < \nu_0$, in the *bottom* panels. The scaling above the arrows correspond to an adiabatic evolution. From Sari et al. (1998).

Chapter 3

Swift Gamma-ray Burst Explorer

3.1 The *Swift* Mission

Swift is a first-of-its-kind multi-wavelength observatory dedicated to the study of gamma-ray burst science (Gehrels et al. 2004). Its three instruments work together to observe GRBs and afterglows in the gamma-ray, X-ray, ultraviolet, and optical wavebands. The main mission objectives for *Swift* are to:

- Determine the origin of gamma-ray bursts.
- Classify gamma-ray bursts and search for new types.
- Determine how the blastwave evolves and interacts with the surroundings.
- Use gamma-ray bursts to study the early universe.
- Perform the first sensitive hard X-ray survey of the sky.

During the first two years of its mission (from December 2004 to the end of September 2006), *Swift* has detected 179 bursts with a sensitivity ~ 3 times fainter than the BATSE detector aboard the Compton Gamma-Ray Observatory. *Swift*'s Burst Alert Telescope detects and acquires high-precision locations for gamma-ray bursts and then relay a 1-4 arc-minute position estimate to the ground within 15 seconds. After the initial burst detection, the spacecraft "swiftly" (approximately 20 to 75 seconds) and autonomously re-points itself to bring the burst location within the field of view of the sensitive narrow-field X-ray and UV/optical telescopes to observe afterglow. *Swift* can provide redshifts for the bursts and multi-wavelength light curves for the duration of the afterglow. Figure 3.1 shows the redshift distribution, where the average is ~ 2.4 with the highest of 6.3: the

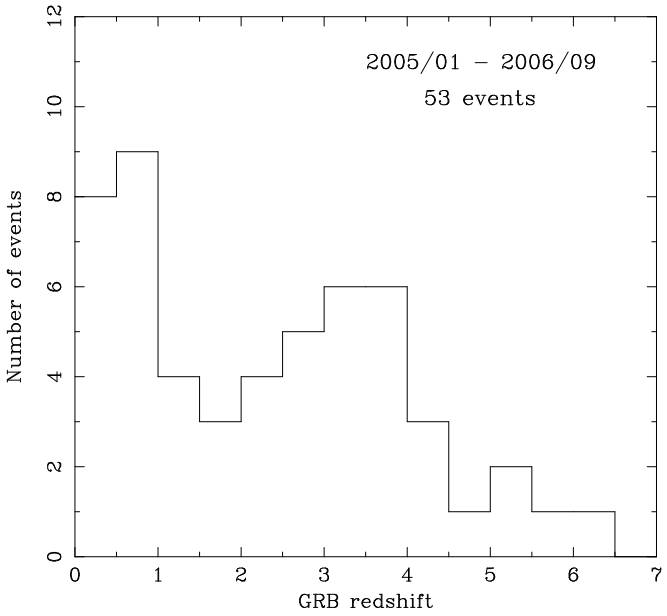

Figure 3.1: Redshift distribution after the *Swift* era.

previous record for a GRB was 4.5, the most distant quasar is at a redshift of 6.4 (Fan et al. 2003), and the most distant galaxy is at a redshift of ~ 7 (Kneib et al. 2004).

Swift measurements are of great interest to the astronomical community and all data products are available to the public via the Internet as soon as they are processed. The *Swift* mission represents the most comprehensive study of GRB afterglow to date. *Swift* is part of NASA's medium explorer (MIDEX) program and was launched into a low-Earth orbit on a Delta 7320 rocket on November 20, 2004. The hardware was developed by an international team from the United States, the United Kingdom, and Italy, with additional scientific involvement in France, Japan, Germany, Denmark, Spain and South Africa.

Baseline Capabilities:

- $>$ 200 GRBs studied over a two year period
- 0.3−5 arcsec positions for each GRB
- Multi-wavelength observatory (gamma, X-ray, UV and optical)
- 20−75 sec reaction time
- Approximately three times more sensitive than BATSE
- Spectroscopy from 1800−6000 $\AA$ and 0.2−150 keV
- Six colors covering 1800−6000 $\AA$

- Capability to directly measure redshift
- Results publicly distributed within seconds

The *Swift* telescope payload is comprised of three instruments which work in tandem to provide rapid identification and multi-wavelength follow-up of Gamma-ray bursts (GRBs) and their afterglows. Within 20 to 75 seconds of a detected GRB, the telescope slew autonomously so that the field-of-view of the pointed instruments overlap the location of the burst. The afterglows are monitored over their durations, and the data rapidly disseminated to the public.

Burst Alert telescope (BAT): 15−150 keV With its large field-of-view (1.4 sr half-coded & 2.3 sr partially coded) and high sensitivity, the BAT detect about 100 GRBs per year, and computes burst positions onboard the satellite with arc-minute positional accuracy. The BAT has been produced by the Exploration of the Universe Division at NASA's Goddard Space Flight Center (GSFC) with science flight software developed by Los Alamos National Laboratory.

X-ray Telescope (XRT): 0.3−10 keV The XRT was built with existing hardware from JET-X. The XRT takes images and is able to obtain spectra of GRB afterglows during pointed follow-up observations. The images are used for higher accuracy position localizations, while the spectra are used to determine redshifts from X-ray absorption lines. The XRT is a joint product of Pennsylvania State University, the Brera Astronomical Observatory (OAB), and the University of Leicester.

UV/Optical telescope (UVOT): 170−650 nm The UVOT is essentially a copy of the XMM Optical Monitor (OM). The UVOT takes images and obtains spectra (via a grism filter) of GRB afterglows during pointed follow-up observations. The images are used for 0.3−2.5 arc-second position localizations, while the spectra are used to determine redshifts and Lyman-alpha cut-offs. The UVOT is a joint product of Pennsylvania State University, and the Mullard Space Science Laboratory (MSSL).

In this thesis, we utilize the data obtained with BAT and XRT. We now summarize the properties of the three instruments (http://swift.gsfc.nasa.gov/; Gehrels et al. 2004).

3.2 Burst Alert Telescope (BAT)

3.2.1 Instrument Description

The Burst Alert Telescope (BAT) is a highly sensitive, large FOV instrument designed to provide critical GRB triggers and 4−arcmin positions (Fig.3.3). It is a coded aperture

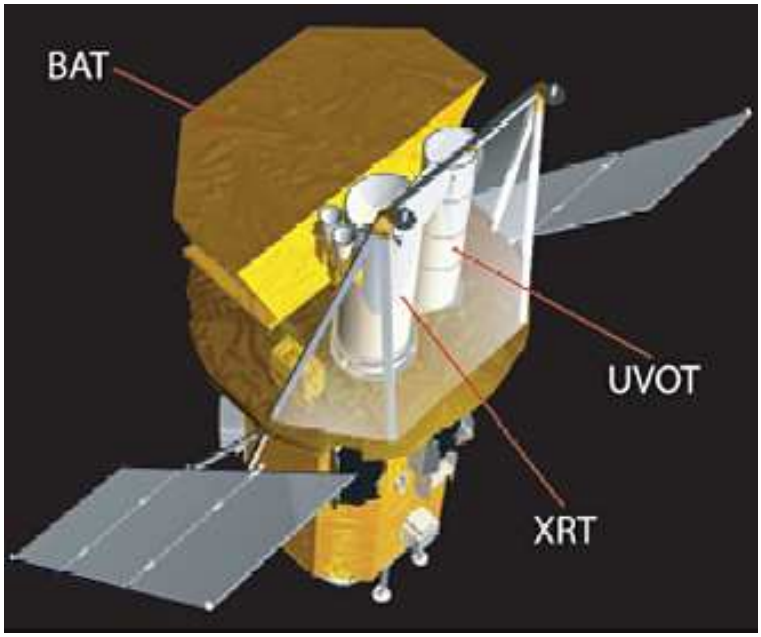

Figure 3.2: Swift's three scientific instruments (NASA/GSFC)

imaging instrument with a 1.4 steradian field-of-view (half coded). The energy range is 15−150 keV for imaging with a non-coded response up to 500 keV. Within several seconds of detecting a burst, the BAT calculates an initial position, decides whether the burst merits a spacecraft slew and, if so, sends the position to the spacecraft.

In order to study bursts with a variety of intensities, durations, and temporal structures, the BAT must have a large dynamic range and trigger capabilities. The BAT uses a two-dimensional coded aperture mask and a large area solid state detector array to detect weak bursts, and has a large FOV to detect a good fraction of bright bursts. Since the BAT coded aperture FOV always includes the XRT and UVOT fields-of-view, long duration gamma-ray emission from the burst can be studied simultaneously with the X-ray and UV/optical emission. The data from the BAT can also produce a sensitive hard X-ray all-sky survey over the course of $Swift$'s two year mission. The parameters of the BAT instrument are listed in Table 3.1. Further information on the BAT is given by Barthelmy (2003).

3.2.2 Technical Description

The BAT's 32,768 pieces of $4 \times 4 \times 2$ mm CdZnTe (CZT) form a 1.2×0.6 m sensitive area in the detector plane. Groups of 128 detector elements are assembled into 8×16 arrays, each connected to 128-channel readout Application Specific Integrated Circuits (ASICs). Detector modules (Fig. 3.4), each containing two such arrays, are further grouped by

Table 3.1: BAT Instrument Parameters.

Property	Description
Aperture	**Coded mask**
Detecting Area	**5200 cm^2**
Detector	**CdZnTe**
Detector Operation	**Photon counting**
Field of View	**1.4 sr (half-coded)**
Detection Elements	**256 modules of 128 elements**
Detector Size	**4 mm×4 mm×2 mm**
Telescope PSF	**17 arcmin**
Energy Range	**15−150 keV**

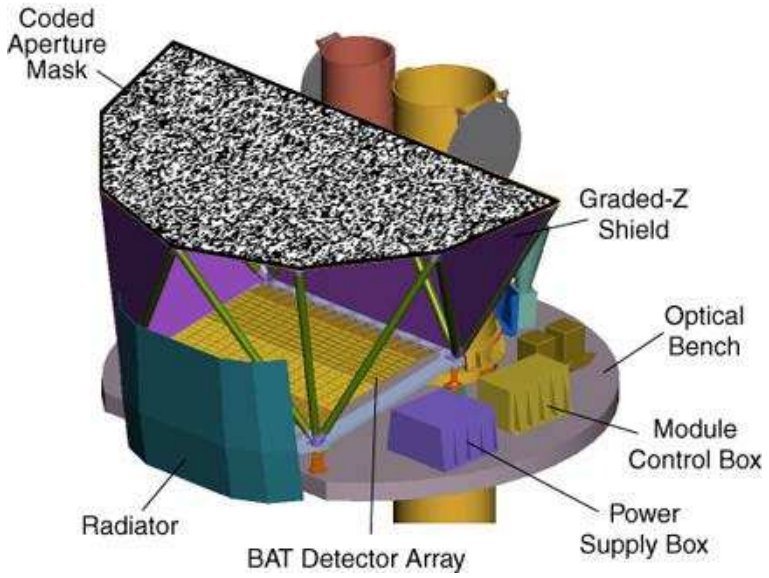

Figure 3.3: Burst Alert Telescope (BAT) on-board the *Swift* satellite (NASA/GSFC).

eights into blocks. This hierarchical structure, along with the forgiving nature of the coded aperture technique, means that the BAT can tolerate the loss of individual pixels, individual detector modules, and even whole blocks without losing the ability to detect bursts and determine locations. The CZT array has a nominal operating temperature of 20°C, and its thermal gradients (temporal and spatial) are kept to within ±1°C.

The CZT pixel elements have planar electrodes and are biased typically to −200 volts. The anode of each CZT piece is AC-coupled to an input on the XA1 ASIC along with a bleed resistor to ground for the CZT leakage current. The XA1 ASIC is made by IDEAS

(Hovik, Norway). Is has 128 channels of charge sensitive pre-amps, shaping amps, and discriminators. It is a self-triggering device. When supplied with a threshold control voltage, the ASIC will recognize an event on one of its 128 input channels, block out the remaining 127 channels, and present the pulse height of the event on its output for digitization. In addition, the chip provides an address in two parts - a group address and a segment address, which are combined by the following detector module controller to give the detector ID.

The BAT has a D-shaped coded aperture mask, made of $\sim 54,000$ lead tiles ($5 \times 5 \times 1$ mm) mounted on a 5 cm thick composite honeycomb panel, which is mounted by composite fiber struts 1 meter above the detector plane. Because the large FOV requires the aperture to be much larger than the detector plane and the detector plane is not uniform due to gaps between the detector modules, the BAT coded-aperture uses a completely random, 50% open-50% closed pattern, rather than the commonly used Uniformly Redundant Array pattern. The mask has an area of 2.7 m^2, yielding a half-coded FOV of 100 degrees$\times$60 degrees, or 1.4 steradian. A graded-Z fringe shield, located both under the detector plane and surrounding the mask and detector plane, reduces background from the isotropic cosmic diffuse flux and the anisotropic Earth albedo flux by $\sim 95\%$. The reduction of K X-ray from the shield itself is also desirable. A graded-Z shield, therefore, works by providing materials with decreasing atomic numbers toward the detector in order to absorb the K X-ray photoelectrically and emit a secondary X-ray of lower energy. The shield used on the BAT instrument is composed of layers of Pb, Ta, Sn, and Cu, which are thicker nearest the detector plane and thinner near the mask.

A figure-of-merit (FOM) algorithm resides within the BAT flight software and decides if a burst detected by the BAT is worth requesting a slew maneuver by the spacecraft. If the new burst has more "merit" than the pre-programmed observations, a slew request is sent to the spacecraft. Uploaded, rapid-reaction positions are processed exactly the same as events discovered by the BAT. The FOM is implemented entirely in software and can be changed either by adjusting the parameters of the current criteria or by adding new criteria.

3.2.3 BAT Operations

The BAT runs in two modes: burst mode, which produces burst positions, and survey mode, which produces hard X-ray survey data. In the survey mode the instrument collects count-rate data in 5-minute time bins for 80 energy intervals. When a burst occurs it switches into a photon-by-photon mode with a ring-buffer to save pre-burst information.

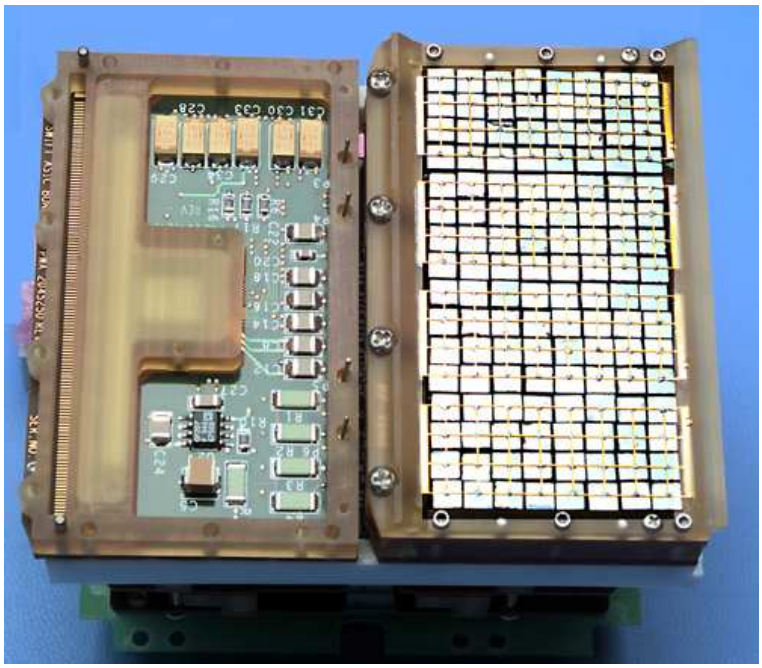

Figure 3.4: BAT Detector Module (DM). Two sub-arrays of 8×16 pieces of CdZnTe tile the top surface of the DM (NASA/GSFC).

3.2.4 Burst Detection

The burst trigger algorithm looks for excesses in the detector count rate above expected background and constant sources. It is based on algorithms developed for the HETE-2 GRB observatory, upgraded based on HETE-2 experience. The algorithm continuously applies a large number of criteria that specify the pre-burst background intervals, the order of the extrapolation of the background rate, the duration of the burst emission test interval, the region of the detector plane illuminated, and the energy range. The BAT processor continuously tracks hundreds of these criteria sets simultaneously. The table of criteria can be adjusted. The burst trigger threshold is commandable, ranging from 4 to 11 sigma above background noise with a typical value of 8 sigma. A key feature of the BAT instrument for burst detection is its imaging capability. Following the burst trigger, the on-board software checks for and requires that the trigger corresponds to a point source, thereby eliminating many sources of background such as magnetospheric particle events and flickering in bright galactic sources. Time-stamping of events within the BAT has a relative accuracy of 100 microsec and an absolute accuracy from the spacecraft clock of ∼200 microsec. When a burst is detected, the sky location and intensity are immediately sent to the ground and distributed to the community through the Gamma-Ray Burst Coordinates Network (GCN) (Barthelmy et al. 2000).

Fig 3.5 is an example of the response of the BAT to a simulated GRB. This shows a moderately difficult case: a GRB near the BATSE threshold (0.3 cts/s/cm^2 in the 50−300 keV band) in crowded field (point sources and diffuse+internal background total 25x and 10x GRB count rate, respectively). When the count rate in the entire detector plane increases by a significant amount, the background-subtracted count rates in the individual detectors are processed by a fast (but low resolution) algorithm to produce an image of the entire FOV. The region of this coarse image containing the brightest source (i, top middle) is selected for detailed imaging. This high-resolution imaging uses an algorithm that is slower but more accurate than the full-field algorithm. The image that results (ii, top right) gives an accurate location for the GRB.

If there is no background subtraction, the resulting image will contain bright steady sources that can be confused with the transient. Images iii and iv (bottom middle and right) show that, in this simulation, the GRB is still detectable in the coarse and fine images, even though the steady sources are much brighter.

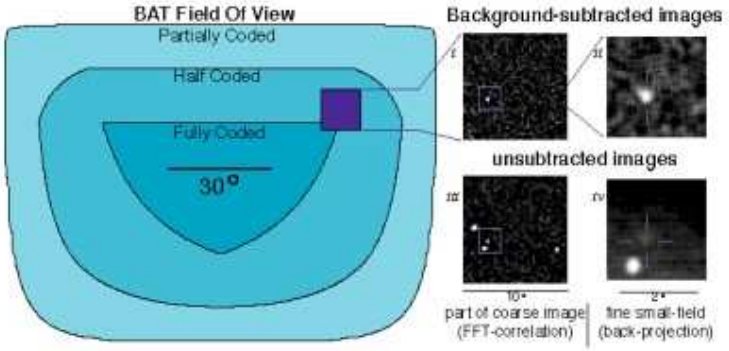

Figure 3.5: Response of the BAT to a simulated GRB. (NASA/GSFC)

3.2.5 Hard X-ray Survey

While searching for bursts, the BAT performs an all-sky hard X-ray survey and monitor for hard X-ray transients. The BAT accumulates detector plane maps every 5 minutes, which are included in the normal spacecraft telemetry stream. Sky images are searched to detect and position sources. The sensitivity of the survey is about 1 mCrab in the 15−150 keV band for 2 years. For regions where there are perpetually numerous strong sources in the BAT FOV (i.e. the Galactic Plane), the limiting sensitivity will be ∼3 mCrab.

For on-board transient detection, 1-minute and 5-minute detector plane count-rate maps and ∼30-minute long average maps are accumulated in 4 energy band-passes. Sources found in these images are compared against an on-board catalog of sources. Those

sources either not listed in the catalog or showing large variability are deemed transients. A subclass of long, smooth GRBs that are not detected by the burst trigger algorithm may be detected with this process. All hard X-ray transients are distributed to the world community through the Internet, just like the bursts.

3.3 Swift's X-Ray Telescope (XRT)

3.3.1 Instrument Description

Swift's X-Ray Telescope (XRT) is designed to measure the fluxes, spectra, and light curves of GRBs and afterglows over a wide dynamic range covering more than 7 orders of magnitude in flux. The XRT can pinpoint GRBs to 5-arcsec accuracy within 10 seconds of target acquisition for a typical GRB and can study the X-ray counterparts of GRBs beginning 20-70 seconds from burst discovery and continuing for days to weeks. The layout of the XRT is shown in the schematic below; the table after it summarizes the instrument's parameters. Further information on the XRT is given by Burrows et al. (2000) and Hill et al. (2000).

Table 3.2: XRT Instrument Parameters.

Property	**Description**
Telescope	**JET-X Wolter I**
Focal Length	**3.5 m**
Effective Area	**110 cm^2 at 1.5 keV**
Telescope PSF	**18 arcsec HPD at 1.5 keV**
Detector EEV	**600×600 pixels**
Detector Operation	**Imaging, Timing, and Photon counting**
Detection Element	**40×40 micron pixels**
Pixel Scale	**2.36 arcsec/pixel**
Energy Range	**0.2−10 keV**
Sensitivity	**2×10^{-14} erg/cm^2/s in 10^4 seconds**

3.3.2 Technical Description

The XRT is a focusing X-ray telescope with a 110 cm^2 effective area, 23 arcmin FOV, 18 arcsec resolution (half-power diameter), and 0.2-10 keV energy range. The XRT uses a grazing incidence Wolter 1 telescope to focus X-rays onto a state-of-the-art CCD.

The complete mirror module for the XRT consists of the X-ray mirrors, thermal baffle, a mirror collar, and an electron deflector (see Figure 3.6). The X-ray mirrors (Fig 3.6 $left$) are the FM3 units built, qualified and calibrated as flight spares for the JET-X instrument on the Spectrum X-Gamma mission (Citterio et al. 1996; Wells et al. 1992; Wells et al. 1997). To prevent on-orbit degradation of the mirror module's performance, it is maintained at 20±5 °C, with gradients of ≤ 1 °C by an actively controlled thermal baffle (purple, in schematic below) similar to the one used for JET-X. A composite telescope tube holds the focal plane camera (red), containing a single CCD-22 detector. The CCD-22 detector, designed for the EPIC MOS instruments on the XMM-Newton mission, is a three-phase frame-transfer device, using high resistivity silicon and an open-electrode structure (Holland et al. 1996) to achieve a useful bandpass of 0.2-10 keV (Short, Keay, & Turner 1998).

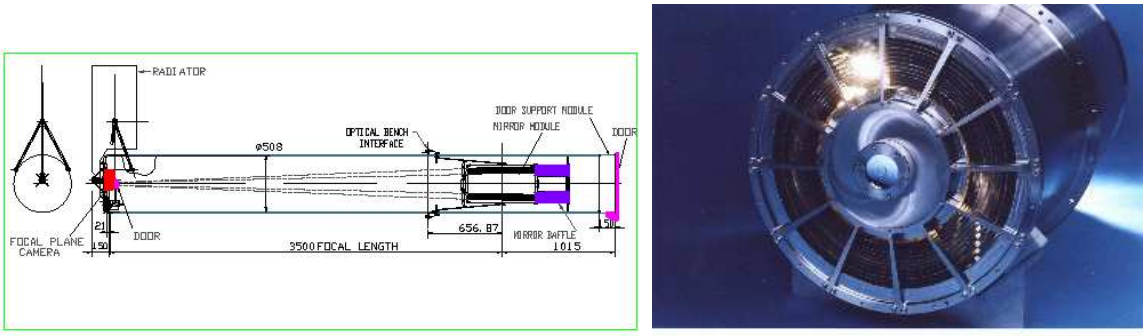

Figure 3.6: Layout of X-Ray Telescope (XRT) ($left$) and X-ray mirrors ($right$) (NASA/GSFC).

The CCD consists of an image area with 600×602 pixels (40×40 microns) and a storage region of 600×602 pixels (39×12 microns). The FWHM energy resolution of the CCDs decreases from ∼190 eV at 10 keV to ∼50 eV at 0.1 keV, where below ∼0.5 keV the effects of charge trapping and loss to surface states become significant. A special "open-gate" electrode structure gives the CCD-22 excellent low energy quantum efficiency (QE) while high resistivity silicon provides a depletion depth of 30 to 35 microns to give good QE at high energies. The detectors operate at approximately −100 degrees C to ensure low dark current and to reduce the CCD's sensitivity to irradiation by protons (which can create electron traps that ultimately affect the detector's spectroscopy).

3.3.3 Operation and Control

The XRT supports three readout modes to enable it to cover the dynamic range and rapid variability expected from GRB afterglows, and autonomously determines which

readout mode to use. Imaging Mode produces an integrated image measuring the total energy deposited per pixel and does not permit spectroscopy, so will only be used to position bright sources. Timing Mode sacrifices position information to achieve high time resolution and bright source spectroscopy through rapid CCD readouts. Photon-counting Mode uses sub-array windows to permit full spectral and spatial information to be obtained for source fluxes ranging from the XRT sensitivity limit of 2×10^{-14} to 9×10^{-10} erg/cm^2/s.

3.3.4 Instrument Performance

The mirror point spread function has a 15 arcsec half-energy width, and, given sufficient photons, the centroid of a point source image can be determined to sub-arcsec accuracy in detector coordinates. Based on BeppoSAX and RXTE observations, it is expected that a typical X-ray afterglow will have a flux of 0.5−5 Crabs in the 0.2−10 keV band immediately after the burst. This flux should allow the XRT to obtain source positions to better than 1 arcsec in detector coordinates, which will increase to ∼5 arcsec when projected back into the sky due to alignment uncertainty between the star tracker and the XRT.

Below is a simulated XRT image (central part of the field of view) comparing the worst-case BAT error circle with the XRT's resolution. The brightest source in the XRT field of view during the initial observation will almost always be the GRB counterpart, and so this source's position can be sent to the ground-based observers for rapid followup with narrow FOV instruments, such as spectrographs.

The XRT resolution at launch was ∼140 eV at 6 keV, with spectra similar to that shown below. Fe emission lines, if detected, can provide a redshift measurement accurate to about 10%. The resolution will degrade during the mission, but will remain above 300 eV at the end of the mission life for a worst-case environment. Photometric accuracy is be good to 10% or better for source fluxes from the XRT's sensitivity limit of 2×10^{-14} erg cm^{-2} s^{-1} to $\sim8\times10^{-7}$ erg cm^{-2} s^{-1} (about 2 times brighter than the brightest X-ray burst observed to date).

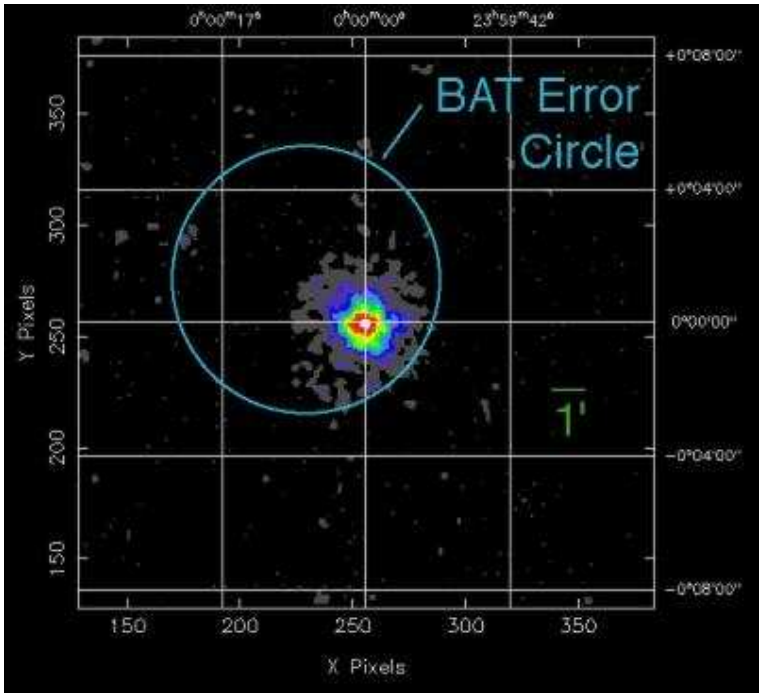

Figure 3.7: Simulated XRT image (central part of the field of view) comparing the worst-case BAT error circle. (NASA/GSFC)

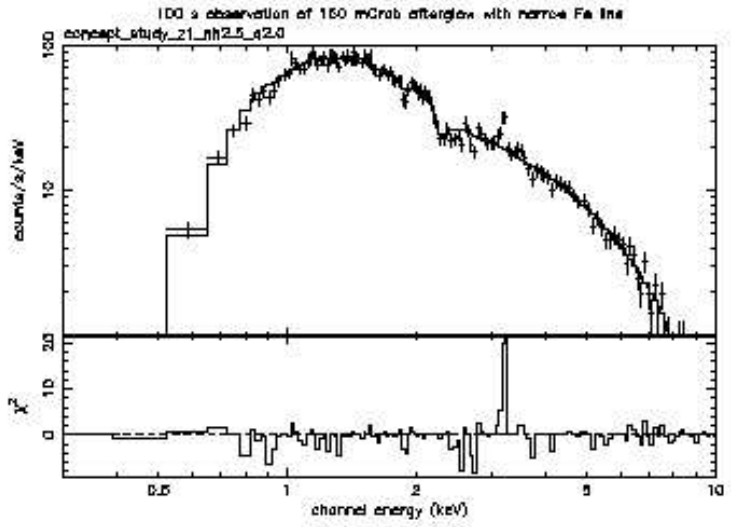

Figure 3.8: Simulated XRT spectrum of 100s observation assuming a typical 150 mcrab afterglow at z = 1.0.(NASA/GSFC)

Chapter 4

Analysis and Results of *Swift* BAT Observations

4.1 Data Sample and Reduction

We consider all GRBs detected by *Swift* between 2005 January and 2006 September 30. In Appendix A, we list the 160 GRBs that were selected for the analysis.

The BAT data for the GRB sample were processed using standard Swift-BAT analysis software as described in the BAT Ground Analysis Software Manual (Krimm, Parsons & Markwardt 2004). Each BAT event was mask-tagged using *batmaskwtevt* task with the best fit source position. Mask-tagging is a technique for subtracting background from an event file[1]. All of the BAT light curves and spectra have been background subtracted by this method.

4.2 Results from Temporal Studies

Figure 4.1 shows the background subtracted GRB light curves in the energy range of $15 - 150$ keV. These light curves show various properties. Some events have a single

[1]The technique takes advantage of the fact that background counts are randomly distributed across the detector plane, while counts for particular source fall in a calculable pattern. The mask tagging process involves forward projecting photons from a known position in the sky through the coded mask onto the detector plane. In event tagging, for each event a single ray is traced from the source location to the particular detector in the event. The event is given a weighting from -1.0 to $+1.0$ based on the fraction of the detector that is shadowed by lead tiles. If the detector is fully shadowed it receives a weight of -1.0. If it is fully open it gets a weight of $+1.0$ and if half-shadowed, a weight of 0.0. Counts from the background and other sources averages to zero with this method. This method is effective even when the spacecraft is moving since complete aspect information is available during the maneuver.

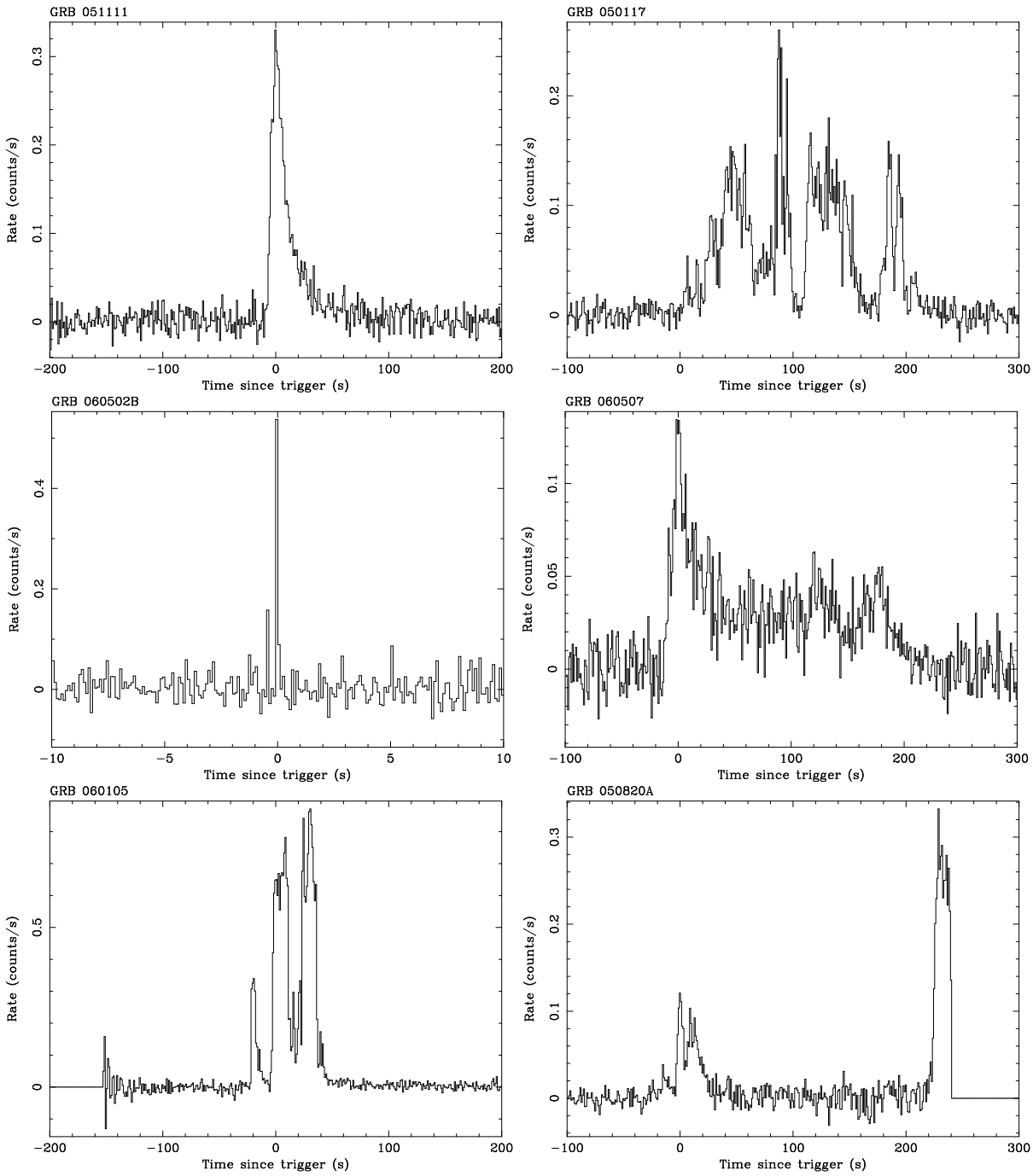

Figure 4.1: Examples of GRB light curves detected by the BAT.

pulse, while others have multiple pulses. The burst duration and Time interval of the pulses are also varying and range from milliseconds to tens of minutes. In Appendix B, we show all of the 160 light curves in the energy range of $15 - 150$ keV.

Fig 4.2 shows the distribution of the burst durations (T_{90}) calculated from the light curves. T_{90} of *Swift* (*top* panel) are clustered around $10 - 100$ seconds which is approximately comparable to the the BASTE samples (*bottom* panel). However, *Swift* GRBs

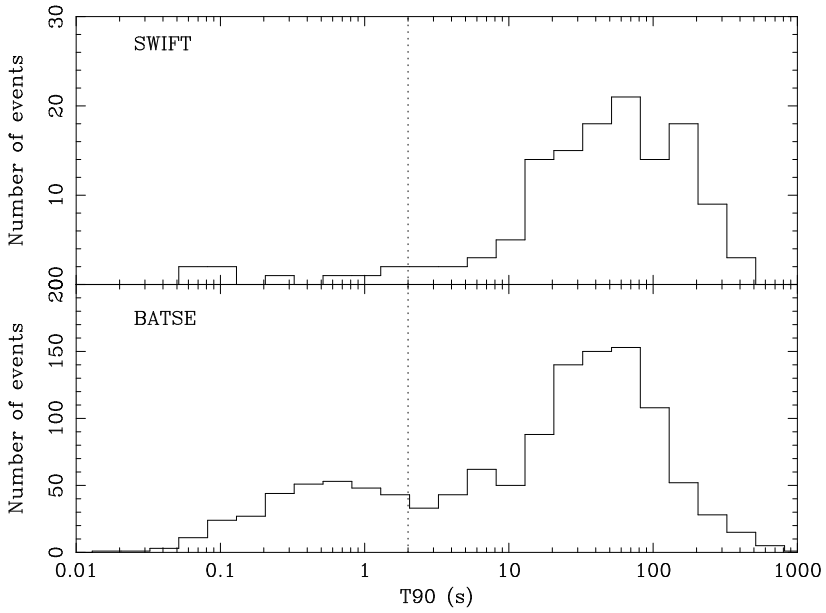

Figure 4.2: Distribution of the burst duration (T_{90}) of the Swift GRBs (*top* panel) and BATSE GRBs (*bottom* panel).

do not show a clear "bimodal" distribution as seen in BASTE samples. It may be due to differences of the energy band and trigger system.

4.3 Results from Spectral Studies

We extracted the spectra in the energy range $15 - 150$ keV over the period corresponding to T_{90} excluded during slew. If the satellite started to slew during T_{90}, we extracted the spectrum before the slew start times. If the satellite did not slew during T_{90}, we extracted the spectrum over the whole T_{90}. The extracted time regions are shown in Appendix B. Dashed lines show start and end times of the burst duration T_{90}. The slew start time are shown as dash-dotted line. All spectra were fitted with XSPEC version 11.3.2. The detector responses are generated from *batmaskevt*.

We performed spectral fitting with three models. The first model is the simple power-law function:

$$\frac{dN}{dE} = N_0 \times E^{-\Gamma}, \tag{4.1}$$

where N_0 is the normalization in units of photons/cm^2/s at 1 keV, Γ is the photon index.

The second model is the cutoff power-law function:

$$\frac{dN}{dE} = N_0 \times E^{-\Gamma} \times \exp(-E/E_{\rm cut}), \tag{4.2}$$

where N_0 is the normalization in units of photons/cm^2/s at 1 keV, Γ is the photon index and $E_{\rm cut}$ is the cutoff energy, respectively.

The third model if the Band function (Eq. 1.1)

$$N(E) = \begin{cases} A\left(\frac{E}{100\rm keV}\right)^{-\Gamma_1} \exp\left(-\frac{E}{E_0}\right) & \text{for } E \leq (-\Gamma_1+\Gamma_2)E_0, \\ A\left(\frac{E}{100\rm keV}\right)^{-\Gamma_2} \left(\frac{(-\Gamma_1+\Gamma_2)E_0}{100\rm keV}\right)^{-\Gamma_1+\Gamma_2} \exp(-\Gamma_2+\Gamma_1) & \text{for } E \geq (-\Gamma_1+\Gamma_2)E_0, \end{cases} \tag{4.3}$$

where the four parameters are the the normalization N_0, the low-energy photon index Γ_1, the high-energy photon index Γ_2, and νF_ν peaks at $E^{\rm obs}_{\rm peak} = E^2N(E) = (2-\Gamma_1)E_0$.

As a result, a single power-law provides in most cases a statistically acceptable fit to the BAT data. For 26 GRBs, cut-off power-law models provide a significantly better fit with well determined $E_{\rm cut}$. Since the νf_ν spectrum is expressed as $E^2\frac{dN}{dE} = N_0 \times E^{2-\Gamma} \times exp(-E/E_{\rm cut})$, the peak energy is given as $E_{\rm p} = (2-\Gamma)E_{\rm cut}$. For those GRBs, we tried to fit the spectra with the Band function. However, no significant improvements are obtained compared with the cutoff power-law model. The results are listed in Appendix A. The spectral parameters of the mean fluxes and spectral indices derived from fitting by single power-laws are summarized in Table A.1. In Table A.2., the fit results with a cutoff power-law function are listed. Throughout this thesis all quoted errors for the fit parameters correspond to 90% confidence for a single parameter.

Figure 4.3 shows the distribution of photon indices from a single power-law fits, clustering around 1.5. The typical photon indices of BATSE GRBs for lower and higher energy index are $\Gamma_1 \sim 1$ and $\Gamma_2 \sim 2.2$ of a Band function (Preece et al. 2000). The photon indices obtained from the 160 *Swift* GRBs are distributed between BATSE's Γ_1 and Γ_2 values. While it is possible that the source spectra intrinsically follow with a single power-law with photon index of ~ 1.5, it is more likely that we are observing the middle part of the Band function.

There are six *Swift* GRB events which obtained both redshift and spectral peak energy. We tested these samples for the relation proposed by Amati et al. (2002) and Yonetoku et al. (2004) (see Section 1.2.1). Figure 4.4 is plot of the peak energy in the GRB source frame ($\rm E^{src}_{peak}$) and the isotropic equivalent energy $\rm E_{\gamma,iso}$. $\rm E_{\gamma,iso}$ with the proper k-correction is calculated as

$$E_{\gamma,\rm iso} = \frac{4\pi d_{\rm L}^2 S_\gamma k}{1+z}, \tag{4.4}$$

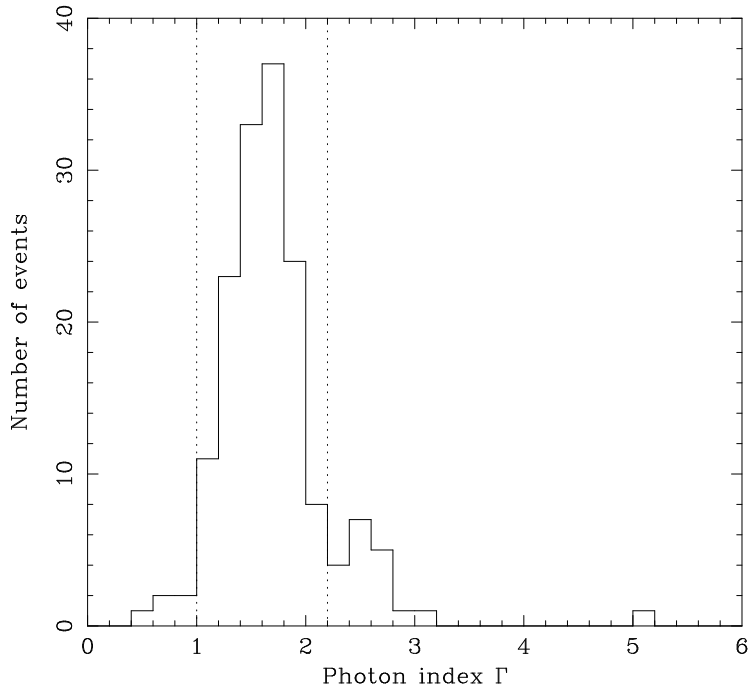

Figure 4.3: Distribution of photon indices of 160 *Swift* GRBs obtained by fitting with a single power-law model. The dashed lines are the typical photon indices of BATSE GRBs for lower and higher energy index $\Gamma_1 \sim 1$ and $\Gamma_2 \sim 2.2$ of a Band function (Preece et al. 2000).

where $d_{\rm L}$ is the luminosity distance, S_γ is the γ-ray flux integrated over the burst duration $\rm T_{90}$, k is the bolometric correction factor needed to find the energy emitted between 1 and 10,000 keV in the source frame. Throughout this thesis the cosmological parameters $H_0 = 71$ km s^{-1} Mpc^{-1}, $\Omega_{\rm M} = 0.27$, and $\Omega_\Lambda = 0.7$ have been adopted. Figure 4.5 is plot of $\rm E^{src}_{peak}$ and the peak luminosity between 1 and 10,000 keV with the proper k-correction derived from the peak flux. We calculated the peak flux as the following steps. 1) find the time of the peak counts ($T_{\rm p}$) in the BAT light curve, 2) create the 5 s spectrum from $T_{\rm p} \pm 2.5$ s, 3) perform the spectral fitting for this 5 s spectrum and calculate the flux, 4) calculate the counts from $T_{\rm p} \pm 2.5$ s and from $T_{\rm p} \pm 0.5$ s, 5) calculate the ratio of 1s counts to 5s counts, and 6) multiply this ratio by the flux value calculated in 3) to get the 1s peak flux. The six *Swift* GRBs are overlaid with the samples from Amati et al. (2006) and Yonetoku et al. (2004). As seen in these plots, *Swift* GRBs follow this relation remarkably well.

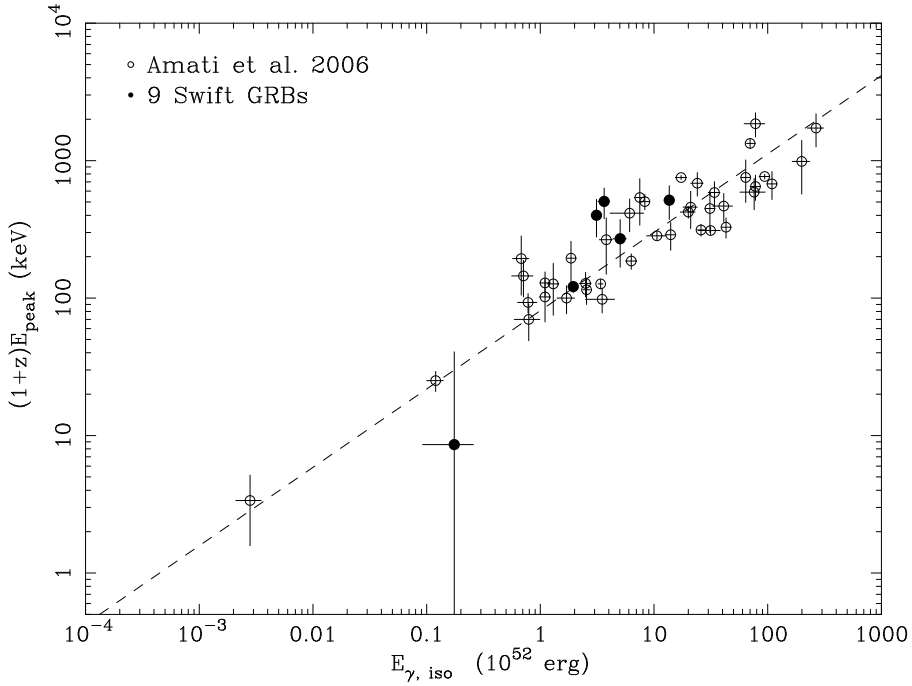

Figure 4.4: Correlation of the isotropic equivalent energy $E_{\gamma,\mathrm{iso}}$ and the peak energy $E^{\mathrm{src}}_{\mathrm{peak}}$. The opened circles are from Amati (2006). The filled circles are the *Swift* GRB events. The dashed line is $E^{\mathrm{src}}_{\mathrm{peak}} = 81 \times (E_{\gamma,\mathrm{iso}}/10^{52}\ \mathrm{erg})^{0.57}$ (Amati 2006).

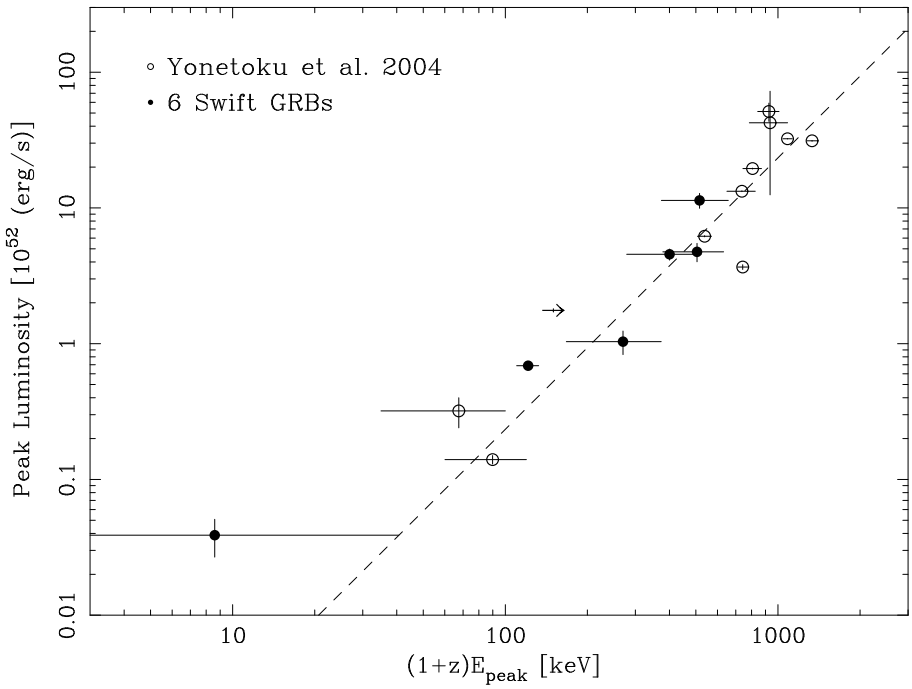

Figure 4.5: Correlation of the peak luminosity L_{peak} and the peak energy $E^{\mathrm{src}}_{\mathrm{peak}}$. The open circles are from Yonetoku et al. (2004). The filled circles are the six *Swift* GRBs. The dashed line is $L_{\mathrm{peak}} = 2.34 \times 10^{-5} \times {E^{\mathrm{src}}_{\mathrm{peak}}}^{2.0}$ (Yonetoku et al. 2004).

Chapter 5

Analysis and Results of *Swift* XRT Observations

5.1 Data Sample and Reduction

We consider all XRT data obtained by *Swift* between 2005 January and 2006 September 30. In Appendix D and E, we list the 128 GRBs that were selected for the analysis.

The XRT observations used here began after the slew starting with the GRB trigger time determined by the BAT. The XRT observations incorporate data taken in various operating modes of the instrument (Hill et al. 2004) and were corrected for pile-up where appropriate using the method described in Nousek et al. (2006). The bulk of the XRT data presented here were obtained using Window Timing (WT) and/or Photon Counting (PC) modes (event grades $0-2$ and $0-12$ respectively). The XRT data were processed using *xrtpipline* into filtered event lists. Data were filtered to eliminate time periods when the CCD temperature was warmer than -50°C. These filtered data were then used to extract spectra and light curves in the 0.5-10 keV energy range.

For PC data, the light curves and spectra are extracted from a circular region with a radius of 47" to 70" (20 to 30 pixels). The backgrounds are extracted from the annulus region with radii of 94" and 188" (40 and 80 pixels) excluding the X-ray source region near the GRB position (Figure 5.1). For WT data, the light curves and spectra are extracted from a rectangular region of 94" by 47" (40 by 20 pixels). The background is extracted from a rectangle of the same size as for the source region.

The data obtained in PC mode sometimes suffered from pile-up. The pile-up limit is 0.5 cts/s. For these data, we used an annular extraction region, with a 9.4" inner radius and a 47"-70" outer radius. To determine the combined correction factor for the annular aperture, we modeled the PSF using XIMAGE. The effective area is corrected using the

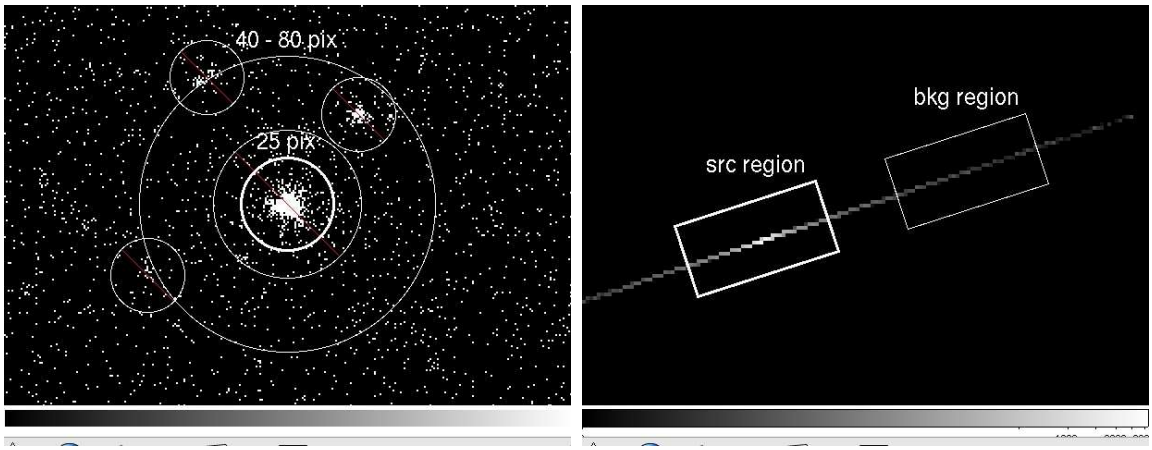

Figure 5.1: X-ray PC and WT image of the GRB 050502B afterglow. *Left*: The source photons are extracted from the circular region with a radius of 59" (25 pixels) in this case. The background are extracted from the annulus with radii of 94" and 188". *Right*: the source and background regions are extracted from a rectangle region of 94" by 47".

calibration data and $xrtmkarf$.

5.2 Results from Temporal Studies

5.2.1 Properties of X-ray Afterglows

Fig 5.2 show the temporal evolution and the typical "temporal index" for each segment of X-ray afterglow (Zhang et al. 2005). It was found with the $Swift$ data that the light curves of X-ray afterglows show three distinct power-law segments, where $F_\nu \propto \nu^{-\beta} t^{-\alpha}$ (Nousek et al. 2005): (1) an initial steep decay with a temporal index $\alpha_1 \sim 3-5$, (2) a shallow decay with $\alpha_2 \sim 0.5-1.0$ and (3) a normal decay with $\alpha_3 \sim 1.0-1.5$. X-ray "flares" which occur over short time intervals are also observed at early time in many events and sometimes at a later epoch. Moreover, Zhang et al. (2005) propose the existence of an additional segment: (4) a steeper decay with $\alpha_4 \sim -2$ based on the jet break scenario (Section 1.3).

Figure 5.3 shows the light curves of X-ray afterglows in the energy range of $0.5-10$ keV. These light curves show various properties. Some events show three distinct power-law segments, while some other show two segments (without shallow decay phase). Furthermore, some events show "flares". The number of flares and the flare start times are varying. In Appendix C, we show all of the light curves of 128 X-ray afterglows in the energy range of $0.5-10$ keV.

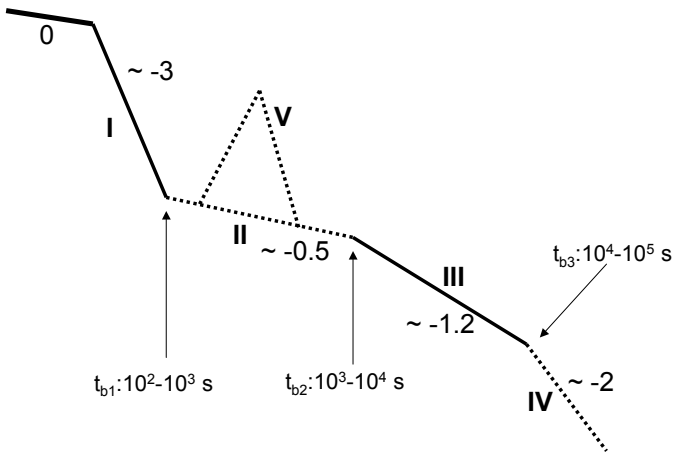

Figure 5.2: Canonical behavior of X-ray afterglows proposed by Zhang et al. (2005) and Nousek et al. (2005).

First, we performed light curve fitting with a broken power-law model:

$$N(t) = \begin{cases} N_0 \times (t - t_0)^{-\alpha_1} & (t < t_{\rm brk}), \\ N_0 \times (t_{\rm brk} - t_0)^{-\alpha_1} \times \left(\frac{t_{\rm brk} - t_0}{t - t_0}\right)^{-\alpha_2} & (t > t_{\rm brk}), \end{cases} \tag{5.1}$$

where N_0 is the normalization in units of photons/cm^2/s/keV, α_1 and α_2 are the temporal photon indices before and after the break time $t_{\rm brk}$.

The temporal decay slopes and the break times are summarized in Appendix D and were determined using the BAT trigger time as t_0. The distribution of all temporal indices (α_1, α_2 and α_3) are shown in Fig.5.4. The initial steep decay slope (α_1), the shallow decay slope (α_2) and the normal decay slope (α_3) are distributed around $2-5$, $0-1$ and $1-2$, respectively.

Figure 5.5 shows the distribution of the break times in the light curves. The distribution of the first break time (rapid to shallow decay) has a peak around ~ 400 s. On the other hand, the second break times (shallow to normal decay) are distributed around $\sim 10,000$ s.

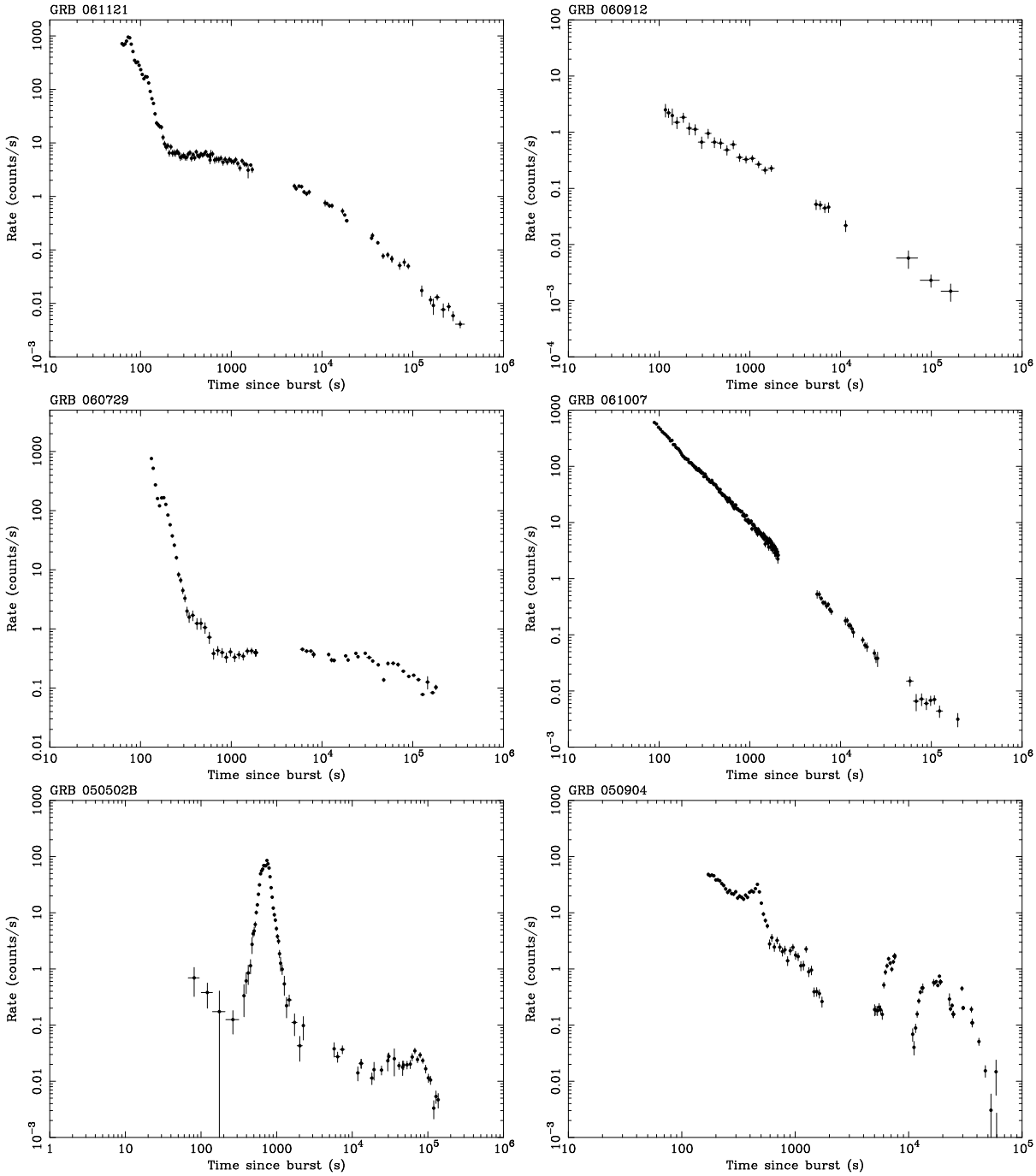

Figure 5.3: Examples of the light curves of X-ray afterglows detected by the XRT.

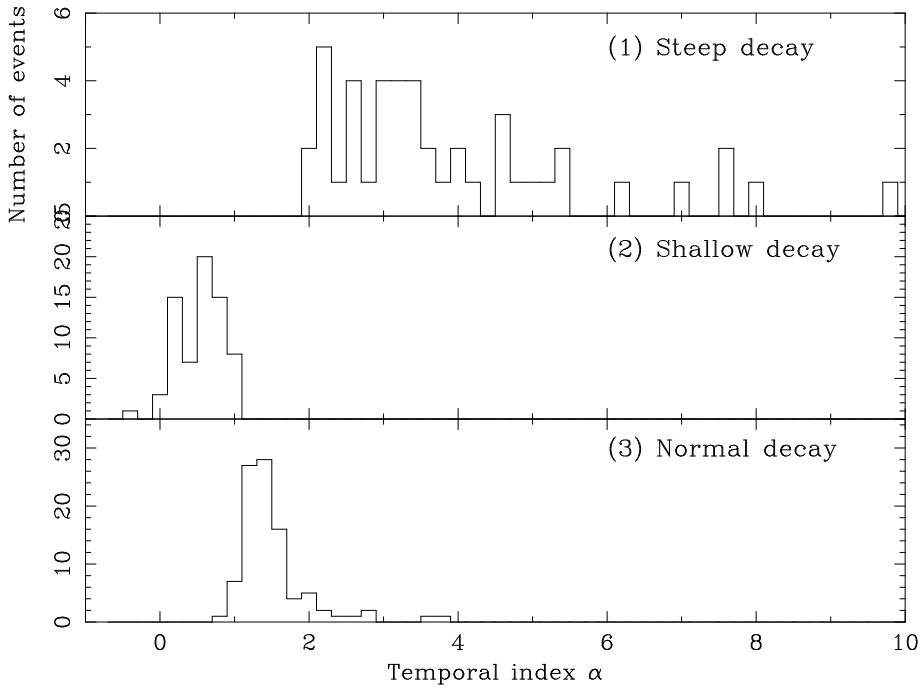

Figure 5.4: Distribution of the temporal indices α for the three segments in the X-ray light curves.

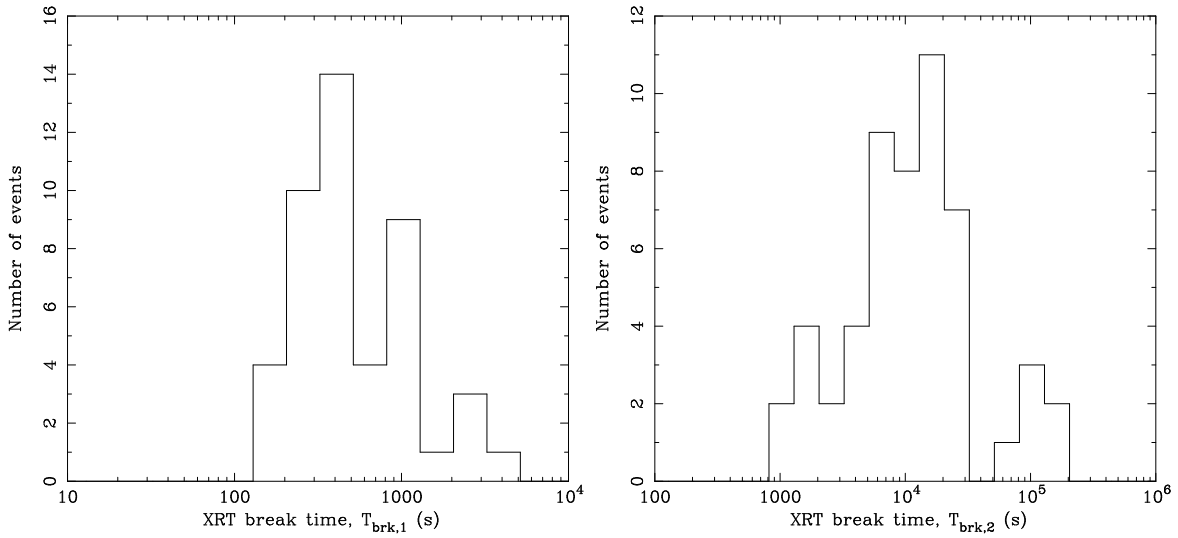

Figure 5.5: Distribution of the first (beginning of shallow decay phase) and second break time (end of shallow decay phase) in the X-ray light curves.

5.2.2 Temporal Profiles of X-ray Flares

Norris et al. (1996) found that temporal profiles of prompt emission show an asymmetry/width/siftening correlation (Figure 5.6): the rise-to-decay ratio of the GRB pulse is usually unity or less; as this ratio decreases, pulses tend to be wider, and the pulse centroid is shifted to later times at lower energies.

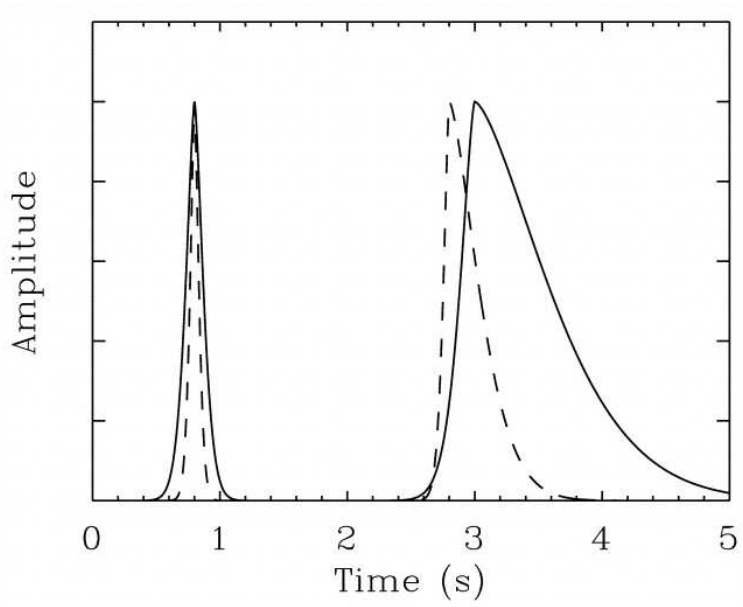

Figure 5.6: Pulse asymmetry/energy-shift paradigm. Solid lines show the low energy and dashed lines show the high energy emission.

We examined the temporal profiles of X-ray flares. The aim of the analysis was to study the properties of X-ray flares and to find out if there are any similarities or differences with the prompt emission. We analyzed 42 flares which have well separated peaks. The definition of the temporal profile and their properties are given by Norris et al. (1996):

$$\begin{aligned} I(t) &= A \times \exp[-(|t - t_{\rm max}/\sigma_{\rm r}|)^{\nu}] \quad (\text{for} \quad t \leq t_{\rm max}), \\ &= A \times \exp[-(|t - t_{\rm max}/\sigma_{\rm d}|)^{\nu}] \quad (\text{for} \quad t > t_{\rm max}), \end{aligned}$$

where $t_{\rm max}$ is the time of the flare's maximum intensity A, $\sigma_{\rm r}$ and $\sigma_{\rm d}$ are the rise ($t < t_{\rm max}$) and decay ($t > t_{\rm max}$) time constants. If the light curve is symmetric in time, $\sigma_{\rm r}$ and $\sigma_{\rm d}$ are expected to be equal. ν is a measure of pulse sharpness.

We applied this function to background (afterglow component) subtracted X-ray flares and single prompt emission pulses for comparison. The fitting results of X-ray flares are

summarized in Table 5.1.

Figure 5.7 shows pulse width distributions of prompt emission (dashed line) and X-ray flare (solid line). Pulse FWHM of the X-ray flare (0.5-10 keV) distributed around ∼50 s, whereas prompt emission (15-150 keV) is ∼ 2 s.

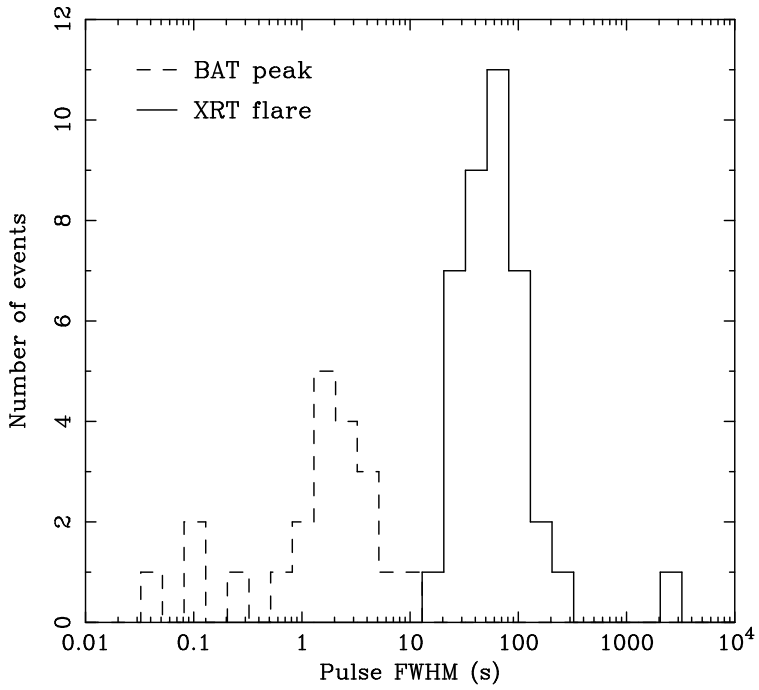

Figure 5.7: Pulse width distributions for prompt emission (dashed line) and X-ray flares (solid line). FWHM of prompt emission pulse is distributed around ∼ 2 s and of X-ray flares is distributed around ∼ 50 s.

Figure 5.8 shows distributions of the pulse sharpness. The pulse sharpness ν has a sharp peak around $\sim 1-2$ for both prompt emission and X-ray flares. Note that values for ν of exactly 1 and 2 correspond to exponential and Gaussian shapes, respectively.

The distribution of the ratio rise time - decay time ($\sigma_{\rm r}/\sigma_{\rm d}$) is shown in figure 5.9. The majority has rise-to-decay ratios < 1 for both prompt emission pulses and X-ray flares, which indicate that pulses rise more quickly than they decay.

Therefore, the temporal profiles of both X-ray flares and prompt emission are FRED (fast-rise exponential decay) with different pulse widths.

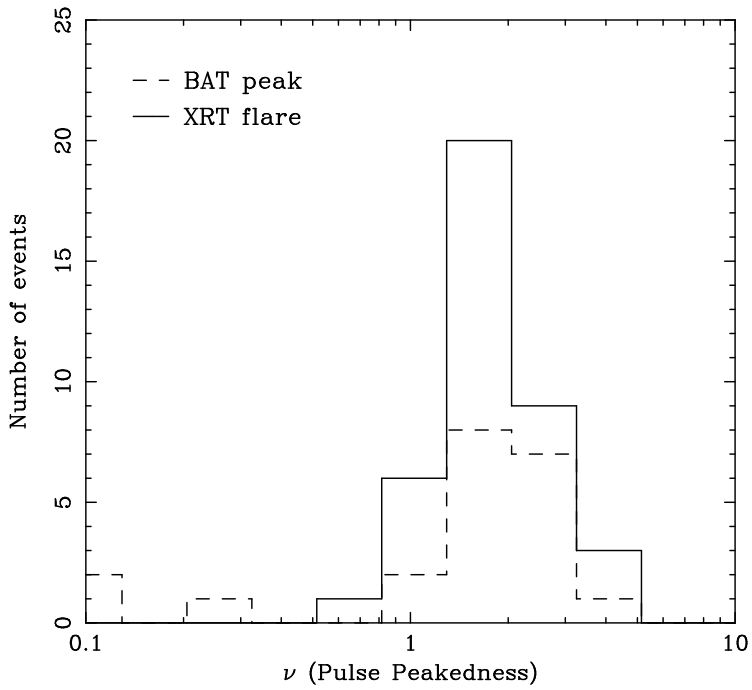

Figure 5.8: Distribution of pulse sharpness ν. Pulse sharpness is clustered around $\sim 1-2$.

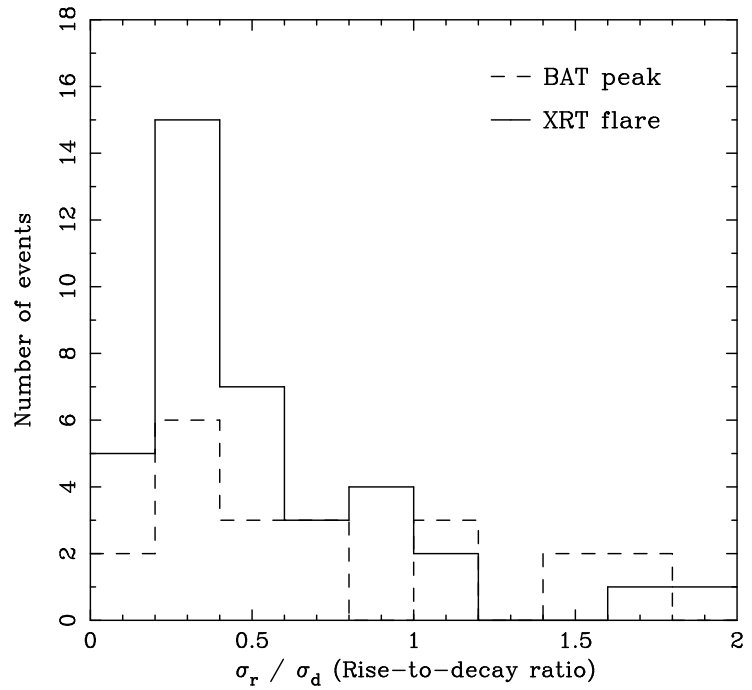

Figure 5.9: Distribution of the ratio rise time - decay time ($\sigma_{\rm r}/\sigma_{\rm d}$).

GRB		Peak intensity A (counts/s)	Peak time $t_{\rm max}$ (s)	Rise time $\sigma_{\rm r}$ (s)	Decay time $\sigma_{\rm d}$ (s)	Sharpness ν
050406		4.53±1.80	199±17	20.2±18.9	48.5±19.4	1.30±0.62
050607		27.3±9.75	300±16	14.4±13.0	66.6±18.2	1.25±0.41
050712		12.1±15.4	479±8	9.64±17.8	24.6±49.4	0.630±0.473
050713A	p1	200±42	110±3	7.56±2.84	17.6±3.0	1.16±0.24
050713A	p2	35.7±5.68	168±2	11.9±4.6	23.7±5.0	1.03±0.19
050714B		6.04±0.87	376±15	48.7±19.0	93.0±18.7	1.97±0.56
050716		4.61±0.99	371±13	22.3±14.5	86.4±21.7	1.42±0.45
050726		6.13±1.16	260±15	19.2±16.1	44.9±12.4	1.72±0.80
050730	p1	15.8±2.7	230±6	22.2±8.5	31.6±9.8	1.43±0.51
050730	p2	23.9±2.1	429±3	47.1±4.9	61.2±8.1	1.28±0.19
050730	p3	12.9±2.1	682±0.3	30.3±9.0	66.6±15.1	0.89±0.26
050822	p1	43.1±2.39	135±3	20.0±5.0	31.2±3.8	2.46±0.43
050822	p2	14.2±2.37	239±2	12.8±3.3	15.6±3.8	1.36±0.33
050822	p3	27.3±1.07	433±5	20.6±5.1	90.4±6.1	2.63±0.38
050904		24.5±1.76	464±2	90.3±6.5	44.4±5.3	1.33±0.14
050908		3.21±1.78	398±12	22.0±1.8	42.7±23.2	1.24±0.72
050916		0.312±0.055	18600±263	433±188	3070±538	0.988±0.135
050922B		74.4±34.9	830±21	85.6±29.4	45.5±39.4	1.31±1.78
060111	p1	33.7±2.4	98.4±3.0	17.8±3.6	21.5±3.5	2.49±0.53
060111	p2	20.9±1.9	164±5	14.4±4.9	27.1±5.4	2.67±0.80
060111	p3	116.1±6.2	278±2	25.4±2.6	68.5±4.5	1.53±0.15
060115		5.86±4.37	395±10	17.3±20.4	46.5±50.9	0.698±0.334
060124	p1	834±501	577±1	26.0±25.6	14.8±14.1	0.633±0.278
060124	p2	542±168	704±4	26.7±11.5	25.1±8.4	1.05±0.43
060204	p1	149±41	119±2	11.4±3.2	11.1±4.4	1.17±0.33
060204	p2	27.1±4.00	309±6	9.40±4.47	46.0±8.0	1.45±0.36
060210	p1	109±17	194±4	25.0±6.7	40.3±6.7	1.07±0.16
060210	p2	52.1±10.5	371±4	15.6±6.3	51.1±10.2	1.10±0.43
060413		4.09±0.67	607±23	32.6±21.0	173±27	1.51±0.37
060418		356±93	129±5	6.37±5.61	25.5±5.2	1.31±0.52
060510B	p1	32.5±3.33	196±4	15.2±4.6	18.7±4.7	2.57±0.87
060510B	p2	67.3±4.16	298±1	16.0±1.9	22.6±2.0	2.02±0.30
060512		7.54±1.89	188±66	2.00±167.	75.1±62.2	2.48±1.97
060526	p1	324±37	249±2	6.86±2.31	31.6±3.3	1.21±0.28
060526	p2	159±4	298±4	12.4±8.2	58.0±4.5	1.94±0.19
060607	p1	114±55	96.9±2.6	3.38±3.23	15.1±9.4	0.790±0.315
060607	p2	103±20	261±1	21.3±5.6	25.2±7.4	0.745±0.113
060814		115±11	126±2	5.07±1.76	31.5±2.9	1.71±0.32
060904	p1	13.7±1.2	299±5	27.0±6.9	76.3e±8.1	1.74±0.27
060904	p2	5.20±8.23	658±123	2.75±88.7	81.0±49.5	0.992±0.425
060904B		142±32	171±6	16.6±154.0	48.2±4.0	1.20±0.08
060926		70.3±3.4	520±1	36.9±2.7	93.9±5.2	1.28±0.07

Table 5.1: Temporal Profiles of X-ray Flares.

5.2.3 Spectral Evolution of X-ray Flares

In Appendix F, light curves in two energy band (0.5-2 keV and 2-10 keV) and the hardness ratios are shown. We defined the hardness ratio as the photon counts in the higher energy band (2-10 keV) divided by those in lower energy band (0.5-2 keV). The spectra of X-ray flares sometimes show evolution between the rise part and the decay part. Such properties have also been observed in the prompt GRB emission (Norris et al. 1996, Zhang et al. 2006).

To characterize the spectral evolution of X-ray flares, we plotted the correlation between the count rates (0.5-10 keV) and the hardness ratios. Some cases show significant hard-to-soft evolution (Figure 5.10). We present a systematic spectral analysis of X-ray flares in Section 5.3.

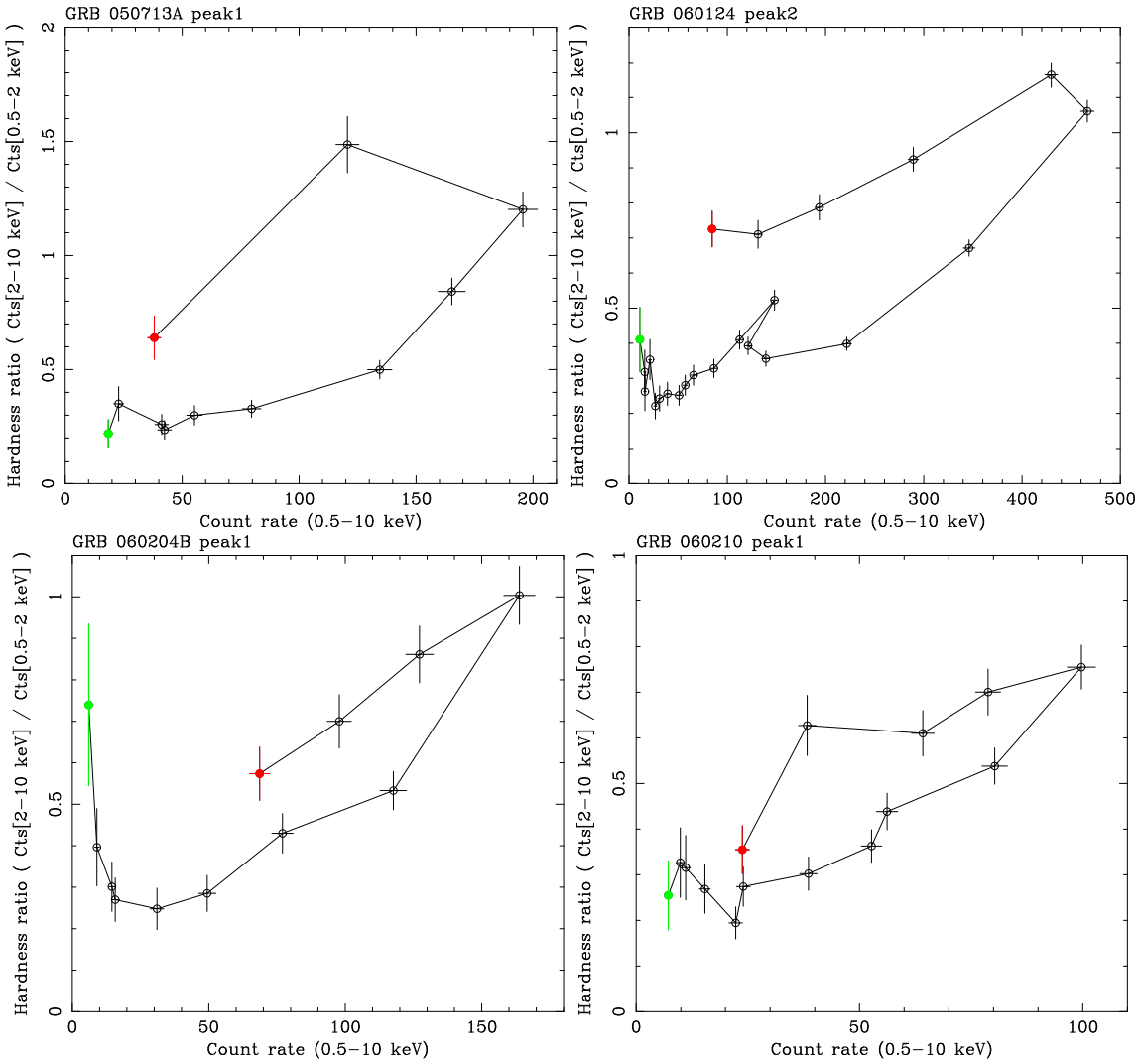

Figure 5.10: Count rate (0.5-10 keV) versus hardness ratio of X-ray flares. The red filled circle represents the start point of the X-ray flare.

5.2.4 Time Lags of X-ray Flares

Next, we study the time lags of the X-ray flares. Norris found that, in a single burst, the higher-energy gamma-rays arrives before the lower-energy gamma-rays. The same tendency is observed in the X-ray flares. To demonstrate the spectral lag dependences on energy, we show the X-ray flares in the energy bands of 0.5-1,1-3, and 3-10 keV band in figure 5.11. Clearly seen is the time lag of X-ray flare where the light curve in the harder band peaks earlier.

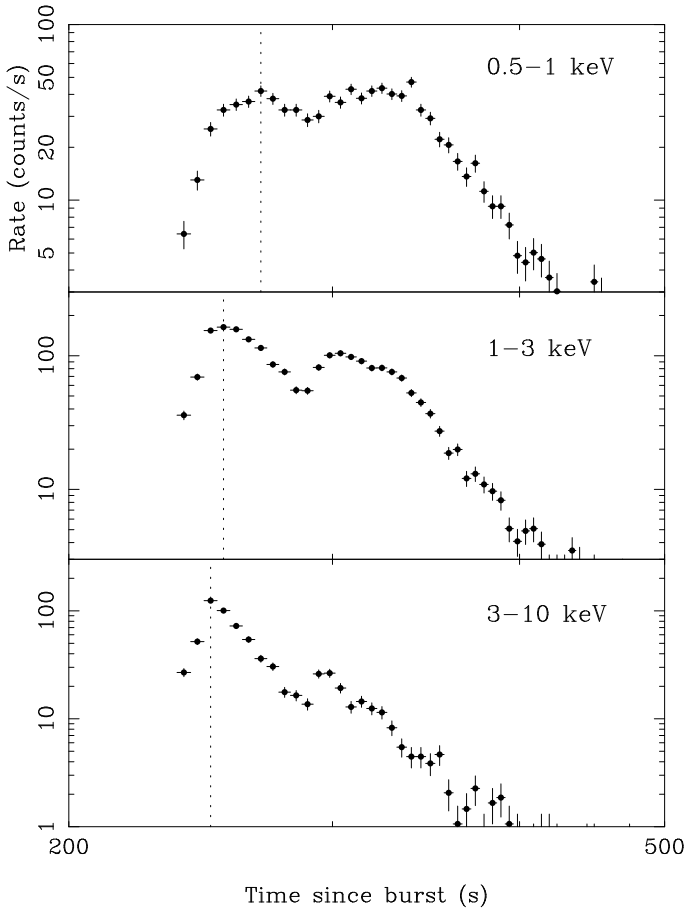

Figure 5.11: Light curves in the energy bands of 0.5-1 keV (*top*), 1-3 keV (*center*), and 3-10 (*bottom*) keV, respectively. The dotted lines show the peak times of the flares.

We use the 31 flares and calculate the time lags between the 0.5-1 keV and 1-10 keV energy band in the following way. In order to analyze the time series in various energy bands quantitatively, we apply the discrete correlation function given by Edelson & Krolik (1998). This technique was specifically designed to analyze unevenly sampled data sets. The first step is to calculate the set of unbinned discrete functions (UDCF) between each data point in the two data streams. This is defined in the time domain as

$$\mathrm{UDCF_{ij}} = \frac{(a_i - \bar{a})(b_j - \bar{b})}{\sqrt{\sigma_a^2 \sigma_b^2}} \tag{5.2}$$

where a_i and b_j are points of the data set a and b, $\bar{a}$ and $\bar{b}$ are the means of the data sets, and σ_a and σ_b are the standard deviation of each data set. The discrete correlation function (DCF) for each time lag τ is defined as an average of the UDCF that have the separation time of $\tau - \Delta\tau/2 \leq \Delta t_{ij} \leq \tau + \Delta\tau/2$,

$$\mathrm{DCF}(\tau) = \frac{1}{N} \Sigma \mathrm{UDCF_{ij}}(\tau) \tag{5.3}$$

where N is the number of pairs in the bin.

The average of the DCF lies in the fact that it uses all the data points available, does not introduce new errors through interpolation, and calculates a meaningful error estimate. The standard error for each bin is calculated as

$$\sigma_{\mathrm{DCF}} = \frac{1}{N-1} (\Sigma [\mathrm{UDCF_{ij}} - \mathrm{DCF}(\tau)]^2)^{1/2}. \tag{5.4}$$

In the following, we calculated the time lags of X-ray flares between the 0.5-1 keV energy band and the 1-10 keV energy band. The error on the lags was determined from the uncertainty (1 σ error) of the peak parameter obtained by the minimum χ^2 fitting of the DCF distribution to a Gaussian (see Appendix I).

The results are summarized in Table 5.2. Figure shows the distribution of time lag values of the X-ray flares. We find that the soft X-ray (0.5-1 keV) variation lags behind that in the harder (1-10 keV) X-ray band (soft lag) by typically seconds to tens of seconds.

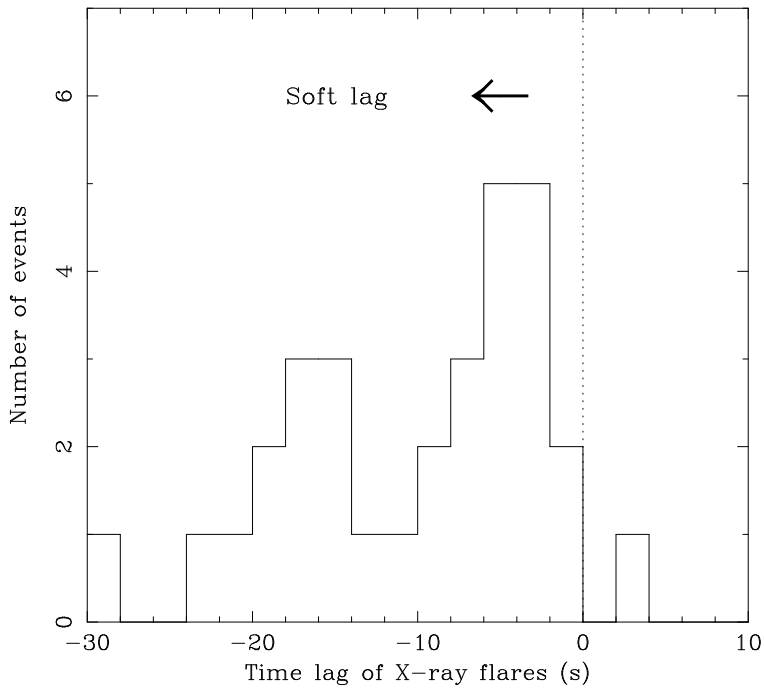

Figure 5.12: Distribution of the time lag values. The soft X-ray (0.5-1 keV) variation lags behind that in the harder (1-10 keV) X-ray band (soft lag) by typically seconds to tens of seconds.

GRB		time lag (s)
050406		-3.54±4.27
050502B		-19.9±3.4
050607		-14.5±4.3
050712		-3.38±7.79
050713A		-6.86±1.68
050713A		-6.21±1.79
050714B		-16.4±3.8
050730	p2	+2.04±3.55
050730	p3	-14.8±3.3
050904		-1.27±3.90
050908		-4.53±6.69
060111A		-4.53±1.80
060124	p1	-17.3±1.6
060124	p2	-6.29±1.70
060204B		-16.3±3.9
060210	p1	-8.22±1.85
060210	p2	-5.52±1.81
060418		-5.94±1.81
060510B		-3.66±1.79
060512		-19.1±5.7
060526		-10.1±1.7
060604	p1	-1.17±1.09
060604	p2	-2.65±0.97
060607	p1	-8.78±1.93
060607	p2	-14.8±1.6
060714		-2.46±1.29
060814		-12.2±1.5
050904	p1	-23.6±3.9
050904	p2	-5.03±3.60
060904B		-21.3±2.1
060929		-29.8±2.9

Table 5.2: DCF lag of the X-ray flares in the 1-10 keV band against in the 0.5-1 keV band.

5.3 Results from Spectral Studies

5.3.1 Properties of X-ray Afterglows

We extracted the spectra of X-ray afterglows in the energy range $0.5 - 10$ keV for each segment; (1) the initial steep decay, (2) the shallow decay, and (3) the normal decay). All spectra were fitted with XSPEC version 11.3.2. The detector responses were swxpc0to12_20010101v008.rmf (PC data) and swxwt0to2_20010101v008.rmf (WT data), and ancillary response files generated with $xrtmkarf$.

The spectra of the X-ray afterglows can be fitted by a simple power-law function plus absorption arising from neutral material;

$$\frac{dN}{dE} = N_0 \times exp(-N_{\rm H} \times \sigma(E)) \times E^{-\Gamma}, \tag{5.5}$$

where N_0 is the normalization in units of photons/cm^2/s/keV, Γ is the photon index and $\sigma(E)$ is the cross section for photo-electric absorption with solar abundances (Morrison & McCammon 1983). The absorption column was parametrized in terms of the equivalent Hydrogen column density $N_{\rm H}$.

We first fixed the column density at the Galactic column density. Then we fitted the spectrum with the column density $N_{\rm H}$ allowed to be free. In Appendix E, the best fit values are listed. The distribution of the spectral indices for each segment are shown in Fig 5.13, and values of the spectral indices plotted against the temporal indices are shown in Figure 5.14. The spectral indices remain unchanged for segments (2), (3) with an average value of the photon index $\Gamma \sim 2.1$. The hardness ratio is approximately constant over segments (2) and (3). Segment (1) sometimes has a softer spectrum, but in some other cases it has a similar spectral index as the other segments. The average value of β in segment (1) is 2.4.

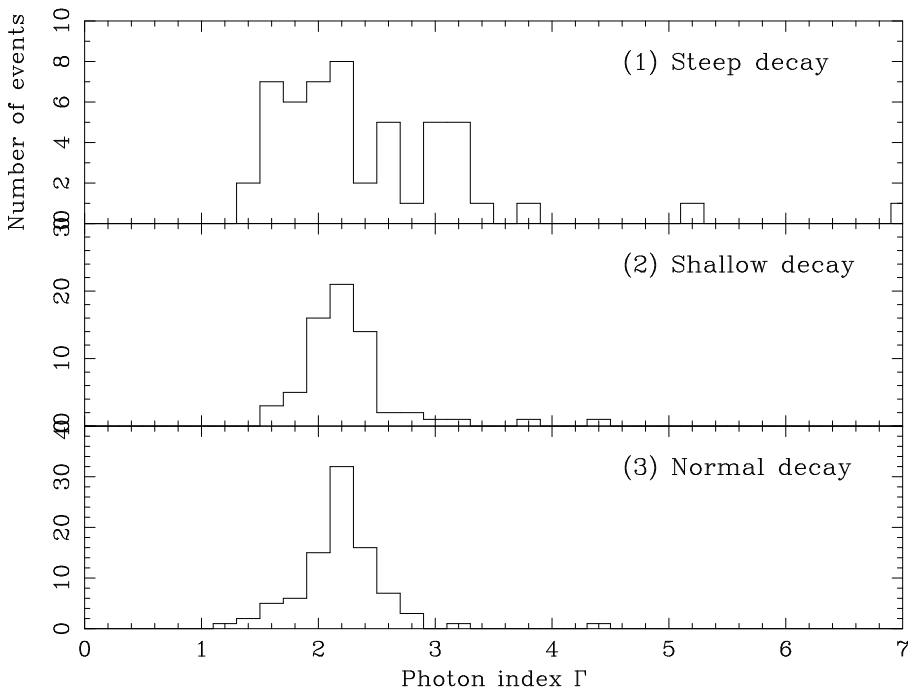

Figure 5.13: Distribution of the photon indices Γ for three segment in X-ray light curve.

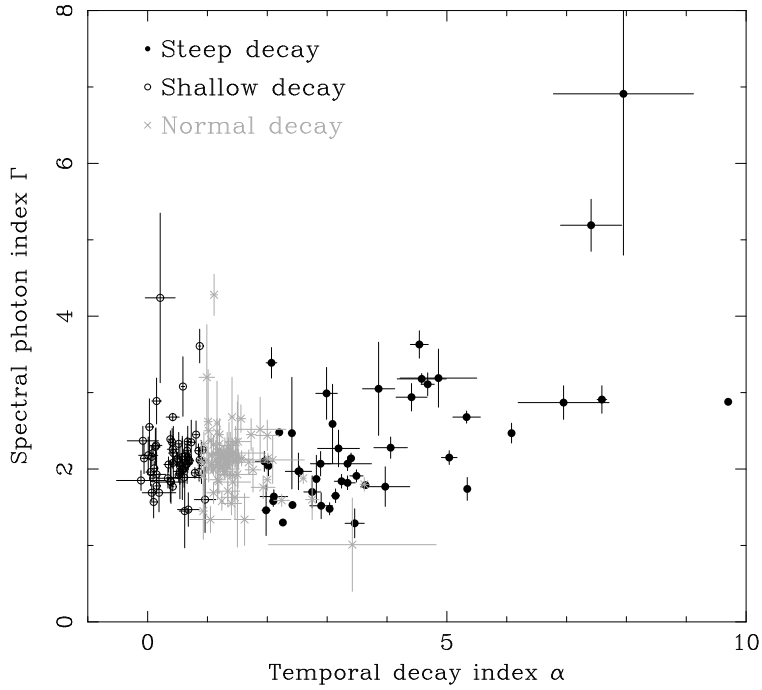

Figure 5.14: Distribution of the spectral indices Γ and temporal indices α.

5.3.2 Spectral Properties of X-ray Flares

We examined the spectral properties of individual X-ray flares in their rise part, the decay part, and the whole. When only the XRT data are used, spectra from any part of X-ray flares can be fitted by a simple power-law function with photoelectric absorption (Eq. 5.5). The resultant spectral parameters are shown in Table 5.3. We found that the most X-ray flares are harder in the rise part than in the decay (Fig 5.15). The distribution of photon indices of the rise part has a sharp peak around $\sim 1-2$. The decay part shows a softer spectrum and photon indices are clustered around $2-3$. Furthermore, if there are more than one flare in a single GRB afterglow, the spectra of the later flares become progressively softer. This tendency is similar to that found for the multiple pulses in the prompt emission (Ford et al. 1995).

Figure 5.16, we compared the photon indices of the prompt emission and X-ray flare. There is no correlation between them. We only found that X-ray flare is generally softer than the prompt emission. We also compared the flux of the prompt emission and X-ray flare. As the BAT and XRT data cover different energy bands, the XRT data was extrapolated into the bandpass of the BAT to compare them. We have chosen to use the BAT energy range of 15-150 keV to determine fluxes. The results are shown in Figure 5.17, and the flux of the X-ray flare is smaller than these prompt emission.

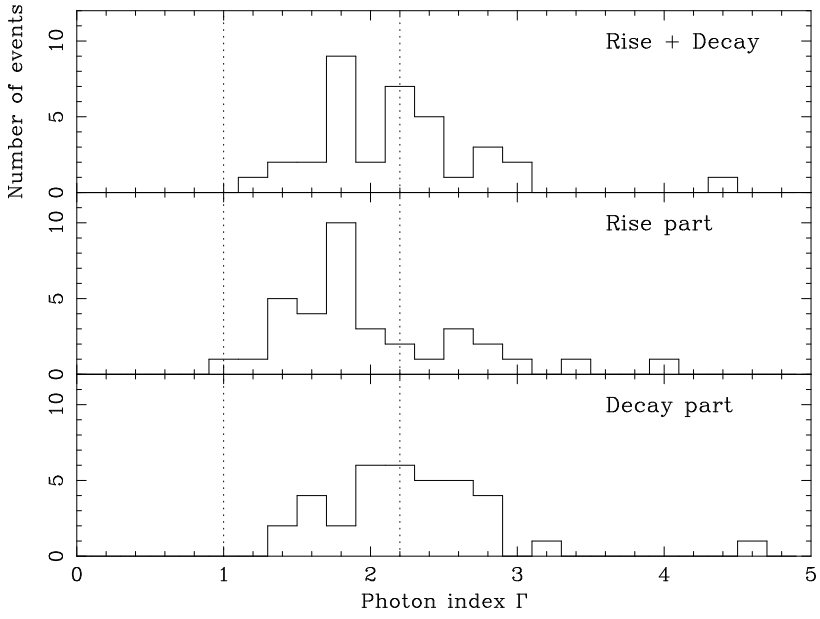

Figure 5.15: Distribution of the photon indices Γ for X-ray flares (*top* panel), the rise part (*center* panel), and the decay part (*bottom* panel). Fitted model is an absorbed simple power-law. The vertical dotted lines are the typical photon indices of prompt GRBs, $\Gamma_1 \sim 1$ and $\Gamma_2 \sim 2.2$, respectively.

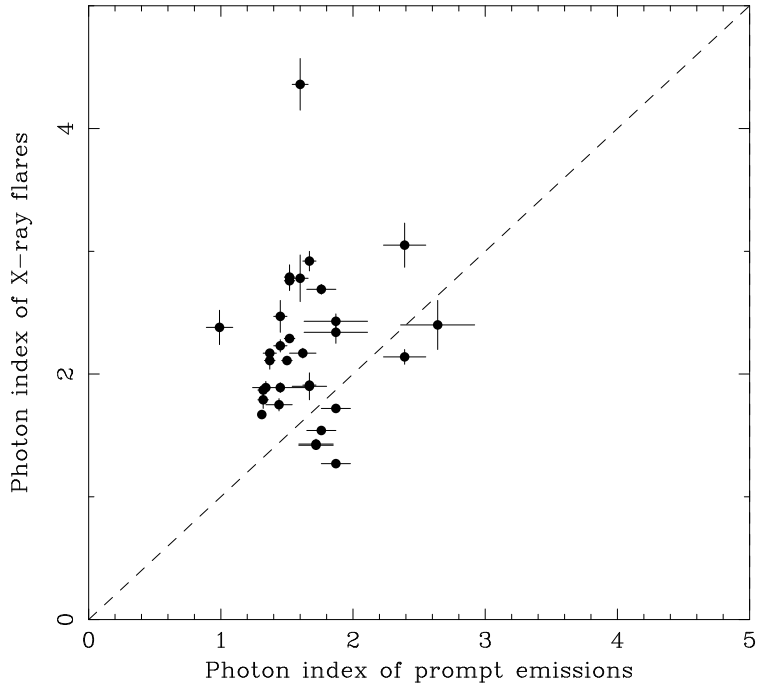

Figure 5.16: The photon indices of X-ray flares are plotted against those of the prompt emission. The dashed line shows equality.

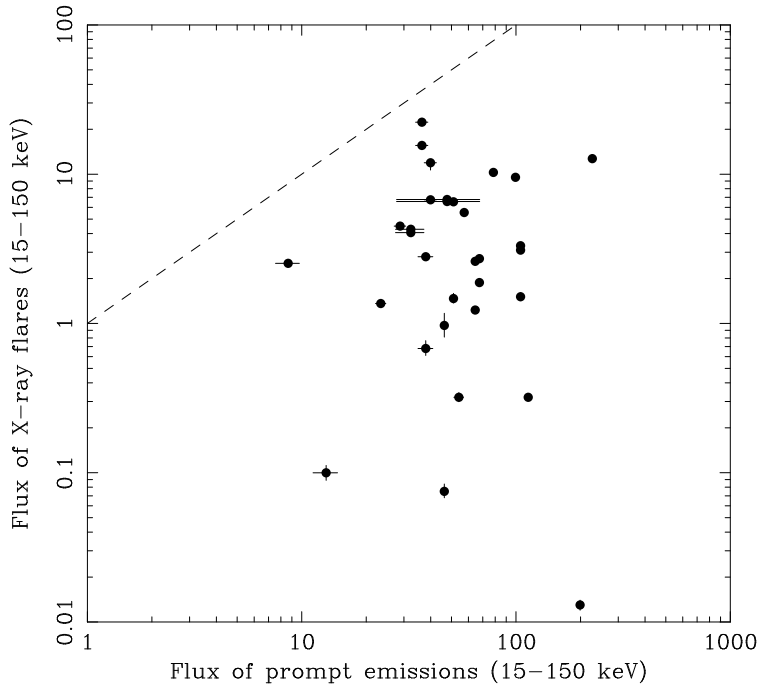

Figure 5.17: The flux of X-ray flares are plotted against those of the prompt emission. The dashed line shows equality.

GRB			N_H $10^{20}/cm^2$	Photon Index	Flux (0.5-10 keV) 10^{-9} erg/cm^2/s	Fluence (0.5-10 keV) 10^{-9} erg/cm^2	χ^2 (d.o.f)
050406		rise	2.57 fix	2.12	0.09	-	2.11 (1)
		decay	2.57 fix	2.34±0.20	0.11±0.01	-	0.975 (10)
		whole	2.57 fix	2.40±0.20	0.10±0.01	$5.12^{+0.62}_{-0.56}$	0.760 (12)
050713	p1	rise	$57.6^{+9.2}_{-8.0}$	1.61±0.11	$8.61^{+0.46}_{-0.43}$	-	1.69 (40)
		decay	$55.1^{+3.2}_{-3.1}$	2.45±0.06	$6.51^{+0.29}_{-0.27}$	-	1.02 (231)
		whole	$52.9^{+2.9}_{-2.8}$	2.23±0.05	$6.53^{+0.22}_{-0.20}$	326^{+11}_{-10}	1.02 (278)
050713	p2	rise	$41.0^{+10.6}_{-9.4}$	2.55±0.23	$1.71^{+0.32}_{-0.23}$	-	0.764 (25)
		decay	$31.9^{+5.1}_{-4.8}$	2.41±0.15	$1.36^{+0.12}_{-0.10}$	-	0.940 (54)
		whole	$34.7^{+4.7}_{-4.4}$	2.47±0.13	$1.47^{+0.12}_{-0.10}$	$58.7^{+4.8}_{-4.0}$	1.26 (40)
050716		rise	9.96 fix	1.99±0.11	0.37±0.03	-	0.845 (24)
		decay	9.96 fix	2.23±0.09	0.30±0.02	-	0.976 (44)
		whole	9.96 fix	2.11±0.07	0.32±0.02	38.3±1.8	0.929 (66)
050726		rise	4.78 fix	2.22±0.16	$0.27^{+0.03}_{-0.02}$	-	1.08 (21)
		decay	$30.6^{+6.3}_{-5.7}$	2.73±0.17	0.37±0.03	-	0.845 (24)
		whole	$17.5^{+4.2}_{-3.9}$	2.38±0.14	0.32±0.02	$32.0^{+2.4}_{-2.1}$	0.814 (60)
050730	p1	rise	$12.9^{+7.4}_{-6.5}$	1.37±0.14	0.12±0.08	-	0.691 (36)
		decay	$17.1^{+4.5}_{-4.2}$	2.03±0.13	0.83±0.05	-	0.830 (65)
		whole	$14.7^{+3.3}_{-3.1}$	1.77±0.09	0.91±0.04	63.6±2.7	0.830 (97)
050730	p2	rise	$10.2^{+2.7}_{-2.6}$	1.80±0.08	0.92±0.03	-	1.01 (122)
		decay	$4.7^{+2.3}_{-2.2}$	1.65±0.07	0.95±0.03	-	0.880 (147)
		whole	$8.7^{+1.7}_{-1.6}$	1.76±0.05	0.95±0.02	171±4	0.897 (234)
050730	p3	rise	2.98 fix	1.80±0.06	0.52±0.02	-	0.697 (80)
		decay	2.98 fix	2.05±0.05	0.49±0.02	-	0.810 (109)
		whole	2.98 fix	1.96±0.04	0.50±0.01	95.7±2.7	0.785 (173)
050822	p1	rise	$18.7^{+3.1}_{-2.9}$	1.94±0.08	4.63±0.18	-	0.776 (114)
		decay	$17.2^{+2.5}_{-2.5}$	2.29±0.08	2.26±0.09	-	0.929 (148)
		whole	$17.5^{+1.8}_{-1.8}$	2.14±0.06	$2.80^{+0.08}_{-0.07}$	196±5	0.937 (222)
050822	p2	rise	$20.4^{+5.3}_{-4.9}$	2.86±0.20	$0.72^{+0.10}_{-0.08}$	-	0.534 (32)
		decay	$21.8^{+7.1}_{-6.4}$	$3.15^{+0.28}_{-0.25}$	$0.60^{+0.14}_{-0.10}$	-	0.794 (30)
		whole	$23.6^{+4.3}_{-4.1}$	3.05±0.18	$0.68^{+0.09}_{-0.07}$	$45.8^{+5.9}_{-4.7}$	0.841 (59)
050822	p3	rise	-	-			
		decay	$50.2^{+4.1}_{-3.8}$	5.66±0.22	$5.67^{+1.38}_{-1.01}$	-	1.23 (108)
		whole	-	-			
050904		rise	$13.7^{+2.2}_{-2.1}$	1.80±0.06	1.38±0.04	-	0.916 (188)
		decay	$08.7^{+3.2}_{-3.0}$	1.68±0.09	1.26±0.06	-	0.802 (91)
		whole	$12.1^{+1.7}_{-1.7}$	1.75±0.05	1.36±0.03	217±5	0.883 (249)
050916		rise	121 fix	1.70±0.24	0.014±0.001	-	0.207 (9)
		decay	121 fix	1.92±0.14	0.013±0.001	-	0.885 (26)
		whole	121 fix	1.90±0.11	0.013±0.001	54.1±4.2	0.720 (39)
060111	p1	rise	$46.4^{+4.4}_{-4.2}$	3.06±0.12	$4.70^{+0.52}_{-0.44}$	-	0.886 (93)
		decay	$24.0^{+2.9}_{-2.9}$	2.56±0.10	$2.36^{+0.14}_{-0.13}$	-	0.964 (112)
		whole	$33.2^{+2.4}_{-2.4}$	2.76±0.08	$3.10^{+0.17}_{-0.15}$	155^{+8}_{-7}	0.944 (171)
060111	p2	rise	$29.3^{+7.0}_{-6.4}$	2.63±0.18	$1.90^{+0.26}_{-0.21}$	-	0.971 (42)
		decay	$25.0^{+3.4}_{-3.2}$	2.87±0.13	$1.32^{+0.12}_{-0.10}$	-	0.905 (88)
		whole	$27.1^{+2.9}_{-2.7}$	2.79±0.10	$1.51^{+0.10}_{-0.09}$	$90.5^{+6.0}_{-5.4}$	0.673 (123)
060111	p3	rise	$29.3^{+2.1}_{-2.0}$	2.55±0.06	$3.20^{+0.13}_{-0.12}$	-	0.951 (202)
		decay	$21.6^{+1.2}_{-1.2}$	2.17±0.04	3.33±0.06	-	0.998 (330)
		whole	$24.1^{+1.0}_{-1.0}$	2.29±0.03	3.32±0.05	597±9	0.939 (373)
060124	p1	rise	$22.3^{+0.8}_{-0.8}$	1.18±0.01	$23.9^{+0.17}_{-0.19}$	-	0.977 (704)
		decay	$19.3^{+1.0}_{-1.0}$	1.59±0.02	18.6±0.2	-	0.891 (515)
		whole	$19.9^{+0.6}_{-0.6}$	1.27±0.01	22.3±0.1	4460±28	0.928 (740)
060124	p2	rise	$20.8^{+1.2}_{-0.6}$	1.48±0.02	19.3±0.2	-	1.06 (513)

		decay	$22.6^{+0.9}_{-0.9}$	1.97±0.02	13.4±0.2	-	1.00 (479)
		whole	$20.7^{+0.7}_{-0.7}$	1.72±0.02	15.6±0.1	2340±18	1.05 (611)
060204	p1	rise	$22.8^{+3.7}_{-3.5}$	1.64±0.07	6.67±0.24	-	0.951 (132)
		decay	$26.4^{+2.9}_{-2.7}$	2.13±0.08	$4.64^{+0.19}_{-0.17}$	-	1.04 (140)
		whole	$24.6^{+2.2}_{-2.1}$	1.89±0.05	5.54±0.14	194±5	0.853 (237)
060204	p2	rise	-	-			
		decay	$21.5^{+3.7}_{-3.5}$	2.59±0.13	0.70±0.05	-	0.996 (85)
		whole	-	-			
060210	p1	rise	$19.7^{+3.2}_{-3.0}$	1.79±0.07	3.68±0.13	-	0.933 (141)
		decay	$16.4^{+1.7}_{-1.7}$	2.03±0.05	2.19±0.05	-	1.09 (241)
		whole	$16.5^{+1.4}_{-1.4}$	1.91±0.04	2.61±0.05	287±6	0.881 (300)
060210	p2	rise	$23.3^{+3.7}_{-3.5}$	2.90±0.14	$1.02^{+0.10}_{-0.09}$	-	0.807 (70)
		decay	$24.0^{+2.4}_{-2.3}$	2.90±0.09	$1.32^{+0.08}_{-0.07}$	-	0.992 (139)
		whole	$24.0^{+2.0}_{-1.9}$	2.92±0.08	1.23±0.06	147±7	1.03 (173)
060418		rise	$24.6^{+2.6}_{-2.5}$	1.77±0.06	13.4±0.37	-	0.911 (199)
		decay	$26.2^{+1.3}_{-1.2}$	2.23±0.04	9.56±0.17	-	0.918 (355)
		whole	$25.7^{+1.1}_{-1.1}$	2.11±0.03	10.3±0.15	616±9	0.974 (411)
060510B	p1	rise	$15.2^{+2.9}_{-2.7}$	1.37±0.06	6.93±0.22	-	0.873 (163)
		decay	$17.8^{+2.5}_{-2.3}$	1.50±0.06	6.23±0.17	-	0.910 (201)
		whole	$17.0^{+1.8}_{-1.8}$	1.43±0.04	$6.56^{+0.14}_{-0.13}$	295±6	0.842 (309)
060510B	p2	rise	$15.1^{+2.5}_{-2.3}$	1.37±0.04	$6.84^{+0.19}_{-0.18}$	-	0.891 (211)
		decay	$15.1^{+2.0}_{-2.0}$	1.49±0.05	$6.62^{+0.15}_{-0.16}$	-	0.748 (256)
		whole	$14.9^{+1.5}_{-1.5}$	1.42±0.03	6.77±0.12	406±7	0.866 (373)
060526	p1	rise	$26.5^{+5.0}_{-4.6}$	1.09±0.07	12.9±0.4	-	0.865 (145)
		decay	$20.7^{+1.4}_{-1.4}$	1.70±0.04	11.7±0.2	-	0.929 (367)
		whole	$19.6^{+1.3}_{-1.3}$	1.54±0.03	$11.9^{+0.17}_{-1.27}$	536^{+8}_{-57}	0.856 (436)
060526	p2	rise	$12.3^{+3.6}_{-3.4}$	1.87±0.09	6.37±0.28	-	0.754 (96)
		decay	$27.7^{+1.4}_{-1.4}$	2.83±0.05	$7.04^{+0.23}_{-0.22}$	-	1.01 (249)
		whole	$25.6^{+1.3}_{-1.2}$	2.69±0.04	$6.74^{+0.19}_{-0.18}$	387^{+11}_{-10}	1.13 (277)
060604	p1	rise	$27.9^{+8.5}_{-8.3}$	2.35±0.03	$4.26^{+0.22}_{-0.20}$	-	0.865 (122)
		decay	$27.3^{+3.6}_{-3.4}$	2.50±0.10	$4.26^{+0.27}_{-0.24}$	-	0.879 (123)
		whole	$27.4^{+2.3}_{-2.2}$	2.43±0.06	$4.28^{+0.16}_{-0.15}$	171±6	0.911 (206)
060604	p2	rise	$14.3^{+5.6}_{-5.1}$	1.79±0.15	4.23±0.31	-	0.936 (35)
		decay	$25.1^{+3.6}_{-3.4}$	2.60±0.12	$4.20^{+0.31}_{-0.27}$	-	0.861 (91)
		whole	$21.3^{+3.0}_{-2.9}$	2.34±0.09	$4.06^{+0.20}_{-0.19}$	$81.1^{+4.0}_{-3.8}$	0.805 (119)
060607	p1	rise	$6.8^{+6.5}_{-5.9}$	1.58±0.17	$3.27^{+0.27}_{-0.26}$	-	0.485 (29)
		decay	$11.1^{+2.6}_{-2.5}$	1.87±0.08	2.62±0.09	-	1.01 (133)
		whole	$9.2^{+2.3}_{-2.3}$	1.79±0.07	2.72±0.09	109±4	0.900 (15)
060607	p2	rise	$11.0^{+2.3}_{-2.3}$	1.72±0.07	2.58±0.08	-	1.02 (162)
		decay	$6.4^{+1.8}_{-1.7}$	1.97±0.06	1.55±0.04	-	0.969 (197)
		whole	$8.3^{+1.4}_{-1.3}$	1.87±0.04	1.88±0.04	239±5	1.05 (278)
060714		rise	$21.4^{+2.2}_{-2.2}$	1.91±0.06	6.08±0.16	-	0.843 (219)
		decay	$26.0^{+2.6}_{-2.5}$	2.50±0.08	$4.08^{+0.20}_{-0.18}$	-	0.804 (151)
		whole	$22.9^{+1.5}_{-1.5}$	2.17±0.04	$4.49^{+0.10}_{-0.10}$	179±4	0.917 (287)
060814		rise	$32.8^{+3.8}_{-3.7}$	1.39±0.07	14.7±0.4	-	0.888 (176)
		decay	$37.9^{+1.9}_{-1.8}$	1.79±0.04	12.1±0.2	-	1.09 (344)
		whole	$35.8^{+1.6}_{-1.6}$	1.67±0.03	12.7±0.2	571±9	1.06 (416)
060904	p1	rise	$41.8^{+7.3}_{-6.7}$	4.02±0.32	$1.16^{+0.39}_{-0.26}$	-	0.984 (37)
		decay	$33.8^{+6.0}_{-5.5}$	$4.67^{+0.36}_{-0.32}$	$0.98^{+0.34}_{-0.23}$	-	1.16 (69)
		whole	$35.1^{+4.1}_{-3.9}$	$4.36^{+0.23}_{-0.21}$	$0.97^{+0.20}_{-0.16}$	140^{+29}_{-23}	1.17 (95)
060904	p2	rise	$26.6^{+16.2}_{-14.2}$	$3.38^{+0.73}_{-0.62}$	$0.22^{+0.17}_{-0.07}$	-	0.587 (12)
		decay	$13.6^{+5.0}_{-4.6}$	2.64±0.20	$0.060^{+0.007}_{-0.006}$	-	0.809 (38)
		whole	$16.7^{+4.6}_{-4.3}$	2.78±0.19	$0.075^{+0.009}_{-0.007}$	$28.1^{+3.4}_{-2.6}$	0.871 (50)
060904B		rise	$57.3^{+2.8}_{-2.8}$	1.73±0.04	15.5±0.3	-	0.919 (376)
		decay	$40.3^{+1.1}_{-1.0}$	2.53±0.03	$9.20^{+0.17}_{-0.16}$	-	1.02 (419)

	whole	$38.9^{+0.9}_{-0.9}$	2.17±0.02	9.53±0.11	1520±18	1.10 (525)
060929	rise	$26.3^{+3.4}_{-3.2}$	1.75±0.07	2.62±0.09	-	0.955 (151)
	decay	$22.7^{+2.5}_{-2.4}$	2.21±0.07	1.88±0.07	-	0.670 (166)
	whole	$22.5^{+1.5}_{-1.5}$	1.89±0.04	2.53±0.05	351±7	0.892 (331)

Table 5.3: The spectral parameters of the X-ray flares in the 0.5-10 keV fitted with the power-law function plus absorption.

If the photon indices $\Gamma > 2$, it indicates that the spectral peak energy is below the XRT energy band (< 0.5 keV). Whereas the photon indices $\Gamma < 2$, it indicates that the spectral peak energy is within or above the XRT energy band (≥ 10 keV). When the BAT data is available for the X-ray flare, we attempted to fit the spectra using both the BAT and BAT data. We performed spectral fitting with three models: single power-law, cutoff power-law and Band function plus absorption. The results are summarized in Table 5.4. For four X-ray flares, cutoff power-law or Band function provide significantly better fits with well determined peak energies within the BAT and XRT energy band. The other spectra were better fitted with simple power-law function with $\Gamma < 2$, implying that the spectral peak energies are located above the BAT energy range (> 150 keV).

GRB			Model	N_H $10^{20}/cm^2$	Photon Index (Γ_1)	Photon Index (Γ_2)	E_0 (keV)	Flux (0.5-150 keV) 10^{-9} erg/cm^2/s	χ^2 (d.o.f)
050713	p1	rise	PL	69.5±8.7	1.83±0.05	-	-	$20.8^{+1.4}_{-1.6}$	1.19 (94)
			Cut PL	53.9±8.4	1.53±0.13	-	$42.9^{+28.0}_{-14.0}$	$17.5^{+1.7}_{-1.6}$	1.11 (93)
			Band	-	-	-	-	-	
050822	p1	rise	PL	19.2±2.6	1.95±0.07	-	-	$9.40^{+0.89}_{-0.81}$	0.785 (128)
			Cut PL	18.2±3.1	1.91±0.10	-	$155^{+\infty}_{-92}$	$8.64^{+1.45}_{-1.31}$	0.789 (127)
			Band	-	-	-	-	-	
060204B		rise	PL	30.2±3.3	1.85±0.05	-	-	15.8±1.1	1.00 (143)
			Cut PL	21.5±3.9	1.55±0.11	-	$30.8^{+16.8}_{-10.0}$	12.1±1.3	0.922 (142)
			Band	-	-	-	-	-	
		whole	PL	26.4±1.9	1.95±0.04	-	-	11.3±0.6	0.858 (248)
			Cut PL	24.9±2.2	1.89±0.07	-	124^{+828}_{-67}	10.3±1.1	0.856 (247)
			Band	19.7±1.5	$1.15^{+0.09}_{-0.06}$	$2.07^{+0.09}_{-0.08}$	$8.06^{+7.05}_{-5.06}$	$9.91^{+0.38}_{-0.67}$	0.845 (246)
060210		rise	PL	19.0±2.6	1.76±0.05	-	-	$10.2^{+0.9}_{-0.8}$	0.930 (152)
			Cut PL	19.0±2.6	1.76±0.05	-	∞	$10.2^{+0.9}_{-0.8}$	0.936 (151)
			Band	-	-	-	-	-	
		whole	PL	16.1±1.3	1.90±0.03	-	-	5.77±0.3	0.867 (308)
			Cut PL	16.1±1.3	1.90±0.03	-	∞	5.77±0.3	0.870 (307)
			-	-	-	-	-		
060418		rise	PL	31.8±2.4	1.99±0.04	-	-	25.9±1.2	1.02 (210)
			Cut PL	23.6±1.5	$1.66^{+0.09}_{-0.05}$	-	$24.6\ ^{+11.7}_{-7.2}$	$20.1^{+1.6}_{-1.5}$	0.943 (209)
			Band	18.7±2.0	1.31±0.25	2.30±0.15	$6.89^{+11.16}_{-3.39}$	20.4±1.4	0.925 (208)
060510B	p1	rise	PL	21.9±2.4	1.57±0.02	-	-	$26.9^{+1.2}_{-1.3}$	0.901 (178)
			Cut PL	17.8±2.7	1.44±0.05	-	116^{+83}_{-36}	$24.7^{+1.5}_{-1.4}$	0.868 (177)
			Band	8.3±1.7	0.86±0.04	1.65±0.04	$6.37^{+8.60}_{-3.97}$	$25.3^{+0.8}_{-0.6}$	0.828 (176)
		decay	PL	22.2±2.0	1.63±0.02	-	-	21.8±1.0	0.939 (216)
			Cut PL	18.2±2.2	$1.49^{+0.03}_{-0.06}$	-	101^{+56}_{-30}	19.8±1.2	0.904 (215)
			Band	16.9±3.3	$1.43^{+0.09}_{-0.14}$	$1.86^{+8.14}_{-0.16}$	$56.9^{+80.9}_{-47.0}$	$20.5^{+1.1}_{-1.8}$	0.905 (214)
		whole	PL	22.6±1.5	1.61±0.02	-	-	24.0±0.8	0.902 (327)
			Cut PL	18.2±1.7	$1.46^{+0.04}_{-0.02}$	-	$98.8^{+33.4}_{-21.6}$	21.8±0.9	0.850 (326)
			Band	-	-	-	-	-	
	p2	rise	PL	22.3±2.1	1.59±0.02	-	-	25.4±1.1	0.986 (226)
			Cut PL	18.3±2.3	1.46±0.05	-	114^{+65}_{-32}	$23.3^{+1.3}_{-1.2}$	0.950 (225)
			Band	3.8±2.2	$0.38^{+0.39}_{-0.26}$	1.65±0.03	$2.84^{+3.80}_{-1.01}$	23.6±1.1	0.909 (224)
		decay	PL	22.4±1.8	1.68±0.02	-	-	$20.7^{+0.86}_{-0.83}$	0.841 (271)
			Cut PL	16.1±2.2	1.45±0.06	-	$55.2^{+19.5}_{-12.1}$	17.4±1.0	0.763 (270)
			Band	9.2±1.3	1.04±0.03	1.85±0.05	$8.35^{+2.44}_{-4.05}$	$18.3^{+0.4}_{-0.7}$	0.705 (269)
		whole	PL	22.1±1.3	1.64±0.02	-	-	$22.7^{+0.7}_{-0.6}$	0.968 (388)
			Cut PL	17.2±1.6	1.47±0.04	-	$80.1^{+12.3}_{-14.6}$	20.1±0.8	0.899 (387)
			Band	10.3±9.0	1.08±0.07	1.77±0.03	$9.68^{+7.40}_{-4.46}$	$20.7^{+0.4}_{-0.5}$	0.842 (386)
060526	p1	rise	PL	60.9±5.5	1.71±0.03	-	-	38.2±1.6	1.38 (161)
			Cut PL	25.6±5.1	0.95±0.10	-	$17.0^{+3.3}_{-2.5}$	$29.9^{+1.4}_{-1.3}$	0.947 (160)
			Band	19.2±3.0	$0.76^{+0.06}_{-0.08}$	$2.45^{+0.19}_{-0.14}$	$11.7^{+3.0}_{-2.2}$	$34.0^{+1.7}_{-1.8}$	0.865 (159)
		decay	PL	25.4±1.2	1.85±0.02	-	-	27.7±0.8	1.00 (383)
			Cut PL	20.8±1.5	1.67±0.04	-	$63.1^{+19.6}_{-12.9}$	24.2±1.0	0.944 (382)
			Band	19.8±1.6	$1.62^{+0.03}_{-0.06}$	$2.19^{+0.18}_{-0.12}$	$42.1^{+15.0}_{-11.3}$	25.3±0.97	0.935 (381)
		whole	PL	28.0±1.1	1.80±0.01	-	-	$30.5^{+0.8}_{-0.7}$	1.08 (452)
			Cut PL	19.6±1.4	1.49±0.04	-	$38.3^{+6.3}_{-4.7}$	25.5±0.82	0.907 (451)
			Band	18.0±1.4	1.42±0.05	2.29±0.12	$27.2^{+4.3}_{-4.8}$	27.2±0.8	0.879 (450)
060607	p1	rise	PL	5.0±4.4	1.51±0.07	-	-	$15.2^{+2.4}_{-2.3}$	0.548 (35)
			Cut PL	4.9±4.4	1.51±0.07	-	∞	$15.2^{+2.4}_{-2.3}$	0.564 (34)
			Band	-	-	-	-	-	
		decay	PL	7.8±2.1	1.74±0.06	-	-	$7.67^{+0.85}_{-0.79}$	1.08 (139)

			Cut PL	7.8±2.1	1.74±0.06	-	∞	$7.67^{+0.85}_{-0.79}$	1.09 (138)
			Band	-	-	-	-	-	
		whole	PL	6.3±1.8	1.67±0.05	-	-	$9.03^{+0.80}_{-0.79}$	0.936 (162)
			Cut PL	6.3±1.9	1.67±0.05	-	∞	$9.02^{+0.89}_{-0.86}$	0.943 (161)
			Band	-	-	-	-	-	
	p2	rise	PL	13.1±2.1	1.80±0.05	-	-	$6.63^{+0.59}_{-0.57}$	1.06 (168)
			Cut PL	11.3±2.5	1.71±0.09	-	102^{+603}_{-59}	$5.76^{+0.92}_{-0.98}$	1.06 (167)
			Band	9.3±3.0	$1.58^{+0.14}_{-0.11}$	$1.99^{+0.32}_{-0.14}$	$22.9^{+74.3}_{-16.0}$	$5.61^{+0.84}_{-0.87}$	1.06 (166)
		decay	PL	6.6±1.7	1.98±0.06	-	-	$3.05^{+0.25}_{-0.23}$	0.977 (203)
			Cut PL	6.2±1.9	$1.94^{+0.07}_{-0.14}$	-	$124^{+\infty}_{-104}$	$2.68^{+0.59}_{-0.71}$	0.981 (202)
			Band	-	-	-	-	-	
		whole	PL	8.9±1.3	1.89±0.04	-	-	$4.17^{+0.26}_{-0.24}$	1.07 (284)
			Cut PL	8.2±1.5	1.86±0.06	-	$164^{+\infty}_{-105}$	$3.76^{+0.68}_{-0.54}$	1.08 (283)
			Band	-	-	-	-	-	
060814		rise	PL	40.3±2.9	1.56±0.01	-	-	59.2±1.8	0.858 (199)
			Cut PL	37.5±3.1	1.50±0.04	-	280^{+193}_{-106}	57.7±2.0	0.846 (198)
			Band	32.7±4.5	$1.34^{+0.06}_{-0.12}$	$1.65^{+0.03}_{-0.05}$	$40.8^{+72.4}_{-29.0}$	58.3±1.9	0.839 (197)
		decay	PL	35.2±1.3	1.71±0.02	-	-	$37.2^{+0.9}_{-1.0}$	1.08 (367)
			Cut PL	35.2±1.3	1.71±0.01	-	∞	37.2±1.0	1.08 (366)
			Band	-	-	-	-	-	
		whole	PL	35.3±1.2	1.66±0.01	-	-	$43.0^{+0.8}_{-0.9}$	1.03 (439)
			Cut PL	34.7±1.1	1.64±0.02	-	$974^{+\infty}_{-527}$	42.7±1.0	1.03 (438)
			Band	-	-	-	-	-	
060904B		rise	PL	72.9±2.7	2.03±0.02	-	-	30.0±0.7	1.07 (391)
			Cut PL	56.7±3.0	1.65±0.06	-	$27.0^{+5.4}_{-4.2}$	24.4±0.8	0.925 (390)
			Band	54.1±3.6	1.56±0.08	$2.57^{+0.11}_{-0.16}$	$19.2^{+6.45}_{-4.52}$	25.4±0.9	0.921 (389)
060929		rise	PL	28.2±2.9	1.81±0.05	-	-	$6.69^{+0.59}_{-0.53}$	1.00 (162)
			Cut PL	25.3±3.6	1.70±0.10	-	$69.0^{+237.5}_{-38.4}$	$5.40^{+1.08}_{-0.97}$	0.996 (161)
			Band	11.9±4.1	$0.62^{+0.44}_{-0.30}$	$1.95^{+0.15}_{-0.08}$	$2.56^{+4.29}_{-1.07}$	$5.32^{+0.69}_{-0.79}$	0.965 (160)
		whole	PL	22.9±1.4	1.90±0.03	-	-	$5.54^{+0.27}_{-0.25}$	0.889 (342)
			Cut PL	22.1±1.6	1.87±0.05	-	$170^{+\infty}_{-97}$	$5.03^{+0.74}_{-0.54}$	0.889 (341)
			Band	-	-	-	-	-	

Table 5.4: The spectral parameters of the X-ray flares in the 0.5-150 keV fitted with the power-law (PL), the cutoff power-law (Cut PL), and the Band function (Band).

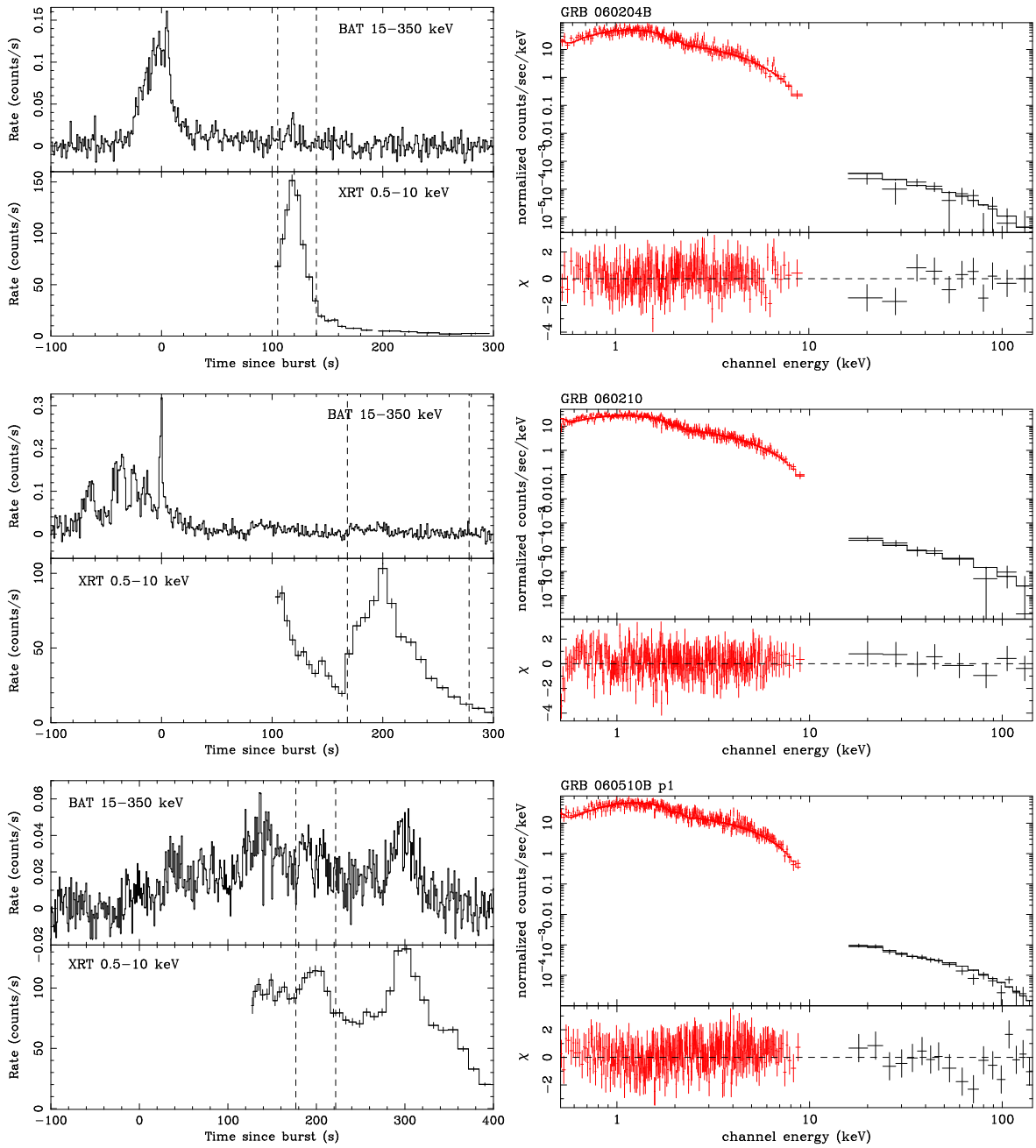

Figure 5.18: *Left* : BAT and XRT light curves. The vertical dashed line represents the source region of the spectrum. *Right* : BAT and XRT spectrum fitted with the power-law function.

x

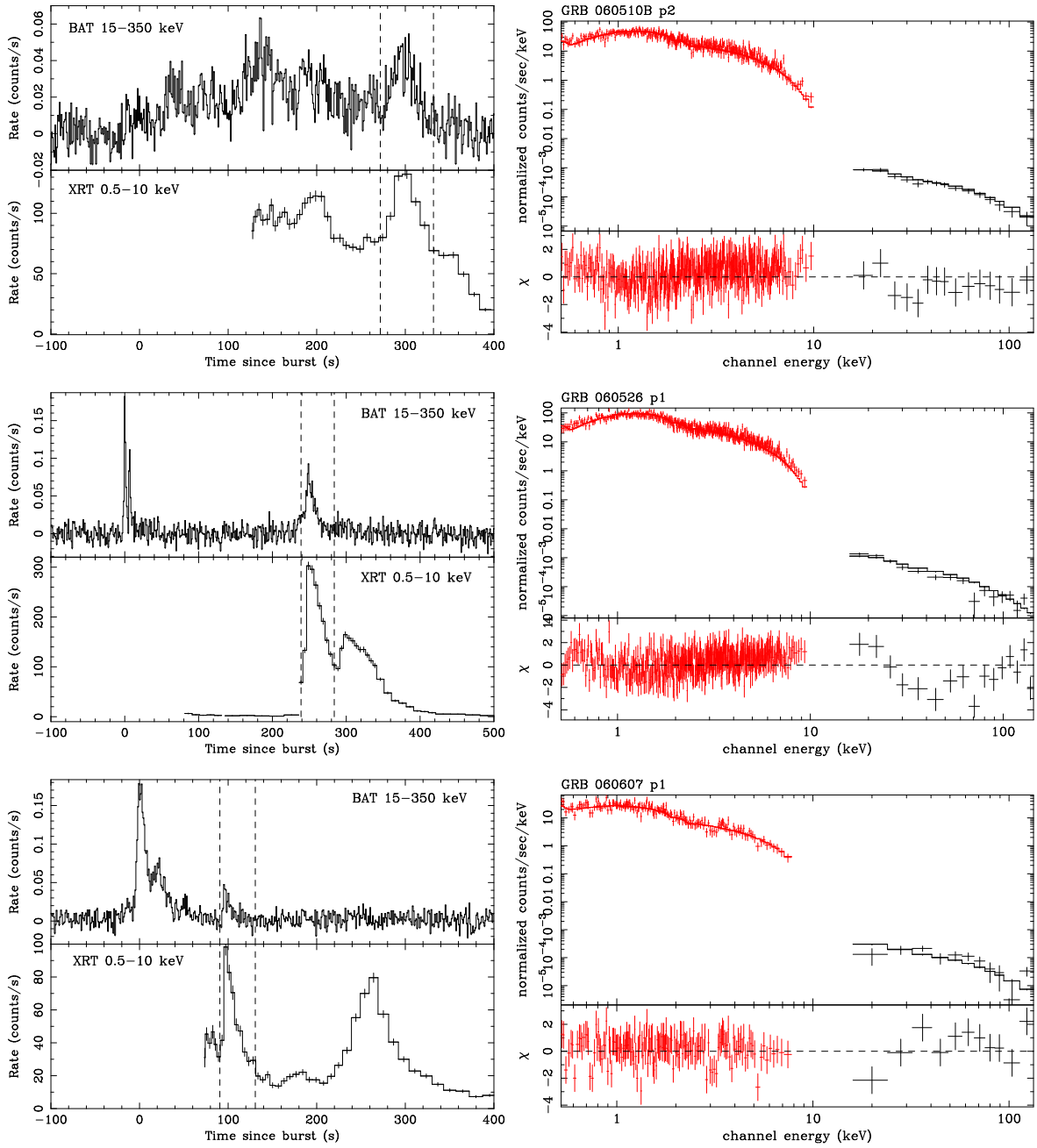

Figure 5.19: *Left* : BAT and XRT light curves. The vertical dashed line represents the source region of the spectrum. *Right* : BAT and XRT spectrum fitted with the power-law function.

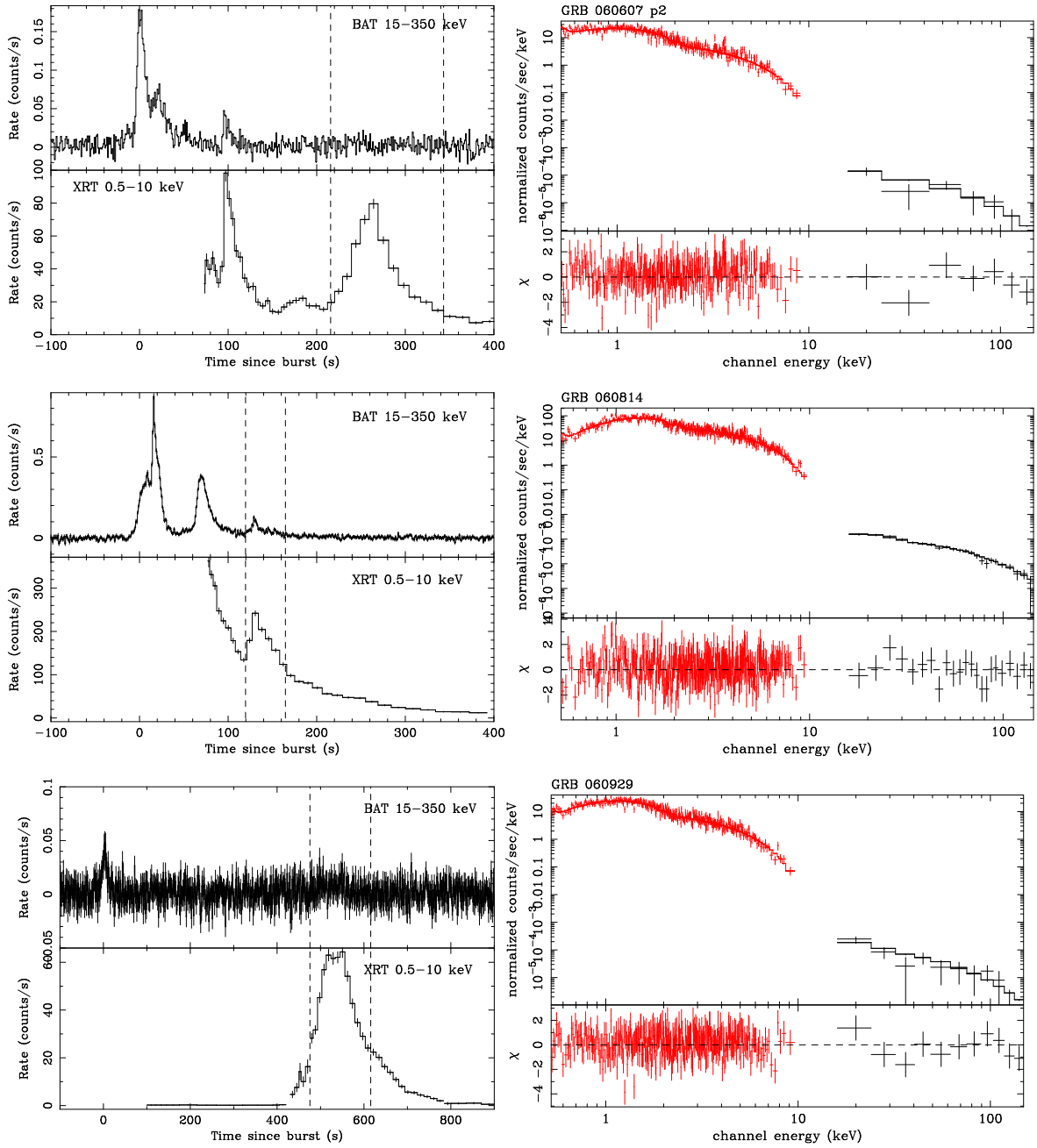

Figure 5.20: *Left* : BAT and XRT light curves. The vertical dashed line represents the source region of the spectrum. *Right* : BAT and XRT spectrum fitted with the power-law function.

Chapter 6

Results & Discussion

6.1 Rapid Decay

The temporal bridge between the GRB prompt emission and the afterglow emission is essential for revealing whether the prompt emission and the afterglow originate from the same component. Before the *Swift* era, no solid observation was available to reveal the origin of the GRB and afterglows.

If the prompt emission and the afterglow arise from different emission sites, as is expected in the internal shock scenario, and if the prompt emission flux level is much higher than the afterglow emission flux level, one expects to see a steeply decaying light curve during the transition from the prompt emission phase to the afterglow phase. Such a steep decay is due to the "curvature effect" (e.g., Kumar & Panaitescu 2000; Dermer 2004; Dyks et al. 2005; Panaitescu et al. 2006). The prompt emission from the large angles ($\theta > \Gamma^{-1}$) relative to our line of sight that reaches us at late times ($\Delta t \sim R\theta^2/2c$), resulting in a steep flux decay with $\alpha_1 = 2+\beta_1$ with the standard convention $F_\nu \propto \nu^{-\beta_1} t^{-\alpha_1}$. Figure 6.1 a plot of the α_1 vs β_1 relation. As can be seen in Figure 6.1, the α_1 - β_1 correlation is satisfied in most cases, but some cases show a steeper temporal decay index ($\alpha_1 > \beta_1 + 2$). Nousek et al. (2006) explain this as follows: The temporal decay index of $\alpha_1 = \beta_1 + 2$ applies separately to each spike in the prompt light curve, as it corresponds to a collision between two sub-shells in the internal shock model, where the emission from that collision decays as $F_\nu \propto (t-t_0)^{-\alpha_1}$, with t_0 as the onset time of a particular spike. Since the power-law fits to the light curve uses the GRB trigger ($T_{\rm GRB}$), which corresponds to the onset of the first spike, as the reference time, this would cause a seemingly steeper power-law decay index for later spikes. The decay of the last pulse, for which $t_0 \sim T_{\rm GRB}$, will approach a power-law decay in t for $t/T_{\rm GRB} \geq$ a few. This would lead to a decrease in α_1 with time until it approaches $\beta_1 + 2$ at $t/T_{\rm GRB} \geq$ a few. Thus, if $t/T_{\rm GRB} \leq$ a few an asymptotic

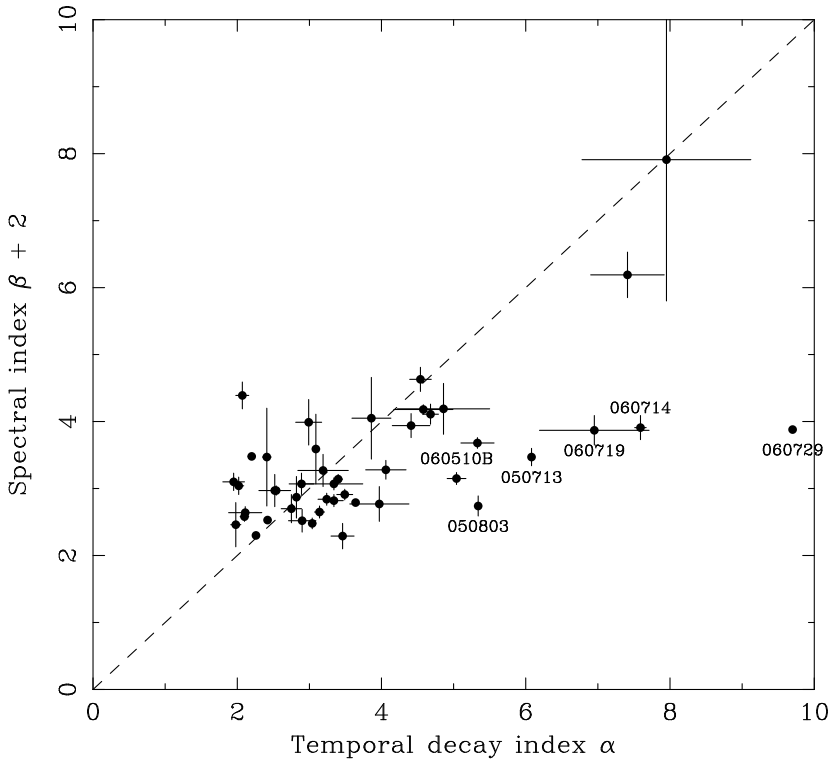

Figure 6.1: The plot of the temporal decay index α and spectral index $\beta + 2$. The solid line shows the theoretical prediction for the prompt GRB tails emitted at large angles ($\theta > \Gamma^{-1}$) relative to our line sight.

value of $\alpha_1 = \beta_1 + 2$ might not be reached. In practice, we calculated the t_0 values by fitting the steep decay light curve of 6 events with the function (Zhang et al. 2006, Liang et al. 2006):

$$F_\nu(t) = A\frac{(t - t_0)}{t_0}^{-(2+\beta_1)} + Bt^{-C}, \tag{6.1}$$

where β_1 is the X-ray spectral index during the steep decay, A and B are normalization parameters for both the rapid decay component and the underlying forward shock component, respectively, and C is the temporal index of the forward shock emission component. Figure 6.2 show fitting results. The joint BAT-XRT light curves were obtained by extrapolating the BAT light curves into the XRT band (0.5-10 keV). As a results, we can understand that the fitted t_0 values correspond to the beginning of the last pulse.

On the other hand, a shallower temporal decay index, $\alpha_1 < 2+\beta_1$, can not be explained by this scenario and might require a different physical origin.

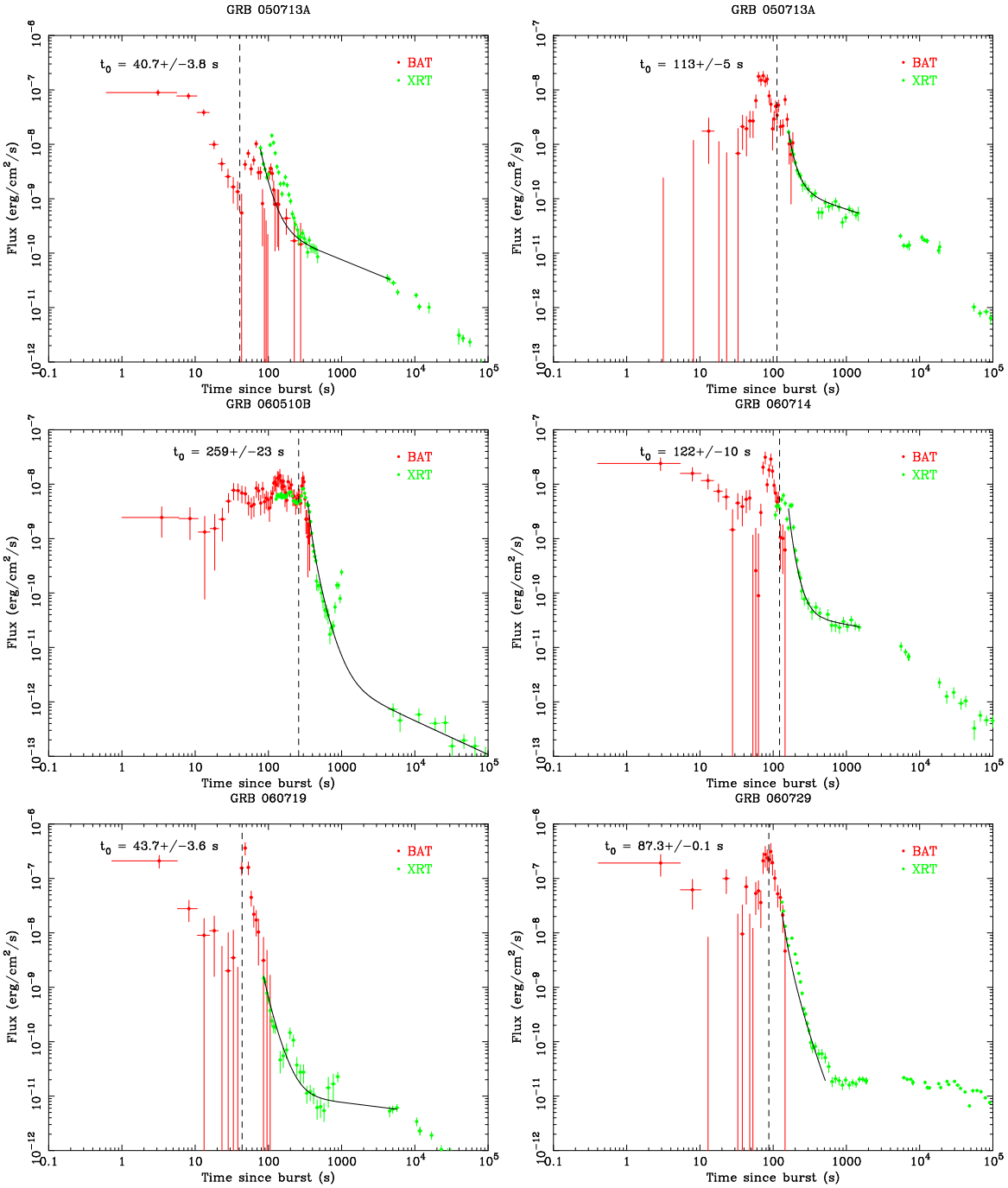

Figure 6.2: XRT light curves with the best-fitting results. The vertical dashed line shows the best-fit t0 value.

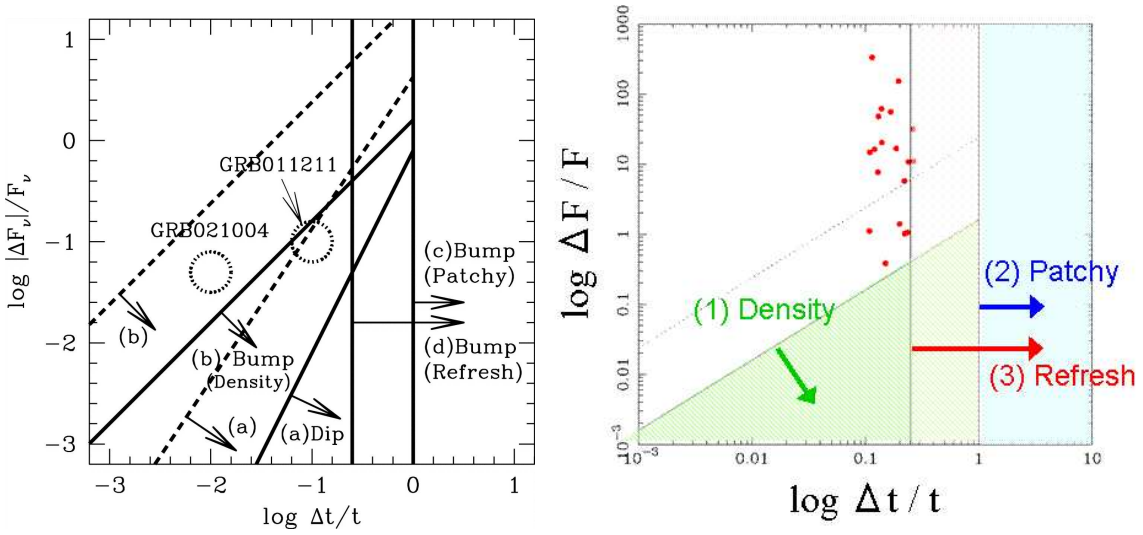

Figure 6.3: *Left*: Kinematically allowed regions for afterglow variabilities shown in the plane of the relative variability timescale $\Delta t/t$ and relative variability flux $\Delta F_\nu/F_\nu$ (Ioka et al. 2005). *Right*: Plot of the observed $\Delta t/t$ and $\Delta F_\nu/F_\nu$ of the X-ray flares.

6.2 X-ray Flares

6.2.1 Theoretical Models of Afterglow Variability

Four major scenarios have been proposed for afterglow variability: (1) fluctuation in the ambient density model, (2) patchy shell model, (3) refreshed model and (4) long-acting engine model.

Ioka et al. (2006) shows that kinematic arguments can give limits on the timescale and amplitude of the variability in GRB afterglows. Theoretical limits are shown in Fig 6.3 (*right*) and for comparison, observed values of X-ray flares are plotted in Fig 6.3 (*left*). The X-ray flares show a large amplitude $\Delta F_\nu/F_\nu \sim 10 - 100$ and the short timescale $\Delta t/t \leq 1$.

(1) Fluctuation in the Ambient Density Model

In this model, afterglow variabilities are due to ambient density fluctuations caused by turbulence in the interstellar medium or variable winds from the progenitor star (Wang & Loeb 2000; Lazzati et al. 2002; Dai & Lu 2002; Nakar et al. 2003). The kinematical upper limit on the timescale and amplitude of this model is shown in Fig 6.3. It is very hard to obtain variability with a large amplitude and short timescale. After entering the dense cloud, the Lorentz factor of the blast wave is decelerated rapidly. The observed time $t \sim R/2\Gamma^2$ is hence stretched. Therefore, the light curves for a blast wave surfing on

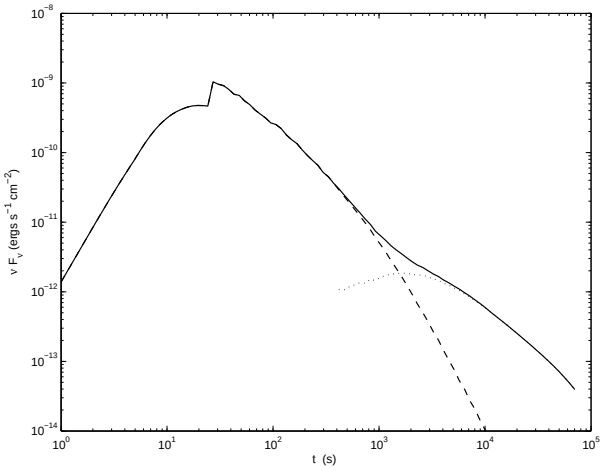

Figure 6.4: X-ray flare powered by a relativistic fireball interacting with a dense cloud simulated by Zhang et al. (2006). The cloud is located at $R = 3.0 - 3.3 \times 10^{16}$ cm with a density n = 100 cm^{-3}. The dashed line is the X-ray emission contributed by the electrons shocked at $R < 3.3 \times 10^{16}$ cm, and the dotted line is the X-ray emission contributed by the electrons shocked at $R > 3.3 \times 10^{16}$ cm. The solid line is the sum of these two components.

a density wave are expected to be smooth. A predicted light curve is shown in Fig 6.4. Therefore, the X-ray flares are likely not caused by this model.

(2) Patchy Shell Model

In this model, the GRB jet consists of many "sub-jets" (Yamazaki et al. 2004, Ioka & Nakamura 2001). Since the visible size $\theta \sim 1/\Gamma$ grows as the Lorentz factor Γ drops, the observed flux varies depending on the angular structure. A predicted light curve is shown in Fig 6.5. The variability timescales in the afterglow at time t should be $\Delta t/t \sim 1$ (Nakar & Oren 2004). Since the variability timescale of X-ray flares are $\Delta t/t < 1$, this model cannot account for the observed X-ray flares.

(3) Refreshed Shock Model

In this model, multiple shells which have different velocities are ejected, and the variability occurs when the slow inner shell catches up with the fast outer shell a later time, since the velocity of the outer shell is decelerated due to the interaction with the ambient medium (Rees & Meszaros 1998; Panaitescu et al. 1998; Kumar & Piran 2000; Sari & Meszaros 2000; Zhang & Meszaros 2002). The variability timescale in the afterglow at time t given

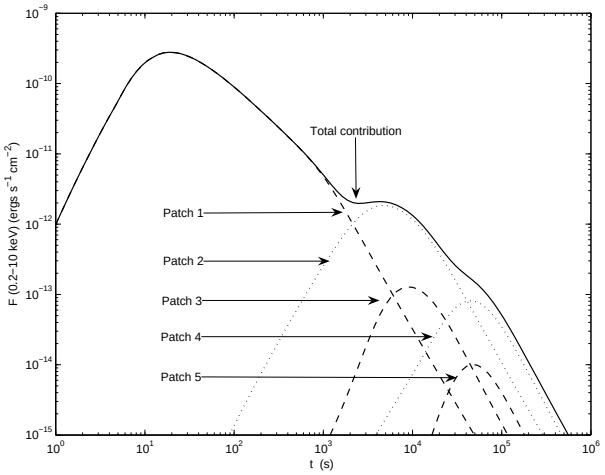

Figure 6.5: X-ray light curve powered by a patchy jet. For simplicity, an annular patchy jet is simulated by Zhang et al. (2006))

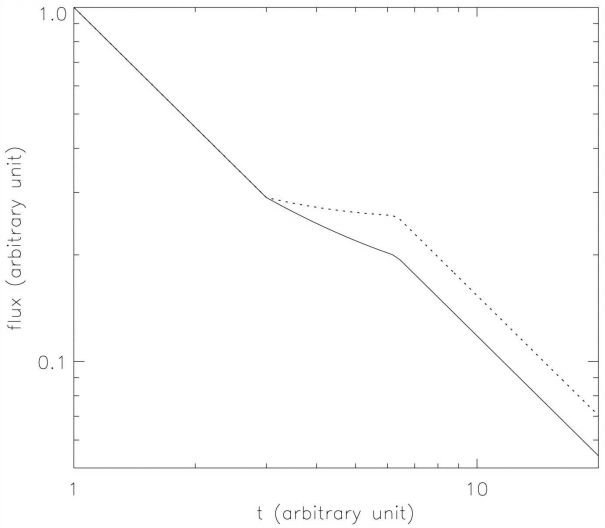

Figure 6.6: Effect of shell collision on the afterglow light curve (Kumar & Piran 2000). The continuous curve corresponds to $E_2/E_1 = 0.4$ and the dashed curve is for $E_2/E_1 = 0.7$.

by $\Delta t/t \geq 1/4$ (Ioka et al. 2005). Since inner shells increase the total energy in the blast wave, the light curve generally shows a step-like signature and the flux level does not resume the previous level (Fig 6.6). This property is inconsistent with the X-ray flares, since the temporal decay index before and after the flare is approximately identical.

(4) Long-acting Engine Model

In this model, the central engine might still be active and emitting shells during the observing time t (Rees & Meszaros 2000; Zhang & Meszaros 2002; Dai & Lu 1998). This model can explain the variability timescale down to milliseconds and there is no limit on the flux variability. Therefore, only this model can explain both the variability timescale and the flux for X-ray flares.

6.2.2 X-ray Flare Start Time

The curvature effect is due to delay of propagation of photons from large angles with respect to the line-of-sight, and the GRB tails can generally be interpreted in this model. Assuming that the tails of X-ray flares are also predominantly caused by the curvature effect, we calculated the t_0 values of these tails by fitting the XRT light curves with equation 6.1. In Appendix J, we show the light curves of X-ray flares in the energy range of $0.5 - 10$ keV. Calculated t_0 values are summarized in Table 6.1. In most cases, the t_0 values are determined near the beginning of the rising segments of X-ray flares (Fig 6.7), which indicates that the tails of X-ray flares follow the power-law decay expected for emission from relativistic shells with curvature, where the t_0 of the power-law agree with the beginning of flares. Therefore, the X-ray flares are due to central engine activity after the early prompt emission is over, sometimes up to few hours after the trigger (e.g., GRB 050916).

6.2.3 Summary of Analysis Results

In Chapter 5 we have analyzed the X-ray flares systematically. The aim of the analysis was to study the properties of X-ray flares and to find out if there are any similarities or differences with the prompt emission. In the following, we briefly summarize the results contained in this thesis.

Temporal Profiles of X-ray Flares

Temporal profiles of GRB pulses are characterized by Norris et al. (1996): The definition of the temporal profile is given by

$$\begin{aligned} I(t) &= A \times \exp[-(|t - t_{\rm max}/\sigma_{\rm r}|)^{\nu}] \quad (\text{for} \quad t \leq t_{\rm max}), \\ &= A \times \exp[-(|t - t_{\rm max}/\sigma_{\rm d}|)^{\nu}] \quad (\text{for} \quad t > t_{\rm max}), \end{aligned}$$

GRB		t_0 (s)	decay norm A (erg/cm^2/s)	AG norm B (erg/cm^2/s)	AG index C
050406		142±43	(2.17±5.59)e-11	(0.29±2.90)e-13	0.08±1.45
050502B		642±8	(1.96±0.36)e-11	(2.20±4.06)e-09	0.82±0.20
050607		255±18	(3.62±2.35)e-11	(3.10±6.24)e-11	0.30±0.26
050712		388±30	(3.66±3.76)e-12	(4.14±5.05)e-10	0.54±0.14
050713A	p1	94.5±5.1	(2.06±1.22)e-10	(17.4±9.9)e-10	0.45±0.09
050713A	p2	109±9	(4.06±2.62)e-10	(11.0±6.4)e-09	0.39±0.09
050714B		191±70	(1.95±7.80)e-09	(8.82±16.0)e-10	0.48±0.18
050716		290±56	(2.34±3.86)e-11	(4.93±2.04)e-08	1.08±0.04
050726		214±26	(2.35±4.53)e-12	(5.35±1.51)e-08	0.99±0.04
050730	p1	108±20	(1.83±1.77)e-09	-	-
050730	p2	304±19	(2.02±0.90)e-10	-	-
050730	p3	339±79	(9.38±12.8)e-10	-	-
050822	p1	77.3±4.8	(2.33±0.94)e-09	-	-
050822	p2	156±17	(7.70±9.44)e-11	-	-
050822	p3	224±20	(3.87±3.97)e-09	(7.82±5.49)e-12	0.03±0.08
050904		405±16	(2.18±1.44)e-11	-	-
050908	p1	74.4±7.3	(1.27±0.79)e-10	-	-
050908	p2	346±11	(5.19±3.43)e-13	(3.50±0.65)e-08	1.22±0.02
050916		17600±1670	(4.06±4.58)e-13	-	-
050922B		878±9	(1.97±0.11)e-12	(2.41±0.01)e-12	-0.01±0.00
060111	p1	1.84±2.44	(5.40±25.1)e-03	(2.77±1.54)e-08	1.01±0.06
060111	p2	66.3±24.5	(1.38±3.04)e-08	(2.83±1.61)e-08	1.01±0.06
060111	p3	206±7	(6.57±1.91)e-10	(2.69±1.53)e-08	1.01±0.06
060115		229±51	(1.10±1.69)e-10	(1.05±1.24)e-10	0.42±0.14
060124	p1	540±7	(5.97±1.90)e-11	-	-
060124	p2	680±20	(5.02±6.59)e-12	-	-
060202		554±30	(1.18±0.54)e-10	(1.39±1.64)e-08	0.78±0.13
060204B	p1	98.1±1.9	(1.01±0.31)e-10	(5.46±2.97)e-09	0.71±0.07
060204B	p2	254±14	(1.81±1.27)e-11	(1.85±1.47)e-09	0.59±0.10
060210	p1	151±2	(1.60±0.31)e-10	(2.14±0.40)e-08	0.72±0.02
060210	p2	283±8	(2.88±1.23)e-11	(1.84±0.49)e-08	0.70±0.03
060312		87.3±1.4	(9.50±1.70)e-11	-	-
060418		102±3	(4.91±1.47)e-10	(4.63±0.89)e-07	1.21±0.03
060510B	p1	28.4±18.5	(6.45±12.2)e-07	-	-
060510B	p2	214±7	(1.03±0.25)e-09	-	-
060512		132±34	(1.46±2.76)e-10	(2.47±8.69)e-10	0.50±0.42
060526	p1	214±2	(2.28±0.26)e-10	(2.37±3.05)e-11	0.19±0.15
060526	p2	275±4	(1.95±0.43)e-11	(1.31±1.20)e-11	0.66±0.11
060604	p1	71.7±10.7	(4.52±4.57)e-09	(9.24±7.78)e-11	0.39±0.09
060604	p2	131±3	(7.58±2.09)e-11	(9.80±8.34)e-11	0.40±0.09
060607	p1	63.7±3.1	(9.91±3.38)e-10	(1.74±0.38)e-09	0.37±0.03
060607	p2	188±5	(2.35±0.61)e-10	(1.73±0.35)e-09	0.37±0.03
060714	p1	98.5±37.3	(2.77±11.4)e-10	(1.14±1.65)e-11	0.22±0.21
060714	p2	154±7	(1.24±0.69)e-11	(1.85±1.80)e-10	0.29±0.14
060814		22.5±6.9	(1.36±1.36)e-06	(5.60±3.94)e-11	0.09±0.08
060904	p1	184±30	(3.31±5.82)e-10	-	-
060904	p2	326±93	(2.57±4.54)e-10	-	-
060904B		95.4±6.6	(1.60±0.71)e-08	(1.49±0.74)e-06	1.39±0.05
060929		428±22	(7.34±4.86)e-11	-	-

Table 6.1: The GRB sample and the fitting results

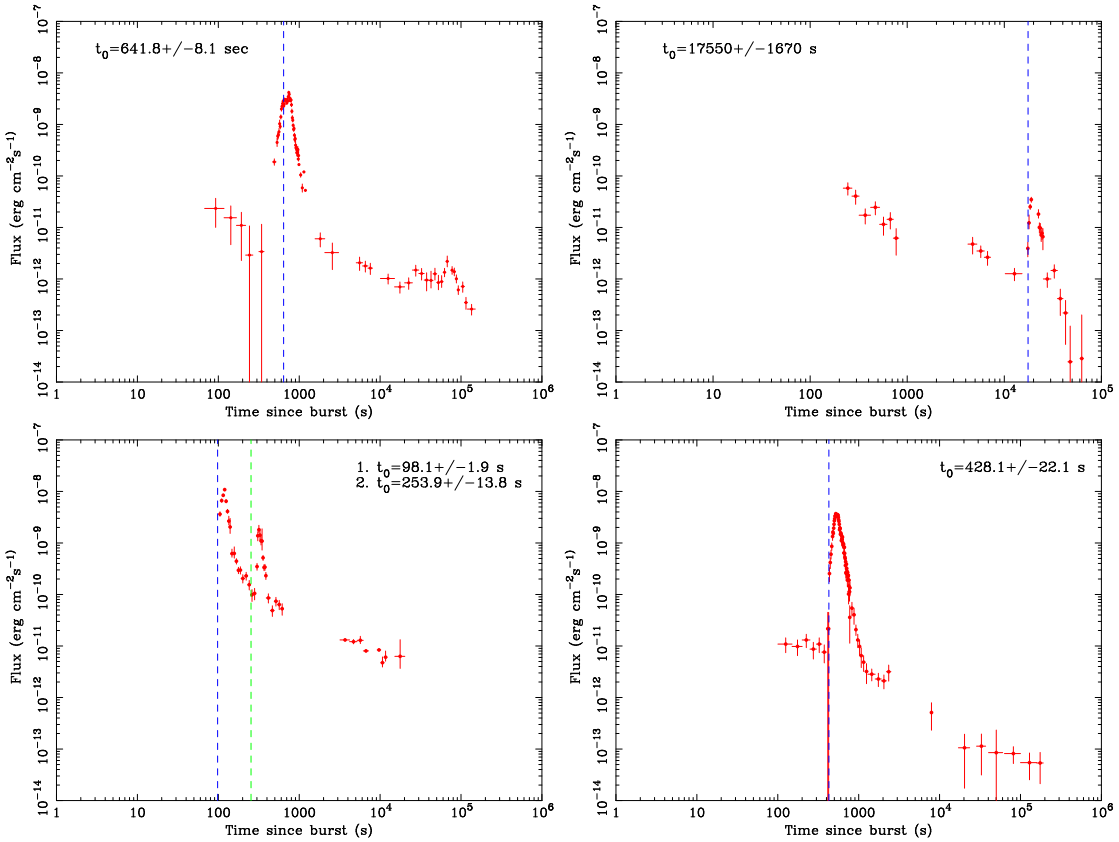

Figure 6.7: XRT Light curves in the 0.5-10 keV band. The vertical dashed lines mark the best-fit t0 values (050502B, 050916, 060204B and 060929).

where $t_{\max}$ is the time of the flare's maximum intensity A, $\sigma_{\rm r}$ and $\sigma_{\rm d}$ are the rise and decay time constants, and ν is a measure of pulse sharpness. From their study, the prompt emission pulses have the following temporal properties:

- Pulse shapes are generally intermediate between exponential and Gaussian ($\nu \sim 1-2$).
- Pulses rise more quickly than they decay, the majority having rise-to-decay rations of $\sigma_{\rm r}/\sigma_{\rm d} \sim 0.3-0.5$, independent of energy.
- The low energy emission is delayed, compared to the high energy mission by $\sim$1 s between $25-50$ keV band and $50-300$ keV.

We examined the temporal profiles of X-ray flares using same methods as Norris et al. (1996). As a result, we found that the pulse shapes of the X-ray flares are very similar to those of prompt emission:

- The peak sharpness is distributed between 1 and 2; this tendency shows that pulse shapes cluster between exponential and Gaussian.

- The majority have rise-to-decay ratios < 1.
- The Pulse FWHM of the X-ray flares (0.5-10 keV) are distributed around $\sim$50 s, whereas for prompt emission (15-150 keV) they are $\sim$ 2 s.
- X-ray flares peak earlier in the harder $(1 - 10$ keV) band than in the soft $(0.5 - 1$ keV) by about few seconds.

The pulse width (Δt) is related to the energy of the observational band as $\Delta t \propto E^{-0.4}$ (Fenimore et al. 1995; Norris et al. 2005). The average photon energy ($\bar{E}$) of the BAT (15-150 keV) and XRT (0.5-10 keV) energy band is $\sim$ 40 keV and $\sim$ 0.8 keV, respectively. Therefore, the pulse width in the XRT band ($\Delta t_{\rm XRT}$) is expected to be 10 s $\sim$ 2 s $\times$ $(0.8/40)^{-0.4}$ if the BAT band (15-150 keV) flare width is same as the pulse width of the prompt emission $\Delta t_{\rm BAT} \sim$ 2 s. However, the observed pulse width for the X-ray flares $\Delta t_{\rm XRT}$ is $\sim$ 50 s.

The pulse width is determined by the angular time $\Delta t = R_{\rm s}/(2c\Gamma_{\rm s})$ (Eq. 2.9), where $R_{\rm s}$ is the radius where collision occurs, and $\Gamma_{\rm s}$ is the Lorentz factors of the shocked emitting region. Therefore, the wide pulse of X-ray flares indicate that the Lorentz factor of the shells are small or the distance at which shocks occur is large compare to those of prompt emission.

Spectral Evolution

The spectra of X-ray flares show an evolution between the rise part and the decay part. Such properties are also observed in the prompt GRB emission (Norris et al. 1996, Zhang et al. 2006).

Within the standard synchrotron shock model, the spectral index does not change unless a spectral break crosses the observational band. The flux expected in the synchrotron shock model (adiabatic evolution) is given by

$$F_\nu \propto \begin{cases} (\nu/\nu_{\rm c})^{1/3} F_{\nu,\rm max} & \nu_{\rm c} > \nu, \\ (\nu/\nu_{\rm c})^{-1/2} F_{\nu,\rm max} & \nu_{\rm m} > \nu > \nu_{\rm c}, \\ (\nu_{\rm m}/\nu_{\rm c})^{-1/2} F_{\nu,\rm max} (\nu/\nu_{\rm m})^{-p/2} & \nu > \nu_{\rm m} \end{cases} \tag{6.2}$$

where $\nu_{\rm m} \equiv \nu(\gamma_{\rm e,min})$, $\nu_{\rm c} \equiv \nu(\gamma_{\rm e,c})$, and $F_{\nu,\rm max}$ is the observed peak flux. On the other hand, the observed spectral indices of the rise part and the decay part of X-ray flares are clustered around $\beta_1 = \Gamma_1 - 1 \sim 0.5 - 1$ and $\beta_2 = \Gamma_2 - 1 \sim 1 - 2$, respectively. These values are consistent with $\nu^{-0.5}$ for $\nu_{\rm m} > \nu > \nu_{\rm c}$ and $\nu^{-p/2} \sim \nu^{-1.15} (p = 2.3)$ for $\nu > \nu_{\rm m}$, respectively. Therefore we consider that the spectral evolutions is due to passing the $\nu_{\rm m}$ gradually through the XRT band.

6.2.4 Conclusion on Properties of X-ray Flare

We performed the temporal and spectral analysis of the X-ray flares and compared properties with GRB pulses. We found that there are many common features. Especially, the following two properties strongly support the interpretation that the X-ray flares are due to continued GRB central engine activity after the early prompt emission is over.

- The t_0 values of most X-ray flares are consistent with being near the beginning of the rising segment of the X-ray flares. This result indicates that the central engine reactivates after the early prompt emission is over.
- The flares with large amplitude and short time scale are difficult to explain with mechanisms associated with the external shock ($\Delta t/t \sim 1$; Ioka et al. 2005, Zhang et al. 2006).

6.3 Shallow Decay

Three kinds of models are proposed for the shallow decay phase. One class of models is the energy injection model, in which continuous energy is injected into the afterglow so that the flux decay becomes slower than the normal decay $\propto t^{-1}$. The injection may be caused by (1) the long-lived central engine or (2) the short-lived central engine ejecting shells with some ranges of Lorentz factors. A second class is (3) the inhomogeneous jet model. In this model, early afterglows are not bright because the jet surface on the line-of-sight is dim and the surrounding off-axis region is observed later. The other class is (4) the time-dependent microphysics model.

Here, we examined if there are any correlation between the parameters of prompt GRBs and the shallow decay phase. We practically compared the isotropic total energy of prompt emissions ($E_{\gamma,\mathrm{iso}}$) to the break time at the shallow-to-normal decay transition (T_{brk})

6.3.1 Correlation between $E_{\gamma,\mathrm{iso}}$ and T_{brk}

Estimation of the $E_{\gamma,\mathrm{iso}}$

As shown in section 1.2, a GRB spectrum is typically described by a Band function (Band et al. 1993), which is a smoothly-joint-broken power-law characterized by two photon indices Γ_1 and Γ_2 and break energy E_0. The peak energy of the νf_ν spectrum is $E_{\mathrm{peak}} = (2+\Gamma_1)E_0$. However, the typical E_{peak} values of GRB is ~ 250 keV, i.e., above the BAT energy band (15-150 keV). Actually most spectra observed by BAT are well fitted by a simple power-law function. BAT's observations cannot well determine E_{peak} and the high energy photon index Γ_2.

Therefore, we predict E_{peak} by using the E_{peak} - isotropic luminosity L_{iso} correlation (Ghirlanda et al. 2005). Since the photon index obtained from the BAT is distributed between 1 and 2.2, which are typical values of the low energy photon index and high energy photon index of GRBs, the peak energy E_{peak} of the bursts should be above the BAT band. Therefore, we assume for the GRB spectra a simple power-law shape:

$$N(E) = \begin{cases} AE^{-\Gamma_1} & \text{for } E \leq E_{\mathrm{peak}}, \\ AE_{\mathrm{peak}}^{-(\Gamma_1-\Gamma_2)}E^{-\Gamma_2} & \text{for } E > E_{\mathrm{peak}}. \end{cases} \tag{6.3}$$

where A is a normalization, Γ_1 and Γ_2 are the low and high energy photon indices, respectively, and E_{peak} is the peak energy. A and Γ_1 can be determined from BAT data, and Γ_2 is assumed to have the typical value of 2.2.

The observed flux at a given bandpass (E_1, E_2) as a function of E_{peak} can be given:

$$F_{E_1-E_2}(E_{\rm peak}) = \int_{E_1}^{E_2} EN(E)dE \tag{6.4}$$

Therefore, the isotropic luminosity is calculated as

$$L_{\rm iso} = 4\pi d_{\rm L}^2 \times F_{E_1-E_2}(E_{\rm peak}), \qquad \sim 4\pi d_{\rm L}^2 \times A\Big(\frac{1}{1-\Gamma_1} - \frac{1}{1-\Gamma_2}\Big) E_{\rm peak}^{1-\Gamma_1}. \tag{6.5}$$

where $d_{\rm L}$ is the luminosity distance.

On the other hand, the $E_{\rm peak} - L_{\rm iso}$ correlation is given by Ghirlanda et al. (2005):

$$\frac{E_{\rm peak}}{100\ {\rm keV}} = (4.88 \pm 0.06)\Big(\frac{L_{\rm iso}}{1.9 \times 10^{52}}\Big)^{0.48\pm0.01}. \tag{6.6}$$

If we assume that equation 6.5 and 6.6 are equivalent, we can obtain the $E_{\rm peak}$. Then we apply the $E_{\rm peak} - E_{\rm iso}$ relation (Amati 2006b) to calculated $E_{\rm peak}$ and estimate the $E_{\gamma,{\rm iso}}$.

First, we try to calculate $E_{\rm peak}$ of 21 GRB events with firm estimates of z and $E_{\rm peak}$, listed in Amati (2006). The calculated $E_{\gamma,{\rm iso}}$ is given in table 6.2. Figure 6.8 shows how the $E_{\gamma,{\rm iso}}$ calculated with our method compares with the $E_{\rm iso}^{\rm obs}$ derived by Konus-Wind and HETE-2 data. Since six GRBs are better fitted with the cutoff power-law model, $E_{\rm peak}$ of these events can be determined directly. We apply the $E_{\rm peak} - E_{\rm iso}$ relation to these observed $E_{\rm peak}$ and estimate the $E_{\gamma,{\rm iso}}$. These are plotted as cross marks. The result suggests that our derived $E_{\gamma,{\rm iso}}$ are approximately consistent with the observed values, especially for GRBs with $E_{\rm iso} \sim 10^{53}$ erg.

Correlation Analysis and Result

We apply the same method to GRBs with known redshift and firm estimates of the break time at the shallow-to-normal decay transition in the X-ray light curve ($T_{\rm brk}$) Derived parameters are summarized in Table 6.3.

Figure 6.9 shows the distribution of $T_{\rm brk}$ in the source frame and the $E_{\gamma,{\rm iso}}$. As a result, we found that the break time is weekly correlated inversely with $E_{\gamma,{\rm iso}}$. This correlation suggests that the larger the isotropic equivalent energy $E_{\gamma,{\rm iso}}$ the earlier the end time of shallow decay phase.

GRB	$E_{\gamma,\mathrm{iso}}$ (10^{52} erg)	Observed $E_{\gamma,\mathrm{iso}}$ (10^{52} erg)
050401	118±28	41±8
050505	36.8±12.7	40±10
050509B	0.185±0.253	0.0007±0.0004
050603	246±135	70±5
050724	0.104±0.044	0.035±0.007
050813	1.50±2.24	0.09±0.06
050904	41.4±32.9	193±127
051109	13.8±9.9	7.5±0.8
051221	7.27±1.31	0.29±0.06
060115	10.8±12.8	9.1±1.5
060124	11.0±6.1	48±7
060418	6.24±1.30	7.5±0.8
060502B	0.442±0.513	0.025±0.020
060614	0.099±0.015	0.25±0.1
061007	34.4±11.0	100±10
050416	0.019±0.121	0.12±0.02
050525	1.81±0.31	3.39±0.17
050922C	21.2±9.2	6.1±2.0
060206	14.2±7.5	5.8±0.6
060707	7.20±4.74	8.0±1.5
060927	21.9±10.5	10±2

Table 6.2: Calculated $E_{\gamma,\mathrm{iso}}$ from our method and observed $E_{\gamma,\mathrm{iso}}$

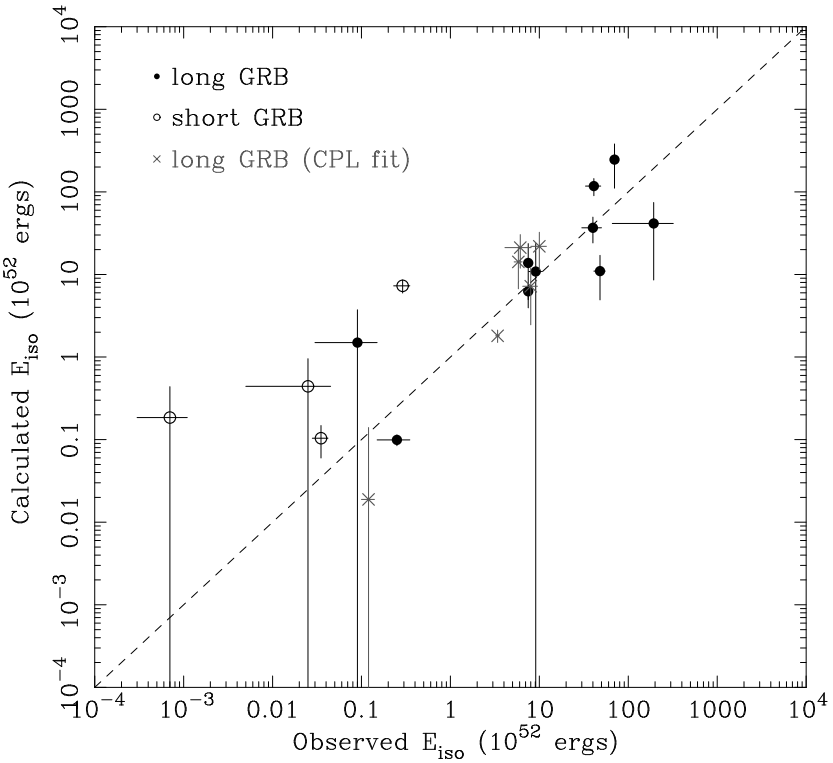

Figure 6.8: Comparison of $E_{\gamma,\mathrm{iso}}$ derived from our method with firm estimated values $E^{\mathrm{obs}}_{\mathrm{peak}}$. The dashed line is the calculated $E_{\gamma,\mathrm{iso}} = E^{\mathrm{obs}}_{\gamma,\mathrm{iso}}$

GRB	E_{peak} (keV)	$E_{\mathrm{p,i}}$ (keV)	$E_{\gamma,\mathrm{iso}}$ (10^{52} erg)	z^{ref}	d_{L} (Mpc)
050802	109±21	294±57	8.35±2.83	1.71	13000
050803	20.3±3.7	28.9±5.3	0.153±0.049	0.422	2310
060108	113±39	417±145	15.2±9.1	2.7	22700
060502	135±21	339±53	10.6±2.9	1.51	11100
060526	114±21	480±90	19.4±6.3	3.22	28100
060604	108±47	396±173	13.9±10.5	2.68	22500
060605	42.2±13.5	199±63	4.23±2.34	3.71	33400
060607	156±23	635±96	31.4±8.4	3.08	26700
060714	81.9±19.2	304±71	8.83±3.61	2.71	22800
060729	11.4±6.6	17.6 ±10.2	0.065±0.065	0.54	3100

Table 6.3: Calculated E_{peak} and $E_{\gamma,\mathrm{iso}}$

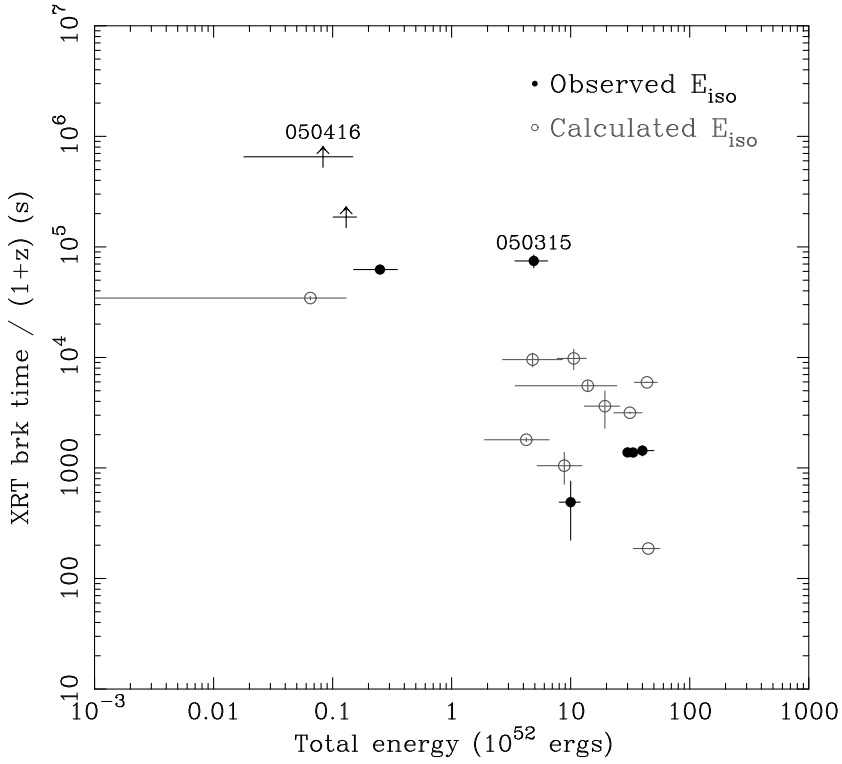

Figure 6.9: Distribution of the break time in the X-ray light curve and $E_{\gamma,\mathrm{iso}}$.

6.3.2 Comparison with theoretical models

We will discussion three kinds of models proposed for the shallow decay phase in X-ray light curve: the energy injection model (Nousek et al. 2006; Zhang et al. 2006; Granot & Kumar 2006a), the inhomogeneous jet model (Toma et al. 2006; Eichler & Granot 2006), and the time-dependent microphysics model.

Energy Injection Model

The energy injection model (Nousek et al. 2006; Zhang et al. 2006; Granot & Kumar 2006a) is considering that continuous energy is injected into the afterglow so that the flux decay becomes slower than the usual $\propto t^{-1}$. The injection may be caused by (1) the long-lived central engine (Dai & Lu 1998; Rees & Meszaros 2000; Zhang & Meszaros 2002) or (2) the short-lived central engine ejecting shells with some range of Lorentz factors (Rees & Meszaros 1998; Kumar & Piran 2000; Sari & Meszaros 2000; Zhang & Meszaros 2002).

First we consider (1), the long-lived central engine model. This scenario requires the central engine to remain active until the end of the shallow decay phase ($T_{\rm brk}$), which is in many cases $1,000 \sim 10,000$ s. Note that the shallow decay phase in GRB 050416A extends to ~ 74.5 days after the GRB (Sato et al. 2006), that is, the central engine remains active for ~ 74.5 days. Within this model, our result of an inverse correlation between $T_{\rm brk}$ and the $E_{\gamma,{\rm iso}}$ indicates that GRBs which have larger the isotropic equivalent energy eject the matter more rapidly.

As shown in section 6.1, the X-ray flares also suggest that the central source remains active after the GRB. The main difference is that the shallow decay scenario requires both smooth and continuous (rather than episodic) energy injection by the central engine at late times.

Next we consider (2), the the short-lived central engine with some range of Lorentz factors of ejected shells. After the internal shocks, shells are rearranged so that outer shells are faster and inner shells are slower. This configuration may also occur if the central engine ejects faster shell earlier. Outer shells are slowed down by making the external shock. Once the Lorentz factor of the shocked shell drops below that of a slower shell, the slower shell catches up with the shocked shell, injecting energy into the forward shock. Within this model, $T_{\rm brk}$ corresponds to the time at which the slower shell finishes to catch up with the outer shell. Therefore, our result of an inverse correlation between $T_{\rm brk}$ and $E_{\gamma,{\rm iso}}$ indicates that GRBs which have larger $E_{\gamma,{\rm iso}}$, eject shells with large Lorentz factors.

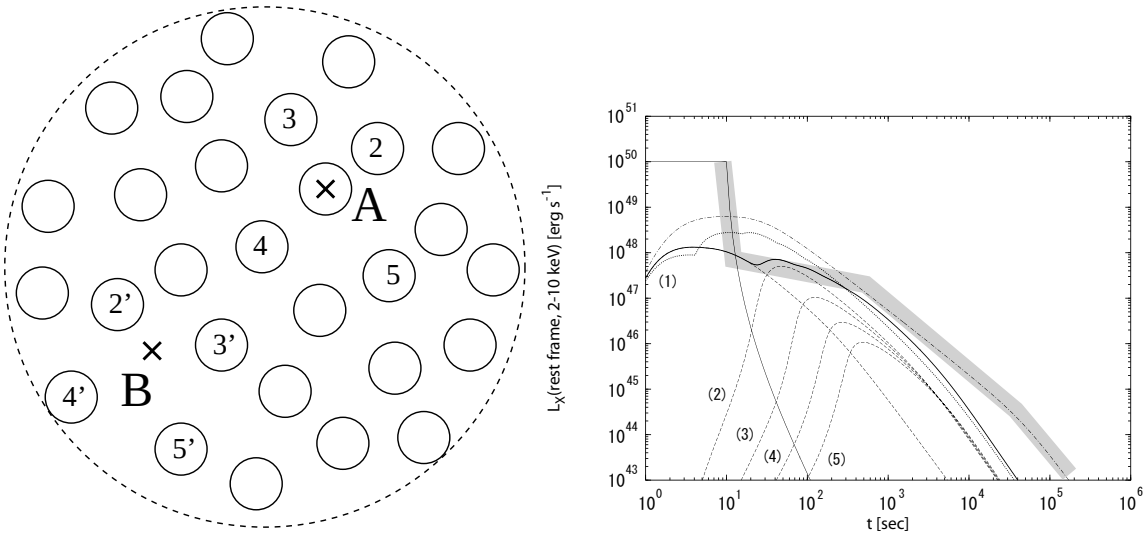

Figure 6.10: *Left*: Inhomogeneous jet structure. The whole jet (dashed circle) consists of multiple components (solid circle). *Right*: Predicted afterglow light curve.

Inhomogeneous Jet Model

In this model, early afterglows are not bright because the jet surface on the line-of-sight is dim and the surrounding off-axis region with ordinary brightness is observed later (Toma et al. 2005). The shallow decay phase is produced by the superposition of the afterglow from off-axis components (Figure 6.10).

Within this model, $T_{\rm brk}$ corresponds to the time when the afterglow from off-axis with the largest off-angle is observed. Toma et al. (2005) determined the necessary conditions to obtain a such "canonical" afterglow for two cases, that is, whether the line-of-sight is along a component or not. The later condition makes the prediction of an inverse correlation between $T_{\rm brk}$ and $E_{\gamma,\rm iso}$. In this case, the isotropic equivalent energy $E_{\gamma,\rm iso}$ is proportional to $\theta_{\rm v}^{-4}$ (Toma et al. 2005), where $\theta_{\rm v}$ is the viewing angle. On the other hand, the break time $T_{\rm brk}$ is estimated as $T_{\rm brk} \propto \theta_{\rm v}^{8/3}$. From these two relations, we can obtain $E_{\rm iso} \propto \theta_{\rm v}^{-4} \propto T_{\rm brk}^{-2/3}$. Figure 6.11 is plot of $T_{\rm brk}$ and $E_{\gamma,\rm iso}$ with the predicted $T_{\rm brk} - E_{\gamma,\rm iso}$ relation for this model. It is approximately consistent with the data.

Time-dependent Microphysics Model

This model considers that the microphysical parameters, such as the energy fraction that is distributed to electrons $\epsilon_{\rm e}$ and magnetic field $\epsilon_{\rm B}$, depends on the shock's Lorentz factor Γ. We usually assume that the micro-physical parameters do not vary and in fact, constant $\epsilon_{\rm e}$ and $\epsilon_{\rm B}$ are consistent with the observation of late time afterglows (Yost et al. 2003).

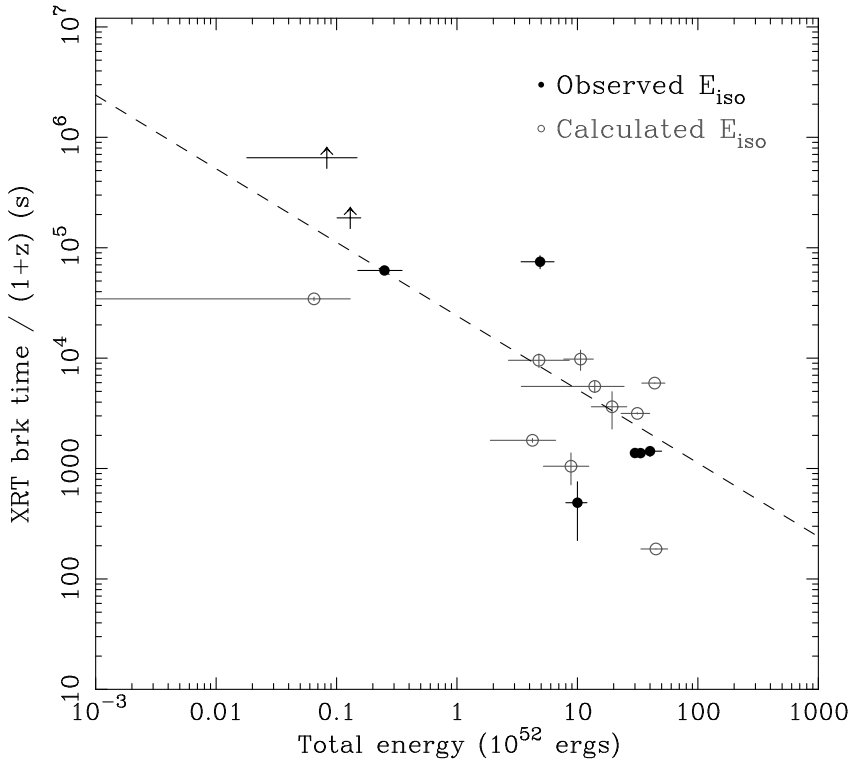

Figure 6.11: The predicted $T_{\rm brk} - E_{\gamma,\rm iso}$ relation for the inhomogeneous jet model.

However, the behavior of these parameters in the early time afterglow has not been known yet.

In the model, the microphysical parameters vary in the early afterglow for $\Gamma \leq \Gamma_0$, where Γ_0 is the Lorenz factor of the outflow at the X-ray decline transition. For $\Gamma > \Gamma_0$, the micro-physical parameters are constant as observed in the late time afterglow. The X-ray luminosity $L_{\rm X}$ is given by the bolometric kinetic luminosity L as $L_{\rm X} \sim \epsilon_{\rm e} L$. Since $L \propto t^{-1}$, the shallow X-ray light curve $L_{\rm X} \propto t^{-1/2}$ suggests that $\epsilon_{\rm e}$ evolves as $\epsilon_{\rm e} \propto t^{1/2}$ (Ioka et al. 2005).

Within this model, $T_{\rm brk}$ corresponds to the time at which the Lorentz factor Γ is decelerated to Γ_0. The Lorentz factor of the external shock evolves as $\Gamma(t) \propto E_{\rm iso}^{1/8} t_{\rm obs}^{-3/8}$. $T_{\rm brk}$ (Eq. 2.11) is rewritten as $T_{\rm brk} \propto \Gamma_0^{8/3} E_{\rm iso}^{1/3}$, which implies the positive correlation between $T_{\rm brk}$ and $E_{\gamma,\rm iso}$. This relation is inconsistent with our results of an inverse correlation between $T_{\rm brk}$ and $E_{\gamma,\rm iso}$.

6.3.3 Conclusion

From our results, we propose that the shallow decay light curves are most likely not due to the "time-dependent microphysics model". However, theoretical models of (1) the energy injection model and (2) the inhomogeneous model have a serious problem, as well

demanding an unreasonably high gamma-ray efficiency of the prompt GRBs, $\geq$ 75-90%, defined by $\epsilon_\gamma \equiv E_\gamma/(E_\gamma + E_k)$, where$E_\gamma$ is the radiated prompt energy and E_k is the kinetic energy of the afterglow remaining after the burst (Ioka et al. 2005). Such an efficiency is difficult to be produced by standard internal shocks.

Chapter 7

Conclusion

We studied the prompt emissions and the early X-ray afterglows observed by $Swift$ during the period January 2005 until the end of September 2006. For our analysis we used 160 prompt GRBs and 128 X-ray afterglows. The results are summarized as follows.

Properties of the prompt emissions

- The distribution of the burst durations is clustered around $10 - 100$ seconds which is approximately comparable to that of the BASTE sample. However, $Swift$ GRBs do not show a clear "bimodal" distribution seen in BASTE samples.

- The $Swift$ GRB spectra in the energy range of $15 - 150$ keV are generally well described by a single power-law. The distribution of the photon indices have a peak at ~ 1.5. However, the typical photon indices of BATSE GRBs were $\alpha \sim 1$ and $\beta \sim 2.2$ for the lower and higher energy band (Preece et al. 2000). The photon indices obtained from $Swift$ are distributed between BATSE's α and β values. Thus, we are likely observing the middle part of the Band function.

- $Swift$ GRBs follow the Amati relation ($E^{\rm src}_{\rm peak} \propto E^{0.5}_{\gamma,{\rm iso}}$) and the Yonetoku relation ($L_{\rm iso} \propto {E^{\rm src}_{\rm peak}}^{2.0}$).

Properties of the X-ray afterglows

- The "rapid decay phase" can be explained by the curvature emission of the relativistic shell. The relation between spectral and temporal indices of the rapid decay part is consistent with $\alpha = \beta + 2$ ($F_\nu \propto t^{-\alpha}\nu^{-\beta}$) in most cases, which is consistent with the curvature emission model.

- Temporal properties of X-ray flares and GRB pulses have following common characteristics:

- The pulse shape is generally intermediate between exponential and Gaussian.

- The rise-to-decay ratio is usually unity or less.

- The pulses peak earlier in the higher energy bands.

Therefore, the temporal profile of an individual X-ray flare is a FRED (fast-rise exponential decay) with a larger pulse with compared with that of a prompt emission. It indicate that the Lorentz factor of the shells are small or the distances at which the shocks occur is larger compare to those of the prompt emissions.

- The zero times of most X-ray flares are consistent with being near the beginning of the rising segment of X-ray flares.

- The X-ray flares with short time scale ($\Delta t/t \ll 1$) are difficult to explain with mechanisms associated with the external shock.

  Therefore, we conclude that X-ray flares are likely due to central engine activity, after the early prompt emission is over.

- We found that the break time at the shallow-to-normal decay transition in the X-ray light curve ($T_{\rm brk}$) is correlated inversely with $E_{\gamma,\rm iso}$. The larger the isotropic equivalent energy $E_{\gamma,\rm iso}$, the later the break time $T_{\rm brk}$.

- From our observational results, the shallow decay is not likely caused by the "time-dependent microphysics model". However, other models of the "energy injection" and the "inhomogeneous jet" have a serious problem, demanding an unreasonably high gamma-ray efficiency of the prompt emissions of $\geq$ 75-90%.

Bibliography

[1] Amati, L., et al. 2002, A&A, 390, 81

[2] Amati, L., et al. 2006a, MNRAS, 372, 233

[3] Amati, L., et al. 2006b, submitted to Il Nuovo Cimento C, astro-ph/0611189

[4] Andersen, M. I., et al. 2000, A&A, 364, L54

[5] Band, D. L., et al. 1993, ApJ, 413, 281

[6] Barthelmy, S. 2003, proc. SPIE, 5165, 175

[7] Barthelmy, S., et al. 2000, AIPC, 526, 731

[8] Bloom, J. S., et al. 2002, ApJ, 572, L45

[9] Briggs, M. S., et al. 1999, ApJ, 524, 82

[10] Blandford, R. D., & Mckee, C. F. 1976, Phys. Fluids, 19, 1130

[11] Burrows, D. N., et al. 2000, proc. SPIE, 4140, 64

[12] Chevalier, R. A. & Li, Z. 2000, ApJ, 536, 195

[13] Citterio, O., et al. 1996, proc. SPIE, 2805, 56

[14] Costa, E., et al. 1997, Nature, 387, 783

[15] Dai, Z. G., & Lu, T. 1998, A&A, 333, L87

[16] Daigne, F., & Mochkovitch, R. 1998, MNRAS, 296, 275

[17] Dyks, J., Zhang, B., & Fan, Y. Z. 2006, ApJ, submitted (astro-ph/0511699)

[18] Edelson, R. A. & Krolik, J. 1988, ApJ, 333, 646

[19] Eichler, D. & Waxman, E. 2005, ApJ, 627, 861

[20] Epstein, R. I., 1986, Radiation Hydrodynamics in Stars and Compact Objects, Proceedings of IAU Colloq. 89, 255, 305

[21] Fan, X., et al. 2003, AJ, 125, 1649

[22] Fishman, G. J. et al. 1994, ApJS, 92, 229

[23] Fishman, G. J. & Meegan, C. A. 1995, ARA&A, 33, 415

[24] Fruchter, A. S. et al. 1999, ApJ, 516, 683

[25] Fox, D. W., et al. 2003, Nature, 422, 284

[26] Galama, T. J., et al. 1998, ApJ, 497, L13

[27] Garnavich, P. M., et al. 2003, ApJ, 582, 924

[28] Gehrels, N., et al. 2004, ApJ, 611, 1005

[29] Gehrels, N., et al. 2005, Nature, 437, 851

[30] Ghirlanda, G., et al. 2005, MNRAS, 360, 45

[31] Granot, J., Nakar, E., & Piran, T., 2003, Nature, 426, 138

[32] Granot, J., & Kumar, P. 2006, MNRAS, 366, L13

[33] Greiner, J., et al. 2003, GCN Circ. 2020

[34] Hill, J. E., et al. 2000, proc. SPIE, 4140, 87

[35] Hill, J. E., et al. 2000, proc. SPIE, 4140, 87

[36] Holland, A. D., et al. 1996, proc. SPIE, 2808, 414

[37] Iwamoto, K., et al. 2000, ApJ, 534, 660

[38] Ioka, K., Kobayashi, S., & Zhang, B. 2005, ApJ, 631, 429

[39] Ioka, K., et al. 2006, A&A, 458, 7

[40] Kneib, J. P., et al. 2004, ApJ, 607, 697

[41] Klebesadel, R. W., Strong, I. B.,& Olson, R. A. 1973, ApJ, 182, L85

[42] Kobayashi, S. & Zhang, B. 2003, ApJL, 582, L75

[43] Kobayashi, S., Piran, T., & Sari, R. 1997, ApJ, 490, 92

[44] Krimm, P., & Piran, T. 2000, ApJ, 532, 286

[45] Kumar, P., & Piran, T. 2000a, ApJ, 532, 286

[46] Kumar, P., & Panaitescu, A. 2000b, ApJ, 541, L51

[47] Liang, E. W., et al. 2006, ApJ, 646, 351

[48] Matheson, T., et al. 2003, ApJ, 599, 394

[49] Mazzali, P. A., Iwamoto, K., & Nomoto, K. 2000, ApJ, 545, 407

[50] Mazzali, P. A., et al. 2002, ApJ, 572, L61

[51] Mirabal, N., et al. 2002, GCN Circ. 1618

[52] Nakar, E., Piran, T., & Granot, J. 2003, New Astronomy, 8, 495

[53] Nemiroff, R. J., 1994, AIP Conference Proceedings, 307, 730

[54] Nousek, J. A., et al. 2006, ApJ, 642, 389

[55] Norris, J. P., et al. 1996, ApJ, 459, 393

[56] van Paradijis, J., et al. 1997, Nature, 386, 686

[57] Paczynski, B., 1986, ApJ, 308, 43

[58] Panaitescu, A., et al. 2006, MNRAS, 366, 1357

[59] Piran, T. 1999, Physics Reports, 314, 575

[60] Preece, R, D., et al. 2000, ApJS, 126, 19

[61] Rees, M. J., & Meszaros, P. 2000, ApJ, 535, L33

[62] Rees, M. J., & Meszaros, P. 1998, ApJ, 496, L1

[63] Rees, M. J., & Meszaros, P. 1994, ApJ, 430, L93

[64] Rhoads, J. E. 1999, ApJ, 525, 737

[65] Rybicki, G. B. & Lightman, A. P. 1979, Radiative Processes in Astrophysics (New York; Wiley)

[66] Sari, R., Piran, T., & Narayan, R. 1998, ApJ, 497, L17

[67] Sari, R., Piran, T., & Halpern, J. P. 1999, ApJL, 519, L17

[68] Sari, R., & Meszaros, P. 2000, ApJ, 535, L33

[69] Sato, R. et al. 2003, ApJL, 599, L9

[70] Short, A.D., Keay, A., & Turner, M. J. 1998, proc. SPIE, 3445, 13

[71] Stanek, K. Z., et al. 2003, ApJ, 591, L17

[72] Toma, K., et al. 2006, ApJ, 640, L139

[73] Uemura, M. et al. 2003, Nature, 423, 843

[74] Villasenor, J. S., et al. 2005, Nature, 437, 855

[75] Wells, A., et al. 1992, proc. SPIE, 1546, 205

[76] Wells, A., et al. 1997, proc. SPIE, 3114, 392

[77] Yonetoku, D., et al. 2004, ApJ, 609, 935

[78] Zhang, B., et al. 2006, ApJ, 642, 354

[79] Zhang, B., & Meszaros, P. 2002, ApJ, 566, 712

Chapter 8

Acknowledgements

I am deeply grateful to Prof. N. Kawai for his support over the six years of my graduate course. I also would like to thank Dr. J. Kataoka, Dr. K. Ioka, Mr. K. Toma, and Prof. T. Nakamura.

I appreciate Dr. T. Sakamoto, G. Sato and K. Ohnuki for discussing about the temporal and spectral analysis of *Swift* BAT and XRT. I also would like to thank Prof. T. Takahashi for giving me the opportunity to visit GSFC.

I want to thank all the staff, the post doctorates, and the graduate students of Tokyo Institute of Technology.

Appendix A

Swift Gamma-ray Bursts Summary

GRB	T_{90} (s)	T_{50} (s)	β	BAT mean flux $(15-150$ keV) 10^{-8} erg cm^{-2} s^{-1}	Reduced χ^2 (d.o.f)	Redshift
050117	167.0	83.2	1.39±0.02	5.96±0.09	1.02 (56)	
050124	4.0	2.0	1.48±0.07	31.4±0.9	1.65 (21)	
050126	38.7	16.2	1.83±0.20	$2.81^{+0.23}_{-0.21}$	1.36 (20)	1.29
050128	23.6	8.1	1.39±0.04	31.6±0.7	1.51 (21)	
050202	0.1	0.1	$1.48^{+0.20}_{-4.48}$	27.6±3.5	1.57 (21)	
050215	88.8	56.2	1.27±0.20	$0.996^{+0.106}_{-0.107}$	1.41 (21)	
050219	23.5	9.9	1.15	20.6	4.44 (21)	
050219B	31.4	7.0	$1.79^{+8.21}_{-4.79}$	$61.5^{+1.8}_{-1.6}$	1.13 (42)	
050223	16.8	8.9	1.89±0.10	$3.15^{+0.20}_{-0.19}$	0.88 (21)	0.5915
050306	158.3	77.2	1.80±0.06	7.76±0.28	1.29 (21)	
050315	96.6	24.5	1.91±0.06	3.37±0.11	0.96 (21)	1.949
050319	151.3	123.9	2.12±0.12	$0.918^{+0.063}_{-0.062}$	0.44 (21)	3.24
050326	29.6	19.4	$1.22^{+0.02}_{-4.22}$	35.8±0.4	1.29 (53)	
050401	34.3	26.0	$1.51^{+8.49}_{-0.04}$	28.6±0.6	0.70 (21)	2.90
050406	6.1	2.5	2.64±0.28	$1.30^{+0.18}_{-0.17}$	1.44 (12)	
050410	24.5	12.7	1.75±0.04	9.38±0.25	1.67 (21)	
050412	28.0	12.1	0.77±0.10	2.33±0.12	0.45 (21)	
050416	2.4	0.8	3.07±0.12	14.9±0.8	1.43 (21)	0.6535
050416B	3.3	1.6	1.45±0.09	41.0±1.8	1.19 (19)	
050418	82.5	61.2	1.66±0.03	$6.59^{+0.12}_{-0.13}$	0.65 (56)	
050421	14.8	9.6	1.66±0.27	$0.940^{+0.155}_{-0.153}$	0.95 (12)	
050422	57.2	40.0	1.51±0.12	1.01±0.07	0.81 (21)	
050502B	17.3	10.0	1.63±0.09	2.54±0.14	1.19 (21)	
050505	63.0	27.3	1.54±0.07	4.48±0.18	1.18 (21)	4.27

050507	27.3	12.4	1.65±0.11	$1.77^{+0.14}_{-0.13}$	1.87 (21)	
050509	13.5	4.2	2.10±0.10	$2.35^{+0.15}_{-0.14}$	0.78 (21)	
050509B	0.04	-	1.39±0.24	25.2±4.1	1.23 (9)	0.226
050525	8.9	5.2	1.89	186	8.19 (35)	0.606
050528	10.8	6.5	2.47±0.17	$4.41^{+0.41}_{-0.40}$	1.54 (13)	
050603	20.0	3.8	$1.20^{+8.80}_{-0.03}$	34.5±0.7	1.41 (56)	2.821
050607	26.0	13.5	1.89±0.09	$2.97^{+0.17}_{-0.16}$	1.18 (21)	
050701	24.2	8.5	1.69±0.04	5.44±0.14	1.25 (56)	
050712	50.0	26.1	1.50±0.11	2.13±0.14	1.23 (21)	
050713	127.4	11.2	1.45±0.05	5.11±0.15	0.90 (21)	
050713B	110.8	39.4	1.39±0.09	7.11±0.36	0.90 (21)	
050714B	48.1	20.4	2.71±0.23	1.31±0.14	1.35 (12)	
050715	49.8	31.6	1.64±0.06	2.54±0.10	1.38 (22)	
050716	85.0	37.0	1.37±0.04	11.4±0.3	1.13 (56)	
050717	67.8	24.7	$1.12^{+8.88}_{-4.12}$	34.3±0.6	0.76 (56)	
050721	43.3	18.0	1.80±0.07	7.48±0.30	0.70 (21)	
050724	177.6	85.9	1.81±0.15	4.53±0.38	0.78 (12)	0.258
050726	113.3	16.1	0.99±0.10	5.41±0.28	1.33 (56)	
050801	19.1	6.2	2.03±0.12	$2.59^{+0.20}_{-0.19}$	1.62 (12)	
050802	31.1	9.2	1.66±0.09	$7.42^{+0.38}_{-0.37}$	1.41 (21)	1.71 ?
050803	96.5	39.4	1.50±0.08	4.43±0.20	1.42 (21)	0.422
050813	0.4	0.3	1.40±0.22	11.2±1.5	0.88 (12)	
050814	113.1	50.9	1.86±0.11	2.24±0.15	0.86 (21)	5.3
050815	3.3	1.9	2.05±0.18	$3.10^{+0.32}_{-0.33}$	1.00 (17)	
050819	36.9	17.9	2.62±0.18	$0.902^{+0.085}_{-0.082}$	1.62 (21)	
050820	240.4	219.	1.73±0.06	4.48±0.16	0.99 (19)	2.612
050820B	12.9	3.9	1.29	16.6	2.32 (56)	
050822	106.9	45.5	2.39±0.16	$3.79^{+0.31}_{-0.30}$	0.79 (12)	
050824	26.5	12.3	2.94±0.27	1.08±0.12	0.84 (21)	0.83
050826	39.3	17.9	1.19±0.16	1.16±0.11	0.52 (12)	
050827	49.1	10.8	1.36±0.05	4.21±0.13	0.86 (21)	
050904	228.8	92.9	1.44±0.10	$2.34^{+0.14}_{-0.13}$	0.82 (21)	6.29
050908	21.3	6.9	1.89±0.10	2.36±0.15	0.92 (21)	3.344
050911	181.4	98.8	1.91±0.21	1.81±0.22	0.58 (11)	
050915	49.6	14.3	1.46±0.09	2.68±0.15	1.38 (12)	
050915B	40.9	21.0	1.84±0.03	8.15±0.14	1.27 (56)	
050916	49.7	27.0	1.67±0.13	1.99±0.16	0.98 (21)	
050922B	156.0	28.0	2.13±0.15	1.42±0.12	0.55 (21)	
050922C	4.6	1.4	$1.32^{+0.03}_{-4.32}$	36.1±0.6	1.16 (56)	2.198
050925	0.2	0.1	$1.40^{+8.60}_{-4.40}$	107±7	0.76 (21)	
051001	188.6	95.7	2.15±0.25	0.556±0.077	1.36 (13)	
051006	35.5	10.5	1.54±0.10	3.67±0.22	0.86 (13)	
051008	12.2	4.7	$1.11^{+8.89}_{-0.03}$	33.4±0.5	1.21 (56)	
051016	20.9	9.8	1.95±0.15	4.41±0.38	0.75 (21)	

051016B	31.1	22.3	2.54±0.23	$0.991^{+0.115}_{-0.112}$	1.13 (16)	0.9364
051021B	46.2	18.7	1.38±0.08	3.73±0.18	1.01 (21)	
051105	0.1	0.1	1.69±0.32	$15.4^{+2.6}_{-2.7}$	0.94 (9)	
051109	36.5	23.3	1.65±0.12	$6.08^{+0.44}_{-0.43}$	0.98 (21)	2.346
051109B	11.2	5.1	1.96±0.15	$1.90^{+0.19}_{-0.18}$	1.76 (21)	0.08 ?
051111	47.6	15.7	1.36±0.03	8.07±0.14	1.10 (56)	1.55
051113	95.4	38.3	1.78±0.08	2.80±0.14	1.08 (21)	
051117A	136.1	58.8	1.87±0.04	4.38±0.12	0.81 (34)	
051117B	10.6	5.2	1.87±0.23	1.70±0.23	0.56 (13)	
051210	1.3	0.6	1.07±0.19	$6.13^{+0.66}_{-0.65}$	0.36 (6)	
051213	72.3	54.9	1.81±0.13	$1.01^{+0.09}_{-0.08}$	1.25 (11)	
051221	1.4	0.6	$1.43^{+8.57}_{-4.43}$	$81.8^{+1.4}_{-1.3}$	1.18 (56)	0.5465
051221B	40.5	22.2	1.45±0.11	2.38±0.16	1.33 (21)	
051227	114.7	69.8	1.63±0.20	1.21±0.15	1.24 (9)	(¿) 0.71
060102	20.2	14.8	1.23±0.23	$1.16^{+0.15}_{-0.14}$	1.04 (9)	
060105	54.6	26.0	$1.06^{+8.94}_{-4.06}$	27.4±0.3	0.99 (56)	
060108	13.9	5.1	1.93±0.10	$2.67^{+0.16}_{-0.15}$	1.09 (21)	¡ 2.7
060109	116.3	84.4	2.16±0.38	$0.426^{+0.087}_{-0.083}$	0.78 (8)	
060110	19.7	7.4	1.64±0.03	7.90±0.17	0.86 (56)	
060111	12.9	5.9	1.52	11.2	3.26 (21)	
060111B	59.3	21.8	0.95±0.09	6.51±0.34	1.82 (21)	
060115	144.4	93.2	1.92±0.12	0.964±0.069	0.89 (21)	3.53
060116	74.4	28.9	1.42±0.11	$2.87_{\pm}0.18$	0.92 (21)	
060117	16.9	9.9	2.00	137	2.33 (42)	
060124	13.6	7.4	1.87±0.11	3.64±0.24	0.85 (21)	2.296
060202	206.9	129.8	1.42±0.15	1.11±0.09	0.35 (9)	
060203	58.7	29.6	1.67±0.14	1.54±0.13	1.27 (9)	
060204B	133.8	23.4	1.34	5.93	2.03 (21)	
060206	7.0	2.3	1.71±0.03	11.9±0.3	1.87 (21)	4.048
060210	253.0	42.5	1.67±0.05	6.45±0.20	0.73 (21)	3.91
060211	124.6	79.8	1.62±0.09	1.14±0.07	0.76 (21)	
060211B	19.5	5.5	1.57±0.13	$1.90^{+0.16}_{-0.15}$	0.85 (13)	
060219	62.9	45.8	2.50±0.21	$0.745^{+0.083}_{-0.081}$	1.00 (13)	
060223	10.9	5.1	1.80±0.07	5.96±0.26	1.07 (16)	4.41
060223B	10.2	5.6	1.48±0.03	15.3±0.3	0.74 (21)	
060306	61.1	42.7	1.80±0.06	7.76±0.28	0.92 (21)	
060312	63.7	16.9	1.79	4.16	2.03 (21)	
060313	0.8	0.5	$0.69^{+9.31}_{-3.69}$	148±3	1.57 (21)	
060319	9.0	5.2	2.47±0.14	$2.42^{+0.19}_{-0.18}$	1.02 (21)	
060322	218.5	168.3	1.57±0.04	2.20±0.05	1.81 (21)	
060323	17.9	9.7	1.52±0.10	2.93±0.18	0.81 (21)	
060403	30.7	14.7	0.93±0.07	5.87±0.18	0.83 (19)	
060413	153.6	39.2	1.79±0.12	$1.71^{+0.13}_{-0.12}$	1.00 (21)	
060418	106.2	25.5	1.50±0.04	$7.84^{+0.18}_{-0.17}$	0.87 (56)	1.489

060421	10.9	5.0	1.46±0.04	10.2±0.2	1.03 (21)	
060424	44.0	14.1	1.69±0.12	1.54±0.12	1.45 (21)	
060427	66.4	31.2	1.83±0.18	$0.740^{+0.081}_{-0.078}$	0.72 (21)	
060428	38.9	21.7	2.01±0.05	$6.79^{+0.21}_{-0.22}$	1.03 (21)	
060428B	58.3	25.0	2.63±0.12	1.27±0.08	1.29 (21)	
060501	12.4	5.7	1.24±0.07	9.36±0.37	1.07 (21)	
060502	34.7	10.6	1.32±0.04	11.6±0.3	1.19 (56)	1.51
060502B	0.06	0.05	$1.05^{+0.13}_{-4.05}$	38.2±3.3	1.12 (21)	0.287 ?
060507	184.7	115.8	1.84±0.06	2.19±0.07	1.17 (21)	
060510	19.6	5.6	1.77±0.07	47.7±2.0	1.18 (21)	
060510B	278.0	139.9	1.72±0.13	1.08±0.09	1.45 (21)	4.9
060512	8.6	3.9	2.57±0.20	$2.60^{+0.27}_{-0.26}$	0.90 (12)	0.4428
060515	51.5	26.1	1.16±0.10	$2.52^{+0.15}_{-0.14}$	0.94 (21)	
060522	70.2	42.4	1.53±0.10	1.52±0.09	1.46 (21)	5.11
060526	295.1	248.8	1.76±0.11	3.99±0.26	0.85 (21)	3.21
060602	75.5	33.1	1.28±0.10	2.03±0.12	0.69 (21)	
060602B	9.4	4.7	5.16±0.31	1.88±0.10	1.46 (21)	
060604	1.9	1.2	1.87±0.24	$3.23^{+0.50}_{-0.49}$	0.70 (21)	2.68
060605	82.6	52.9	1.48±0.13	0.818±0.067	1.79 (21)	3.711
060607	100.6	25.3	1.32±0.04	6.75±0.15	1.10 (21)	3.082
060607B	30.5	13.0	1.60±0.07	5.02±0.21	0.82 (21)	
060614	109.1	43.0	1.77±0.04	23.3±0.6	0.60 (56)	0.125
060707	77.6	35.7	1.72±0.08	2.22±0.11	1.56 (21)	3.43
060708	7.4	2.8	1.57±0.06	6.36±0.23	1.91 (21)	
060712	27.0	13.5	1.80±0.20	4.30±0.47	0.59 (21)	
060714	115.6	85.8	1.62±0.10	2.88±0.18	0.83 (21)	2.71
060717	2.2	0.9	1.52±0.21	2.95±0.40	1.09 (21)	
060719	67.1	44.7	2.34±0.11	$3.49^{+0.22}_{-0.21}$	0.48 (21)	
060729	116.8	22.4	1.75±0.52	$0.609^{+0.202}_{-0.193}$	0.60 (12)	0.54
060801	0.5	0.3	0.46±0.16	14.8±1.2	0.69 (12)	
060804	18.7	10.5	1.92±0.17	3.04±0.31	1.38 (21)	
060805	5.1	2.4	2.41±0.30	$1.24^{+0.22}_{-0.21}$	1.01 (12)	
060807	58.5	17.8	1.52±0.13	1.35±0.11	1.02 (21)	
060813	16.0	4.3	1.16±0.02	62.1	1.34 (56)	
060814	145.3	61.5	1.31±0.02	22.7±0.3	0.82 (56)	
060825	7.9	3.8	1.63±0.03	11.9±0.3	1.71 (21)	
060904	79.9	25.7	1.60±0.06	4.63±0.16	0.79 (21)	
060904B	190.7	150.6	1.37±0.05	9.95±0.32	1.09 (21)	0.703
060906	49.0	18.3	2.26±0.42	$1.14^{+0.27}_{-0.26}$	1.22 (12)	3.685
060908	18.7	7.3	1.25±0.03	13.4±0.3	1.09 (27)	2.43
060912	5.0	1.8	1.80±0.04	24.7±0.7	1.21 (21)	0.937 ?
060919	24.7	7.2	1.99±0.15	$3.25^{+0.28}_{-0.27}$	0.87 (21)	
060923	57.8	39.6	1.95±0.16	1.51±0.15	1.12 (21)	
060923B	8.7	4.3	2.61±0.16	4.88±0.40	1.47 (12)	

060923C	81.4	45.1	2.29±0.16	$1.82^{+0.17}_{-0.16}$	1.07 (18)	
060926	7.9	3.4	2.53±0.13	$2.58^{+0.19}_{-0.18}$	1.11 (21)	3.20
060927	22.4	15.7	1.55±0.04	8.63±0.24	1.55 (21)	5.6
060929	552.1	520.6	1.45±0.21	0.865±0.110	0.71 (21)	

Table A.1: Characteristics of the 160 $Swift$ GRBs. Fitting model is a single power-law.

GRB	Photon Index	E_0 (keV)	$E_{\rm p}$ (keV)	BAT mean flux ($15-150$ keV) 10^{-8} erg/cm^2/s	Reduced χ^2 (d.o.f	$L_{\rm iso,52}$	$E_{\rm iso,52}$	z
050117	$1.06^{+0.13}_{-0.16}$	$155.5^{+44.5}_{-49.8}$	$146.2^{+48.7}_{-53.0}$	5.84±0.09	0.77 (55)			
050124	$0.60^{+0.33}_{-0.35}$	$64.1^{+38.1}_{-18.7}$	$89.7^{+57.9}_{-34.5}$	31.1±0.9	0.61 (20)			
050128	$0.69^{+0.16}_{-0.17}$	$83.1^{+23.8}_{-15.7}$	$108.9^{+34.2}_{-25.0}$	$31.0^{+0.69}_{-0.70}$	0.86 (20)			
050219	$-0.17^{+0.18}_{-0.19}$	$46.0^{+7.4}_{-5.8}$	$99.8^{+18.3}_{-15.3}$	20.2±0.5	1.23 (20)			
050219B	1.17±0.09	$141.3^{+40.2}_{-26.1}$	$117.3^{+35.7}_{-25.1}$	55.6±0.7	1.08 (20)			
050326	0.79±0.07	$145.4^{+32.3}_{-22.6}$	$175.9^{+40.4}_{-29.2}$	35.1±0.4	1.07 (55)			
050410	$1.08^{+0.20}_{-0.21}$	$75.7^{+31.1}_{-17.9}$	$69.6^{+32.7}_{-22.9}$	9.09±0.27	1.08 (20)			
050416	$1.79^{+0.65}_{-0.77}$	$25.0^{+23.2}_{-9.9}$	$5.2^{+19.9}_{-19.4}$	$13.9^{+0.9}_{-0.8}$	1.25 (20)	0.121±0.057	0.175±0.083	0.6535
050507	$-0.62^{+0.71}_{-0.73}$	$21.6^{+9.9}_{-5.1}$	$56.6^{+30.4}_{-20.7}$	1.59±0.14	1.13 (11)			
050525	$0.76^{+0.07}_{-0.08}$	$60.9^{+4.4}_{-4.1}$	$75.5^{+7.3}_{-7.0}$	170.4±1.1	1.04 (34)	0.352±0.010	1.95±0.05	0.606
050716	$0.64^{+0.18}_{-0.19}$	$79.5^{+26.3}_{-16.5}$	$108.1^{+38.8}_{-27.1}$	11.1±0.3	0.81 (55)			
050820B	$0.53^{+0.15}_{-0.16}$	$72.8^{+18.4}_{-12.7}$	$107.0^{+29.4}_{-22.0}$	16.1±0.2	0.92 (55)			
050915B	1.36±0.11	$96.8^{+28.9}_{-18.7}$	$62.0^{+21.3}_{-16.0}$	7.88±0.15	0.90 (55)			
050922C	$0.94^{+0.10}_{-0.11}$	$149.3^{+50.7}_{-34.0}$	$157.9^{+56.5}_{-39.6}$	$37.0^{+1.0}_{-0.9}$	0.93 (55)	2.53±0.29	3.64±0.42	2.198
060111	$0.50^{+0.16}_{-0.17}$	$47.9^{+9.3}_{-7.0}$	$72.0^{+16.2}_{-13.4}$	10.5±0.3	0.98 (20)			
060117	1.53±0.07	$131.0^{+21.9}_{-16.7}$	$61.9^{+13.4}_{-12.2}$	133.1±1.0	1.10 (41)			
060204B	$0.71^{+0.15}_{-0.16}$	$84.2^{+26.1}_{-16.8}$	$108.3^{+36.2}_{-25.5}$	5.73±0.14	1.11 (20)			
060206	1.25±0.14	$106.4^{+45.3}_{-25.4}$	$79.3^{+36.9}_{-24.1}$	11.5±0.3	1.34 (20)	4.32±0.41	3.12±0.30	4.048
060211	$0.75^{+0.41}_{-0.46}$	$54.0^{+47.9}_{-18.9}$	$67.7^{+65.0}_{-34.3}$	1.06±0.08	0.54 (20)			
060312	$1.05^{+0.19}_{-0.20}$	$59.9^{+20.5}_{-13.0}$	$56.9^{+22.8}_{-17.2}$	3.89±0.12	1.19 (20)			
060322	$1.17^{+0.16}_{-0.18}$	$126.0^{+74.0}_{-37.8}$	$105.1^{+65.3}_{-38.1}$	2.14±0.06	1.57 (20)			
060428B	$0.49^{+0.83}_{-1.10}$	$15.1^{+10.3}_{-5.4}$	$22.8^{+22.8}_{-18.5}$	1.08±0.08	0.92 (20)			
060707	$0.52^{+0.38}_{-0.41}$	$41.2^{+19.4}_{-10.8}$	$61.0^{+33.3}_{-23.2}$	2.09±0.12	1.02 (20)	0.288±0.038	5.04±0.66	3.43
060813	$0.82^{+0.06}_{-0.07}$	$168.4^{+31.6}_{-28.3}$	$199.0^{+39.1}_{-35.5}$	61.4±0.7	0.86 (55)			
060825	$1.21^{+0.14}_{-0.15}$	$113.6^{+57.9}_{-29.9}$	$89.6^{+48.8}_{-29.1}$	11.5±0.3	1.32 (20)			
060927	$0.83^{+0.19}_{-0.20}$	$66.6^{+23.5}_{14.5}$	$78.1^{+30.6}_{-21.5}$	8.16±0.27	0.76 (20)	4.00±0.38	13.6±1.3	5.6

Table A.2: Characteristics of the 31 *Swift* GRBs. Fitting model is a cutoff power-law.

Appendix B

BAT Light Curves of Prompt Emissions

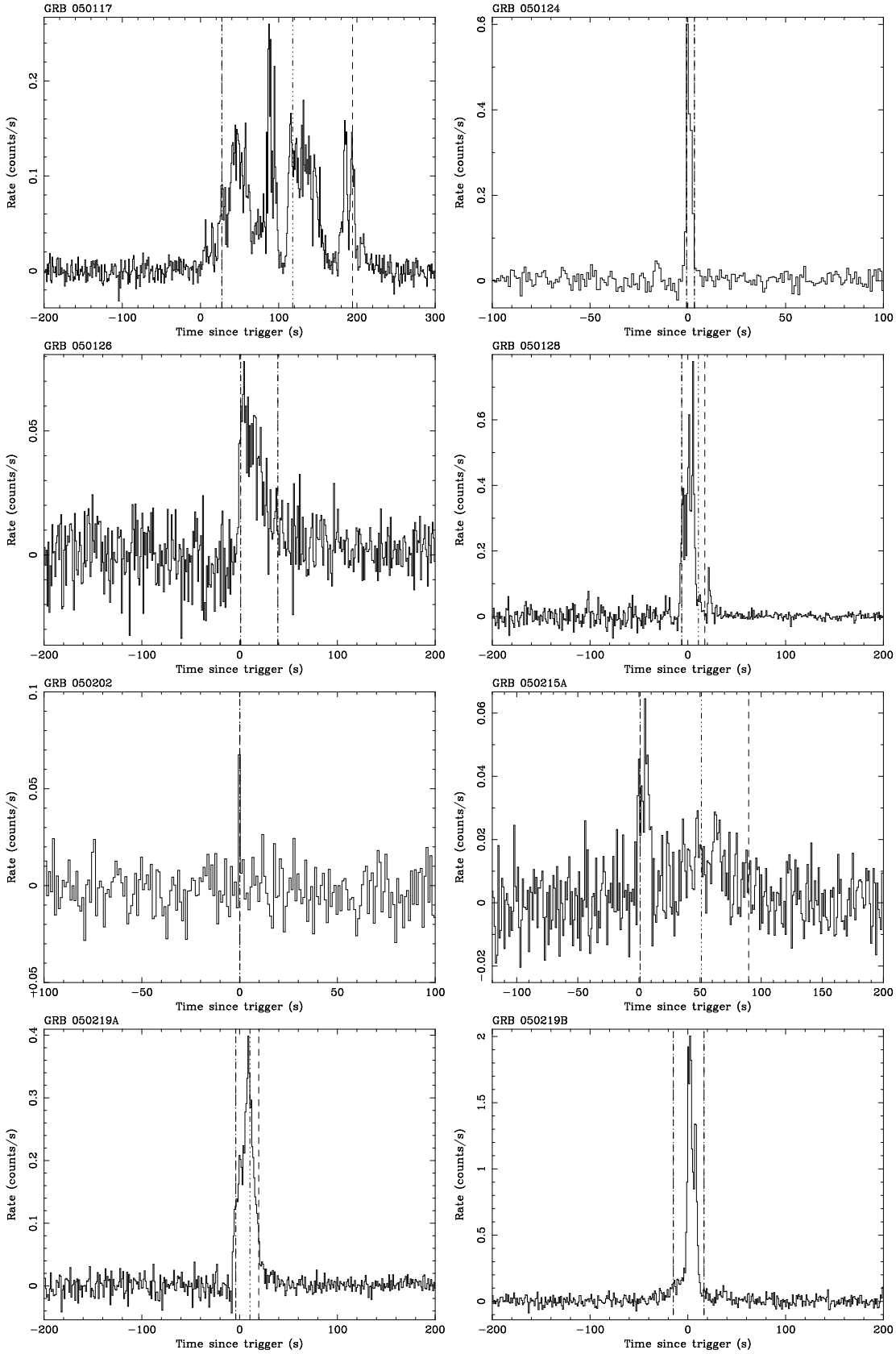

Figure B.1: Temporal parameters of Swift GRBs. The blue dashed lines represent the GRB duration (T_{90}). The green dashed lines represent the end time (or start time) source region of the spectrum.

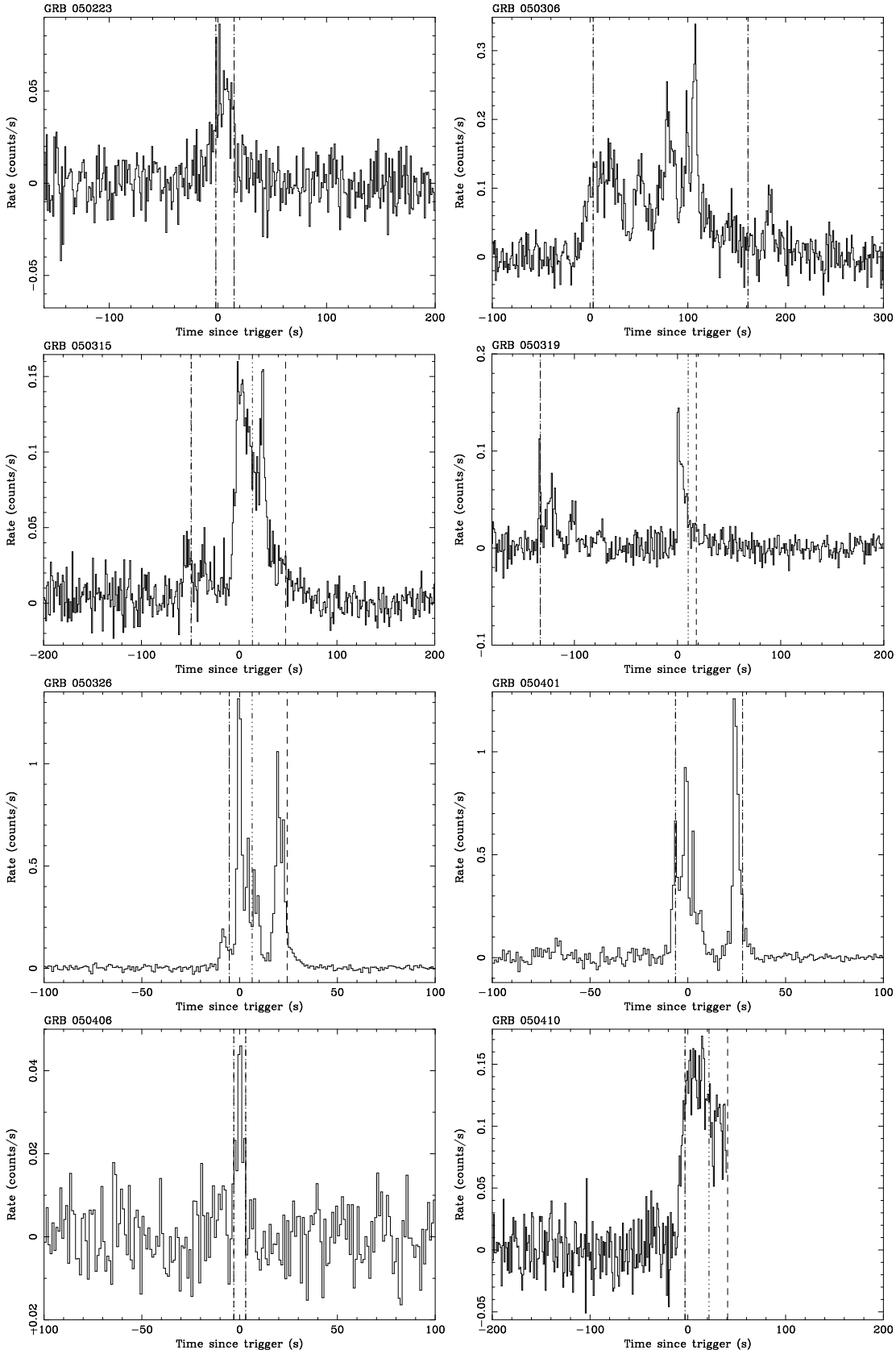

Figure B.2: Temporal parameters of Swift GRBs. The blue dashed lines represent the GRB duration (T_{90}). The green dashed lines represent the end time (or start time) source region of the spectrum.

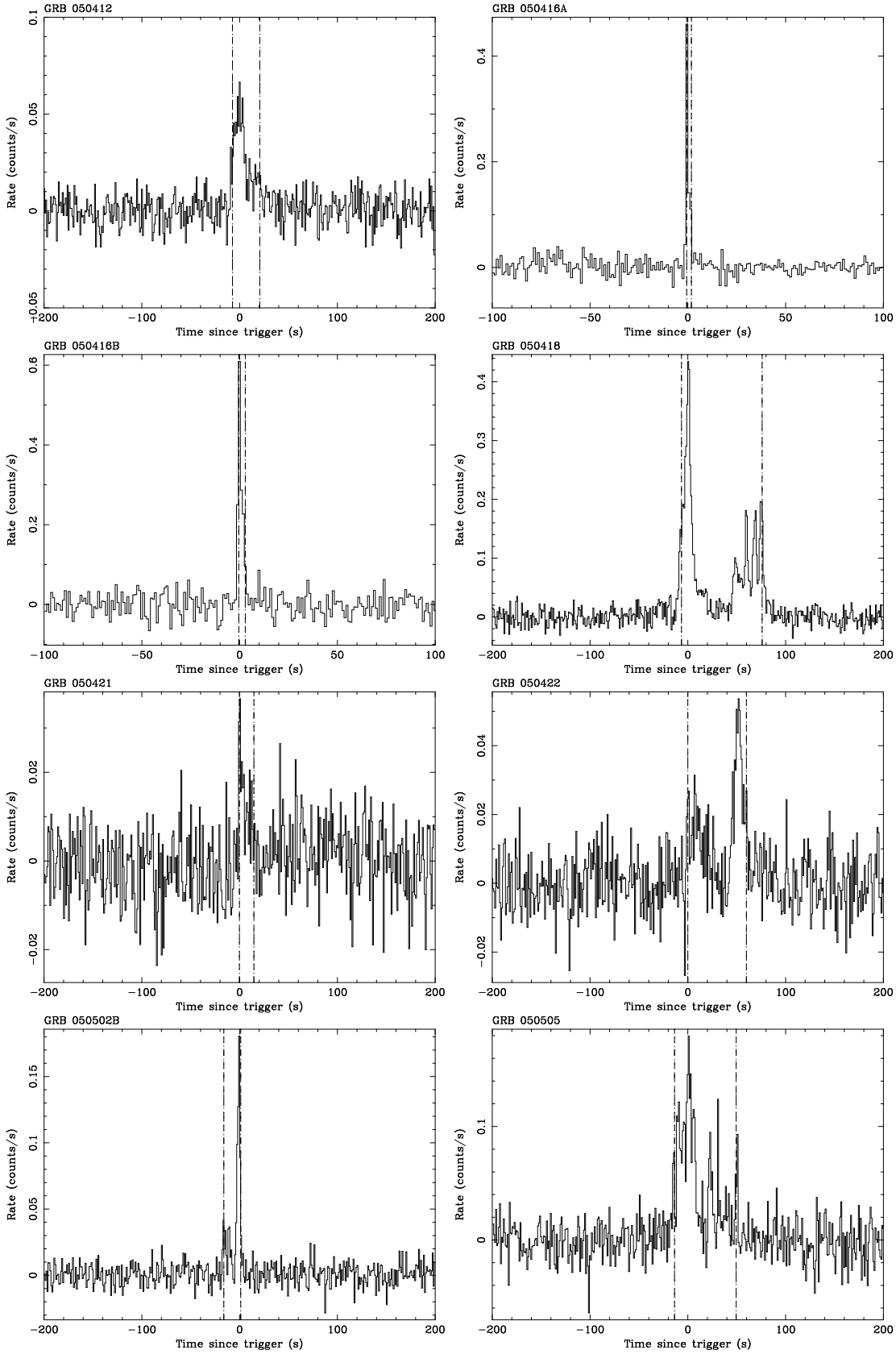

Figure B.3: Temporal parameters of Swift GRBs. The blue dashed lines represent the GRB duration (T_{90}). The green dashed lines represent the end time (or start time) source region of the spectrum.

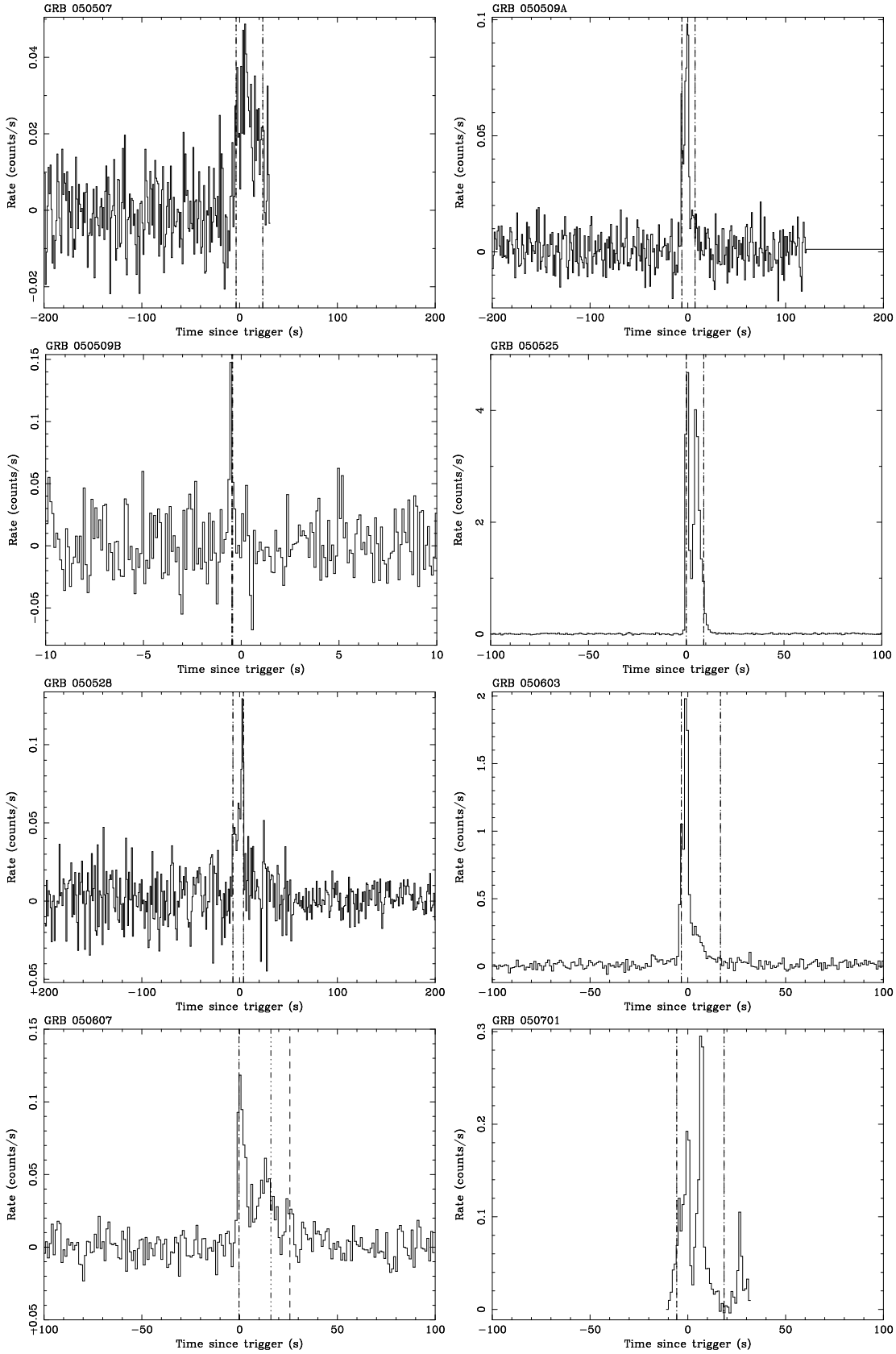

Figure B.4: Temporal parameters of Swift GRBs. The blue dashed lines represent the GRB duration (T_{90}). The green dashed lines represent the end time (or start time) source region of the spectrum.

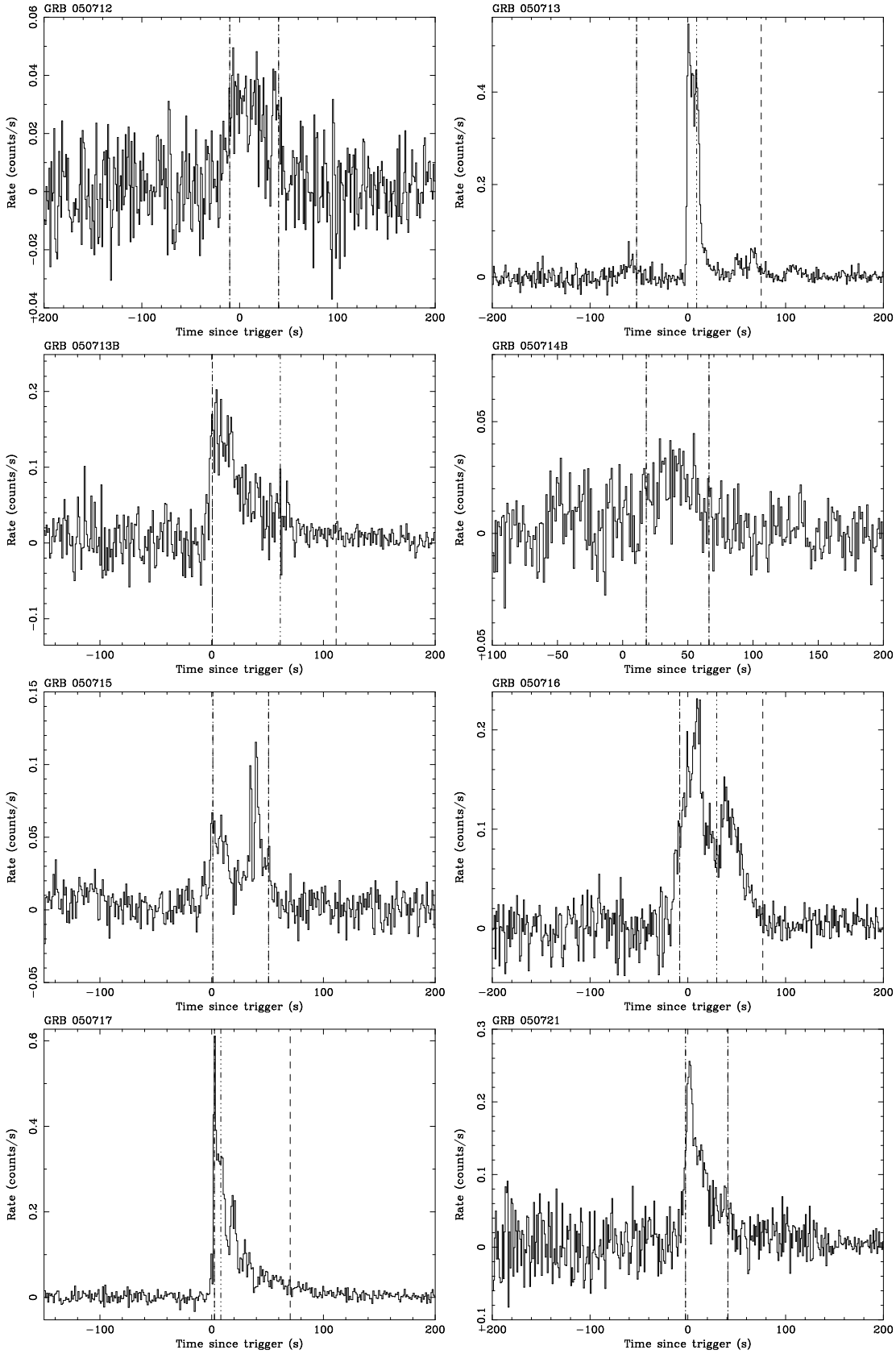

Figure B.5: Temporal parameters of Swift GRBs. The blue dashed lines represent the GRB duration (T_{90}). The green dashed lines represent the end time (or start time) source region of the spectrum.

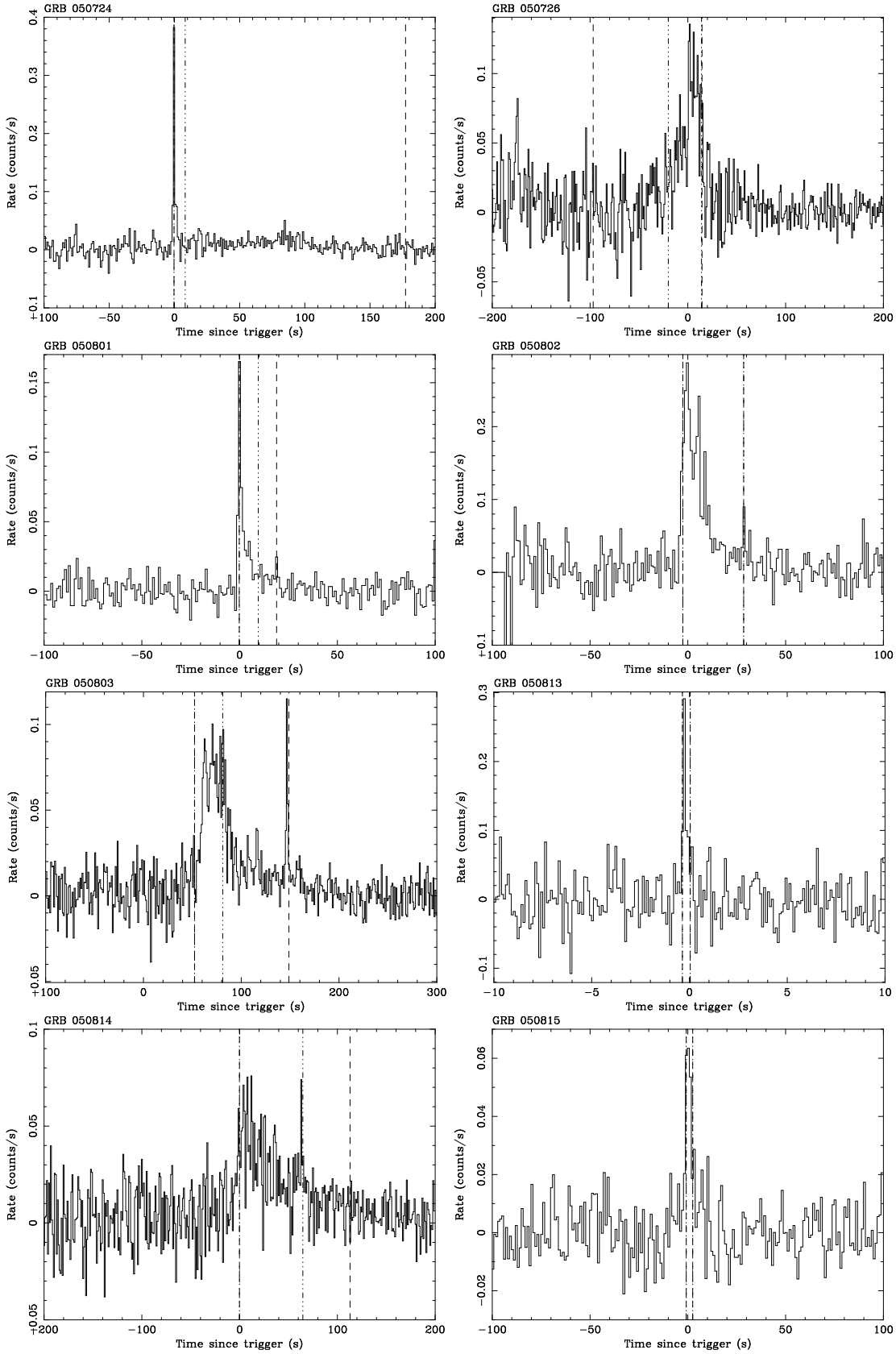

Figure B.6: Temporal parameters of Swift GRBs. The blue dashed lines represent the GRB duration (T_{90}). The green dashed lines represent the end time (or start time) source region of the spectrum.

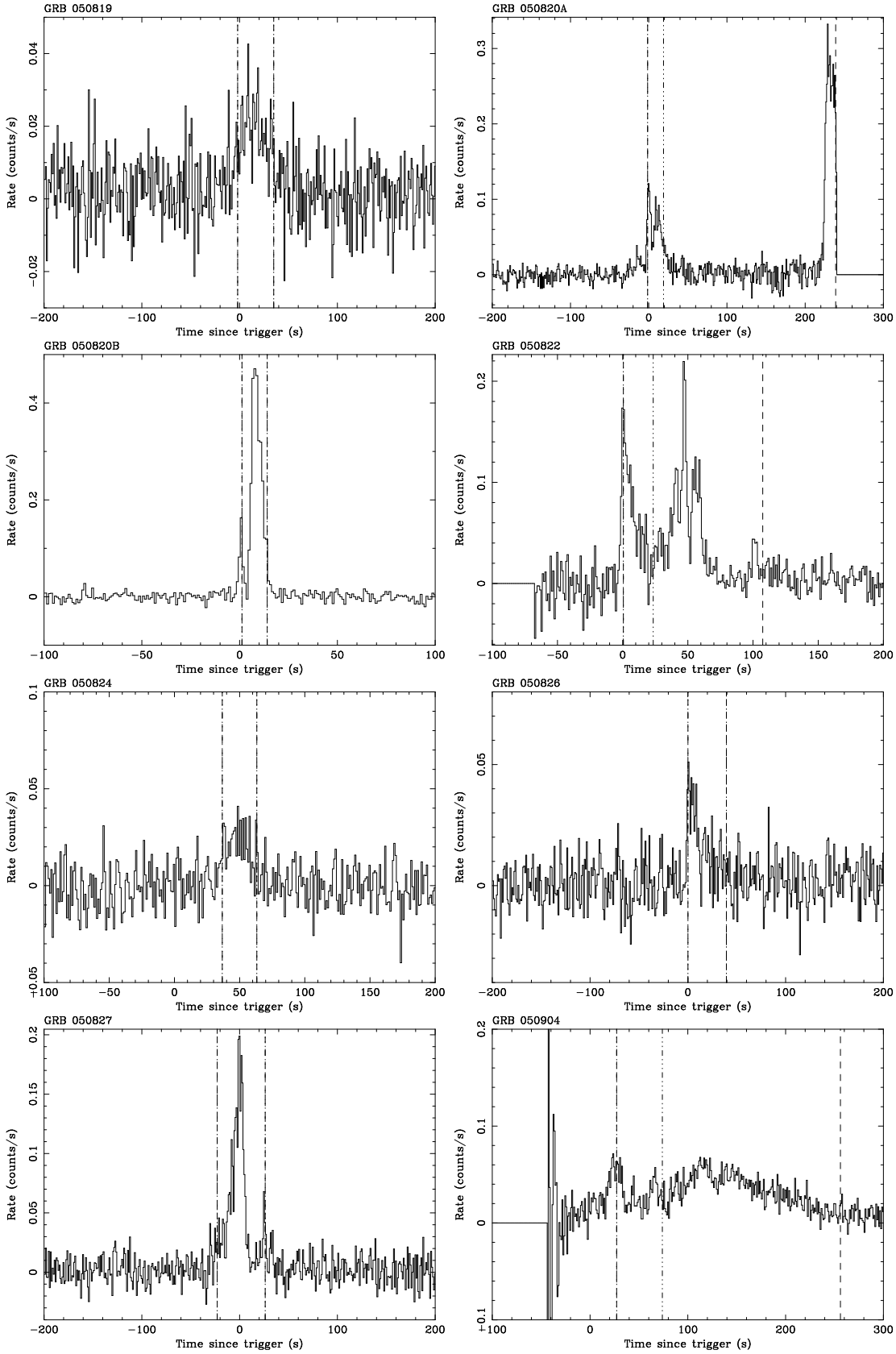

Figure B.7: Temporal parameters of Swift GRBs. The blue dashed lines represent the GRB duration (T_{90}). The green dashed lines represent the end time (or start time) source region of the spectrum.

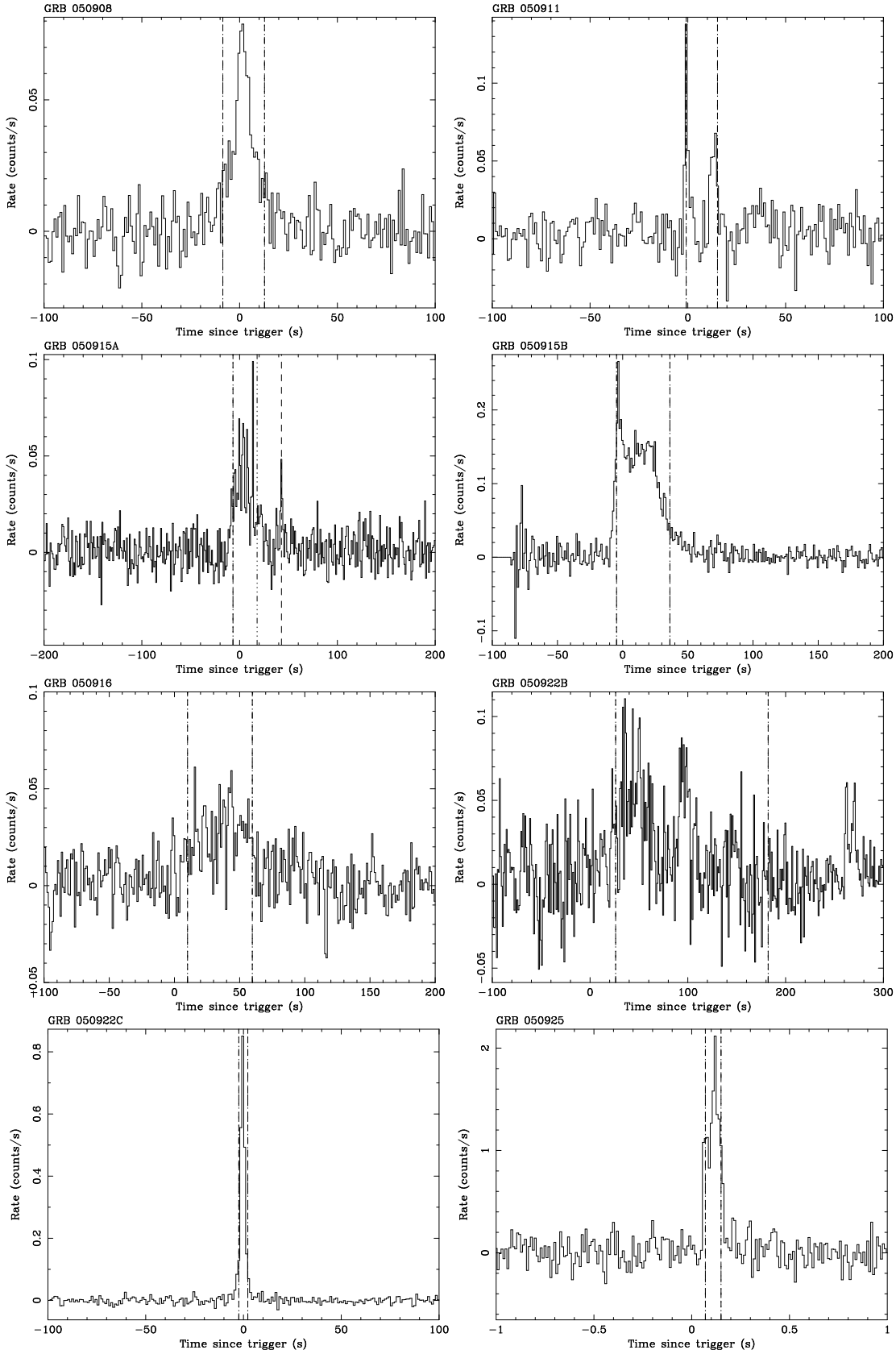

Figure B.8: Temporal parameters of Swift GRBs. The blue dashed lines represent the GRB duration (T_{90}). The green dashed lines represent the end time (or start time) source region of the spectrum.

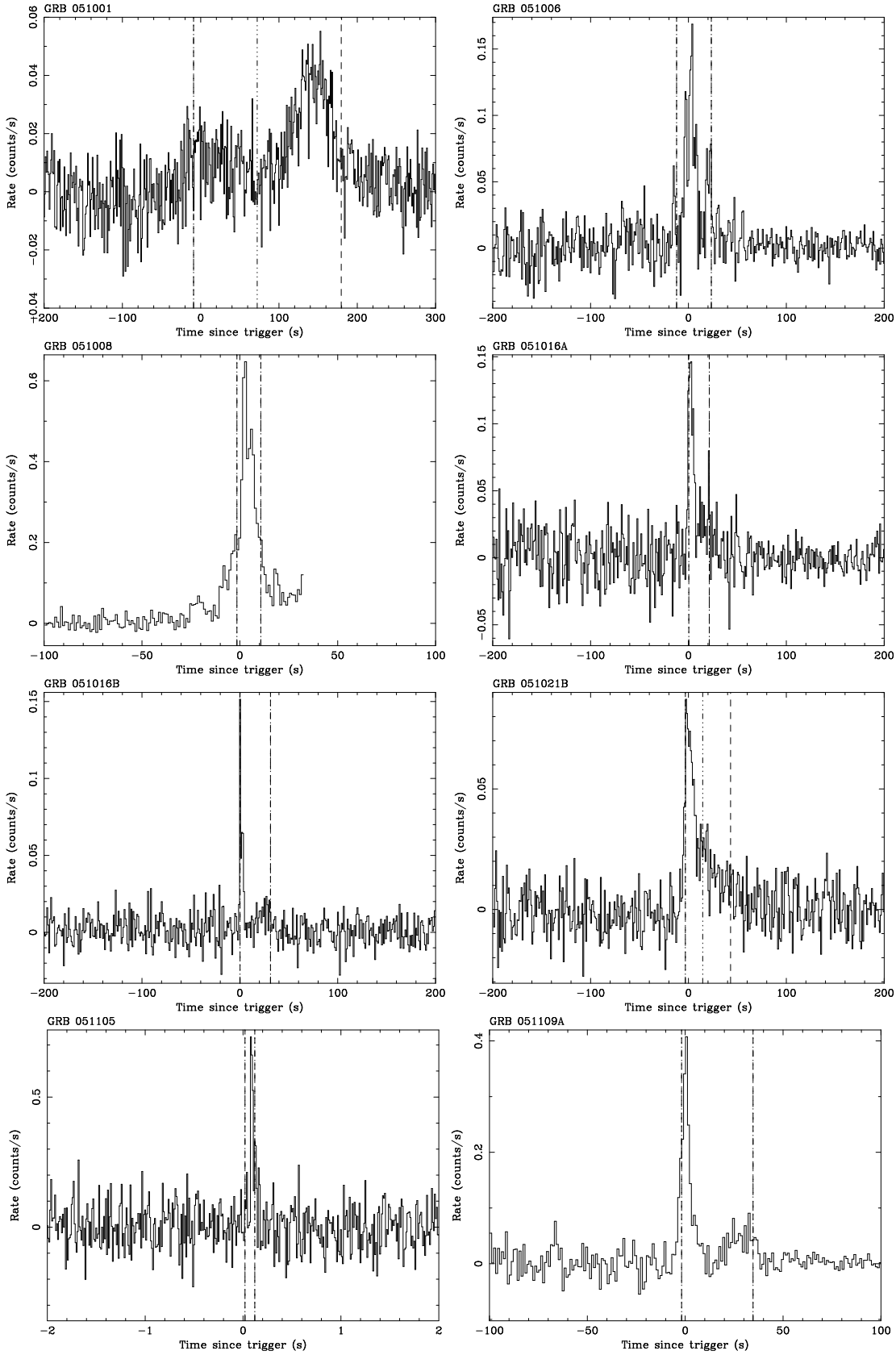

Figure B.9: Temporal parameters of Swift GRBs. The blue dashed lines represent the GRB duration (T_{90}). The green dashed lines represent the end time (or start time) source region of the spectrum.

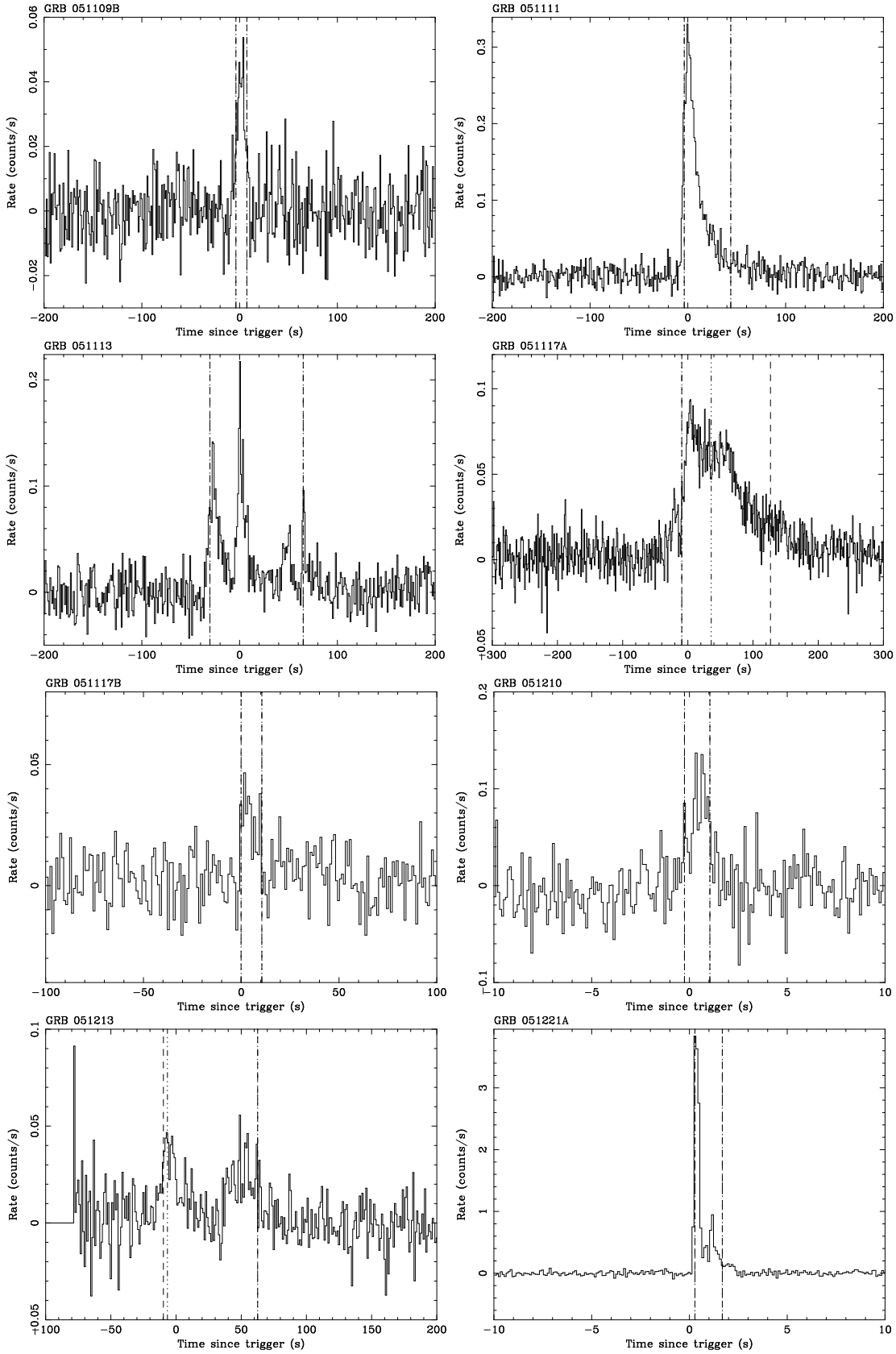

Figure B.10: Temporal parameters of Swift GRBs. The blue dashed lines represent the GRB duration (T_{90}). The green dashed lines represent the end time (or start time) source region of the spectrum.

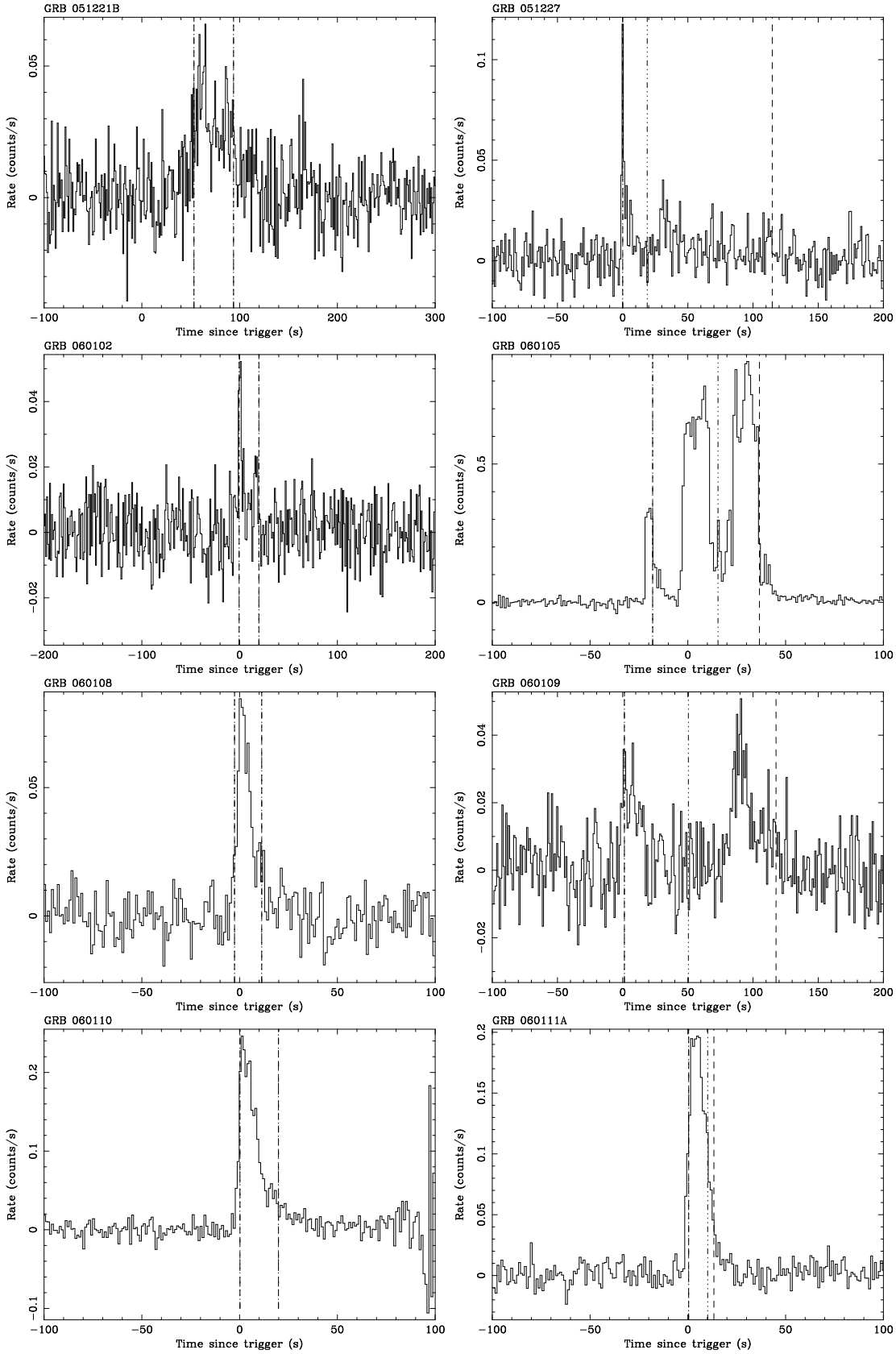

Figure B.11: Temporal parameters of Swift GRBs. The blue dashed lines represent the GRB duration (T_{90}). The green dashed lines represent the end time (or start time) source region of the spectrum.

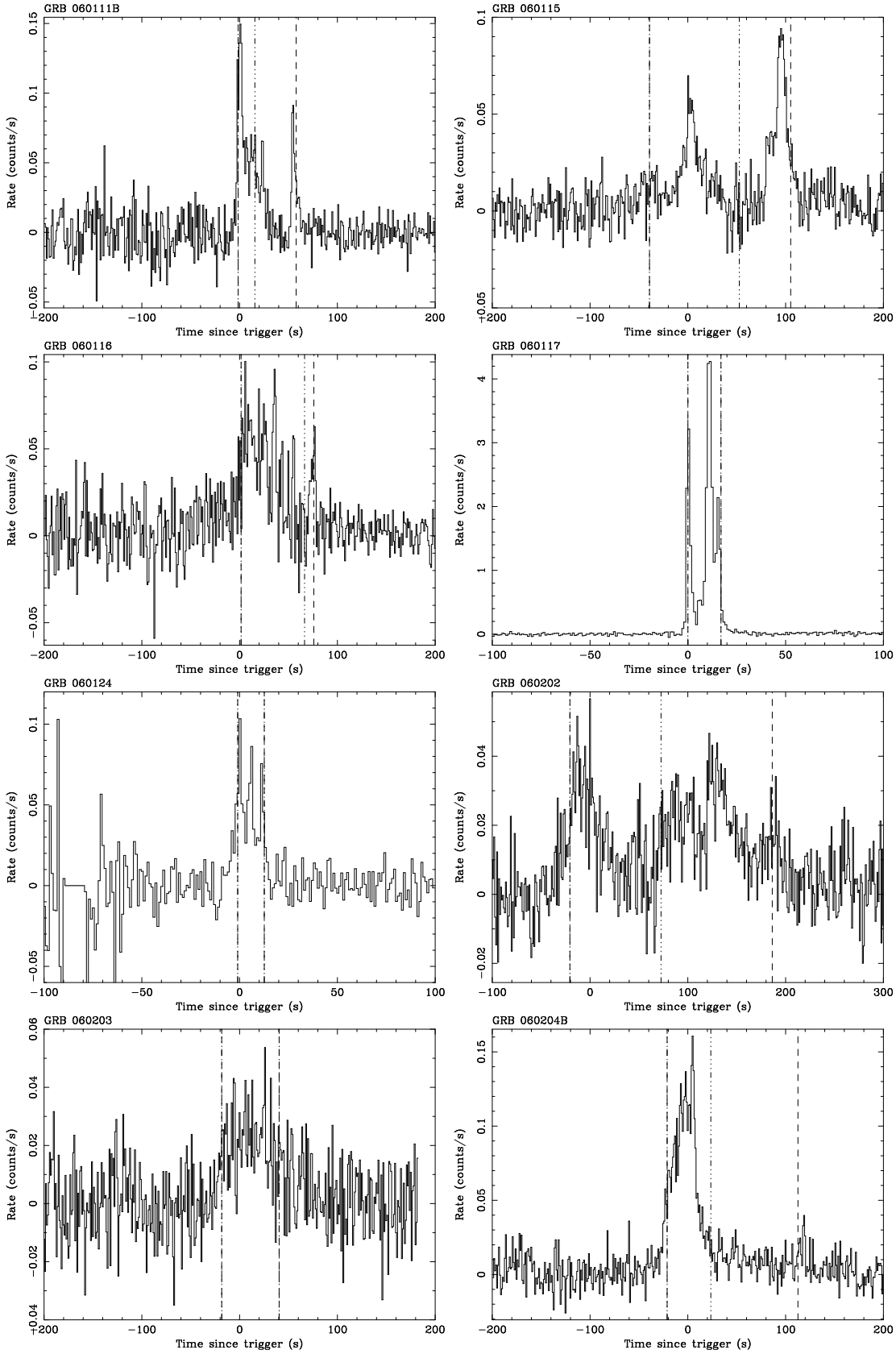

Figure B.12: Temporal parameters of Swift GRBs. The blue dashed lines represent the GRB duration (T_{90}). The green dashed lines represent the end time (or start time) source region of the spectrum.

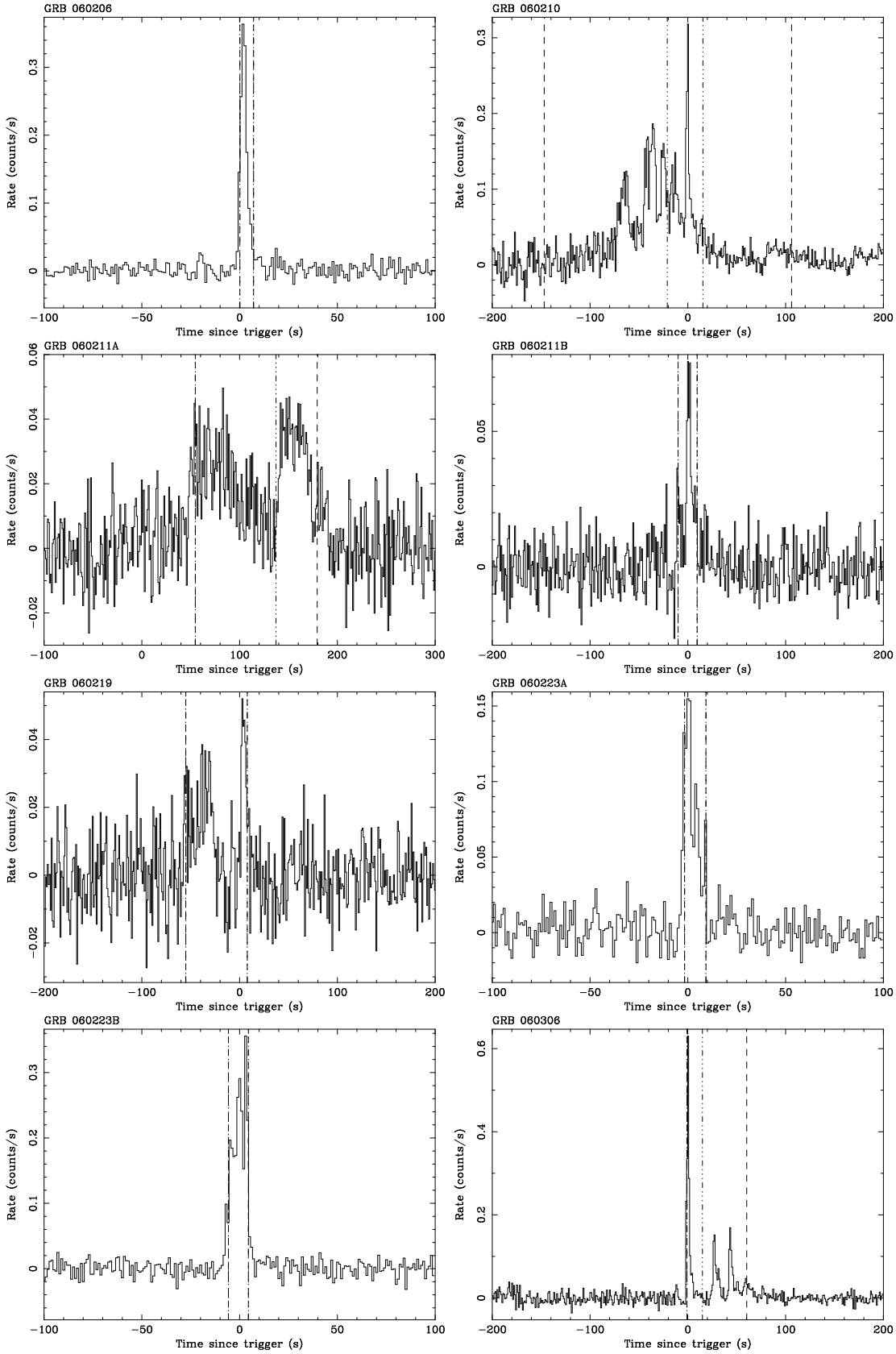

Figure B.13: Temporal parameters of Swift GRBs. The blue dashed lines represent the GRB duration (T_{90}). The green dashed lines represent the end time (or start time) source region of the spectrum.

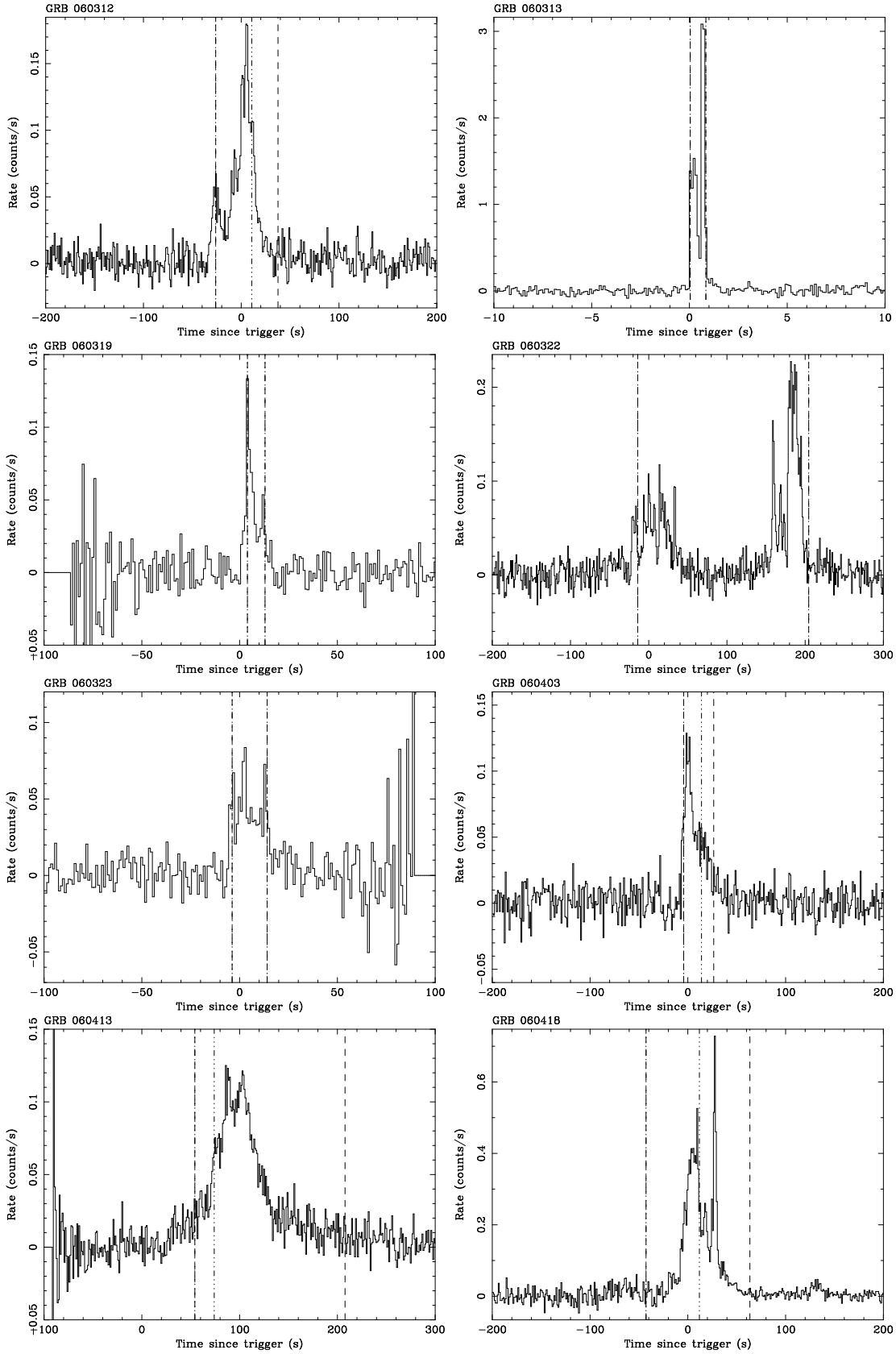

Figure B.14: Temporal parameters of Swift GRBs. The blue dashed lines represent the GRB duration (T_{90}). The green dashed lines represent the end time (or start time) source region of the spectrum.

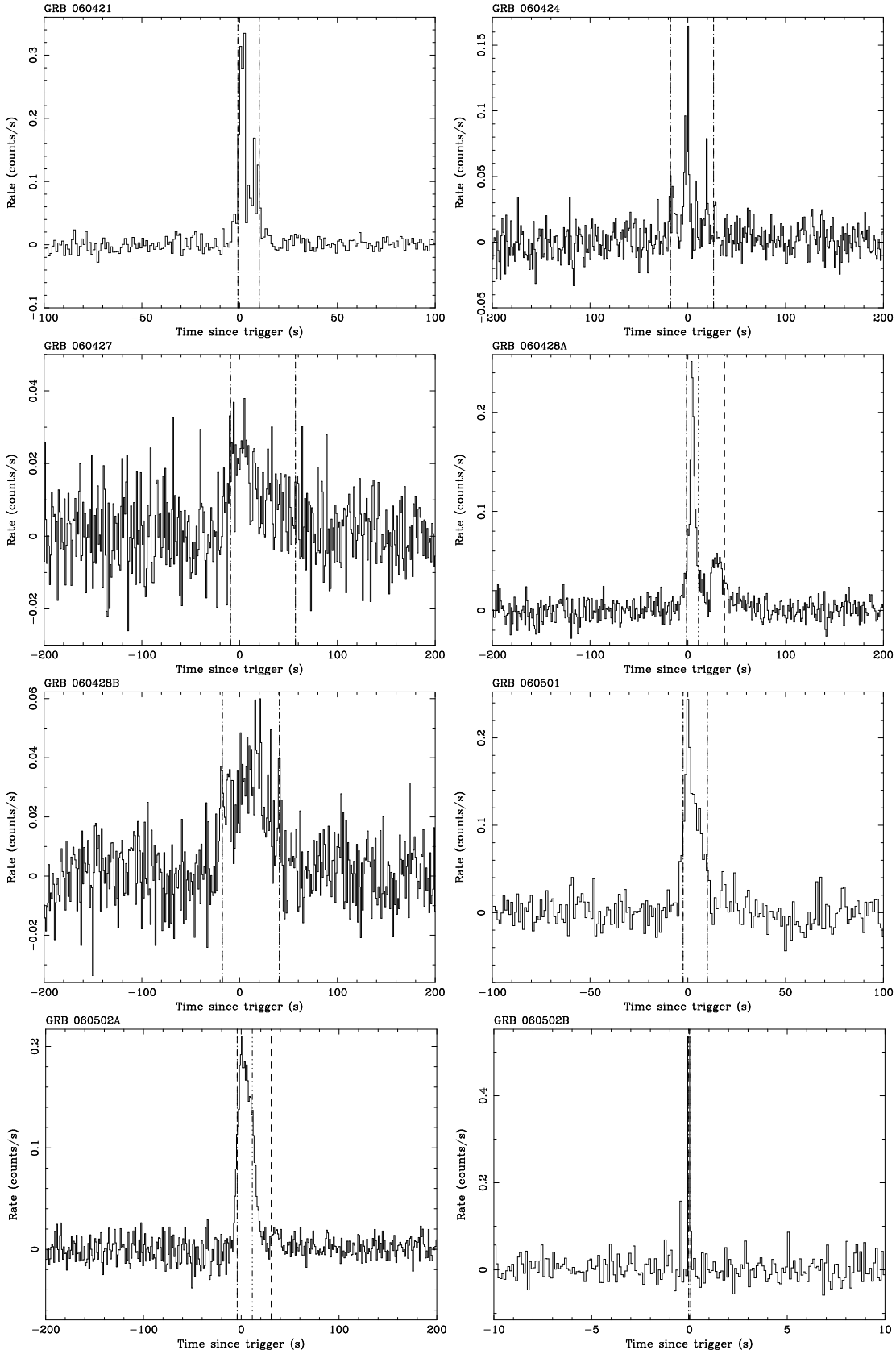

Figure B.15: Temporal parameters of Swift GRBs. The blue dashed lines represent the GRB duration (T_{90}). The green dashed lines represent the end time (or start time) source region of the spectrum.

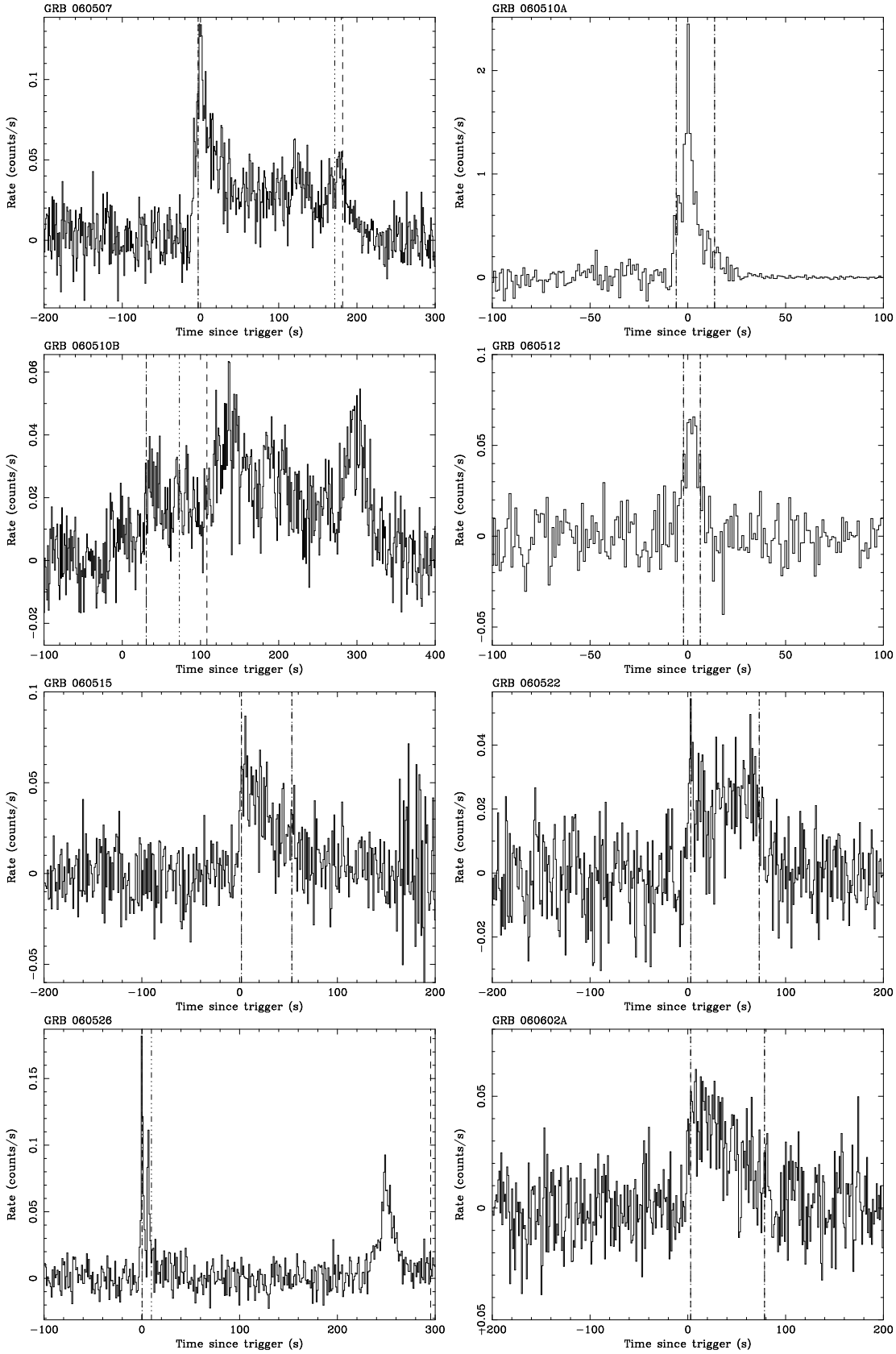

Figure B.16: Temporal parameters of Swift GRBs. The blue dashed lines represent the GRB duration (T_{90}). The green dashed lines represent the end time (or start time) source region of the spectrum.

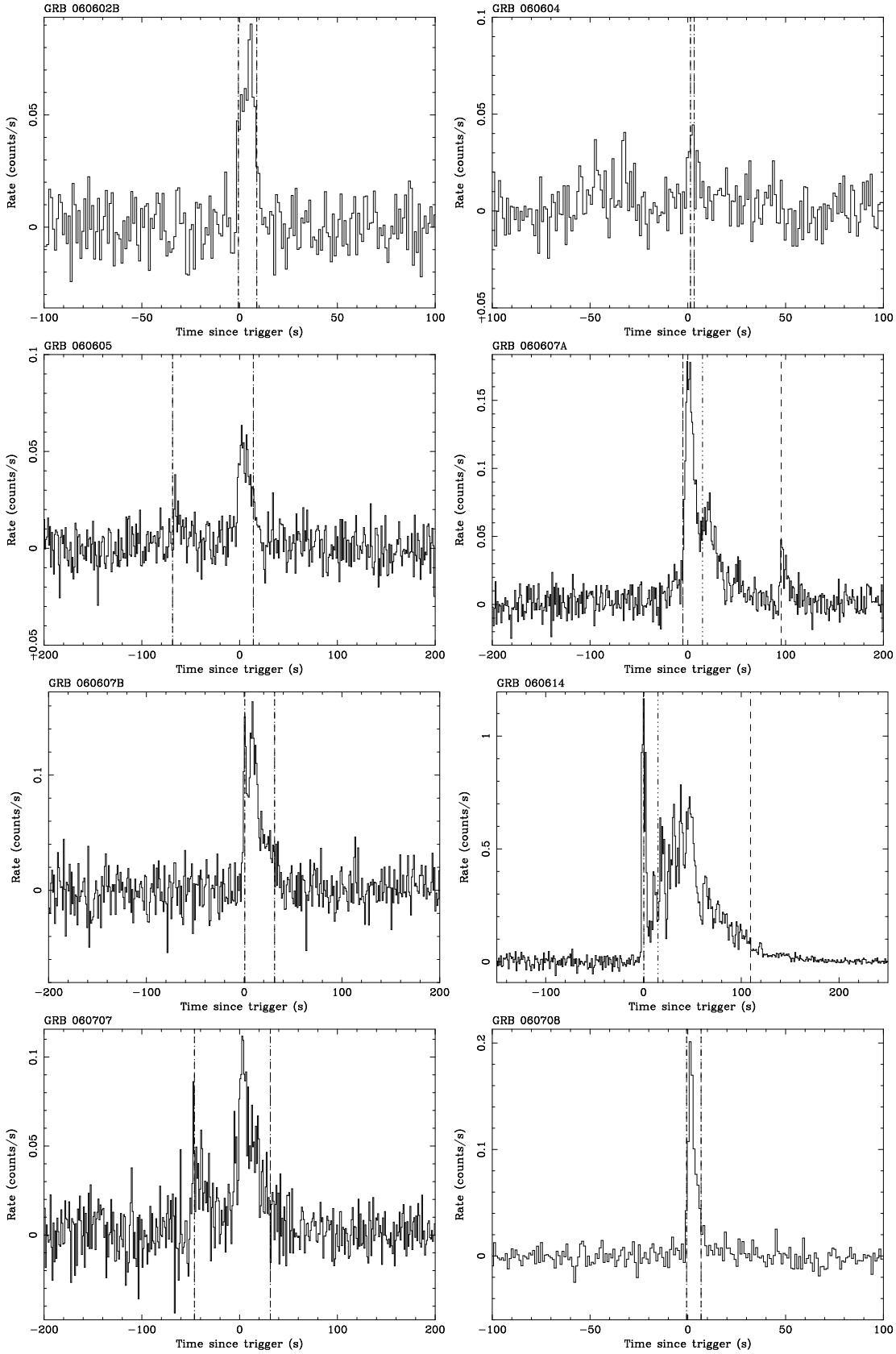

Figure B.17: Temporal parameters of Swift GRBs. The blue dashed lines represent the GRB duration (T_{90}). The green dashed lines represent the end time (or start time) source region of the spectrum.

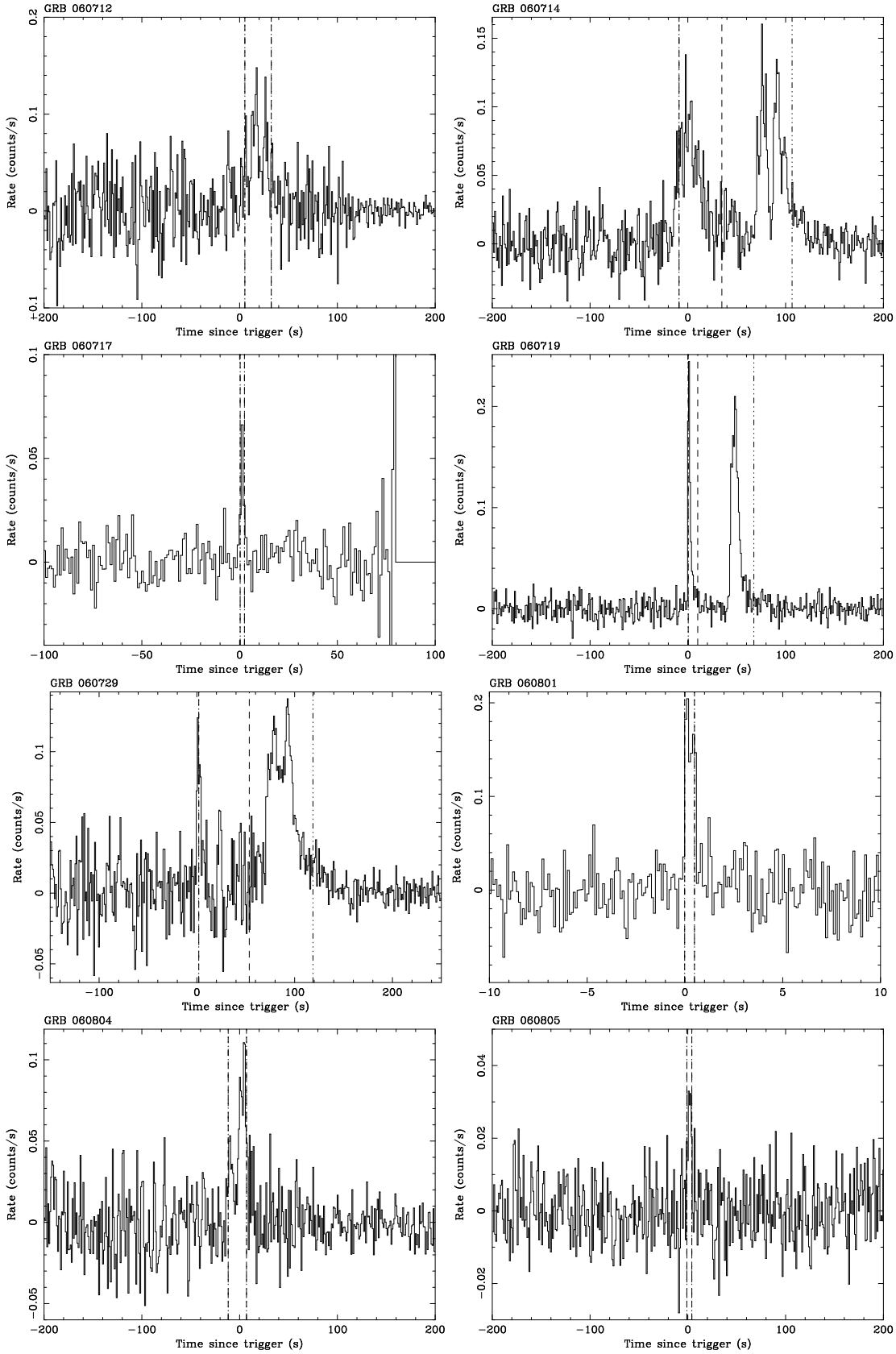

Figure B.18: Temporal parameters of Swift GRBs. The blue dashed lines represent the GRB duration (T_{90}). The green dashed lines represent the end time (or start time) source region of the spectrum.

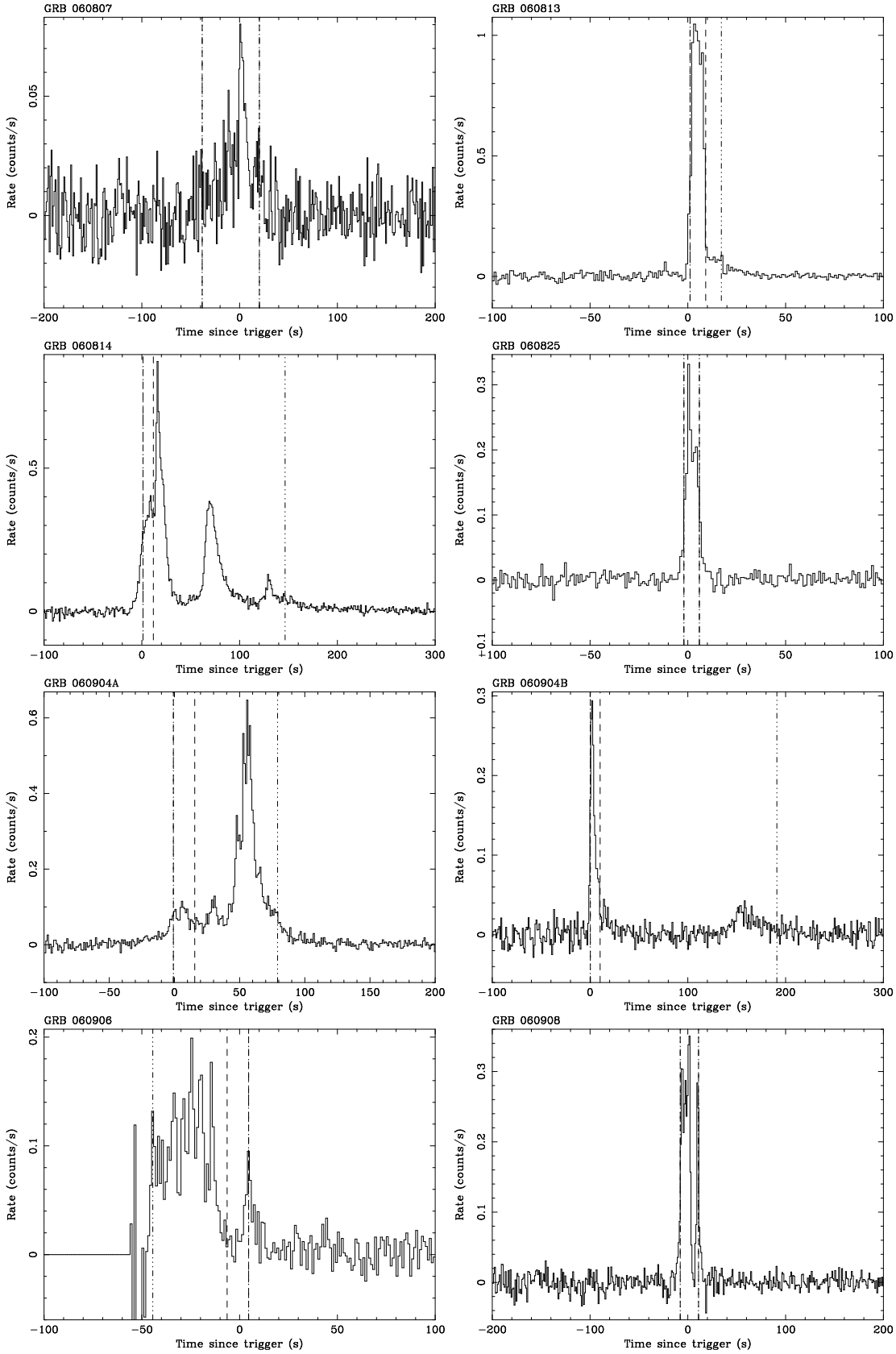

Figure B.19: Temporal parameters of Swift GRBs. The blue dashed lines represent the GRB duration (T_{90}). The green dashed lines represent the end time (or start time) source region of the spectrum.

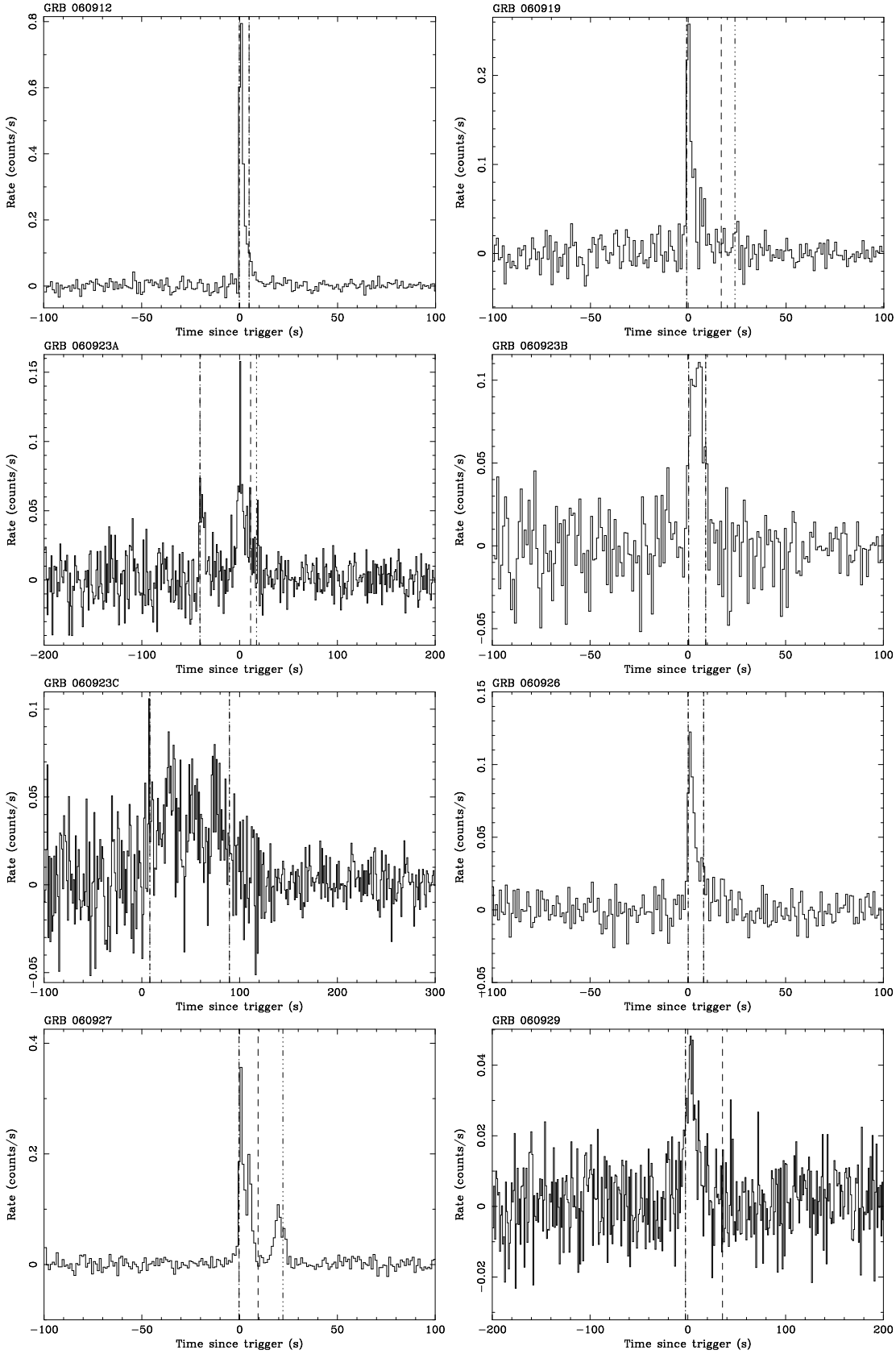

Figure B.20: Temporal parameters of Swift GRBs. The blue dashed lines represent the GRB duration (T_{90}). The green dashed lines represent the end time (or start time) source region of the spectrum.

Appendix C

XRT Light Curves of X-ray Afterglows

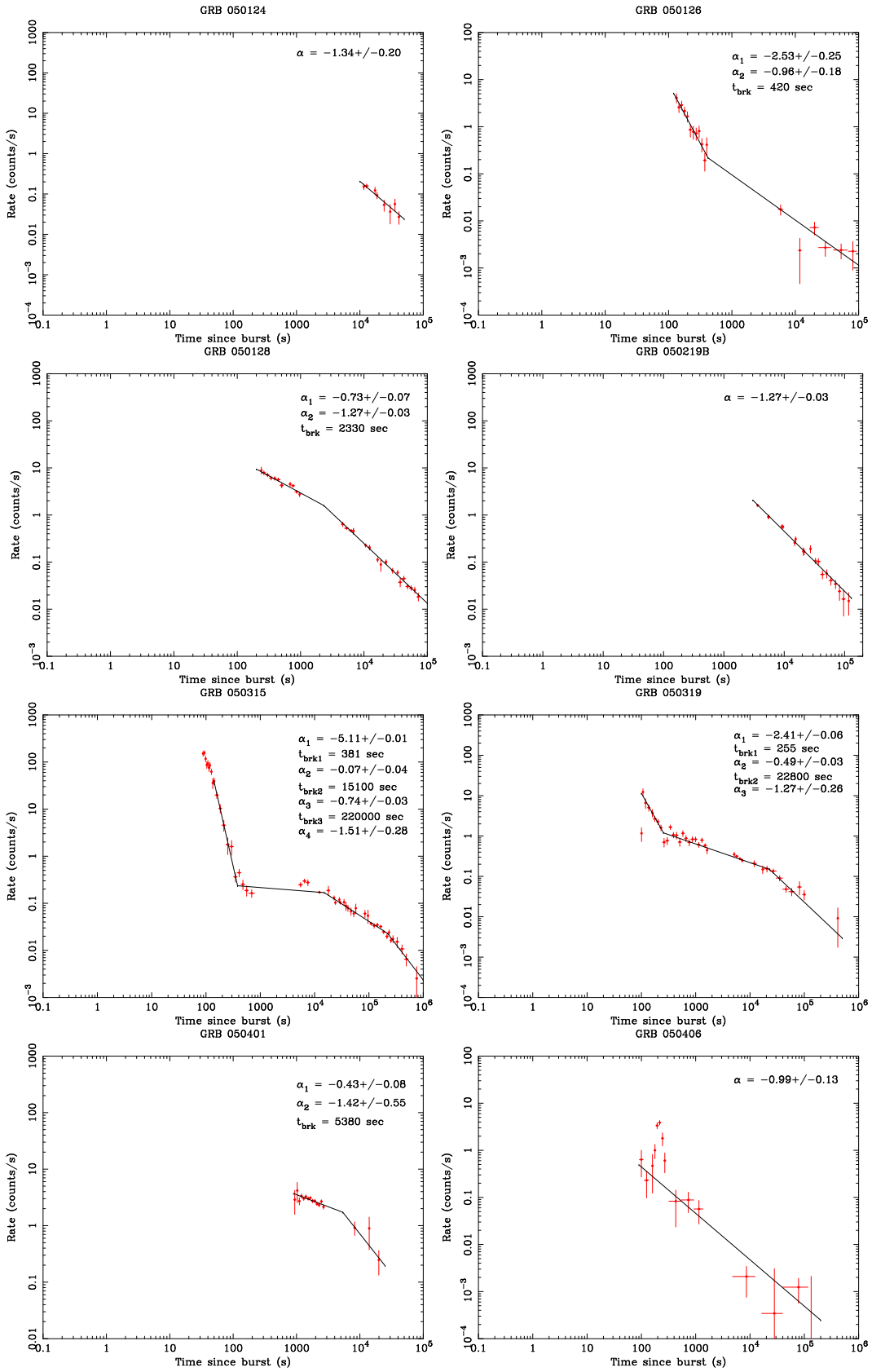

Figure C.1: GRB 050124, 050126, 050128, 050219B, 050315, 050319, 050401, 050406

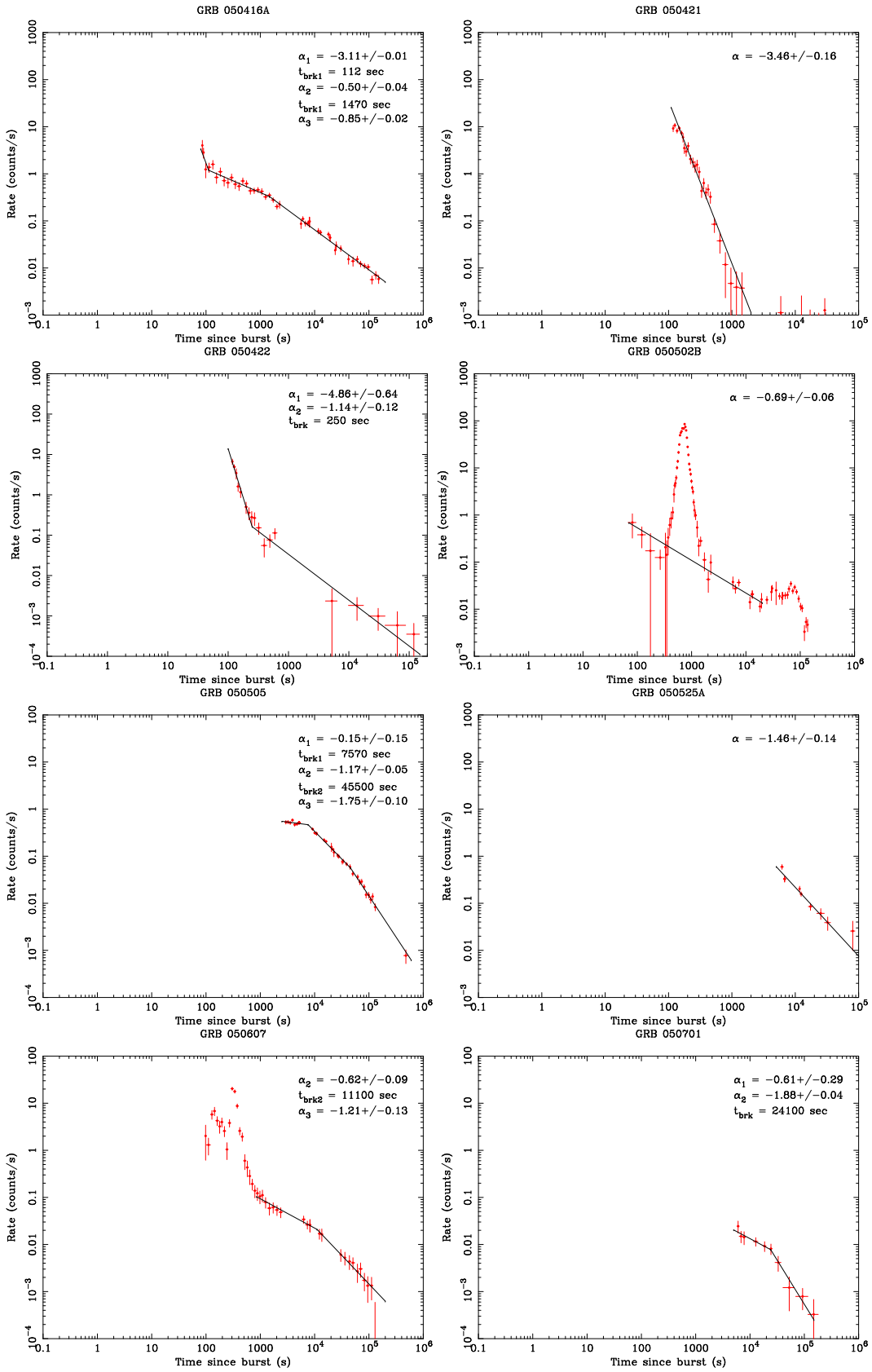

Figure C.2: GRB 050416A, 050421, 050422, 050502B, 050505, 050525, 050607, 050701

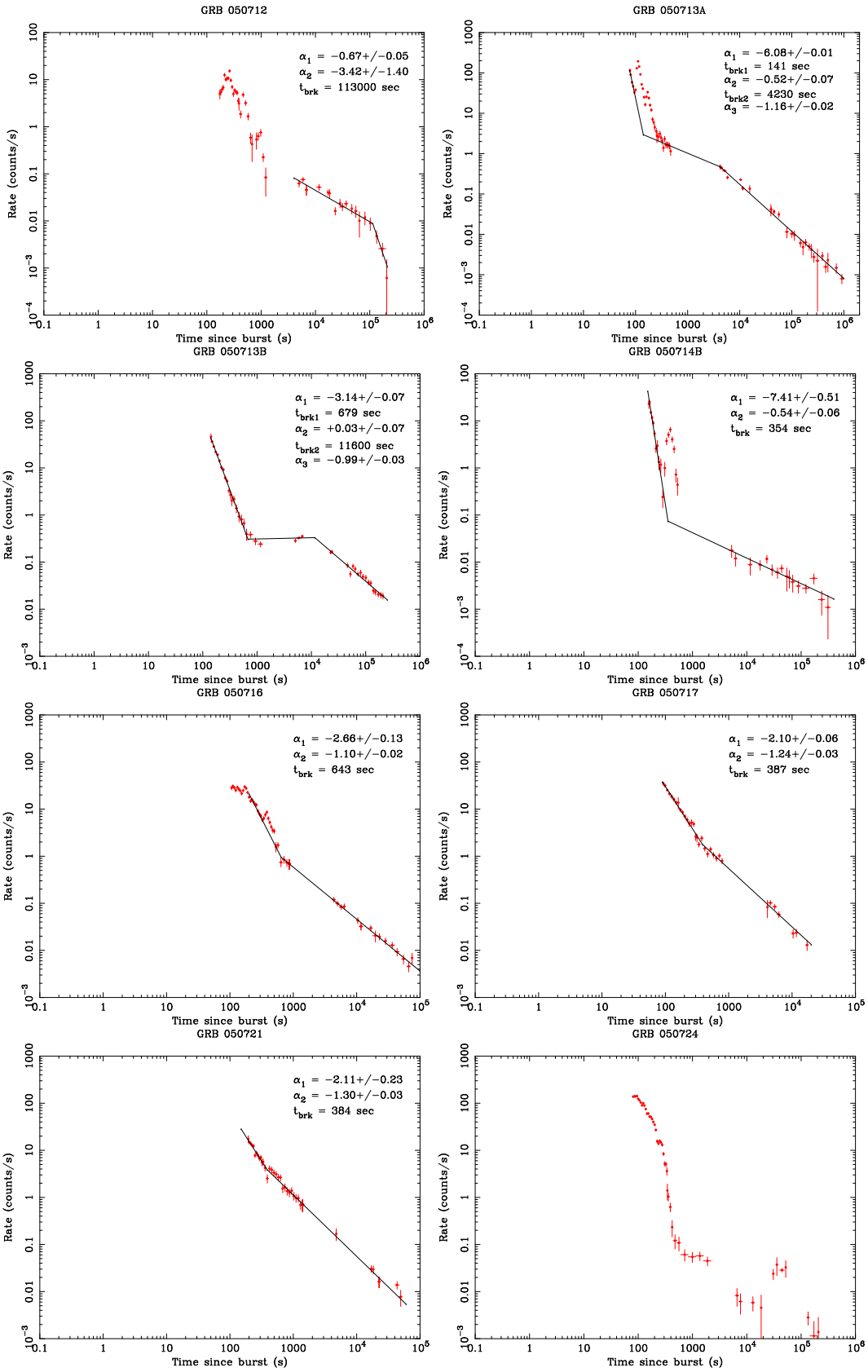

Figure C.3: GRB 050712, 050713A, 050713B, 050714B, 050716, 050717, 050721, 050724

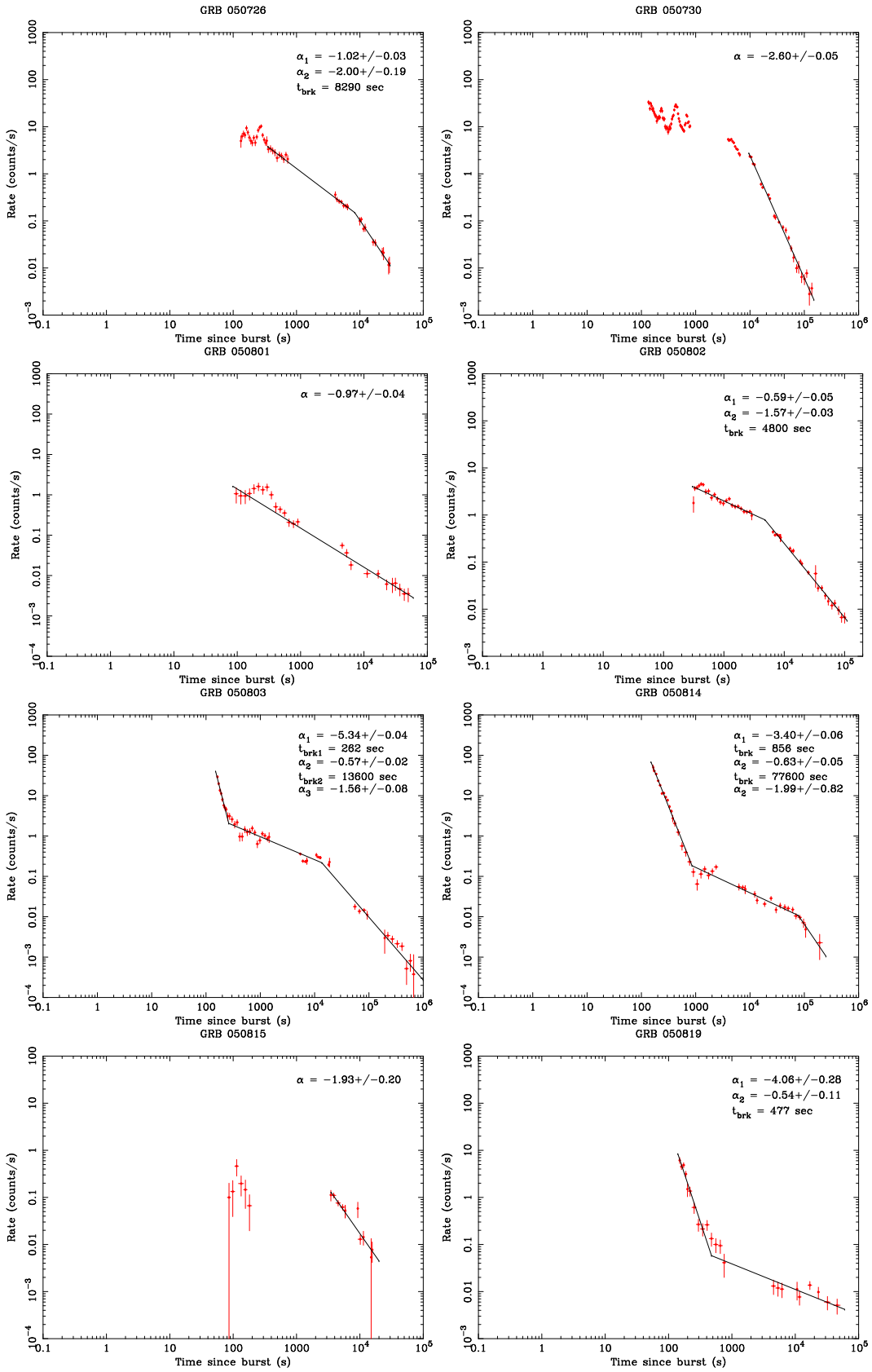

Figure C.4: GRB 050726, 050730, 050801, 050802, 050803, 050814, 050815, 050819

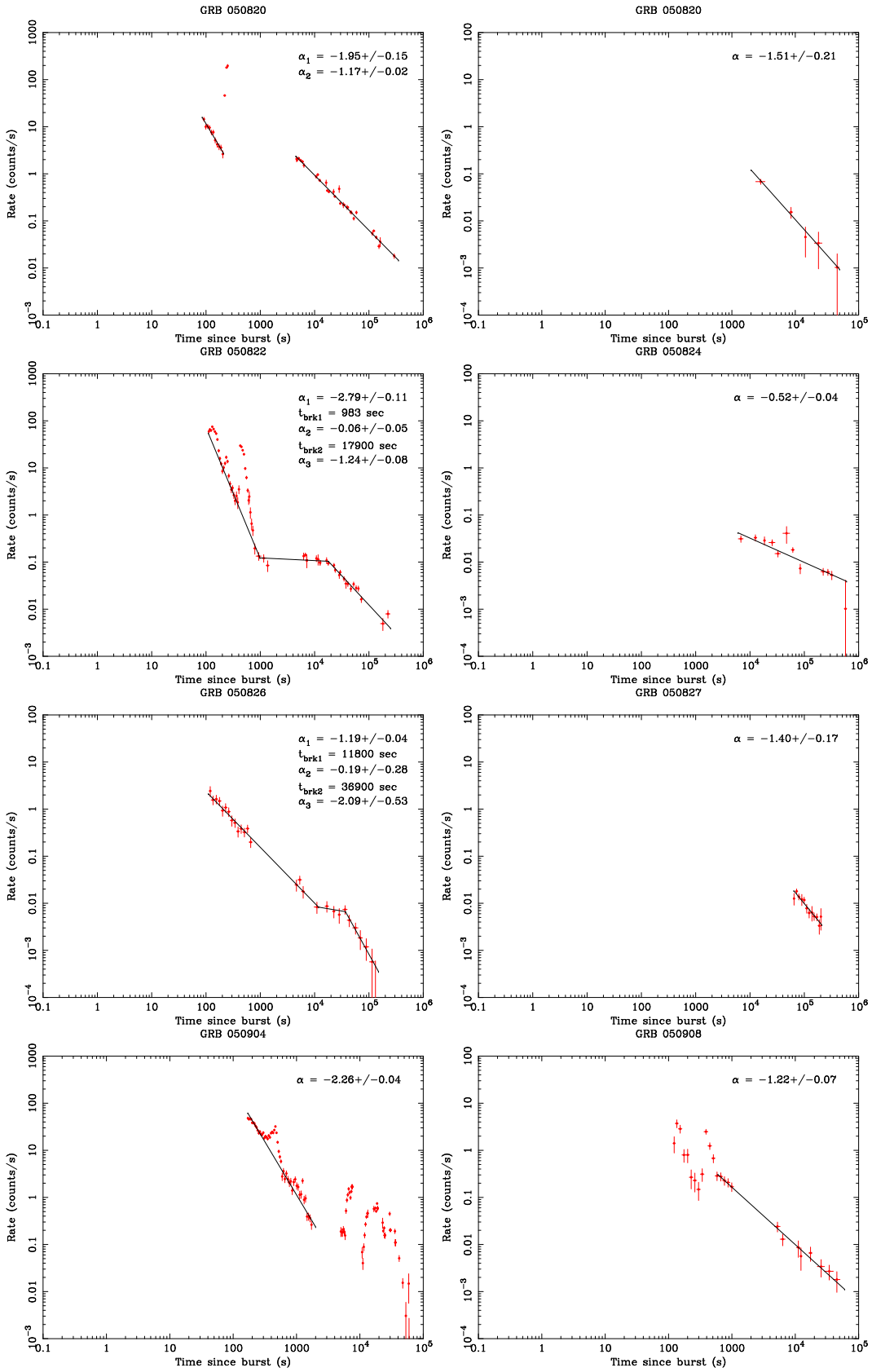

Figure C.5: GRB 050820A, 050820B, 050822, 050824, 050826, 050827, 050904, 050908

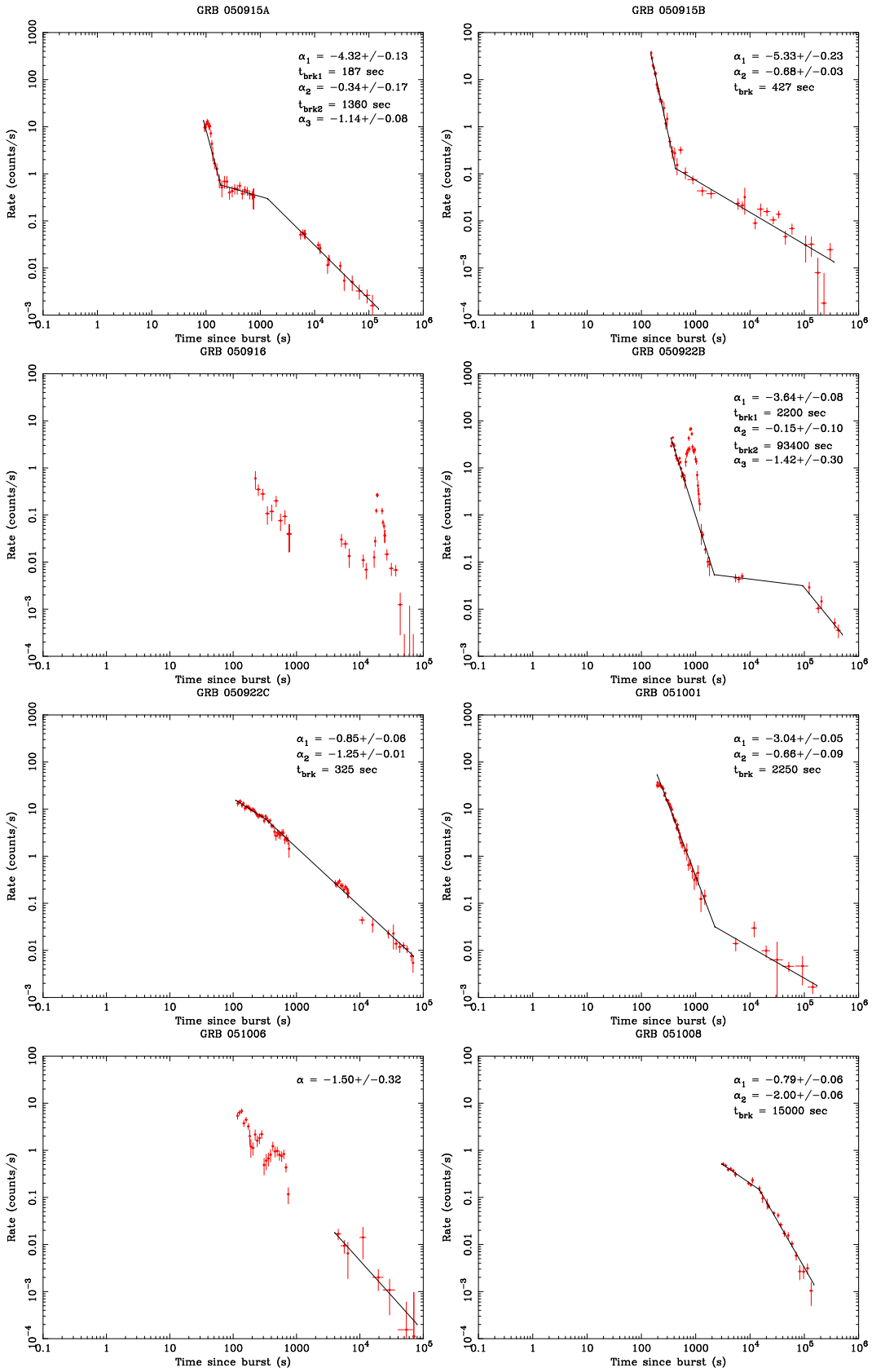

Figure C.6: GRB 050915A, 050915B, 050916, 050922B, 050922C, 051001, 051006, 051008

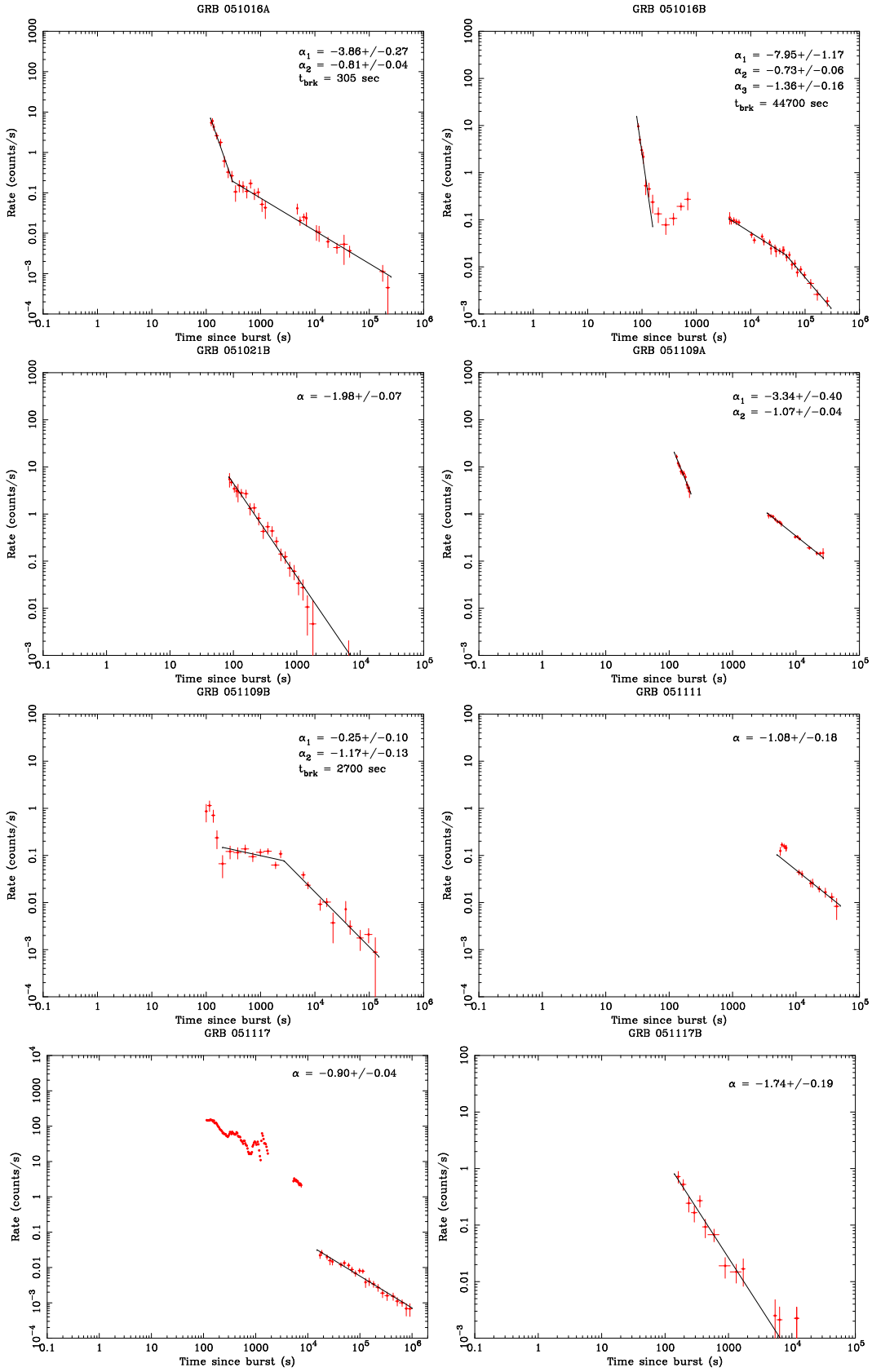

Figure C.7: GRB 051016A, 051016B, 051021B, 051109A, 051109B, 051111, 051117A, 051117B

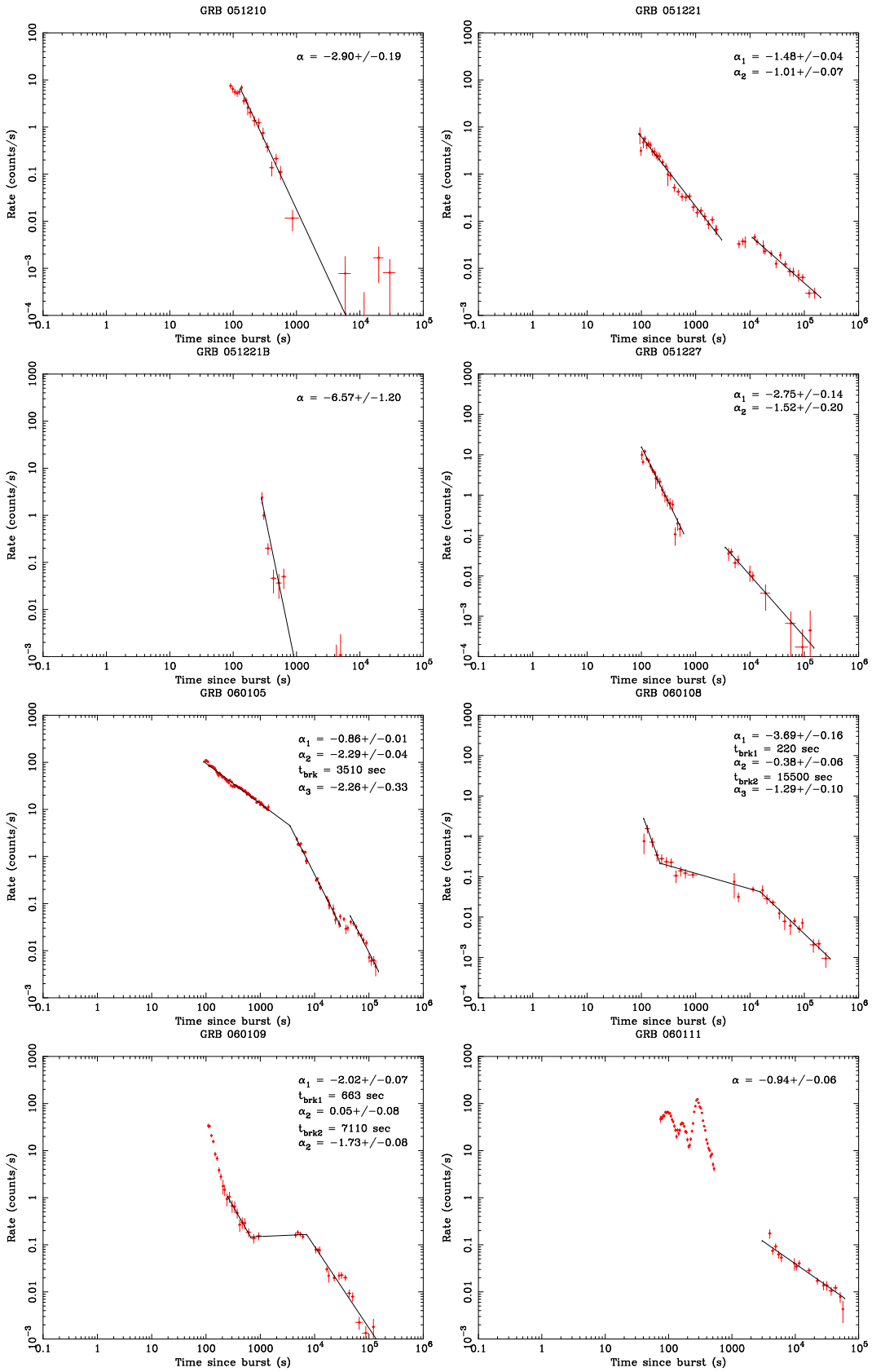

Figure C.8: GRB 051210, 051221A, 051221B, 051227, 060105, 060108, 060109, 060111A

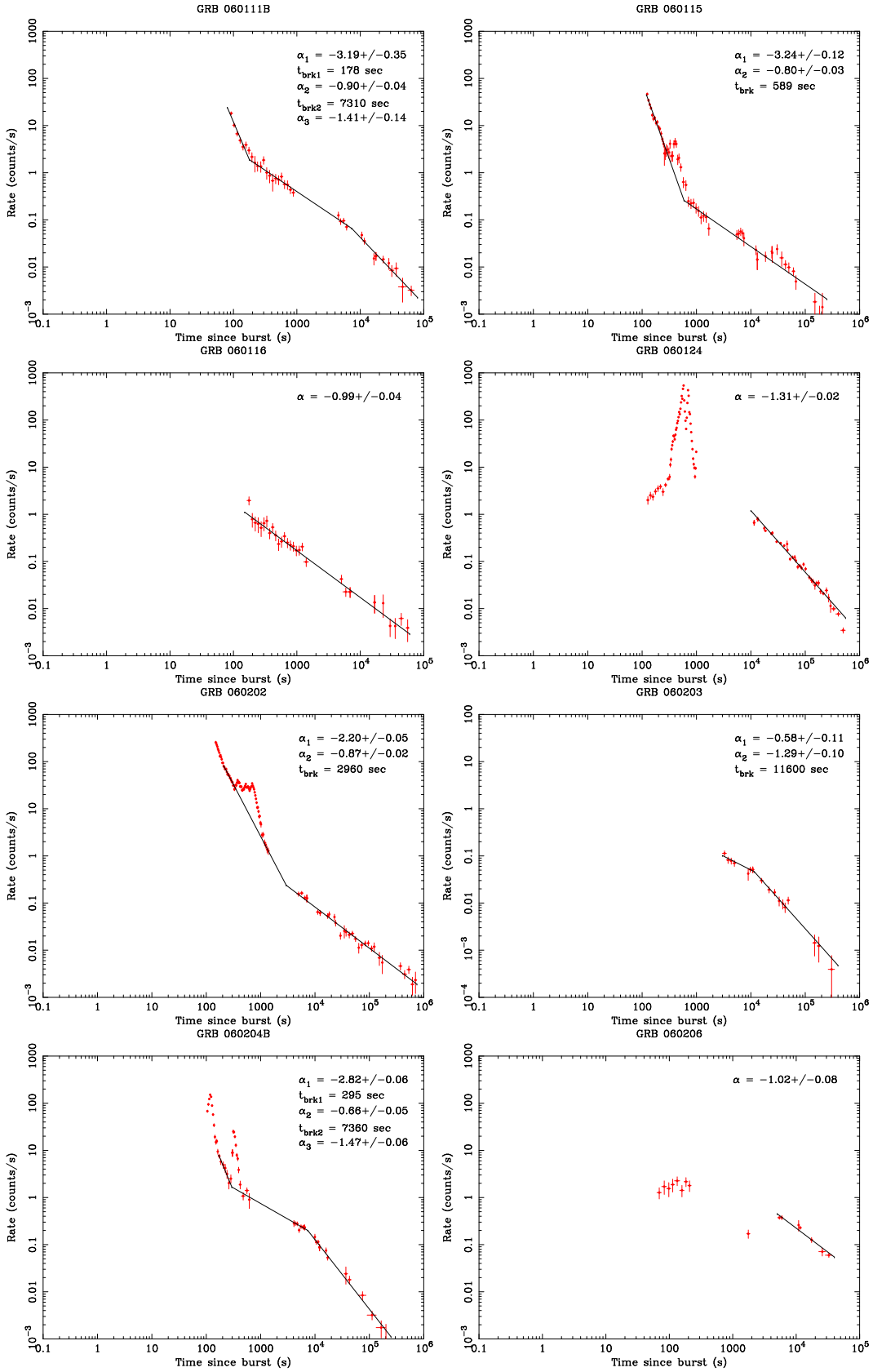

Figure C.9: GRB 060111B, 060115, 060116, 060124, 060202, 060203, 060204B, 060206

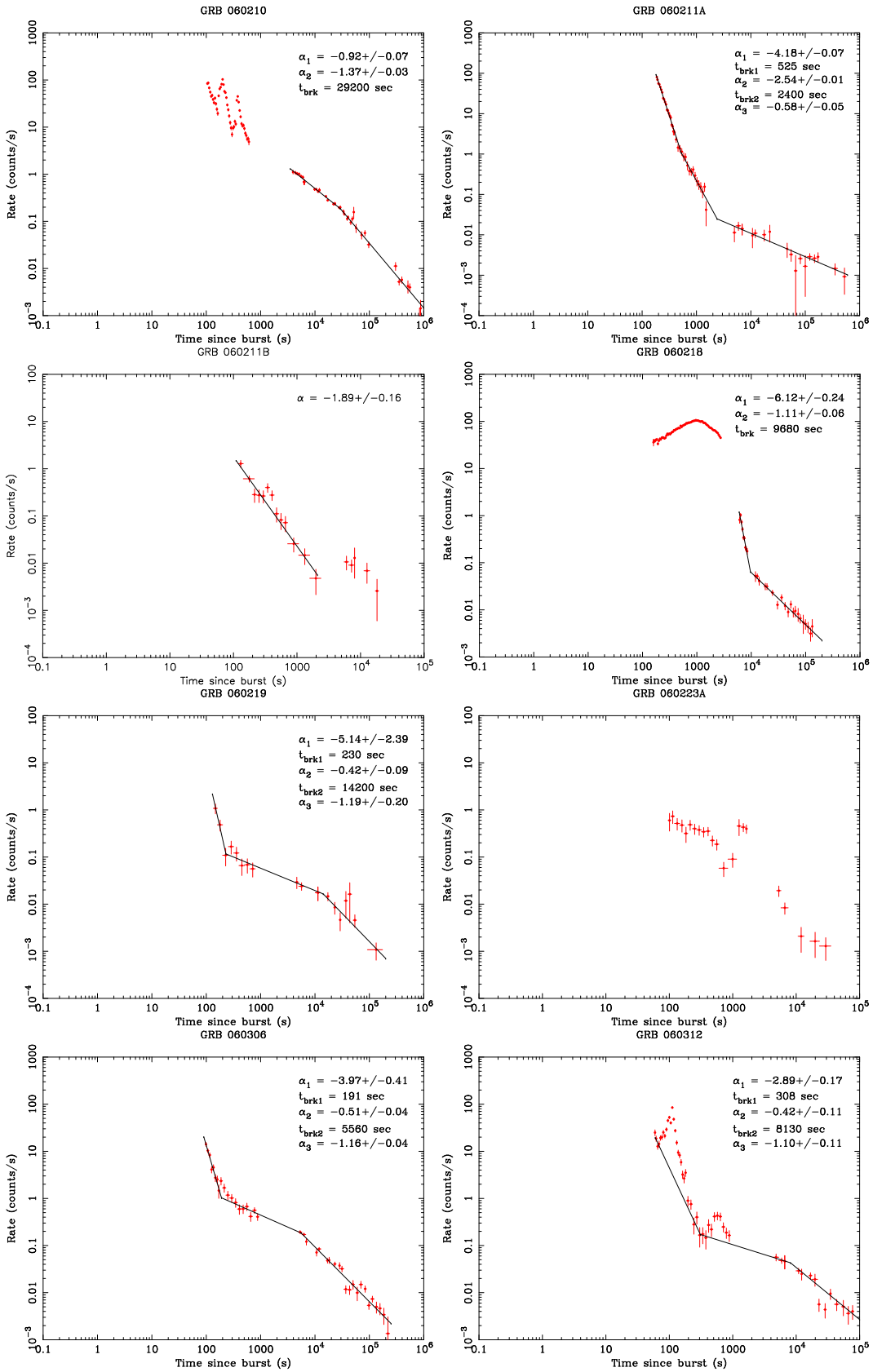

Figure C.10: GRB 060210, 060211A, 060211B, 060218, 060219, 060223A, 060306, 060312

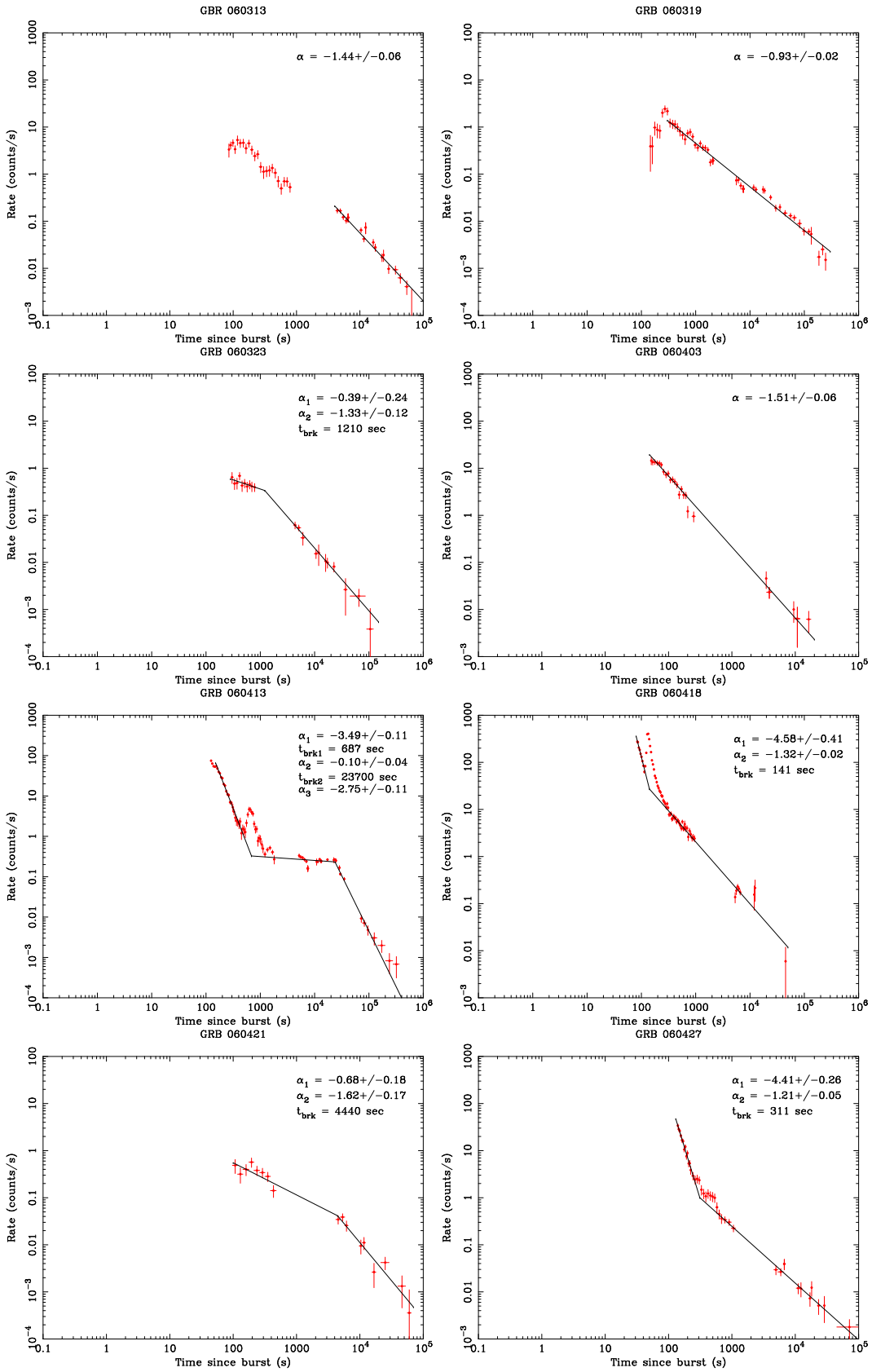

Figure C.11: GRB 060313, 060319, 060323, 060403, 060413, 060418, 060421, 060427

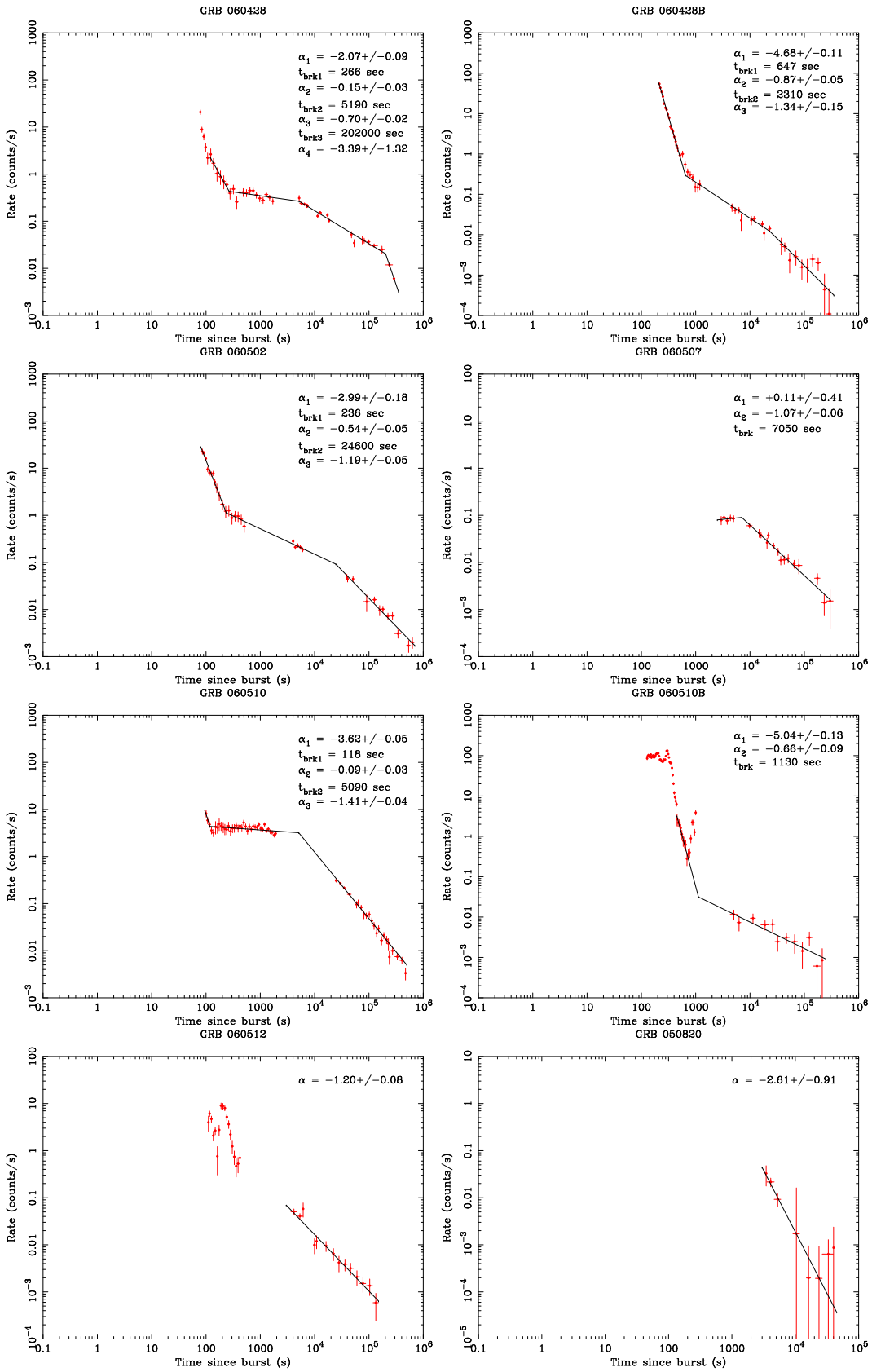

Figure C.12: GRB 060428A, 060428B, 060502, 060507, 060510A, 060510B, 060512, 060515

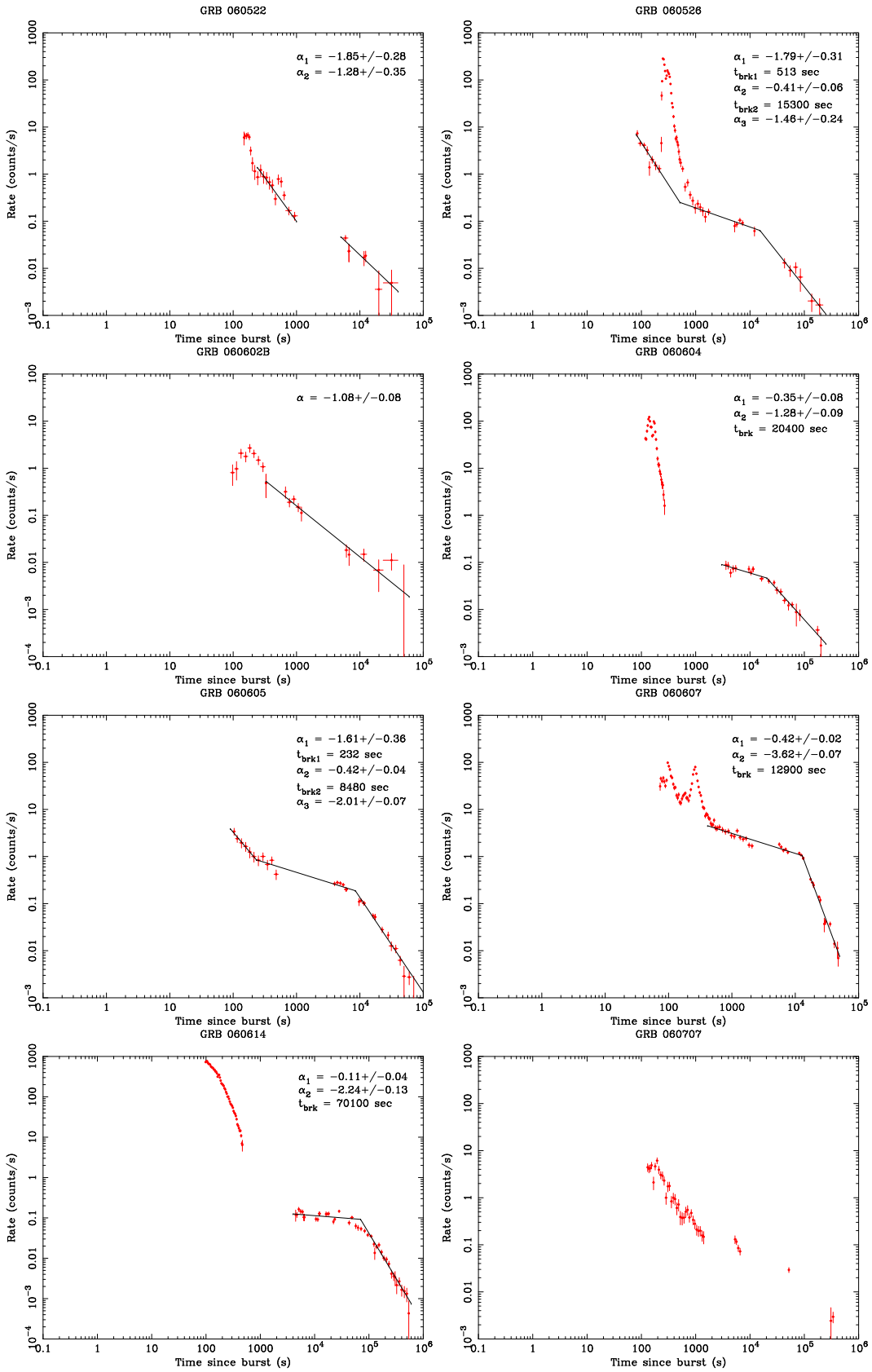

Figure C.13: GRB 060522, 060526, 060602B, 060604, 060605, 060607, 060614, 060707

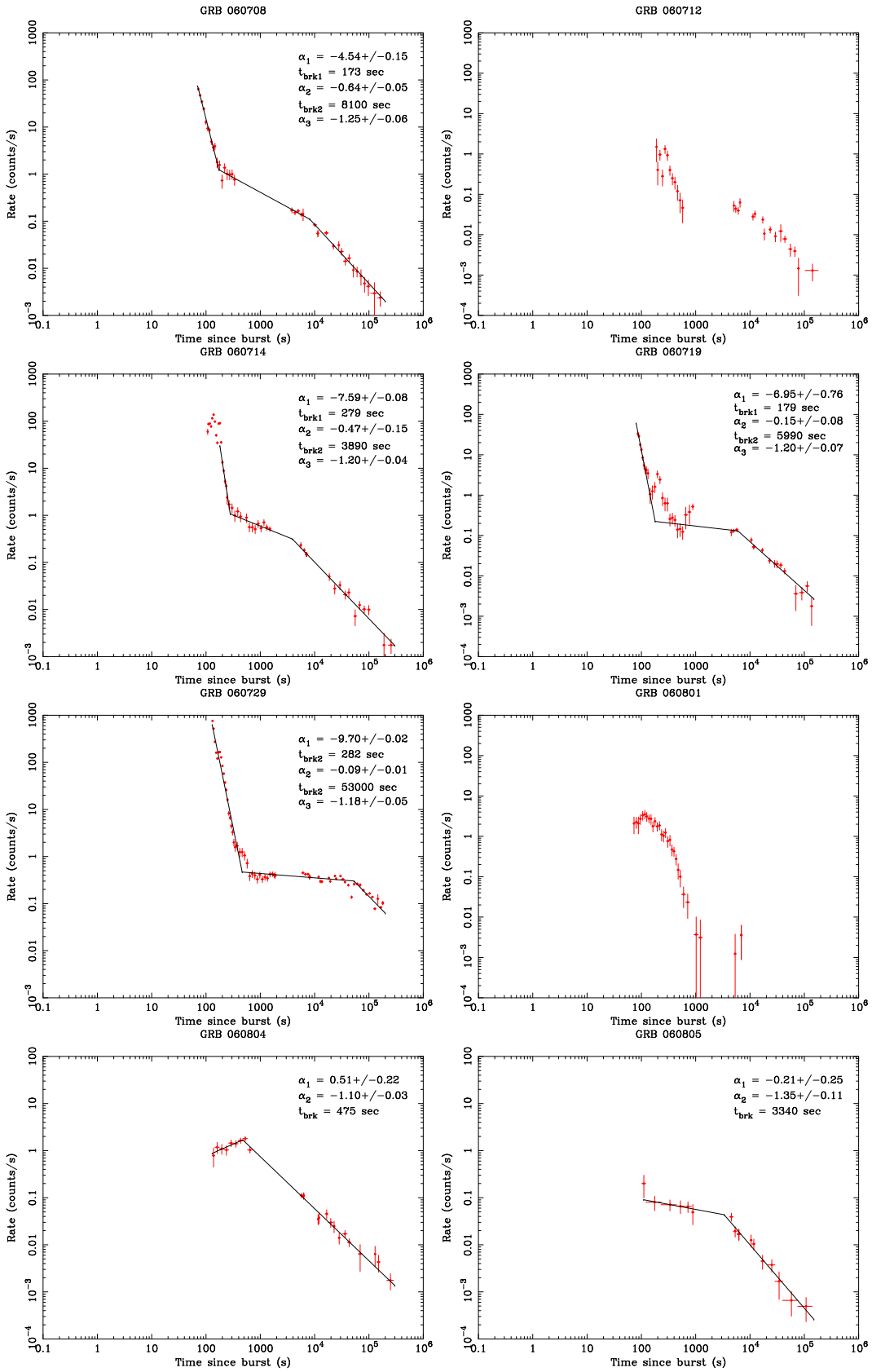

Figure C.14: GRB 060708, 060712, 060714, 060719, 060729, 060801, 060804, 060805

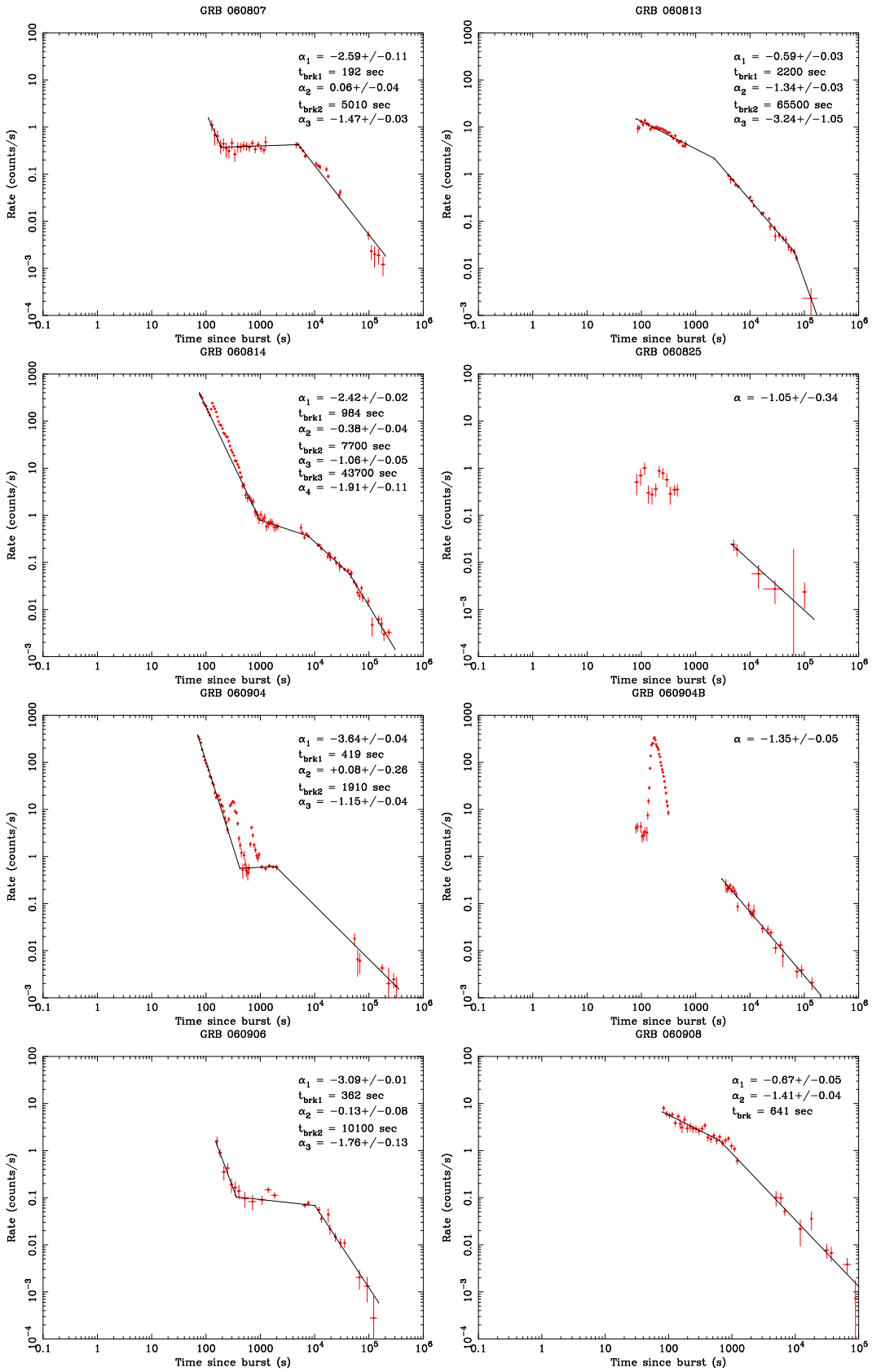

Figure C.15: GRB 060807, 060813, 060814, 060825, 060904A, 060904B, 060906, 060908

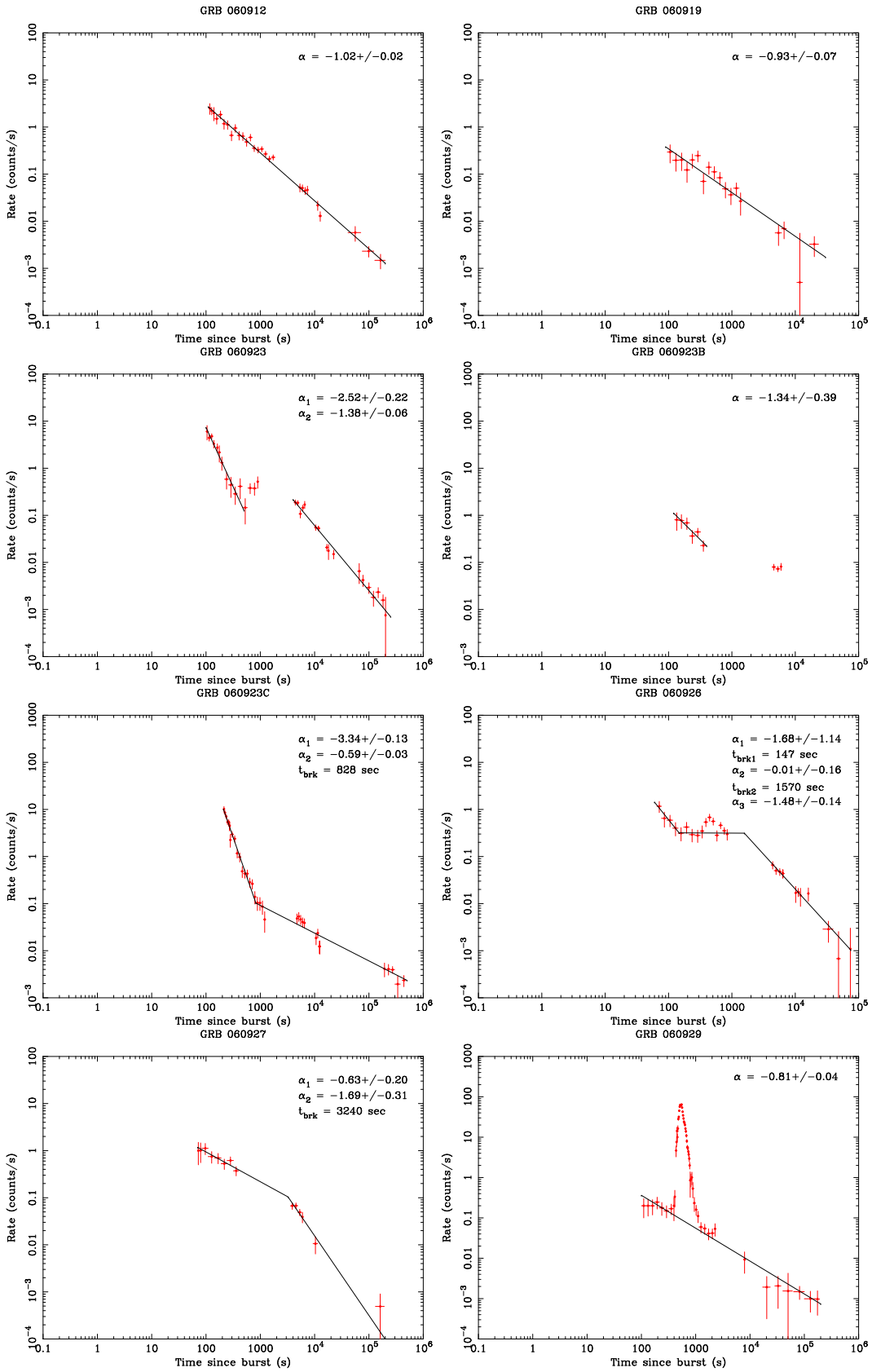

Figure C.16: GRB 060912, 060919, 060923A, 060923B, 060923C, 060926, 060927, 060929

Appendix D

Temporal Fit Results of XRT Observations

GRB	α_1	$t_{brk,1}$	α_2	$t_{brk,2}$	α_3	$t_{brk,3}$	α_4
050124	-	-	-	-	1.34±0.20	-	-
050126	2.53±0.25	420±188	0.96±0.18	-	-	-	-
050128	-	-	0.73±0.07	2330±500	1.27±0.03	-	-
050219B	-	-	-	-	1.27±0.03	-	-
050315	5.11±0.004	381±10	0.07±0.04	15100±1820	0.76±0.03	345000±75500	2.44±1.26
050319	2.41±0.06	255±12	0.49±0.03	22800±5040	1.27±0.26	-	-
050401	-	-	0.43±0.08	5380±243	1.42±0.55	-	-
050406	-	-	-	-	0.99±0.13	-	-
050416	3.11±0.01	112±9	0.50±0.04	1470±4.0	0.85±0.02	-	-
050421	3.46±0.16	-	-	-	-	-	-
050422	4.86±0.64	250±29	-	-	1.14±0.12	-	-
050502B	-	-	0.69±0.06	-	-		
050505	-	-	0.15±0.15	7570±797	1.17±0.05	45500±6520	1.75±0.10
050525	-	-	-	-	1.46±0.14	-	-
050607	-	-	0.62±0.09	11100±4330	1.21±0.13	-	-
050701	-	-	0.61±0.29	24100±6840	1.88±0.43	-	-
050712	-	-	0.67±0.05	113000±19200	3.42±1.40	-	-
050713	6.08±0.01	141±3	0.52±0.07	4230±1010	1.16±0.02	-	-
050713B	3.14±0.07	679±35	0.03±0.07	11600±1100	0.99±0.03	-	-
050714B	7.41±0.51	354±0.2	0.54±0.06	-	-	-	-
050716	2.66±0.13	-	-	643±56	1.10±0.02	-	-
050717	2.10±0.06	-	-	387±37	1.24±0.03	-	-
050721	2.11±0.23	-	-	384±55	1.30±0.03	-	-
050724	-	-	-	-	-	-	-
050726	-	-	-	-	1.02±0.03	8290±1072	2.00±0.19
050730	-	-	-	-	2.60±0.05	-	-
050801	-	-	-	-	0.97±0.04	-	-
050802			0.59±0.05	4800±392	1.57±0.03	-	-
050803	5.34±0.04	262±5	0.57±0.02	13600±1930	1.56±0.08	-	-
050814	3.40±0.06	856±59	0.62±0.06	77600±10200	1.99±0.82	-	-
050815	-	-	-	-	1.93±0.20	-	-
050819	4.06±0.28	477±55	0.54±0.11	-	-	-	-
050820	1.95±0.15	-	-	-	1.17±0.02	-	-
050820B	-	-	-	-	1.51±0.21	-	-

GRB	α_1	$t_{brk,1}$	α_2	$t_{brk,2}$	α_3	$t_{brk,3}$	α_4
050822	2.79±0.11	98.3±71.4	0.07±0.05	17900±1410	1.24±0.08	-	-
050824	-	-	0.52±0.04	-	-	-	-
050826	1.19±0.04	11800±5100	0.19±0.28	36900±6540	2.09±0.53	-	-
050827	-	-	-	-	1.40±0.17	-	-
050904	2.26±0.04	-	-	-	-	-	-
050908	-	-	-	-	1.22±0.07	-	-
050915	4.32±0.13	187±10	0.34±0.17	1360±500	1.14±0.08	-	-
050915B	5.33±0.23	42.7±21.1	0.68±0.03	-	-	-	-
050916	-	-	-	-	-	-	-
050922B	3.64±0.08	2200±125	0.14±0.10	93400±35200	1.42±0.30	-	-
050922C	-	-	0.85±0.06	325±0.2	1.25±0.01	-	-
051001	3.04±0.05	2250±238	0.66±0.09	-	-	-	-
051006	-	-	-	-	1.50±0.32	-	-
051008	-	-	0.79±0.06	15000±975	2.00±0.06	-	-
051016	3.86±0.27	305±22	0.81±0.04	-	-	-	-
051016B	7.95±1.17	-	0.73±0.06	44700±9120	1.36±0.16		
051021B	1.98±0.07	-	-	-	-	-	-
051109	3.34±0.40	-	-	-	1.07±0.04	-	-
051109B	-	-	0.25±0.10	2700±755	1.17±0.13	-	-
051111	-	-	-	-	1.08±0.18	-	-
051117	-	-	-	-	0.90±0.04	-	-
051117B	1.74±0.19	-	-	-	-	-	-
051210	2.90±0.19	-	-	-	-	-	-
051221	1.48±0.04	-	-	-	1.01±0.07	-	-
051221B	6.57±1.20	-	-	-	-	-	-
051227	2.75±0.14	-	-	-	1.52±0.20	-	-
060105	-	-	0.86±0.01	3510±106	2.29±0.04	2.26±0.33	
060108	3.69±0.16	220±14	0.38±0.06	15500±3730	1.29±0.10	-	-
060109	2.02±0.07	663±119	0.05±0.08	7110±460	1.73±0.08	-	-
060111	-	-	-	-	0.94±0.06	-	-
060111B	3.19±0.35	178±15	0.90±0.04	7310±2400	1.41±0.14	-	-
060115	3.24±0.12	589±44	0.80±0.03	-	-	-	-
060116	-	-	0.99±0.04	-	-	-	-
060124	-	-	-	-	1.31±0.02	-	-
060202	2.20±0.05	2960±313	0.87±0.02	-	-	-	-
060203	-	-	0.58±0.11	11600±2270	1.29±0.10	-	-
060204B	2.82±0.06	295±20	0.66±0.05	7360±672	1.47±0.06	-	-
060206	-	-	-	-	1.02±0.08	-	-
060210	-	-	0.92±0.07	29200±66.4	1.37±0.03	-	-
060211	2.54±0.01	2400±220	0.58±0.05	-	-	-	-
060211B	1.89±0.16	-	-	-	-	-	-
060218	6.12±0.24	9680±230	-	-	1.11±0.06	-	-
060219	5.14±2.39	230±38.0	0.42±0.09	14200±4830	1.19±0.20	-	-
060223	-	-	-	-	-	-	-
060306	3.97±0.41	191±12	0.51±0.04	5560±841	1.16±0.04	-	-
060312	2.89±0.17	308±48	0.42±0.11	8130±2020	1.10±0.11	-	-
060313	-	-	-	-	1.44±0.06	-	-
060319	-	-	-	-	0.93±0.02	-	-
060323	-	-	0.39±0.24	1210±417	1.33±0.12	-	-
060403	1.51±0.06	-	-	-	-	-	-
060413	3.49±0.11	687±32.6	0.10±0.04	23700±582	2.75±0.11	-	-
060418	4.58±0.41	141±7	-	-	1.32±0.02	-	-
060421	-	-	0.68±0.18	4440±2590	1.62±0.17	-	-
060427	4.41±0.26	311±20	-	-	1.21±0.05	-	-

GRB	α_1	$t_{brk,1}$	α_2	$t_{brk,2}$	α_3	$t_{brk,3}$	α_4
060428	2.07±0.09	266±24	0.15±0.03	5190±4.1	0.70±0.02	202000±20400	3.39±1.32
060428B	4.68±0.11	647±25	0.87±0.05	23100±226	1.34±0.15	-	-
060502	2.99±0.18	236±17	0.54±0.05	24600±5140	1.19±0.05	-	-
060507	-	-	-0.11±0.41	7050±1580	1.07±0.06	-	-
060510	3.62±0.05	118±3	0.09±0.03	5090±406	1.41±0.04	-	-
060510B	5.04±0.13	1130±80	0.66±0.10	-	-	-	-
060512	-	-	-	-	1.20±0.08	-	-
060515	-	-	-	-	2.61±0.91	-	-
060522	1.85±0.28	-	-	-	1.28±0.35	-	-
060526	1.79±0.31	513±178	0.41±0.06	15300±5680	1.46±0.24	-	-
060602B	-	-	-	-	1.08±0.08	-	-
060604	-	-	0.35±0.08	20400±2400	1.28±0.09	-	-
060605	1.61±0.36	232±46	0.42±0.04	8480±348	2.01±0.07	-	-
060607	-	-	0.42±0.02	12900±192	3.62±0.07	-	-
060614	-	-	0.11±0.04	70100±5060	2.24±0.13	-	-
060707	-	-	-	-	-	-	-
060708	4.54±0.15	173±7	0.64±0.05	8100±1170	1.25±0.06	-	-
060712	-	-	-	-	-	-	-
060714	7.59±0.08	279±6	0.47±0.15	3890±1250	1.20±0.04	-	-
060719	6.95±0.76	179±15	0.15±0.08	5990±671	1.20±0.07	-	-
060729	9.70±0.02	282±2	0.09±0.01	53000±1930	1.18±0.05	-	-
060801	-	-	-	-	-	-	-
060804	-	-	-0.51±0.22	475±45.1	1.10±0.03	-	-
060805	-	-	0.21±0.25	3340±1610	1.35±0.11	-	-
060807	2.59±0.11	192±15	-0.06±0.04	5010±225	1.47±0.03	-	-
060813	-	-	0.59±0.03	2200±221	1.34±0.03	65500±6240	3.24±1.05
060814	2.42±0.02	984±45	0.38±0.04	7700±716	1.06±0.05	43700±4510	1.91±0.11
060825	-	-	-	-	1.05±0.34	-	-
060904	3.64±0.04	419±31	-0.08±0.26	1910±231	1.15±0.04	-	-
060904B	-	-	-	-	1.35±0.05	-	-
060906	3.09±0.01	362±27	0.13±0.08	10100±912	1.76±0.13	-	-
060908	-	-	0.67±0.05	641±1.0	1.41±0.04	-	-
060912	-	-	-	-	1.02±0.02	-	-
060919	-	-	-	-	0.93±0.07	-	-
060923	2.52±0.22	-	-	-	1.38±0.06	-	-
060923B	-	-	-	-	1.34±0.39	-	-
060923C	3.34±0.13	828±55	0.59±0.03	-	-	-	-
060926	1.68±1.14	147±49	0.01±0.16	1570±330	1.48±0.14	-	-
060927	-	-	0.63±0.20	3240±1770	1.69±0.31	-	-
060929	-	-	0.81±0.04	-	-		

Table D.1: Temporal Parameters of X-ray light curves.

Appendix E

Spectral Fit Results of XRT Observations

GRB	β_1	$N_{\rm H}$	β_2	$N_{\rm H}$	β_3	$N_{\rm H}$	Galactic $N_{\rm H}$
050124	-	-	-	-	1.71±0.12	0.0227 (fix)	0.0227
050126	-	-	1.60±0.43	0.0532 (fix)	-	-	0.0532
050128	-	-	-	-	2.15±0.07	0.168±0.024	0.0432
050219B	-	-	-	-	2.21±0.09	0.247±0.033	0.0401
050315	-	-	2.35±0.29	0.372±0.131	2.00±0.09	0.165±0.033	0.0432
050319	2.47±0.71	0.0117 (fix)	2.16±0.11	0.102±0.031	2.21±0.17	0.0967±0.0501	0.0117
050401	-	-	2.10±0.07	0.180±0.023	$3.20^{+0.79}_{-0.69}$	$0.458^{+0.277}_{-0.249}$	0.0481
050406	-	-	-	-	-	-	0.0257
050416	-	-	2.21±0.35	$0.247^{+0.175}_{-0.156}$	2.19±0.11	0.275±0.038	0.020
050421	1.29±0.19	$0.760^{+0.185}_{-0.165}$	-	-	-	-	0.148
050422	3.19±0.38	1.02 (fix)	-	-	2.06±0.46	1.02 (fix)	1.02
050502B	-	-	-	-	-	-	0.0368
050505	-	-	2.13±0.09	0.110±0.027	2.09±0.07	0.0784±0.0194	0.0209
050525	-	-	-	-	2.02±0.14	0.146±0.046	0.0915
050607	-	-	1.93±0.25	0.14 (fix)	$2.52^{+0.52}_{-0.42}$	$0.290^{+0.165}_{-0.134}$	0.14
050701	-	-	1.45±0.48	1.60 (fix)	$1.01^{+0.56}_{-0.61}$	1.60 (fix)	1.60
050712	-	-	1.89±0.13	3.32±0.31		-	0.139
050713	2.47±0.13	0.516±0.058	2.16±0.21	$0.402^{+0.092}_{-0.082}$	2.48±0.18	$0.496^{+0.089}_{-0.081}$	0.107
050713B	1.65±0.09	0.307±0.048	2.33±0.15	0.550±0.090	2.12±0.17	$0.445^{+0.084}_{-0.077}$	0.167
050714B	5.19±0.34	$0.621^{+0.075}_{-0.069}$	2.55±0.37	$0.398^{+0.209}_{-0.188}$	-	-	0.0503
050716	-	-	-	-	1.99±0.07	0.0996 (fix)	0.0996
050717	1.58±0.07	0.451±0.046	-	-	1.58±0.12	0.238 (fix)	0.238
050721	1.64±0.09	0.257±0.038	-	-	-	-	0.163
050724	-	-	-	-	-	-	0.140
050726	-	-	2.04±0.13	0.103±0.042	2.44±0.20	0.163±0.054	0.0478
050730	-	-	-	-	1.88±0.07	0.0863±0.0209	0.0298
050801	-	-	1.79±0.13	0.0706 (fix)	-	-	0.0706
050802	-	-	1.85±0.07	0.0181 (fix)	2.14±0.10	0.157±0.030	0.0181
050803	1.74±0.15	0.118±0.058	2.05±0.09	0.231±0.030	2.66±0.18	0.253±0.052	0.0566
050814	2.14±0.07	0.0566±0.0191	2.17±0.16	0.101±0.047	-	-	0.0255
050815	-	-	-	-	1.76±0.15	0.277 (fix)	0.277
050819	2.28±0.14	0.0467 (fix)	1.97±0.36	0.0467 (fix)	-	-	0.0467
050820	2.10±0.13	0.100±0.043	-	-	2.08±0.05	0.110±0.014	0.0468
050820B	-	-	-	-	$2.36^{+0.66}_{-0.61}$	$0.581^{+0.484}_{-0.433}$	0.0758

050822	-	-	1.69±0.11	0.0194 (fix)	2.14±0.13	0.107±0.040	0.0194
050824	-	-	-	-	1.92±0.09	0.0356	0.0356
050826	1.56±0.18	0.218 (fix)	1.69±0.25	0.218 (fix)	2.12±0.31	0.218 (fix)	0.218
050827	-	-	-	-	1.55±0.15	0.197 (fix)	0.197
050904	1.30±0.04	0.090±0.017	-	-	-	-	0.0495
050908	-	-	-	-	2.15±0.12	0.0201 (fix)	0.0201
050915	-	-	1.88±0.13	0.0190 (fix)	2.12±0.25	0.107±0.068	0.0190
050915B	2.68±0.08	0.311 (fix)	2.12±0.13	0.311 (fix)	-	-	0.311
050916	1.51±0.42	0.121 (fix)	-	-	-	-	0.121
050922B	3.03±0.15	0.227±0.034	2.31±0.23	0.0350 (fix)	1.83±0.25	0.0350 (fix)	0.035
050922C	-	-	2.24±0.09	0.136±0.026	2.19±0.06	0.0609 (fix)	0.0609
051001	1.48±0.08	0.116±0.032	2.07±0.26	0.0139 (fix)	-	-	0.0139
051006	-	-	-	-	$1.93^{+1.38}_{-0.95}$	$0.609^{+0.918}_{-0.459}$	0.0865
051008	-	-	1.95±0.07	0.295±0.029	1.86±0.14	0.202±0.067	0.0101
051016	$3.05^{+0.61}_{-0.51}$	$0.425^{+0.228}_{-0.196}$	2.45±0.18	0.122 (fix)	-	-	0.122
051016	$3.05^{+0.61}_{-0.51}$	$0.425^{+0.228}_{-0.196}$	2.45±0.18	0.122 (fix)	-	0.122	
051016B	$6.91^{+2.11}_{-1.79}$	$0.577^{+0.305}_{-0.253}$	2.01±0.13	0.210±0.048	2.31±0.30	$0.268^{+0.106}_{-0.092}$	0.0365
051021B	1.46±0.33	0.746 (fix)	-	-	-	-	0.746
051109	2.07±0.09	0.168 (fix)	-	-	2.06±0.08	0.189±0.026	0.167
051109B	-	-	$2.74^{+0.43}_{-0.39}$	$0.554^{+0.184}_{-0.167}$	1.86±0.23	0.136 (fix)	0.136
051111	-	-	-	-	2.08±0.14	0.0497 (fix)	0.0497
051117	-	-	2.17±0.13	0.0185 (fix)	-	-	0.0185
051117B	$1.80^{+0.61}_{-0.57}$	$0.474^{+0.419}_{-0.361}$	-	-	-	-	0.0459
051210	1.52±0.17	$0.154^{+0.089}_{-0.078}$	-	-	-	-	0.0220
051221	1.99±0.17	0.123±0.054	1.82±0.25	0.0671 (fix)	2.10±0.22	0.141±0.069	0.0671
051221B	-	-	-	-	-	-	0.507
051227	1.70±0.21	0.297±0.100	-	-	$2.62^{+0.79}_{-0.68}$	$0.258^{+0.241}_{-0.208}$	0.0442
060105	2.09±0.02	0.393±0.079	1.96±0.12	0.362±0.060	2.13±0.13	0.174 (fix)	0.174
060108	-	-	1.84±0.27	0.0173 (fix)	2.15±0.26	$0.137^{+0.076}_{-0.069}$	0.0173
060109	2.04±0.13	0.173±0.047	1.96±0.18	0.237±0.079	2.45±0.21	$0.371^{+0.085}_{-0.078}$	0.113
060111	-	-	-	-	2.33±0.15	0.184±0.048	0.0402
060111B	2.27±0.24	0.156±0.069	2.09±0.28	$0.237^{+0.100}_{-0.088}$	2.18±0.23	$0.253^{+0.100}_{-0.087}$	0.0701
060115	1.84±0.09	0.160±0.032	-	-	-	-	0.0118
060116	-	-	2.07±0.19	0.930±0.170	-	-	0.221
060124	-	-	-	-	2.11±0.07	0.181±0.022	0.0926
060202	2.48±0.04	0.593±0.019	3.61±0.22	0.570±0.070	-	-	0.0480
060203	-	-	$2.16^{+0.30}_{-0.27}$	$0.163^{+0.092}_{-0.084}$	2.06±0.13	0.064 (fix)	0.064
060204B	1.87±0.31	$0.101^{+0.094}_{-0.083}$	2.24±0.18	0.135±0.057	2.35±0.21	0.139±0.055	0.0147
060206	-	-	-	-	2.50±0.17	0.0522±0.0385	0.0094
060210	-	-	2.25±0.05	0.173±0.014	2.09±0.10	0.127±0.032	0.0813
060211	1.97±0.07	0.261±0.028	$2.00^{+0.43}_{-0.40}$	0.116 (fix)	-	-	0.116
060211B	-	-	-	-	-	-	0.188
060218	2.58±0.11	0.114 (fix)	-	-	$4.28^{+0.31}_{-0.27}$	$0.535^{+0.068}_{-0.061}$	0.114
060219	-	-	2.26±0.17	0.0239 (fix)	-	-	0.0239
060223	-	-	-	-	-	-	0.0592
060306	1.77±0.26	$0.292^{+0.117}_{-0.110}$	-	-	$2.60^{+0.61}_{-0.55}$	$0.988^{+0.876}_{-0.816}$	0.0341
060312	2.07±0.16	$0.167^{+0.053}_{-0.049}$	2.68±0.049	$0.427^{+0.219}_{-0.182}$	1.69±0.14	0.148 (fix)	0.148
060313	-	-	-	-	2.22±0.14	0.111±0.038	0.0465
060319	-	-	-	-	1.91±0.19	$0.311^{0.095}_{-0.088}$	0.0134
060323	-	-	1.83±0.28	0.0151 (fix)	$2.21^{+0.30}_{-0.27}$	$0.119410^{+0.086}_{-0.077}$	0.0151
060403	-	-	-	-	1.64±0.19	0.833±0.19	0.505
060413	1.91±0.08	2.21±0.12	1.57±0.21	$2.34^{+0.42}_{-0.39}$	1.60±0.26	$2.40^{+0.52}_{-0.46}$	1.24
060418	3.18±0.07	0.421±0.020	-	-	2.07±0.09	0.181±0.028	0.0919
060421	-	-	1.47±0.22	0.998 (fix)	1.34±0.34	0.998 (fix)	0.998
060427	2.94±0.18	0.167±0.039	-	-	-	-	0.0424

060428	3.39±0.20	0.894 (fix)	1.78±0.10	0.894 (fix)	2.11±0.08	0.894 (fix)	0.894
060428B	3.11±0.15	0.131±0.028	2.12±0.12	0.0171 (fix)	$1.92^{0.44}_{-0.41}$	0.0171 (fix)	0.0171
060502	$2.99^{+0.29}_{-0.34}$	$0.544^{+0.204}_{-0.183}$	1.94±0.14	0.0729±0.043	1.84±0.16	0.0294 (fix)	0.0294
060507	-	-	1.85±0.13	0.0873 (fix)	2.18±0.19	$0.184^{+0.066}_{-0.060}$	0.0873
060510	-	-	1.88±0.04	0.392 (fix)	1.92±0.05	0.392 (fix)	0.392
060510B	2.15±0.09	0.192±0.029	-	-	2.21±0.41	0.0386 (fix)	0.0386
060512	-	-	-	-	2.26±0.27	0.162±0.079	0.0142
060515	-	-	-	-	-	-	0.0240
060522	-	-	-	-	-	-	0.0476
060526	-	-	2.35±0.18	0.170±0.057	1.63±0.29	0.0539 (fix)	0.0539
060602B	-	-	-	-	-	-	1.49
060604	-	-	2.06±0.10	0.0449 (fix)	1.97±0.08	0.0449 (fix)	0.0449
060605	-	-	2.08±0.07	0.0508 (fix)	2.14±0.07	0.0508 (fix)	0.0508
060607	-	-	1.77±0.06	0.0261 (fix)	1.80±0.09	0.102±0.030	0.0261
060614	-	-	2.01±0.09	0.0856±0.0270	1.59±0.08	0.0308 (fix)	0.0308
060707	-	-	-	-	-	-	-
060708	3.63±0.18	0.209±0.030	2.06±0.09	0.0147 (fix)	2.02±0.07	0.0147 (fix)	0.0147
060712	-	-	-	-	-	-	-
060714	2.91±0.18	0.132±0.041	-	-	2.33±0.25	0.165±0.078	0.0672
060719	2.87±0.22	0.175±0.050	2.89±0.30	0.486±0.140	2.45±0.21	0.339±0.077	0.0180
060729	2.88±0.03	0.222±0.007	2.21±0.09	0.152±0.028	2.22±0.05	0.155±0.016	0.0474
060801	-	-	-	-	-	-	-
060804	-	-	-	-	2.32±0.12	0.552 (fix)	0.552
060805	-	-	$4.24^{+1.41}_{-1.11}$	0.441±0.34	2.21±0.20	0.0156 (fix)	0.0156
060807	-	-	2.14±0.20	0.148±0.063	2.12±0.09	0.134±0.026	0.0237
060813	-	-	1.99±0.05	0.448±0.029	2.15±0.08	0.424±0.043	0.316
060814	1.53±0.02	0.368±0.015	2.39±0.11	0.412±0.048	2.38±0.08	0.350±0.031	0.0235
060825	-	-	-	-	1.34±0.17	0.302 (fix)	0.302
060904	1.79±0.03	0.211±0.012	2.37±0.19	0.162±0.062	-	-	0.0139
060904B	-	-	-	-	2.27±0.12	0.262±0.044	0.130
060906	2.59±0.52	0.288±0.195	2.29±0.24	0.240±0.073	1.99±0.29	0.229±0.097	0.0984
060908	-	-	2.36±0.20	$0.079^{+0.051}_{-0.047}$	$2.68^{+0.61}_{-0.52}$	$0.171^{+0.152}_{-0.127}$	0.0237
060912	-	-	-	-	2.00±0.17	$0.124^{+0.071}_{-0.065}$	0.0429
060919	-	-	-	-	1.45±0.37	$0.406^{+0.324}_{-0.286}$	0.0663
060923A	1.97±0.24	$0.145^{+0.077}_{-0.069}$	-	-	2.19±0.29	$0.153^{+0.096}_{-0.086}$	0.0470
060923B	-	-	-	-	$2.04^{+0.54}_{-0.48}$	0.0889 (fix)	0.0889
060923C	1.82±0.09	0.0525 (fix)	$3.08^{+0.43}_{-0.39}$	$0.285^{+0.123}_{-0.106}$	-	-	0.525
060926	2.01±0.56	0.25 (fix)	2.18±0.24	$0.260^{+0.094}_{-0.084}$	2.15±0.26	$0.242^{+0.098}_{-0.086}$	0.25
060927	-	-	-	-	2.09±0.16	0.0529 (fix)	0.0529
060929	-	-	-	-	1.79±0.39	0.0364 (fix)	0.0364

Table E.1: Spectral Parameters of X-ray light curves.

Appendix F

Hardness Ratios for X-ray Afterglows

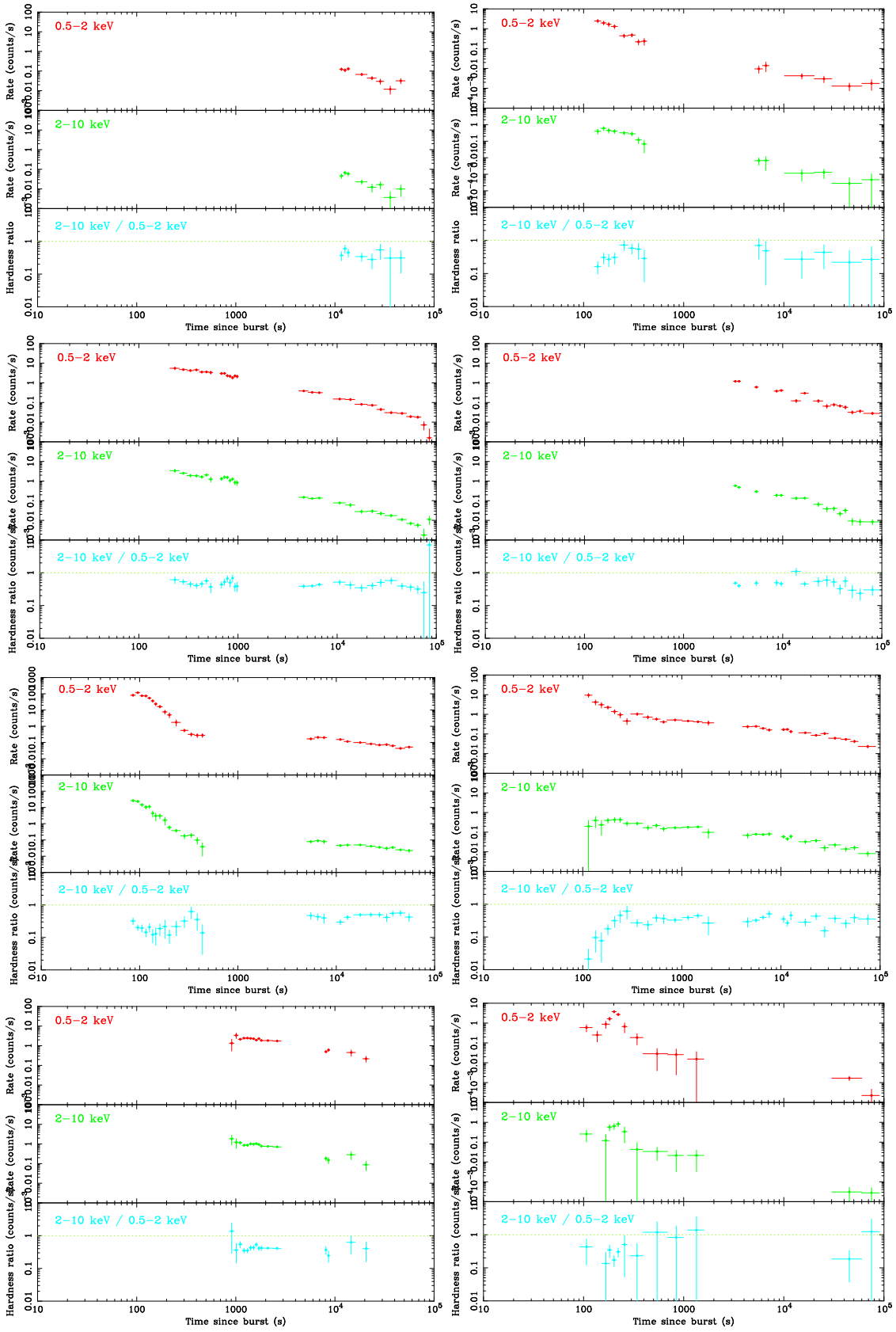

Figure F.1: Light curve in soft band (S = 0.5-2 keV; *top*) and hard band (H =2-10 keV; *center*). The bottom panel shows the band ratios (H/S); GRB 050124, 050126, 050128, 050219B, 050315, 050319, 050401, 050406

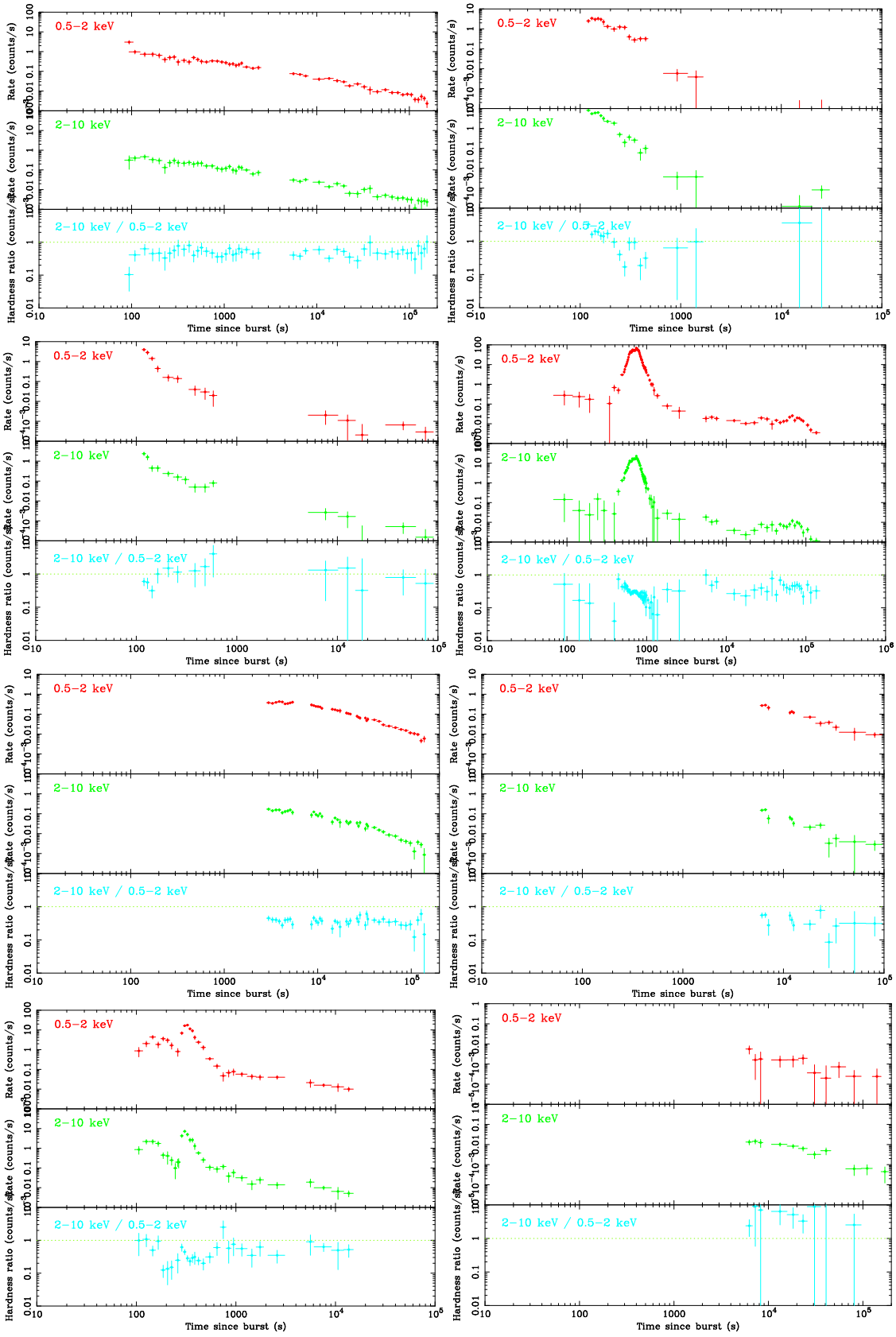

Figure F.2: Light curve in soft band (S = 0.5-2 keV; *top*) and hard band (H =2-10 keV; *center*). The bottom panel shows the band ratios (H/S);GRB 050416A, 050421, 050422, 050502B, 050505, 050525, 050607, 050701

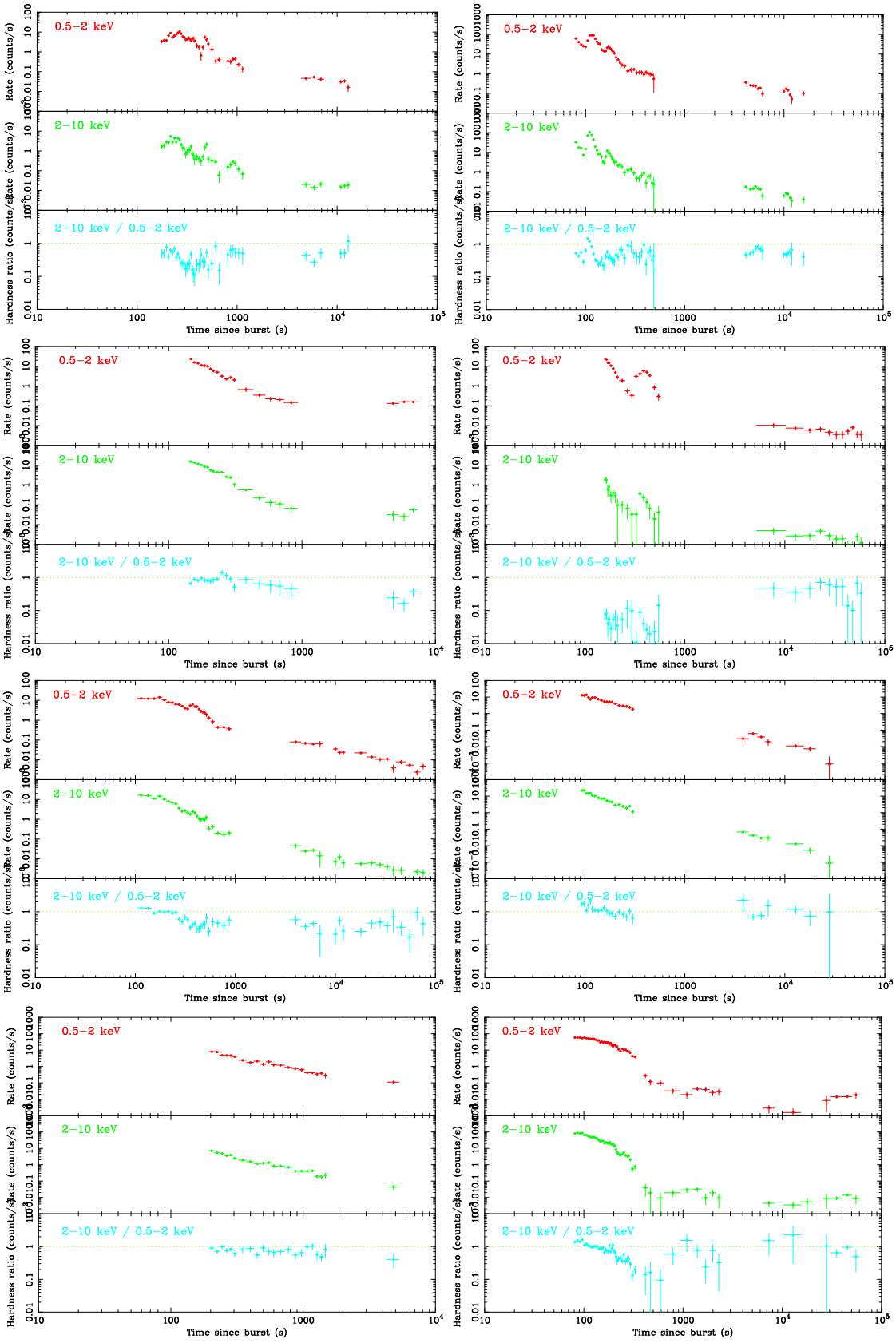

Figure F.3: Light curve in soft band (S = 0.5-2 keV; *top*) and hard band (H =2-10 keV; *center*). The bottom panel shows the band ratios (H/S);GRB 050712, 050713A, 050713B, 050714B, 050716, 050717, 050721, 050724

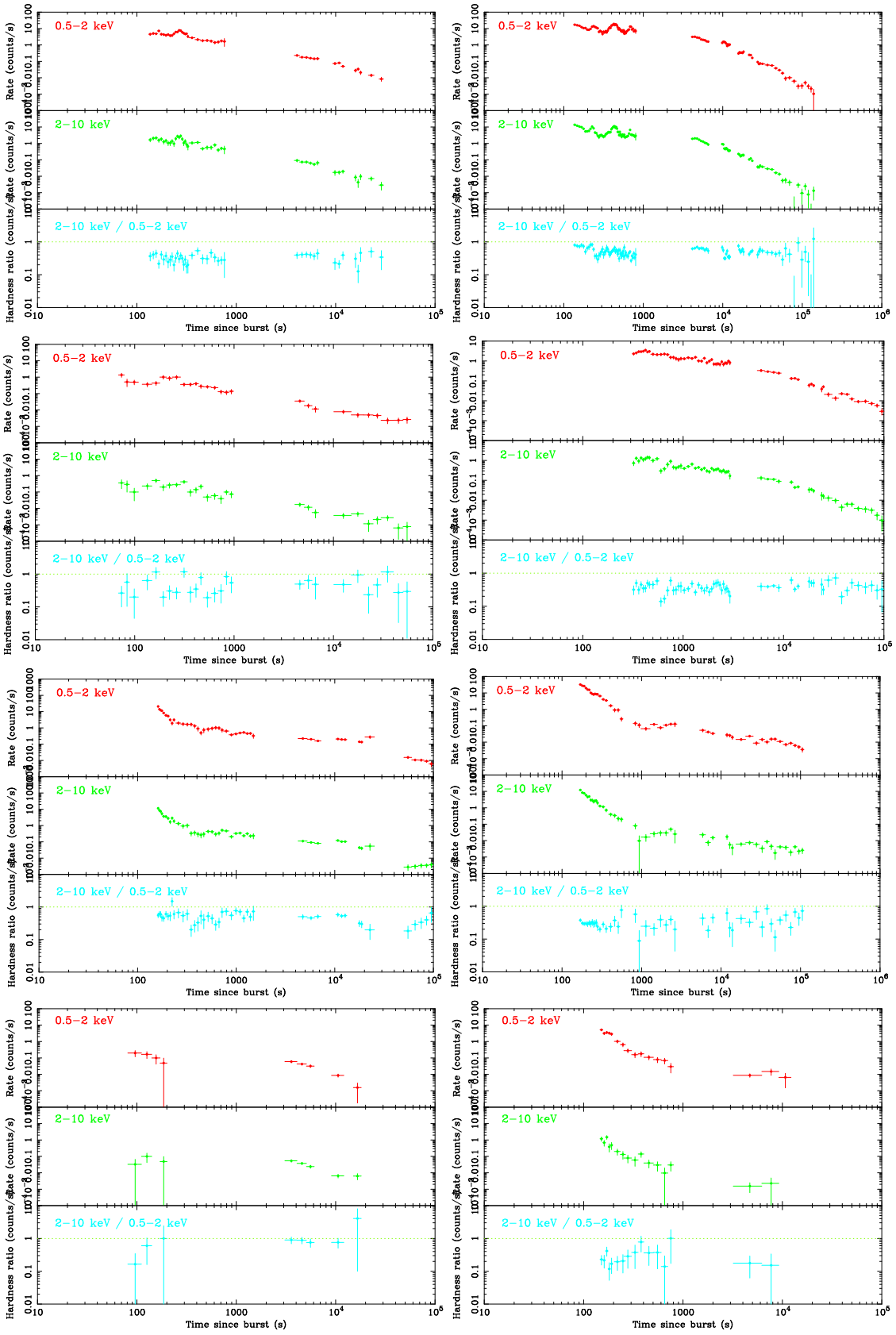

Figure F.4: Light curve in soft band (S = 0.5-2 keV; *top*) and hard band (H =2-10 keV; *center*). The bottom panel shows the band ratios (H/S);GRB 050726, 050730, 050801, 050802, 050803, 050814, 050815, 050819

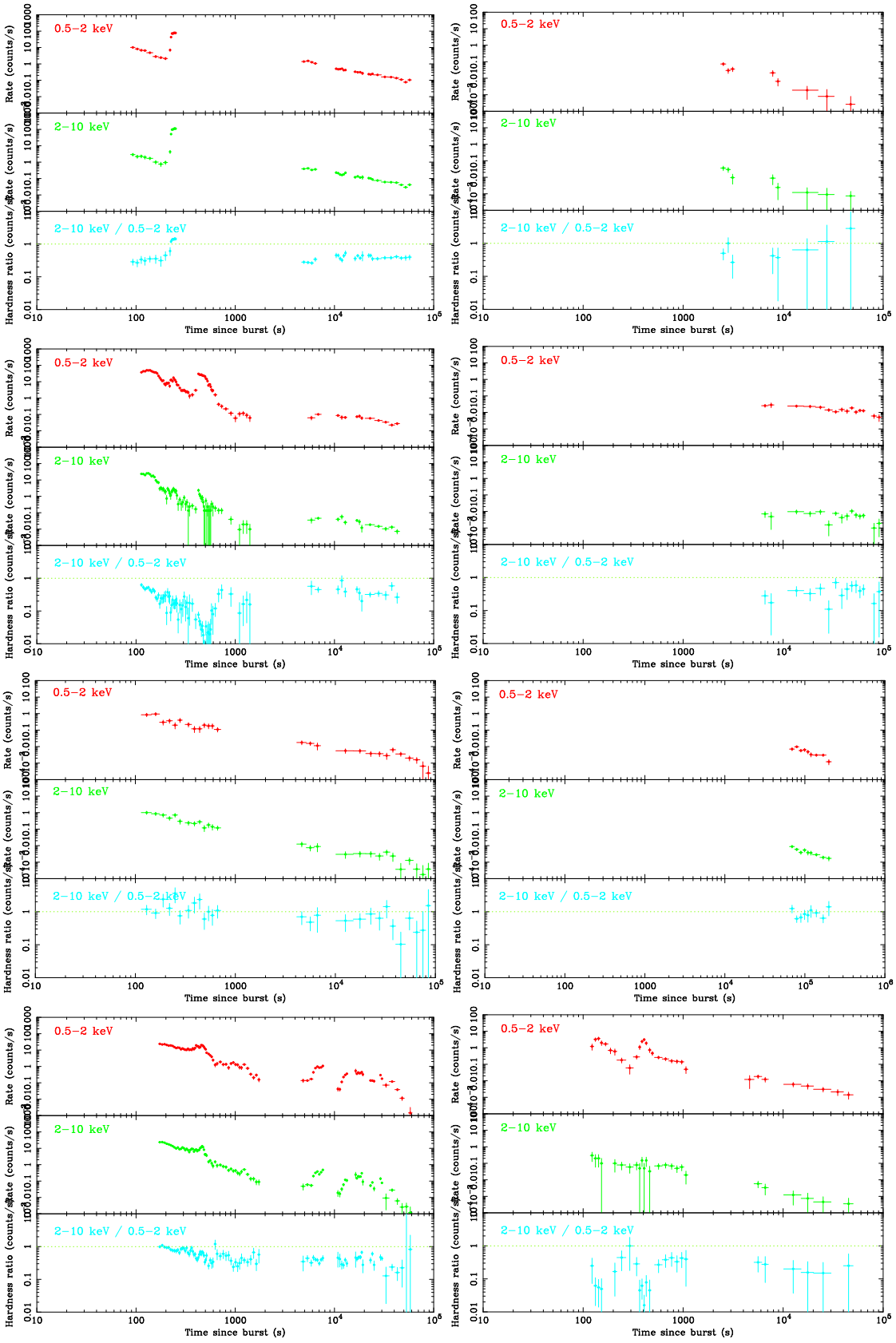

Figure F.5: Light curve in soft band (S = 0.5-2 keV; *top*) and hard band (H =2-10 keV; *center*). The bottom panel shows the band ratios (H/S);GRB 050820A, 050820B, 050822, 050824, 050826, 050827, 050904, 050908

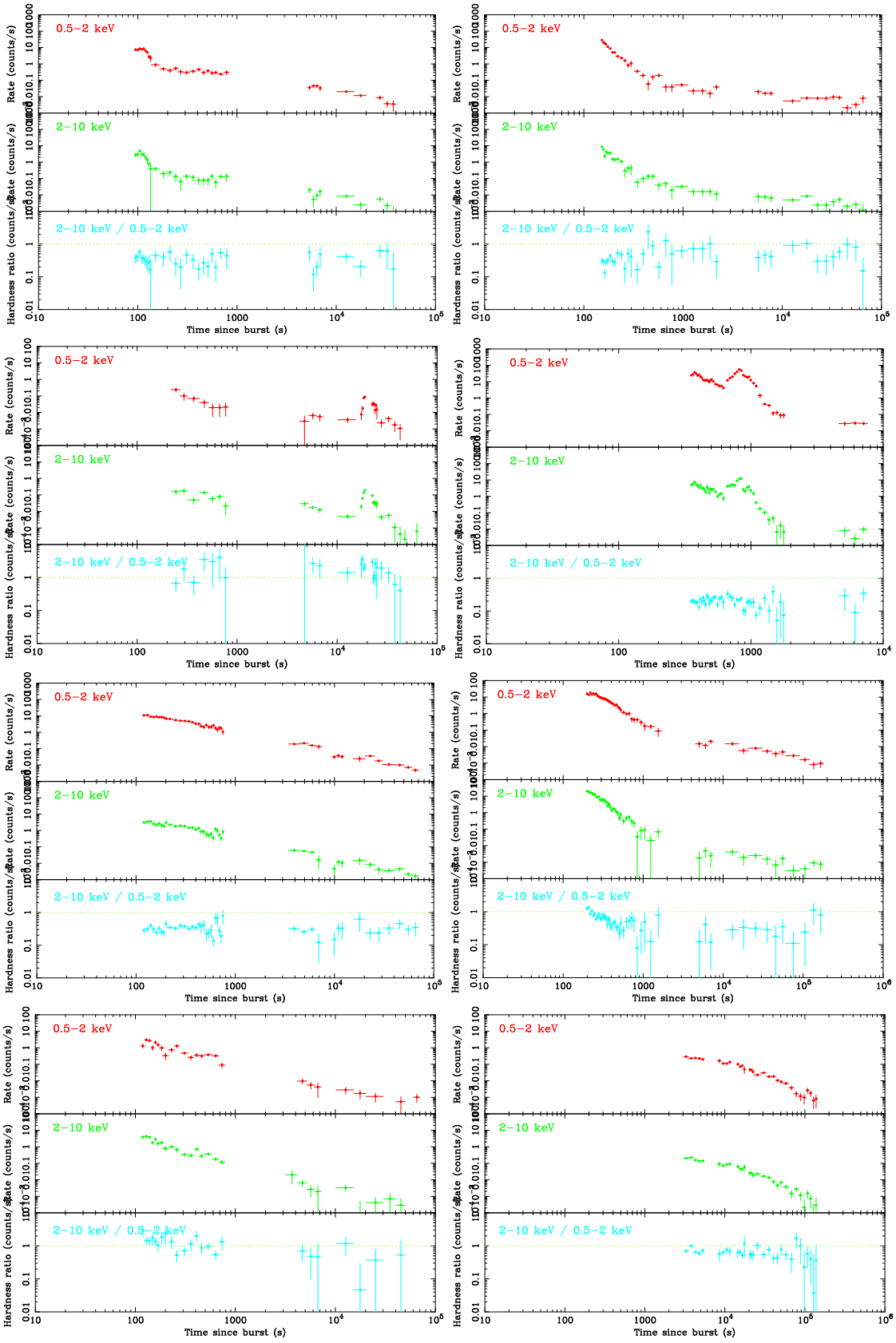

Figure F.6: Light curve in soft band (S = 0.5-2 keV; *top*) and hard band (H =2-10 keV; *center*). The bottom panel shows the band ratios (H/S);GRB 050915A, 050915B, 050916, 050922B, 050922C, 051001, 051006, 051008

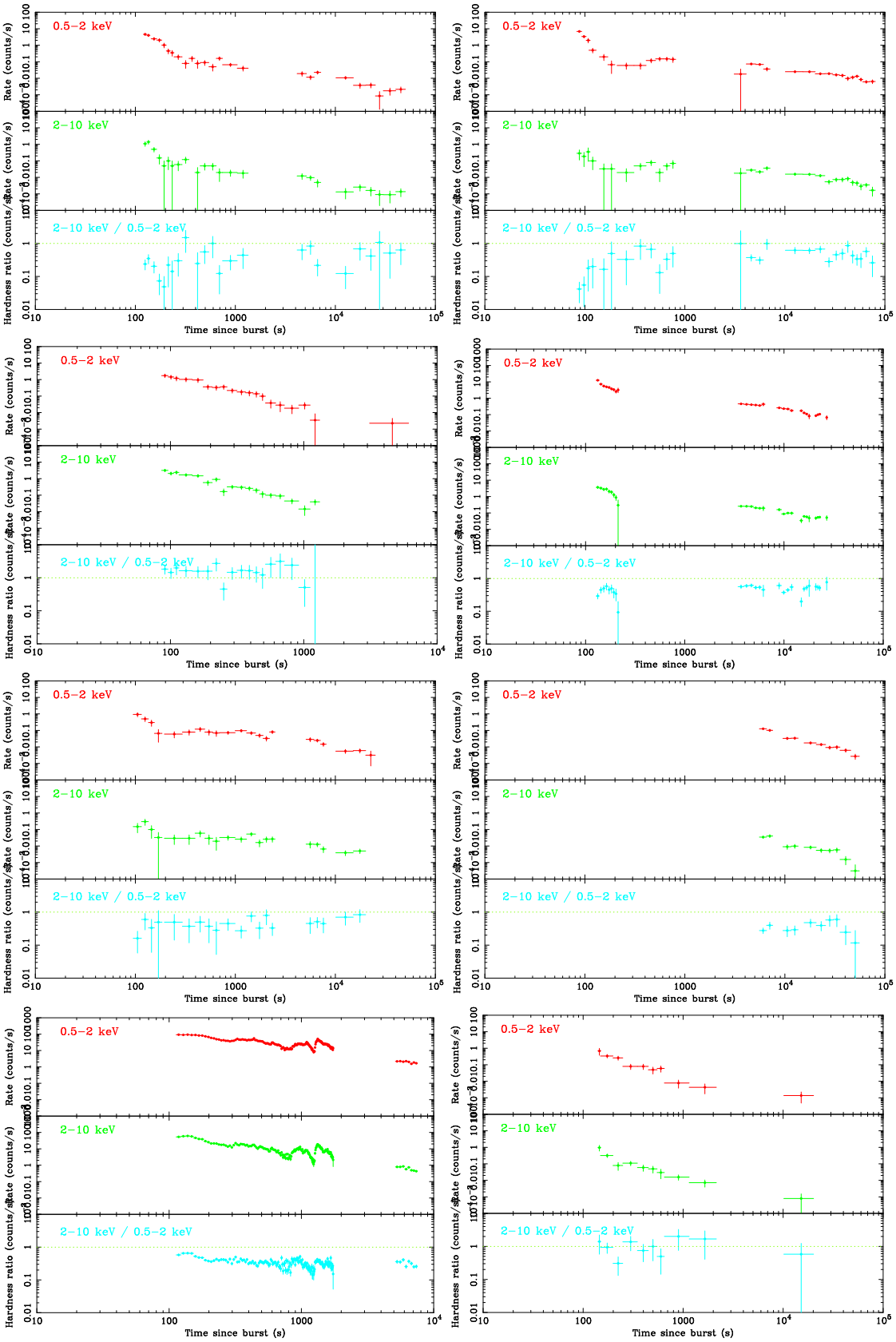

Figure F.7: Light curve in soft band (S = 0.5-2 keV; *top*) and hard band (H =2-10 keV; *center*). The bottom panel shows the band ratios (H/S);GRB 051016A, 051016B, 051021B, 051109A, 051109B, 051111, 051117A, 051117B

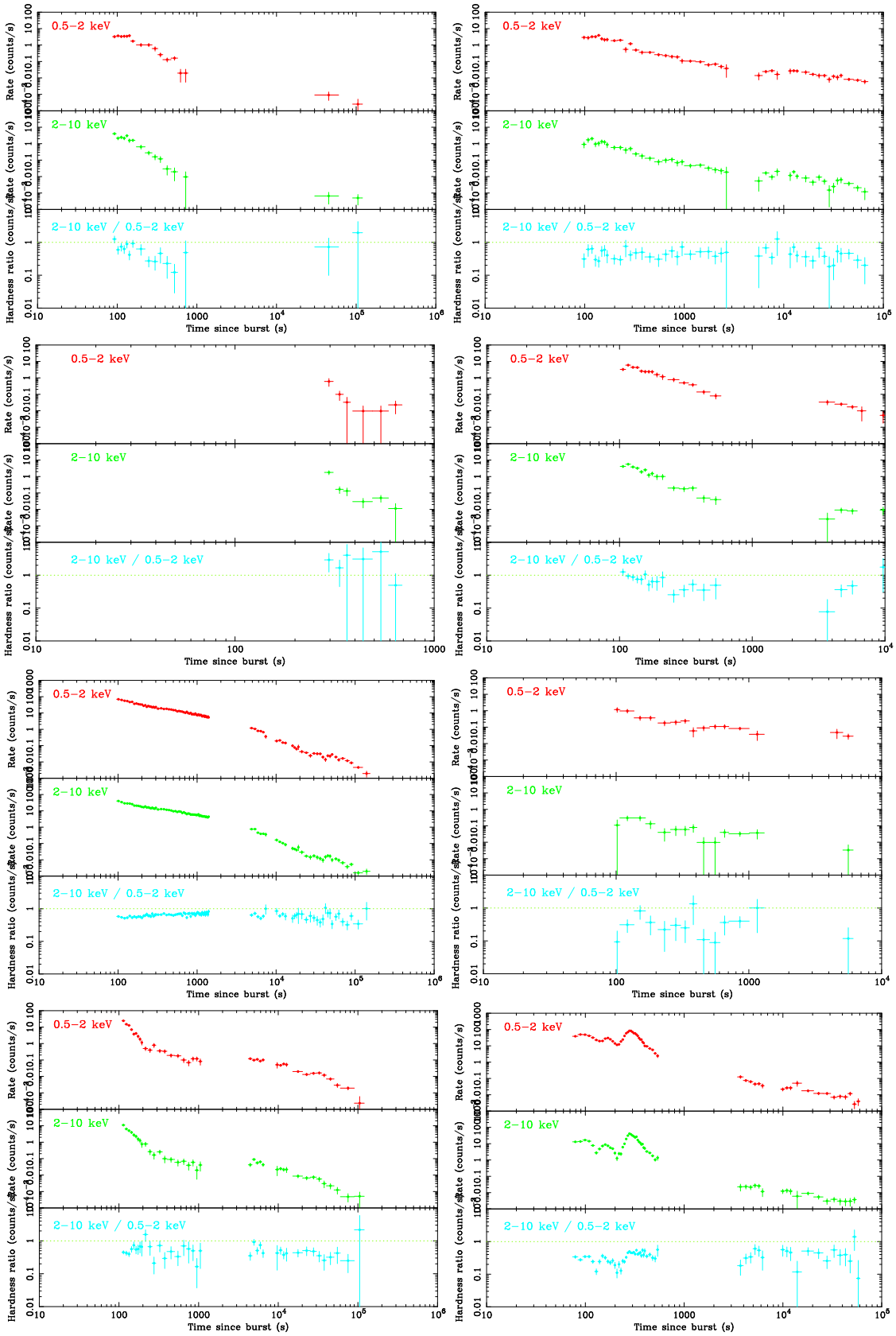

Figure F.8: Light curve in soft band (S = 0.5-2 keV; *top*) and hard band (H =2-10 keV; *center*). The bottom panel shows the band ratios (H/S);GRB 051210, 051221A, 051221B, 051227, 060105, 060108, 060109, 060111A

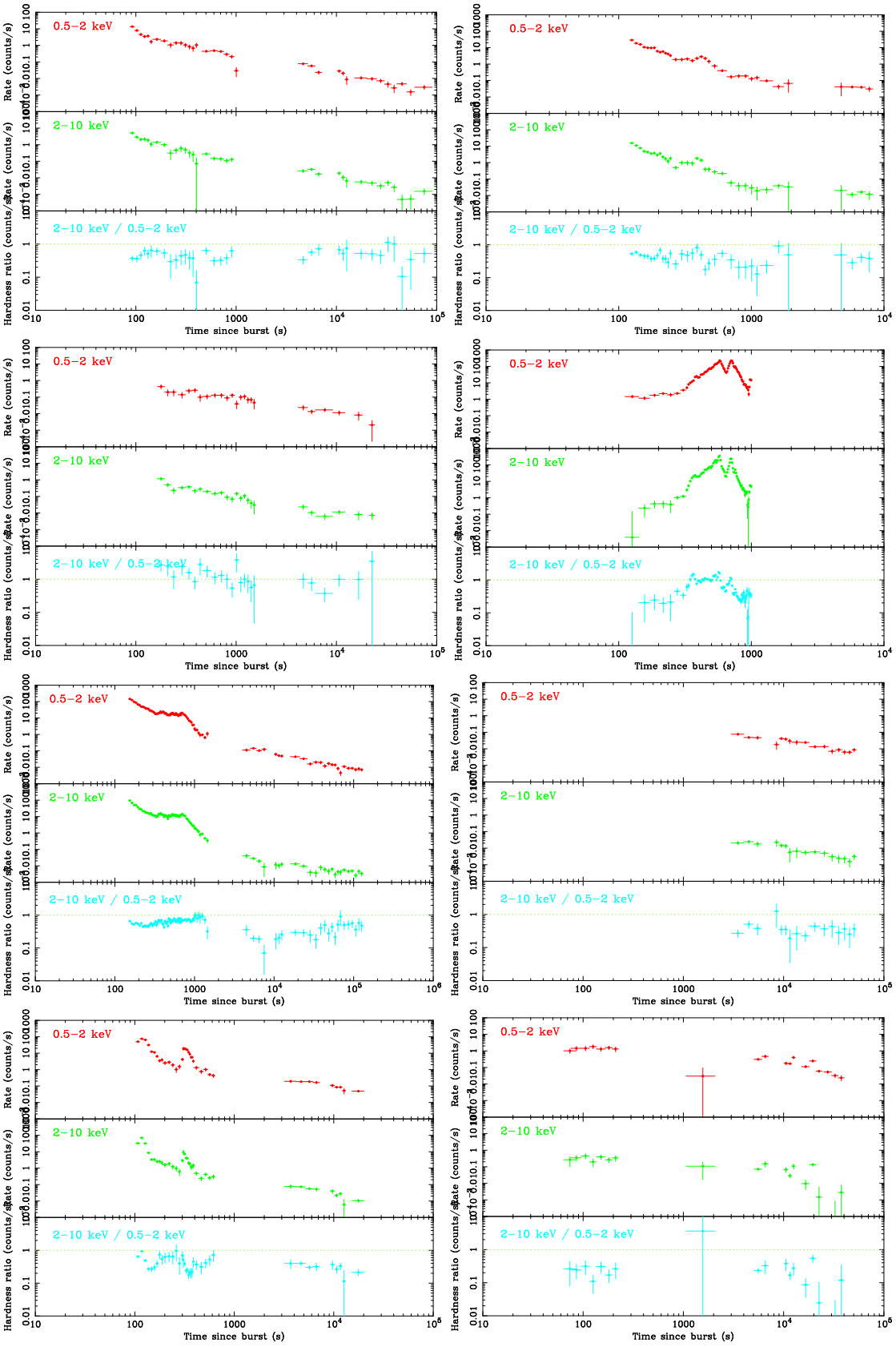

Figure F.9: Light curve in soft band (S = 0.5-2 keV; *top*) and hard band (H =2-10 keV; *center*). The bottom panel shows the band ratios (H/S);GRB 060111B, 060115, 060116, 060124, 060202, 060203, 060204B, 060206

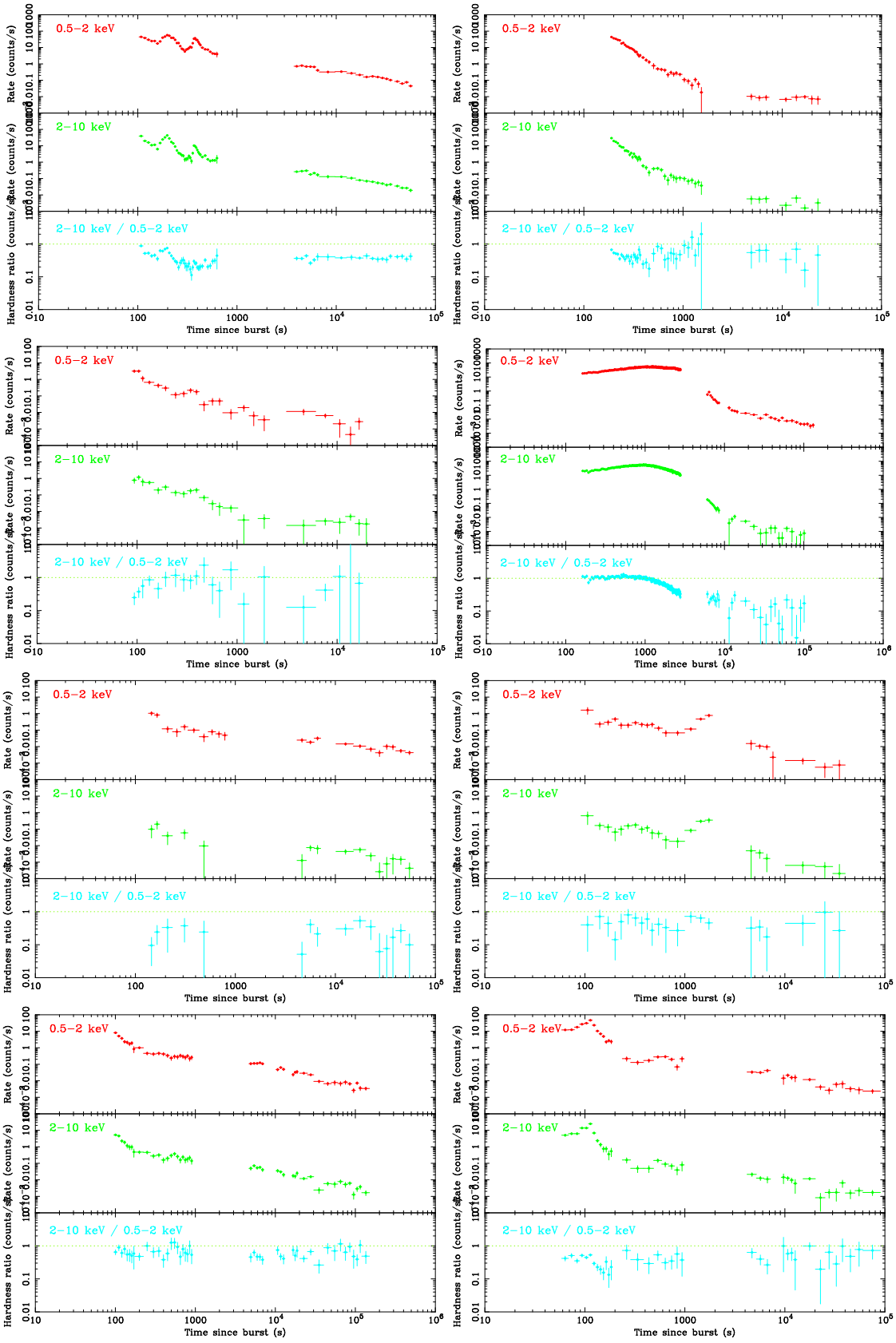

Figure F.10: Light curve in soft band (S = 0.5-2 keV; *top*) and hard band (H =2-10 keV; *center*). The bottom panel shows the band ratios (H/S);GRB 060210, 060211A, 060211B, 060218, 060219, 060223A, 060306, 060312

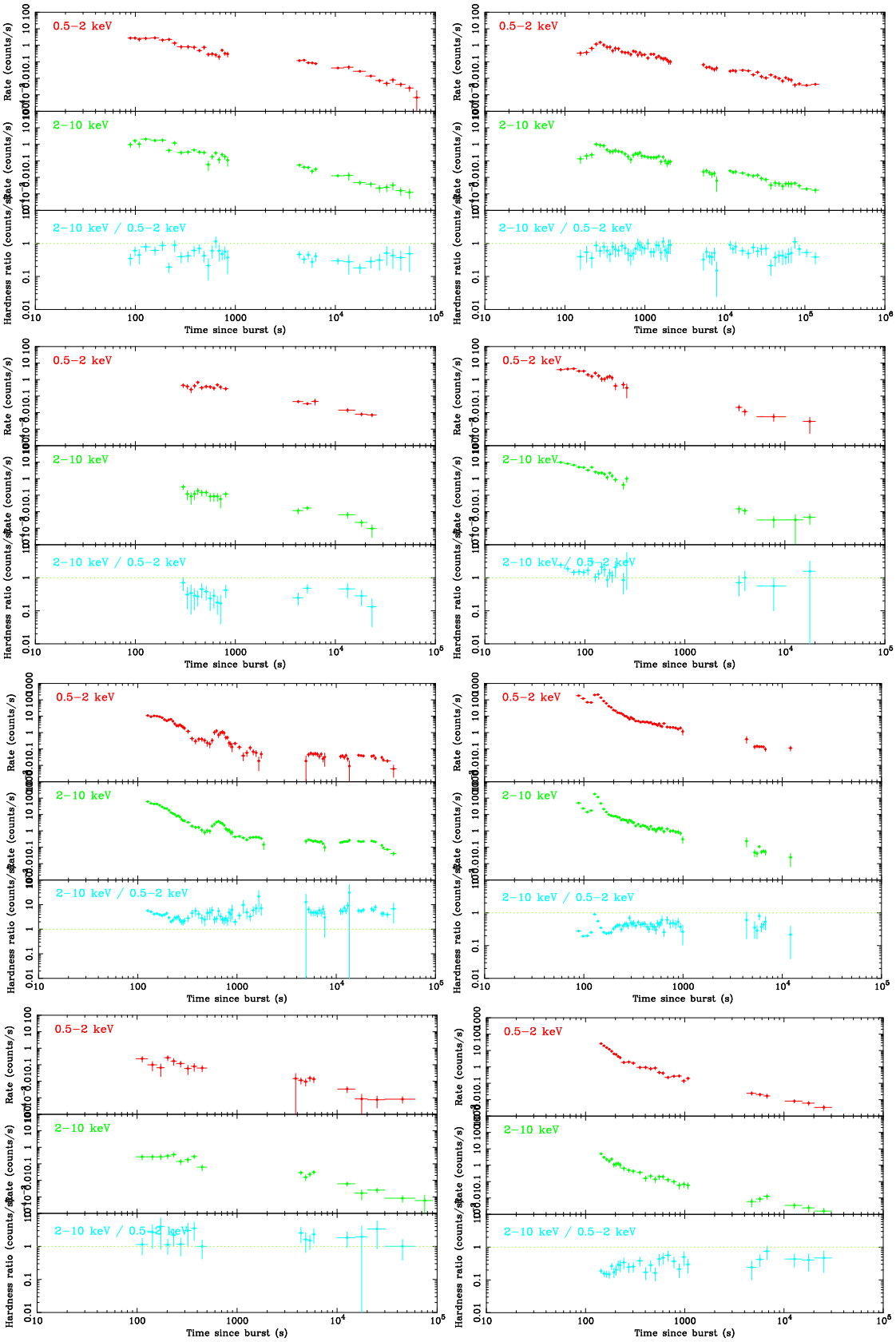

Figure F.11: Light curve in soft band (S = 0.5-2 keV; *top*) and hard band (H =2-10 keV; *center*). The bottom panel shows the band ratios (H/S);GRB 060313, 060319, 060323, 060403, 060413, 060418, 060421, 060427

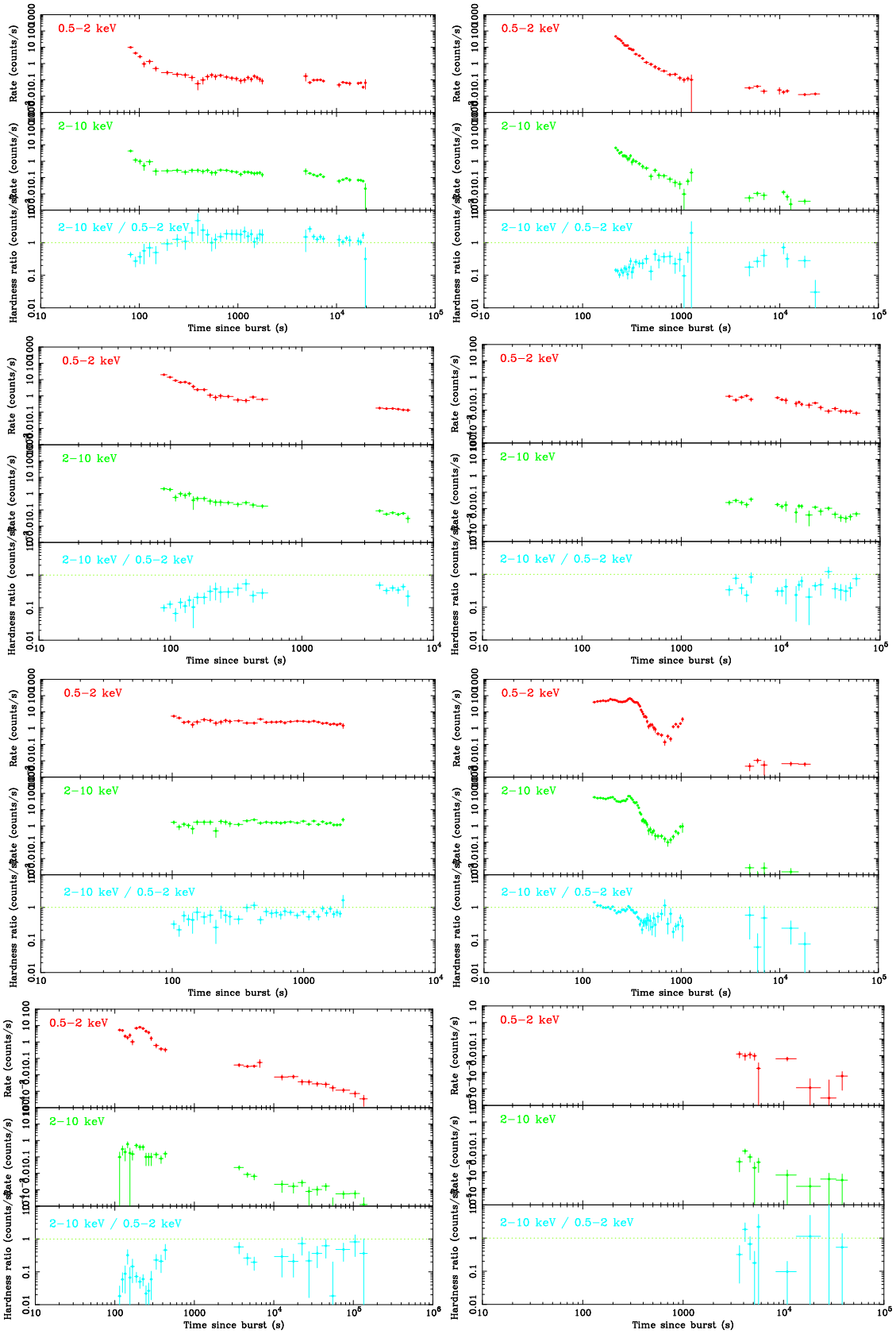

Figure F.12: Light curve in soft band (S = 0.5-2 keV; *top*) and hard band (H =2-10 keV; *center*). The bottom panel shows the band ratios (H/S);GRB 060428A, 060428B, 060502, 060507, 060510A, 060510B, 060512, 060515

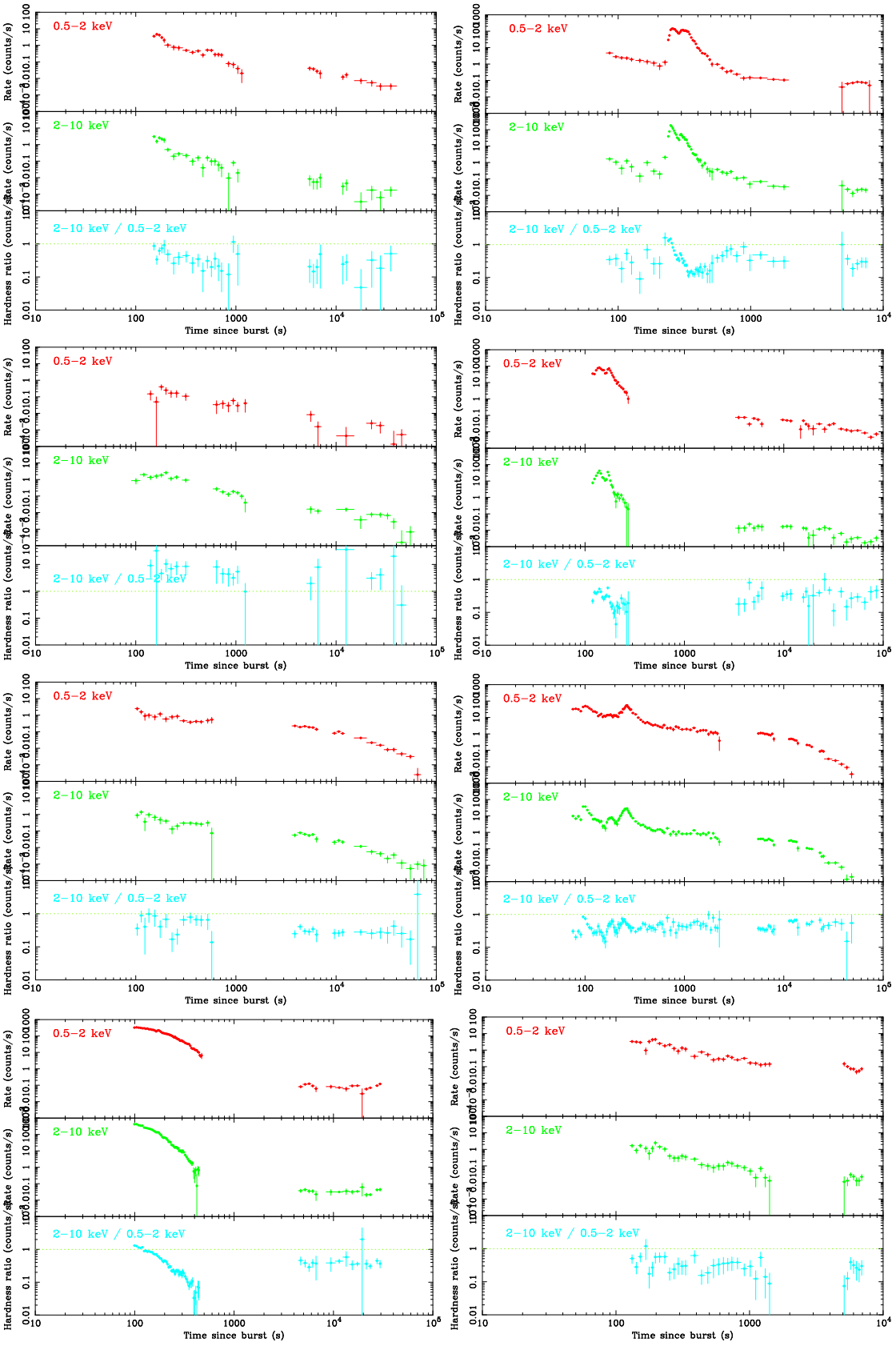

Figure F.13: Light curve in soft band (S = 0.5-2 keV; *top*) and hard band (H =2-10 keV; *center*). The bottom panel shows the band ratios (H/S);GRB 060522, 060526, 060602B, 060604, 060605, 060607, 060614, 060707

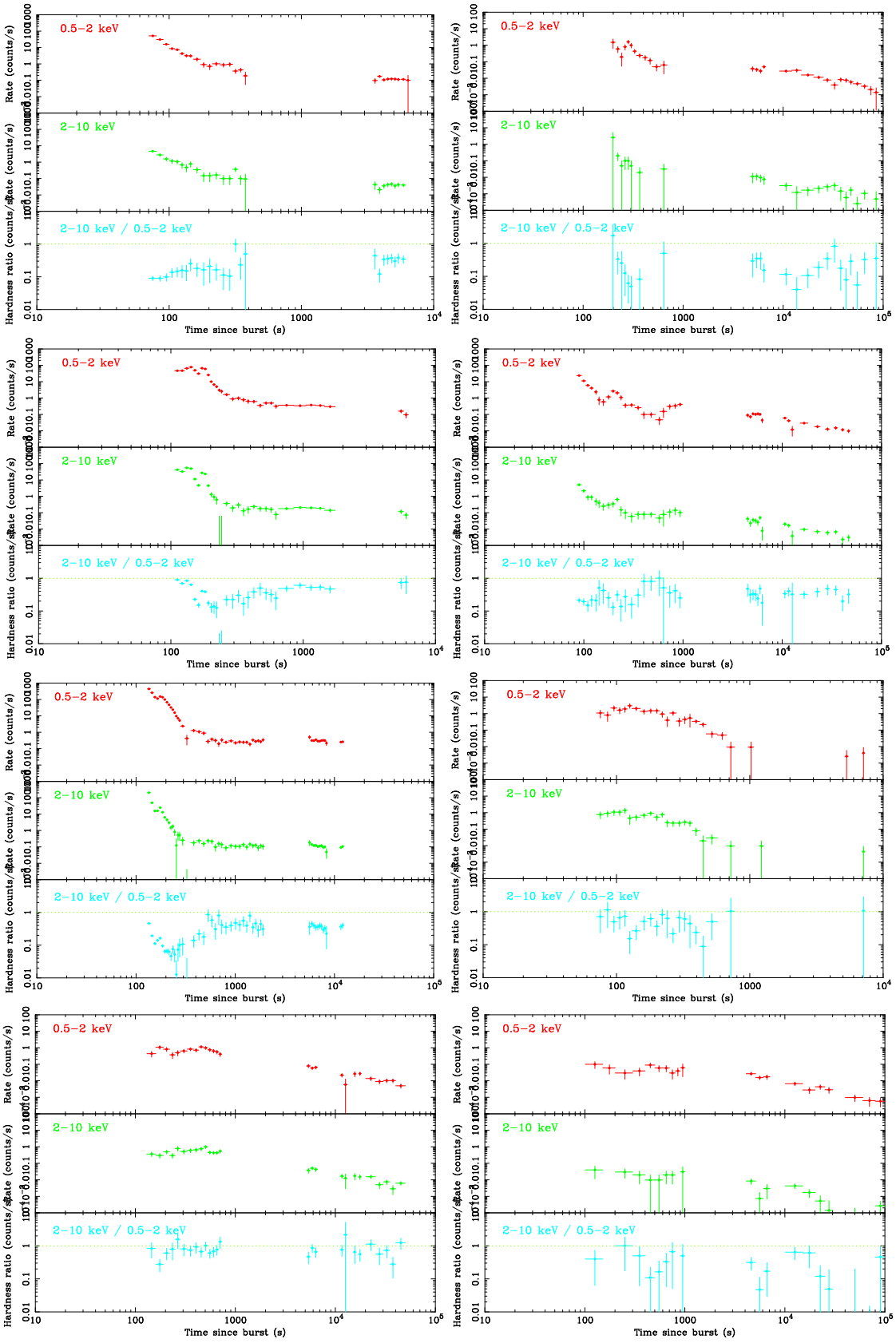

Figure F.14: Light curve in soft band (S = 0.5-2 keV; *top*) and hard band (H =2-10 keV; *center*). The bottom panel shows the band ratios (H/S);GRB 060708, 060712, 060714, 060719, 060729, 060801, 060804, 060805

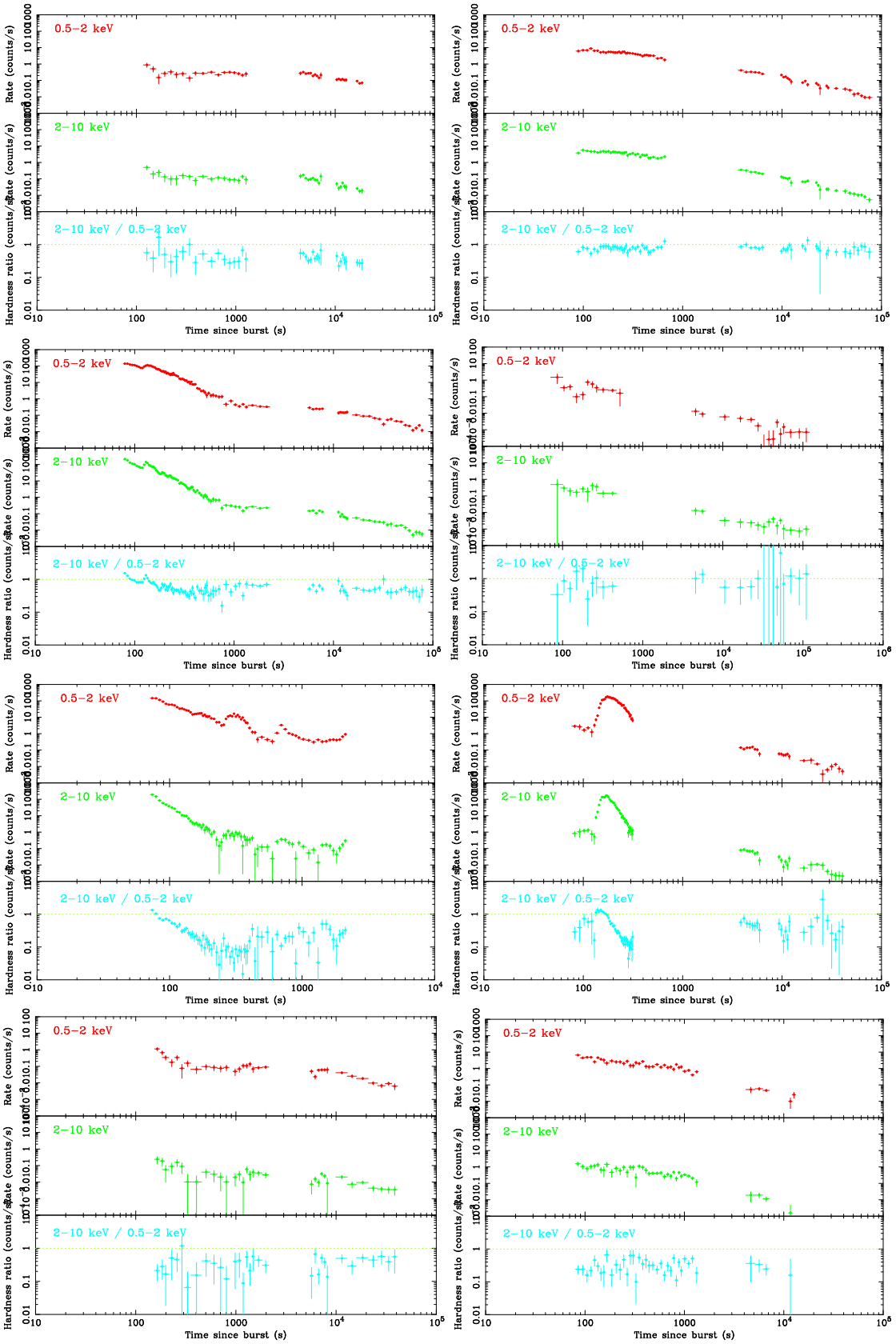

Figure F.15: Light curve in soft band (S = 0.5-2 keV; *top*) and hard band (H =2-10 keV; *center*). The bottom panel shows the band ratios (H/S);GRB 060807, 060813, 060814, 060825, 060904A, 060904B, 060906, 060908

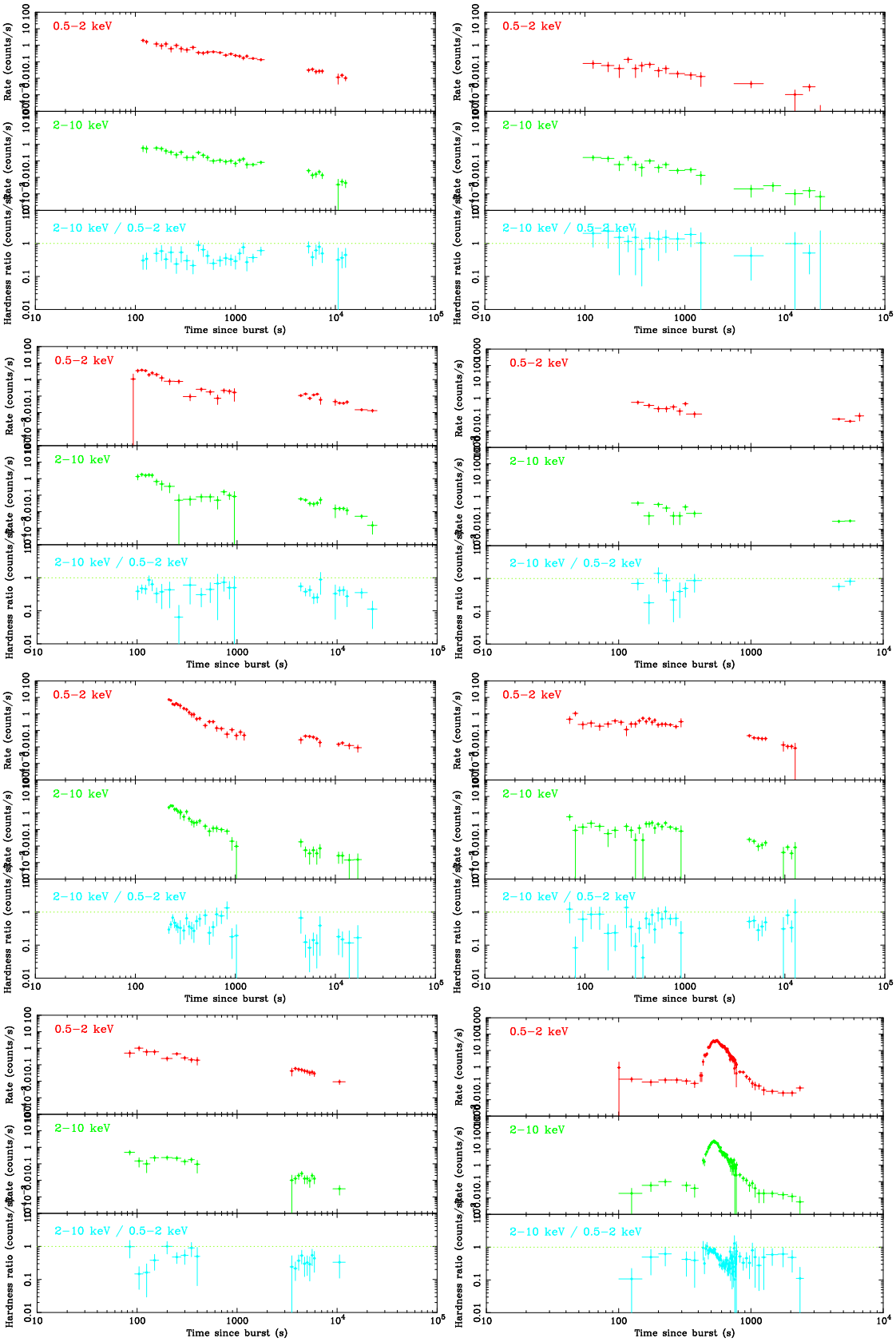

Figure F.16: Light curve in soft band (S = 0.5-2 keV; *top*) and hard band (H =2-10 keV; *center*). The bottom panel shows the band ratios (H/S);GRB 060912, 060919, 060923A, 060923B, 060923C, 060926, 060927, 060929

Appendix G

Spectral Evolution of X-ray Flares

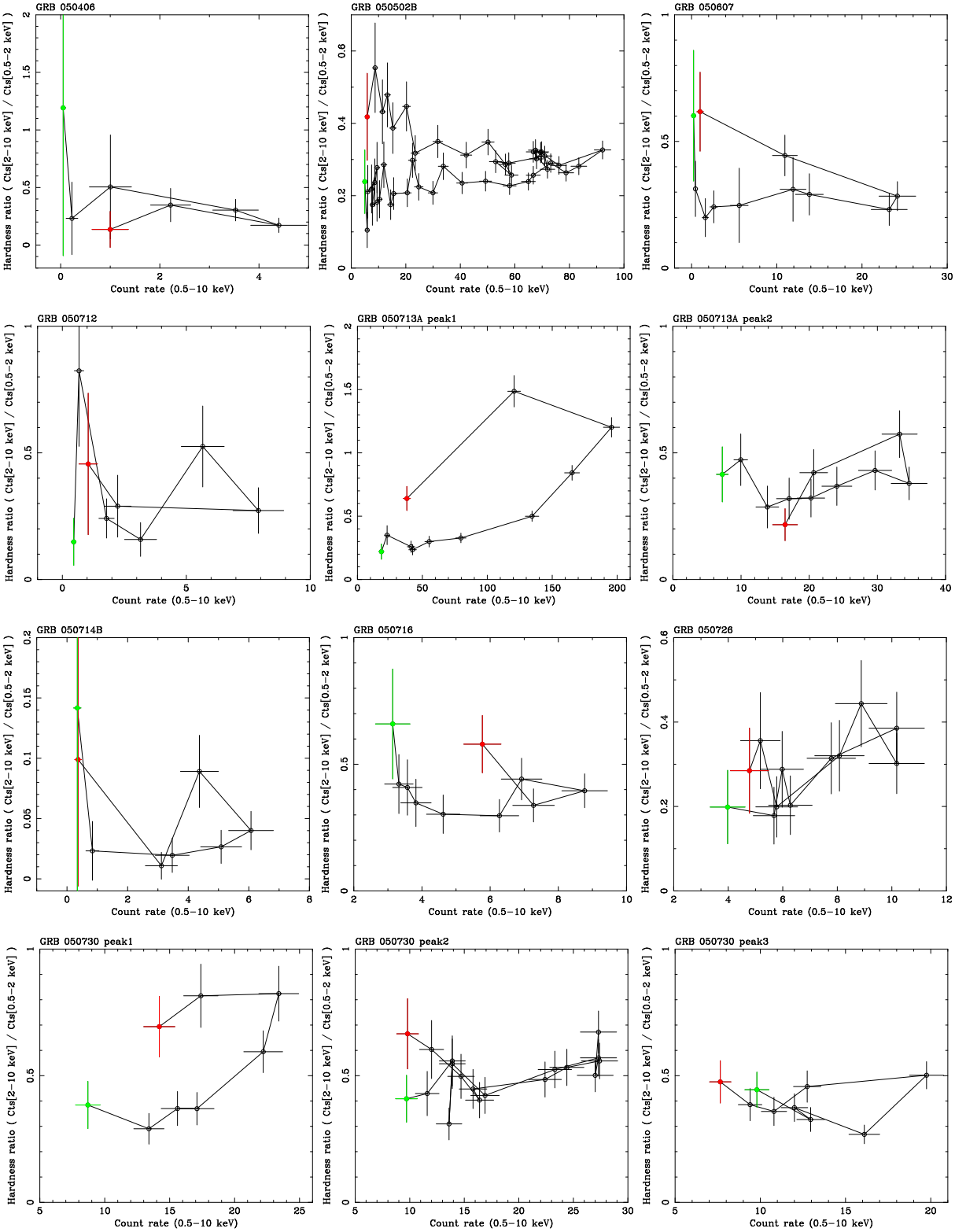

Figure G.1: Count rate (0.5-10 keV) versus hardness ratio of X-ray flares. The filled circle represents the start point of the X-ray flare.

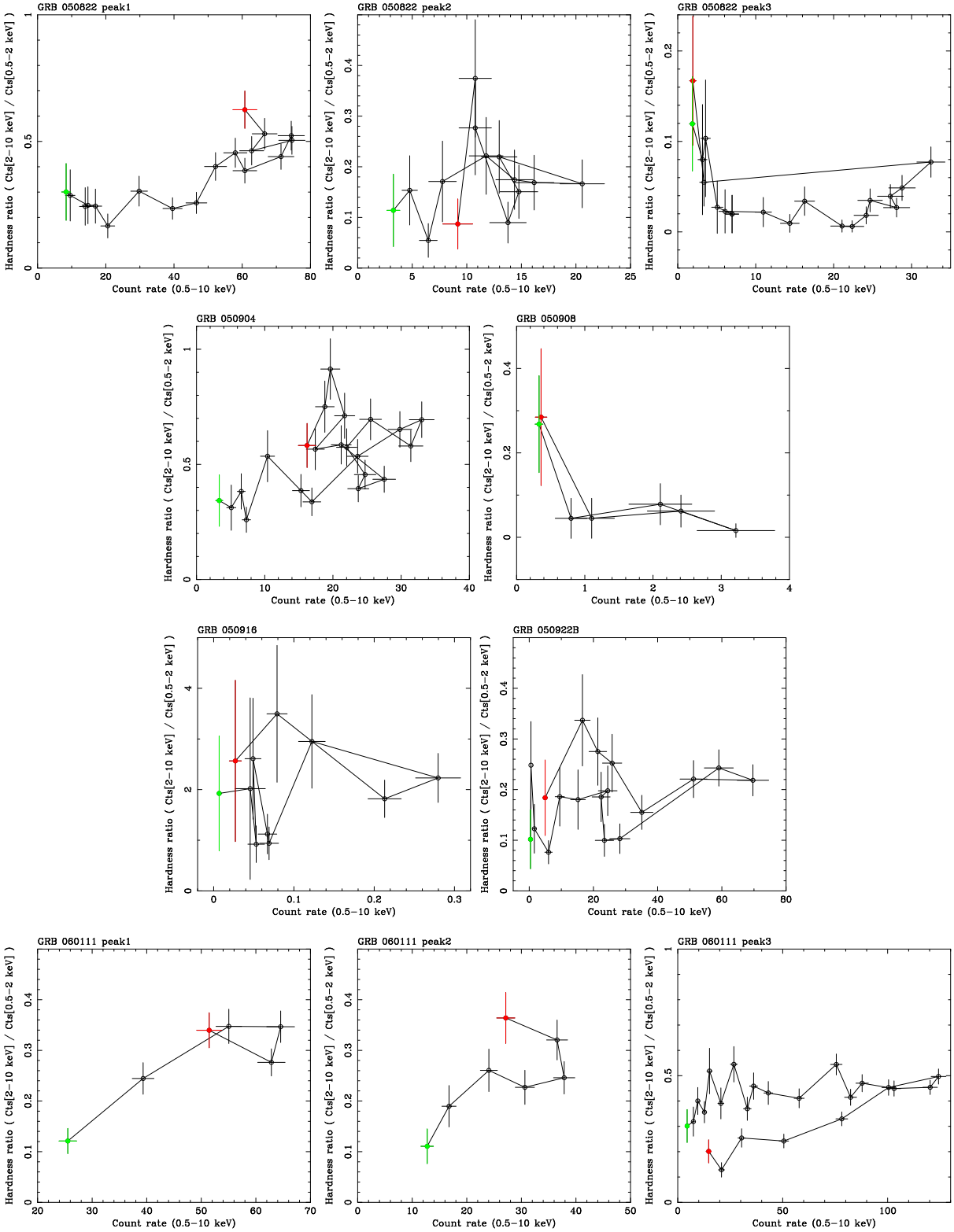

Figure G.2: Count rate (0.5-10 keV) versus hardness ratio of X-ray flares The filled circle represents the start point of the X-ray flare.

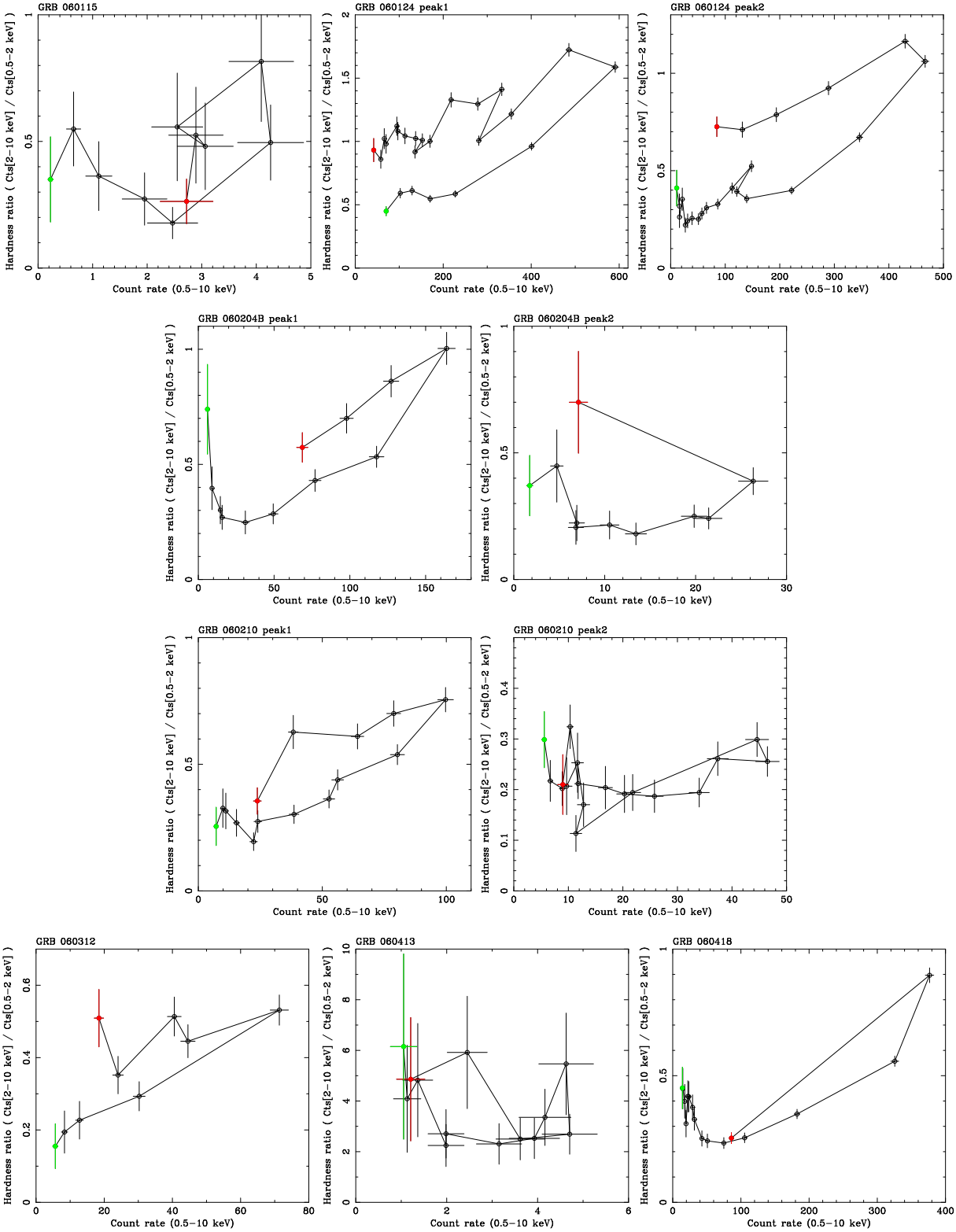

Figure G.3: Count rate (0.5-10 keV) versus hardness ratio of X-ray flares The filled circle represents the start point of the X-ray flare.

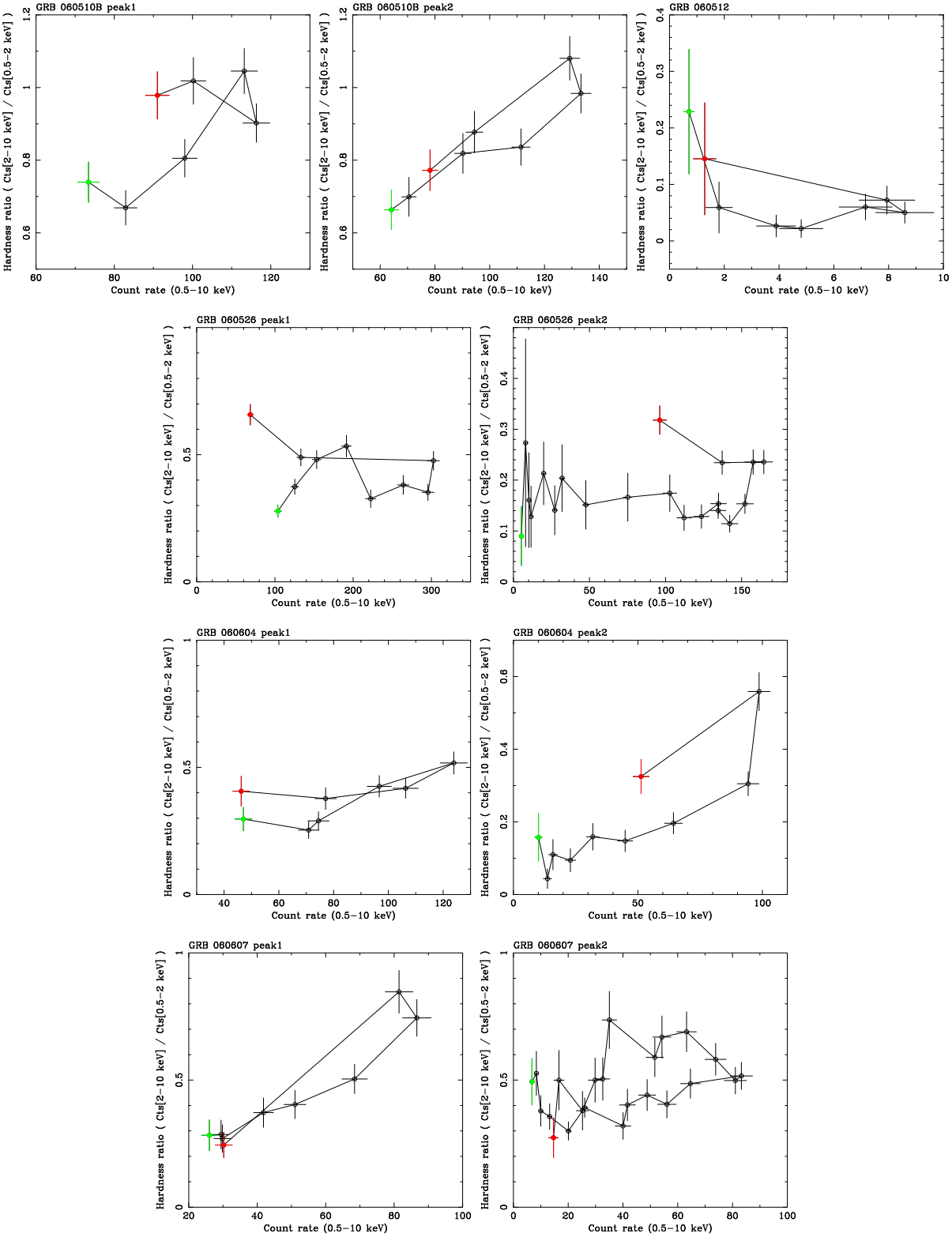

Figure G.4: Count rate (0.5-10 keV) versus hardness ratio of X-ray flares The filled circle represents the start point of the X-ray flare.

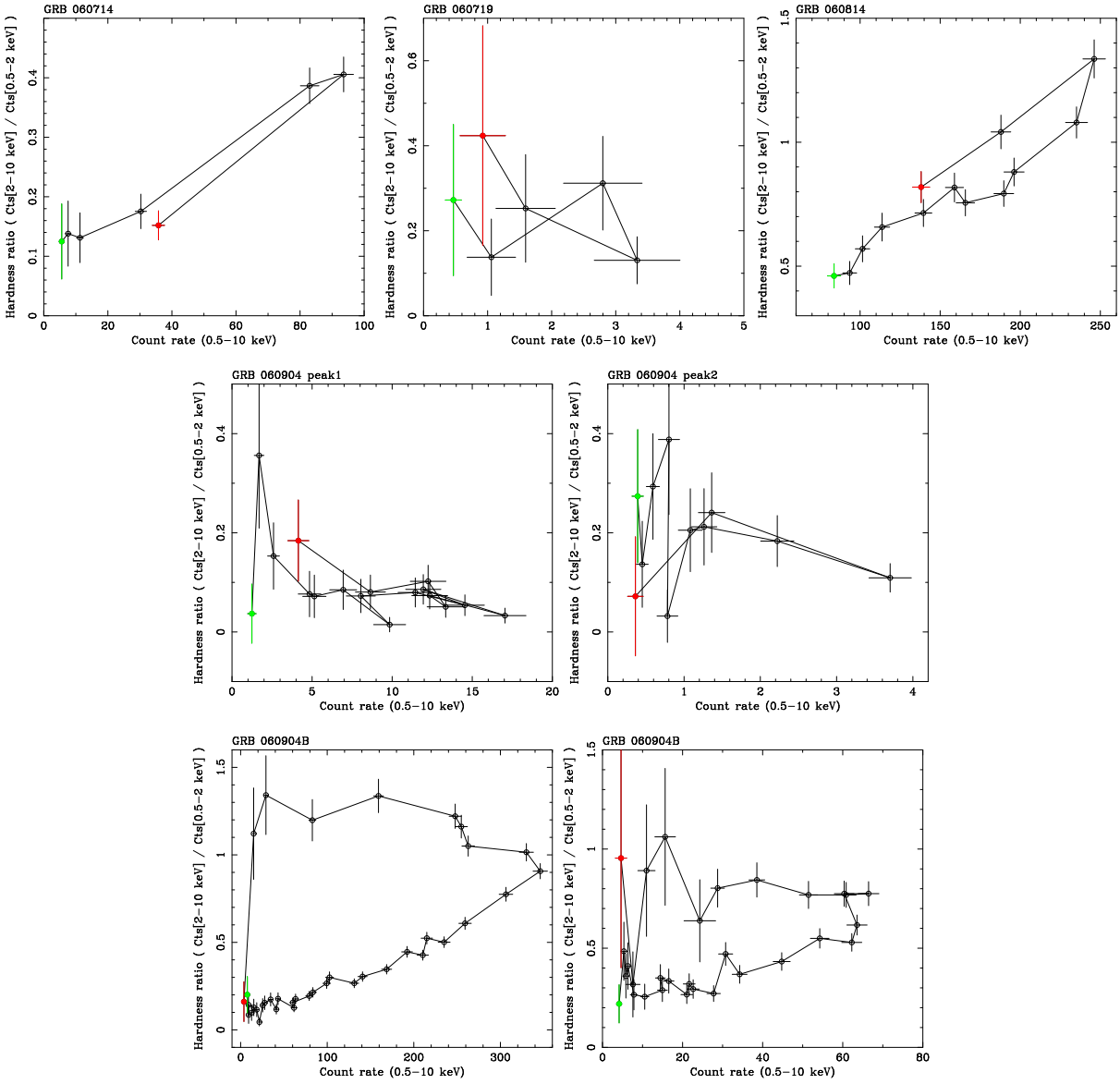

Figure G.5: Count rate (0.5-10 keV) versus hardness ratio of X-ray flares The filled circle represents the start point of the X-ray flare.

Appendix H

Temporal Profiles of X-ray Flares

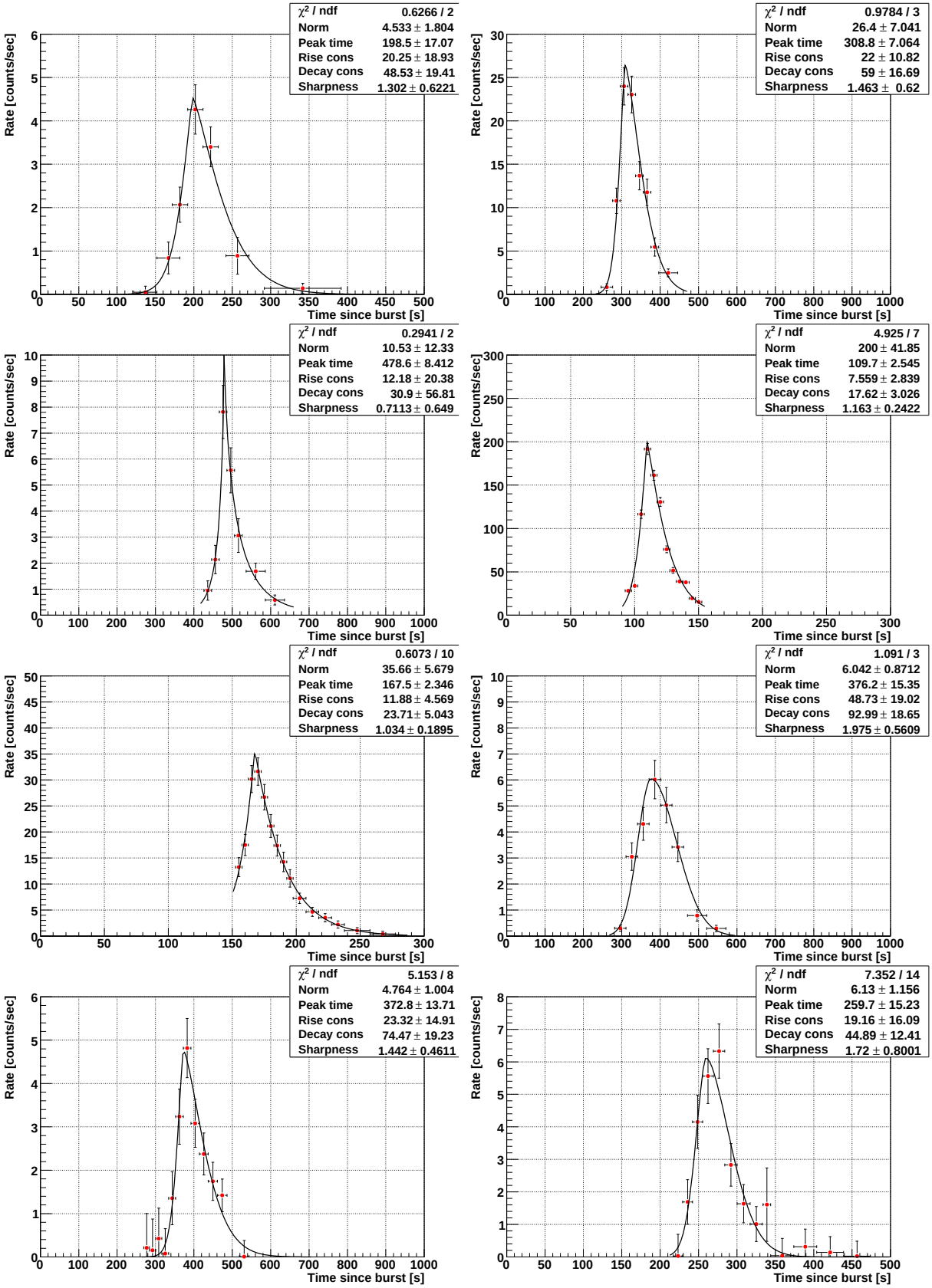

Figure H.1: GRB 050406, 050607, 050712, 050713 p1, 050713 p2, 05050714B, 050716, 050726

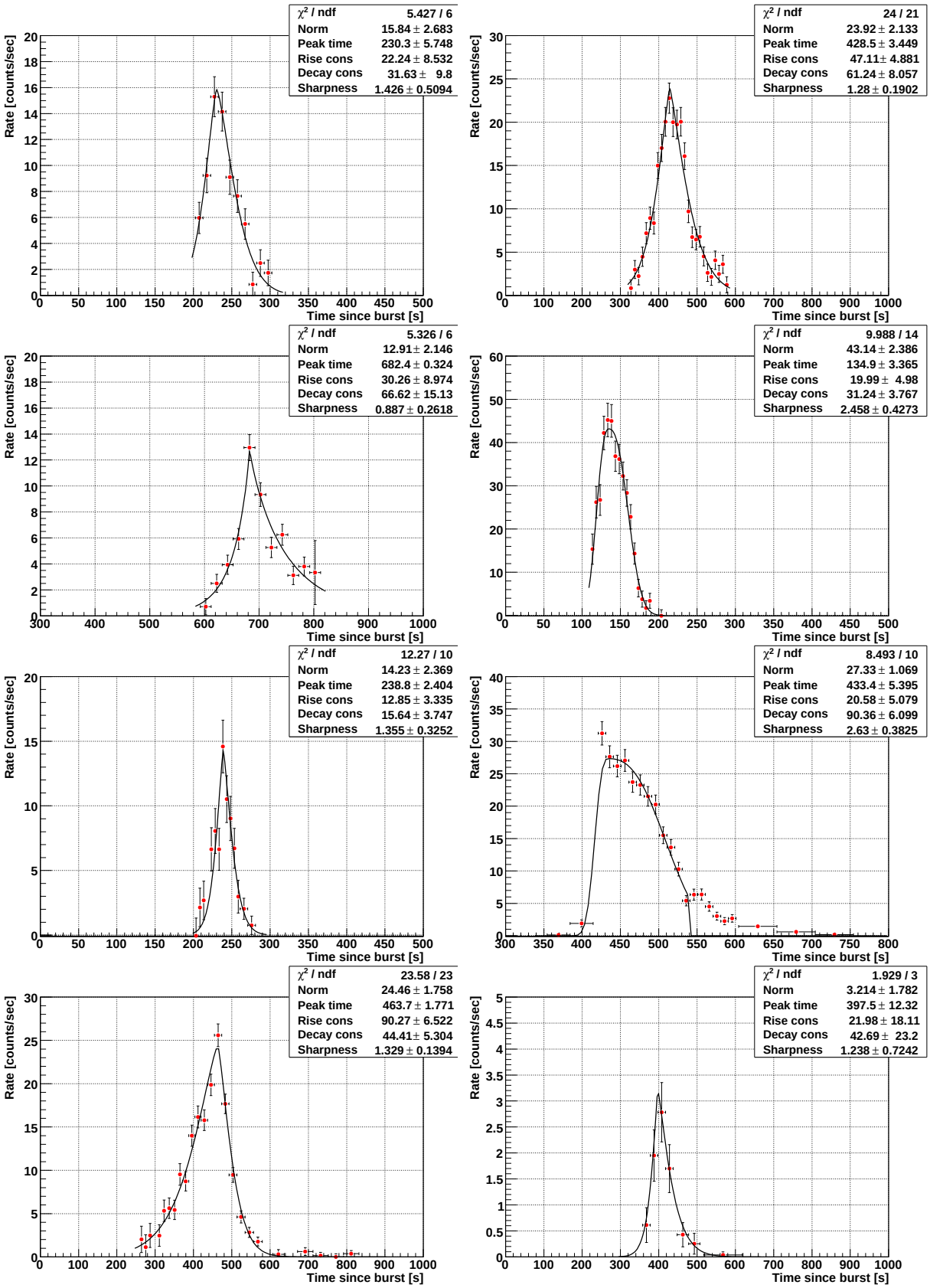

Figure H.2: GRB 050730 p1, 050730 p2, 050730 p3, 050822 p1, 050822 p2, 050822 p3, 050904, 050908

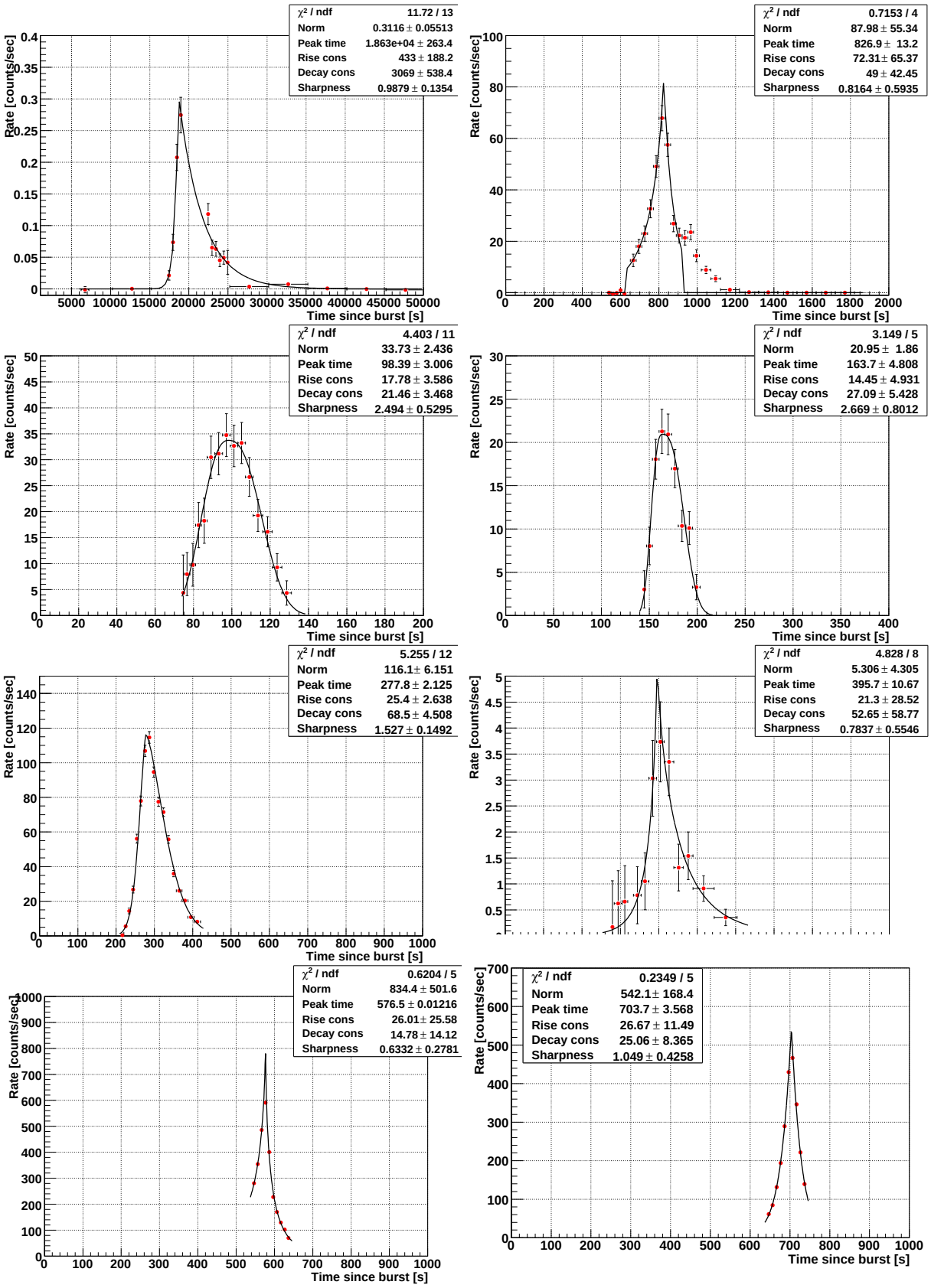

Figure H.3: GRB 050916, 050922B, 060111 p1, 060111 p2, 060111 p3, 060115, 060124 p1, 060124 p2

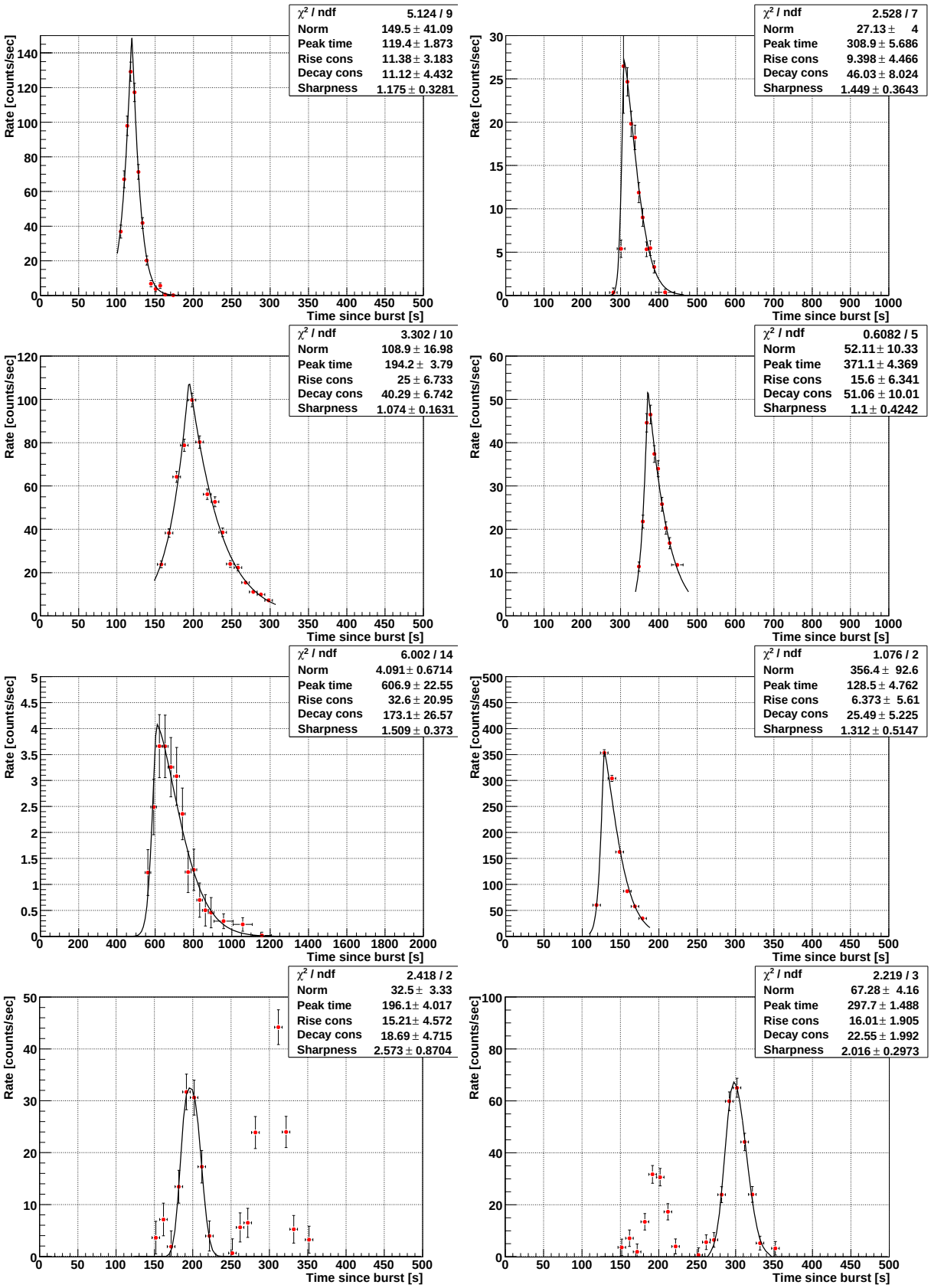

Figure H.4: GRB 060204B p1, 060204B p2, 060210 p1, 060210 p2, 060413, 060418, 060510B p1, 060510B p2

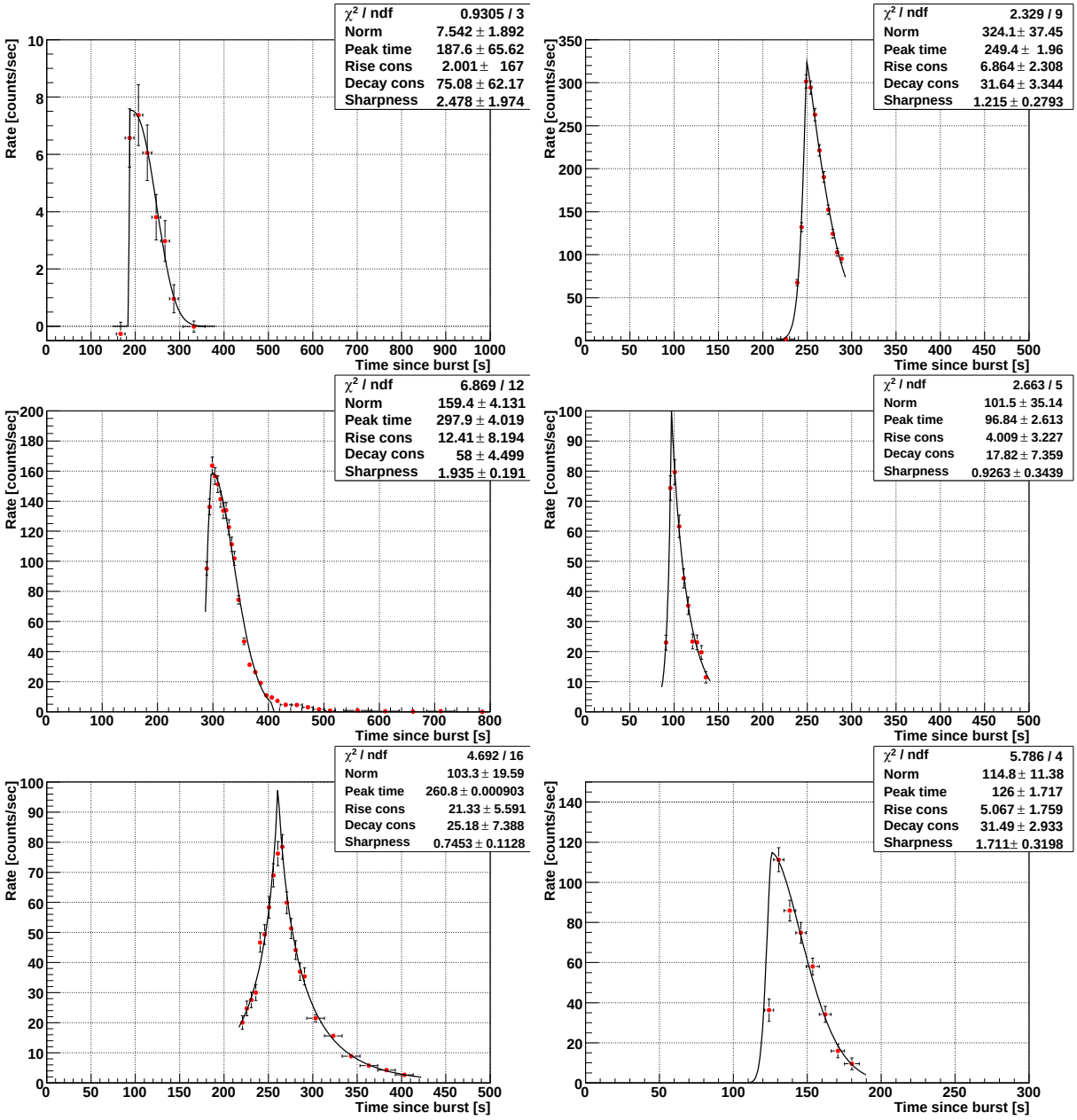

Figure H.5: GRB 060512, 060526 p1, 060526 p2, 060607 p1, 060607 p2, 060814

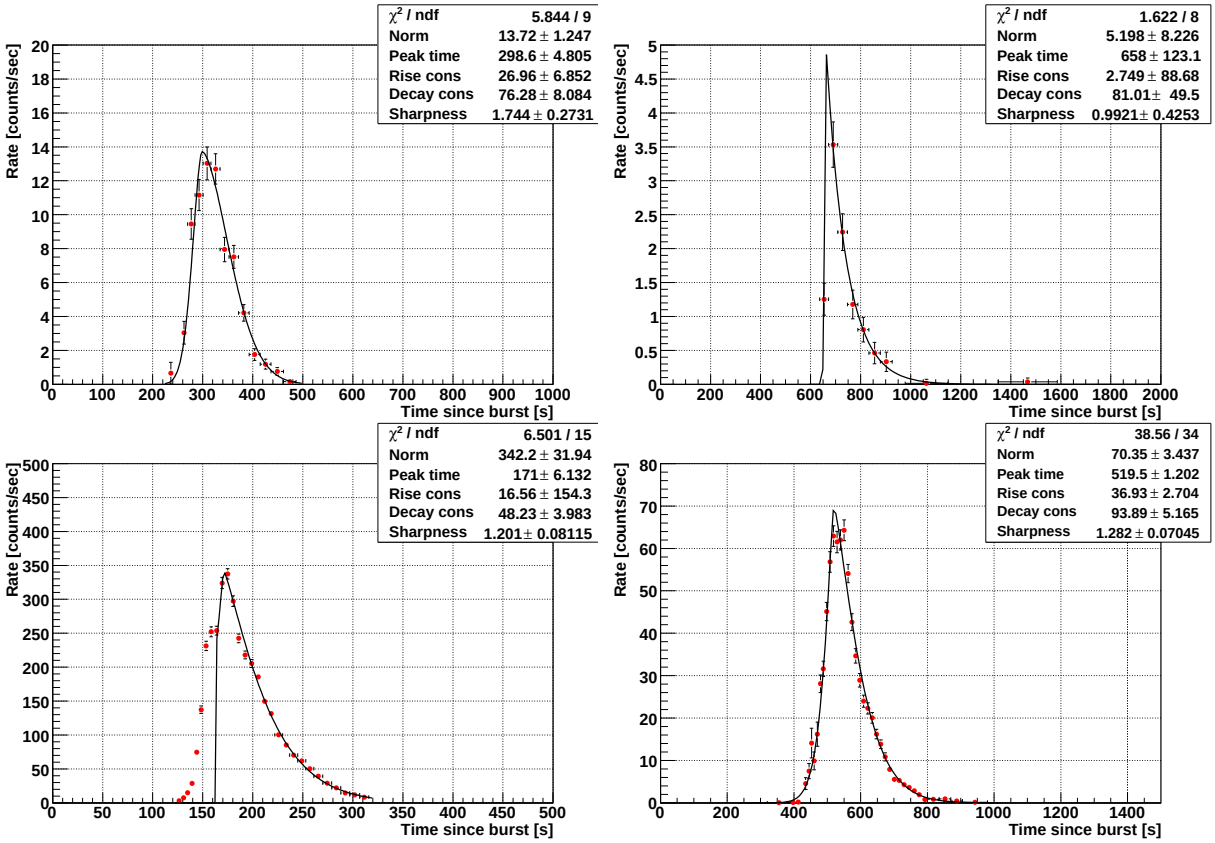

Figure H.6: GRB 060904 p1, 060904 p2, 060904B, 060926

Appendix I

DCF Distribution

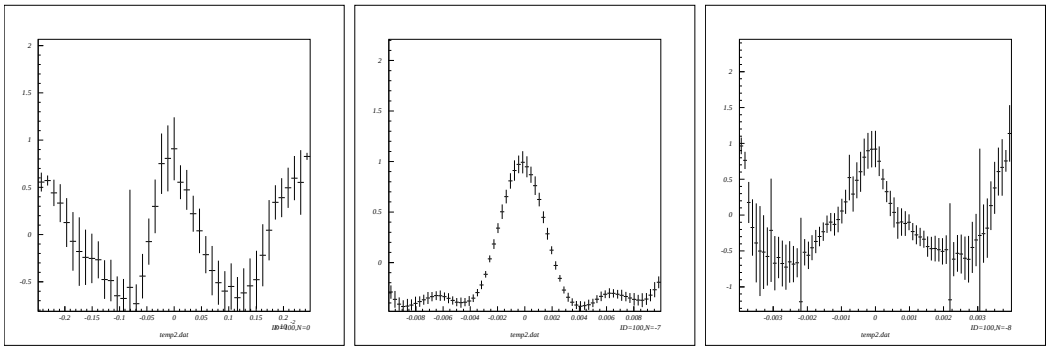

Figure I.1: DCF distribution of GRB 050406, GRB 050502B, GRB 050607

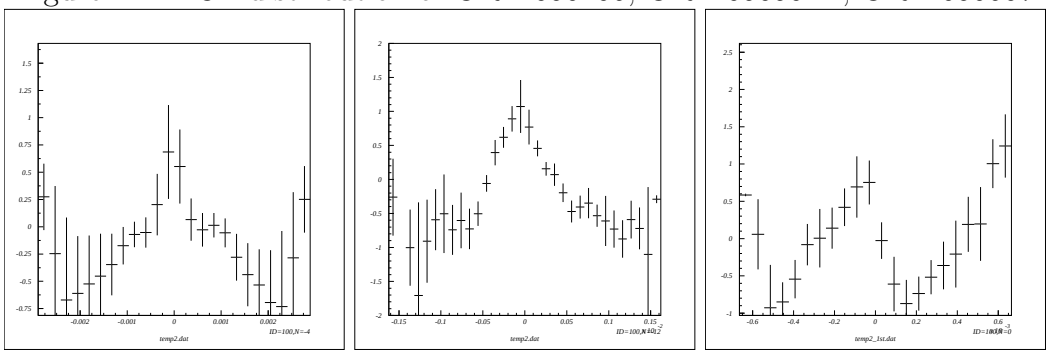

Figure I.2: DCF distribution of GRB 050712, GRB 050713 1st, GRB 05713 2nd

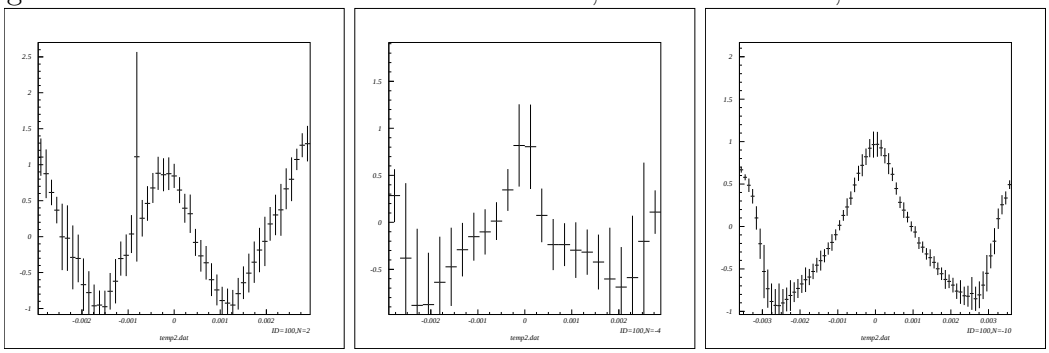

Figure I.3: DCF distribution of GRB 050714B, GRB 050908, GRB 060111

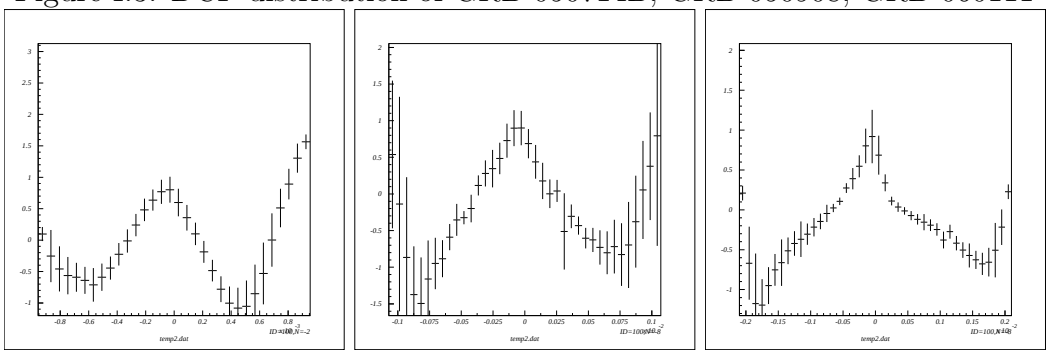

Figure I.4: DCF distribution of GRB 060124, GRB 060210, GRB 060418

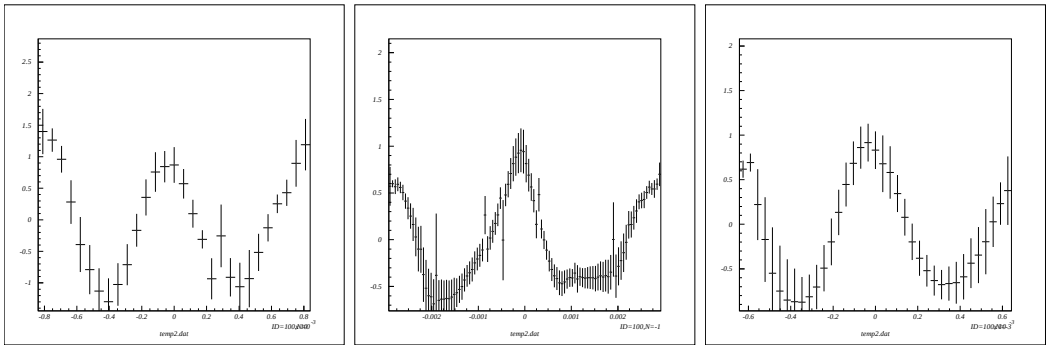

Figure I.5: DCF distribution of GRB 060510B, GRB 060607, GRB 060714

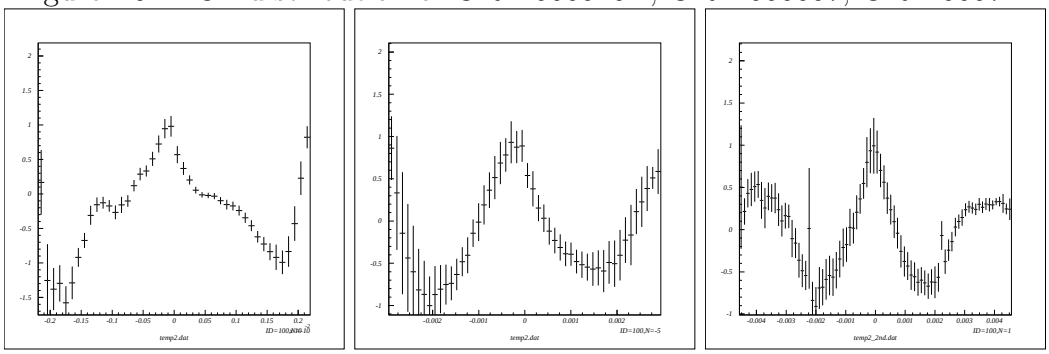

Figure I.6: DCF distribution of GRB 060814, GRB 060904 1st, GRB 060904 2nd

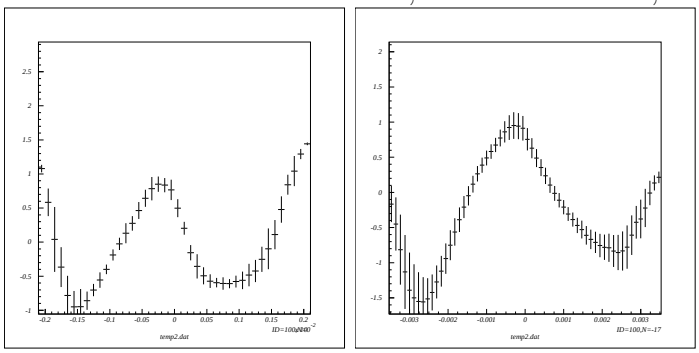

Figure I.7: DCF distribution of GRB 060904B, GRB 060929

Appendix J

X-ray Flare Start Times

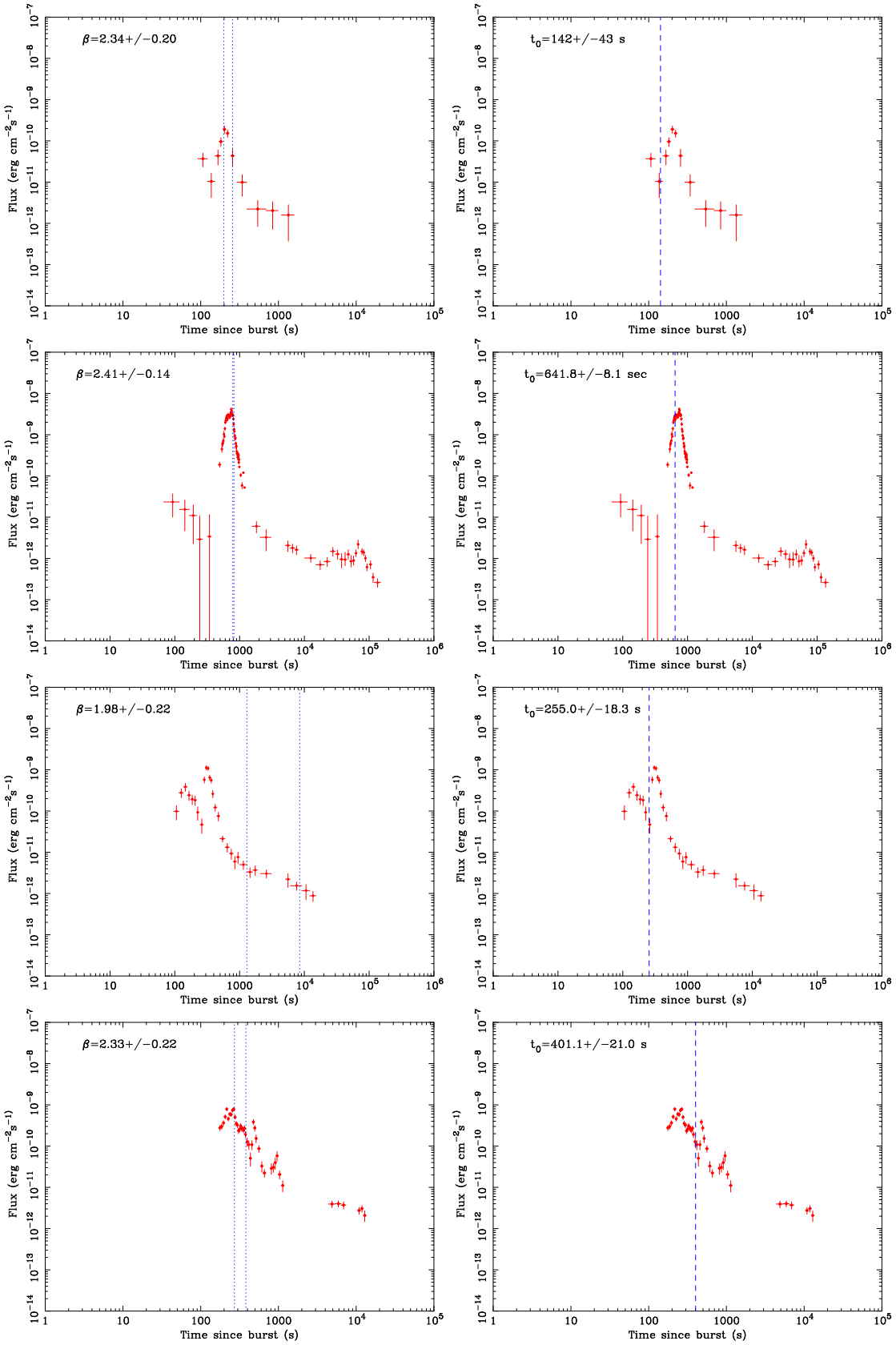

Figure J.1: XRT Light curves in 0.5-10 keV. *Left*: The vertical dotted lines represent the foreground region of the spectrum. *Right*: The vertical dotted lines mark the best-fit t0 values. GRB 050406, GRB 050502B, GRB 050607, GRB 050712

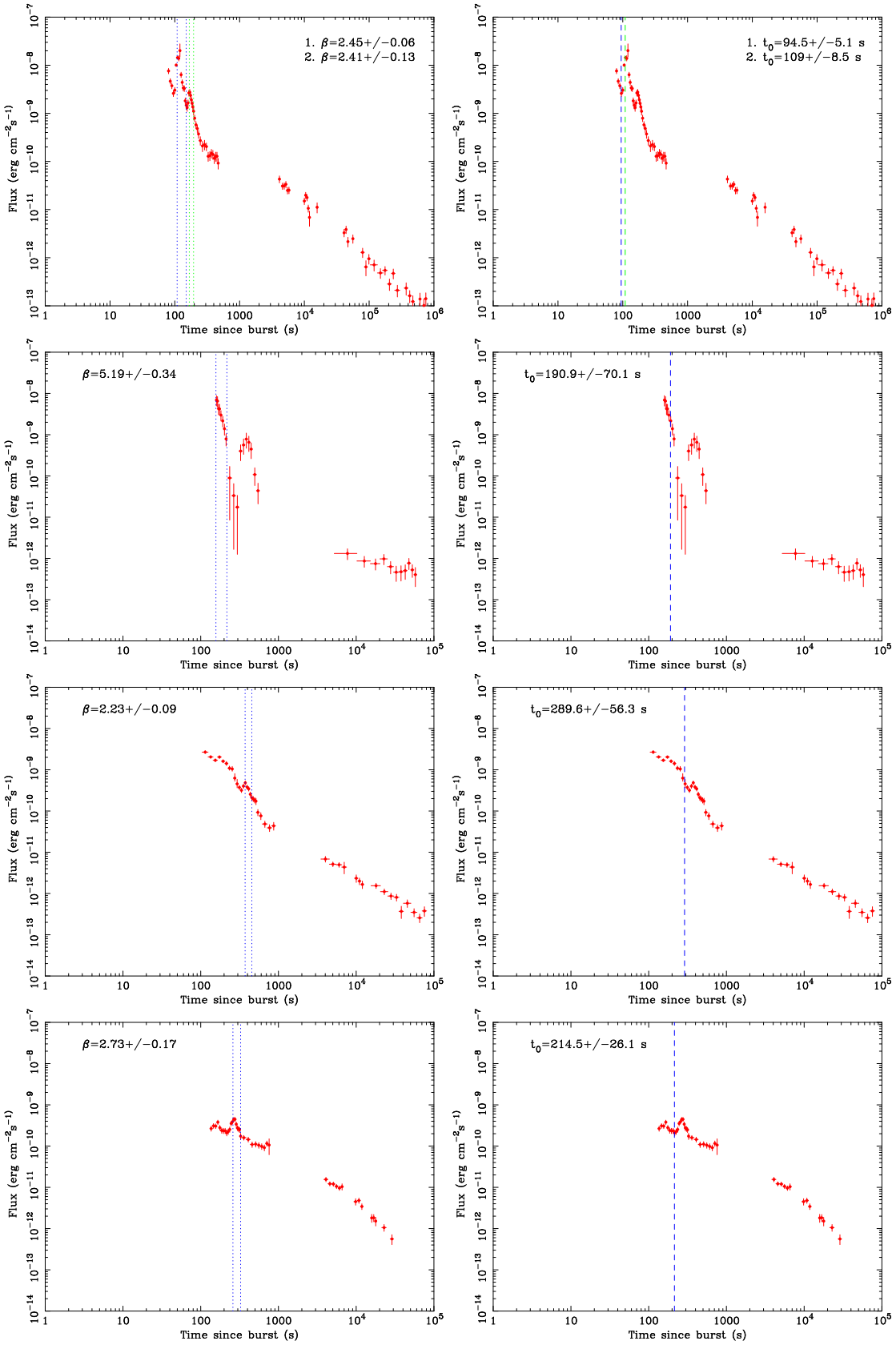

Figure J.2: XRT Light curves in 0.5-10 keV. *Left*: The vertical dotted lines represent the foreground region of the spectrum. *Right*: The vertical dotted lines mark the best-fit t0 values; GRB 050713, GRB 050814B, GRB 050716, GRB 050726

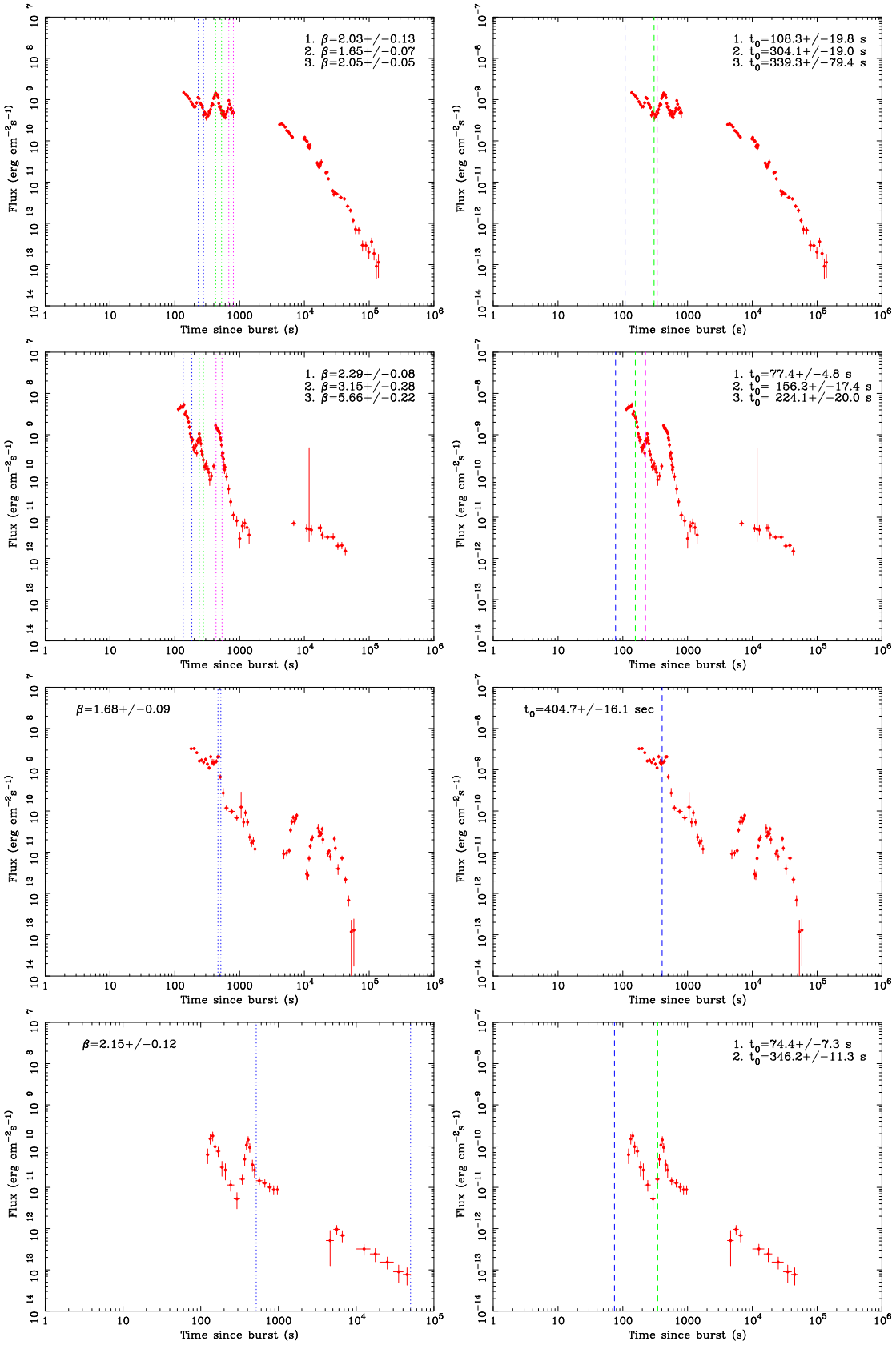

Figure J.3: XRT Light curves in 0.5-10 keV. *Left*: The vertical dotted lines represent the foreground region of the spectrum. *Right*: The vertical dotted lines mark the best-fit t0 values;GRB 050730, GRB 050822, GRB 050904, GRB 050908

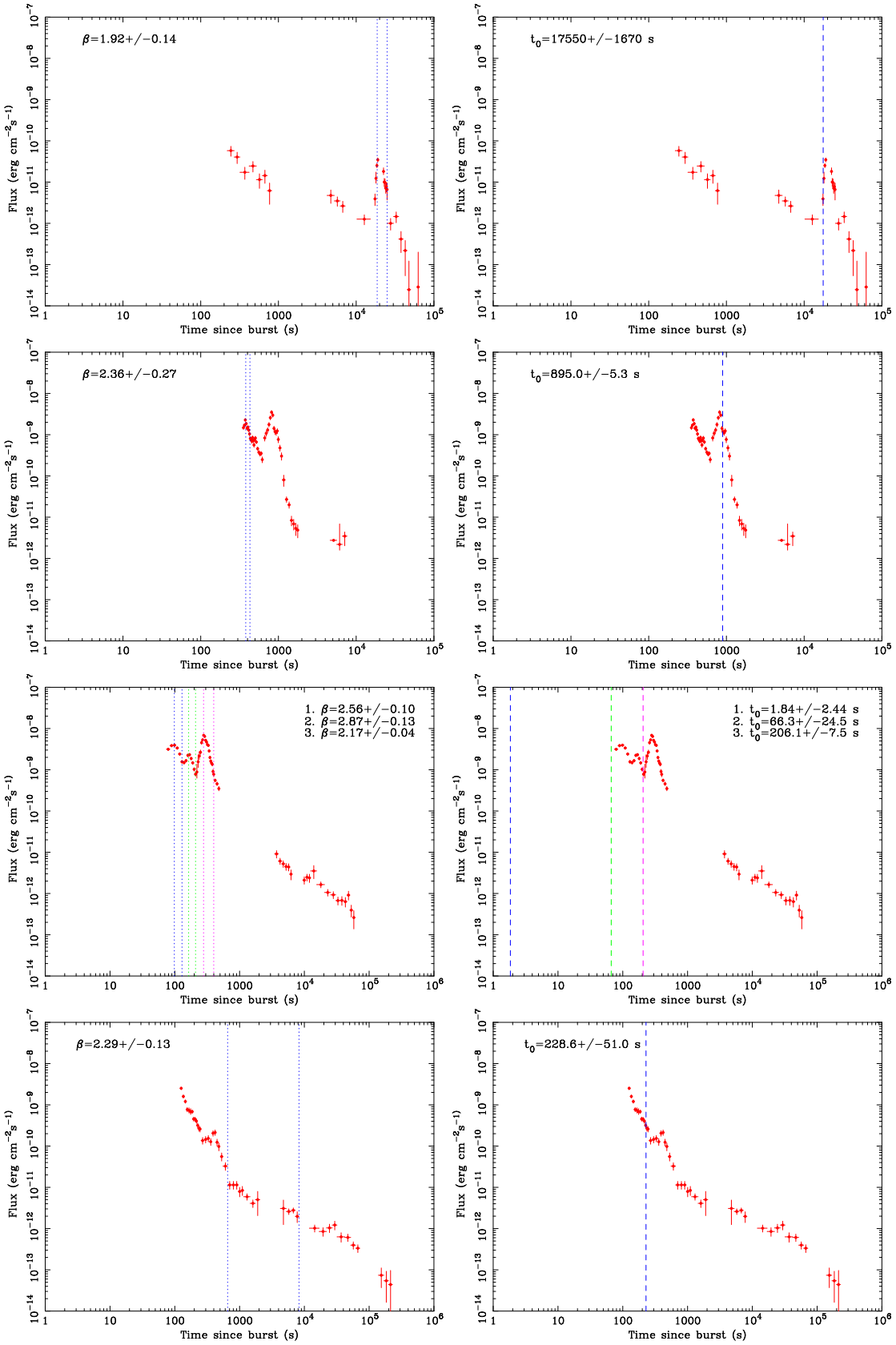

Figure J.4: XRT Light curves in 0.5-10 keV. *Left*: The vertical dotted lines represent the foreground region of the spectrum. *Right*: The vertical dotted lines mark the best-fit t0 values;GRB 050916, GRB 050922B, GRB 060111, GRB 060115

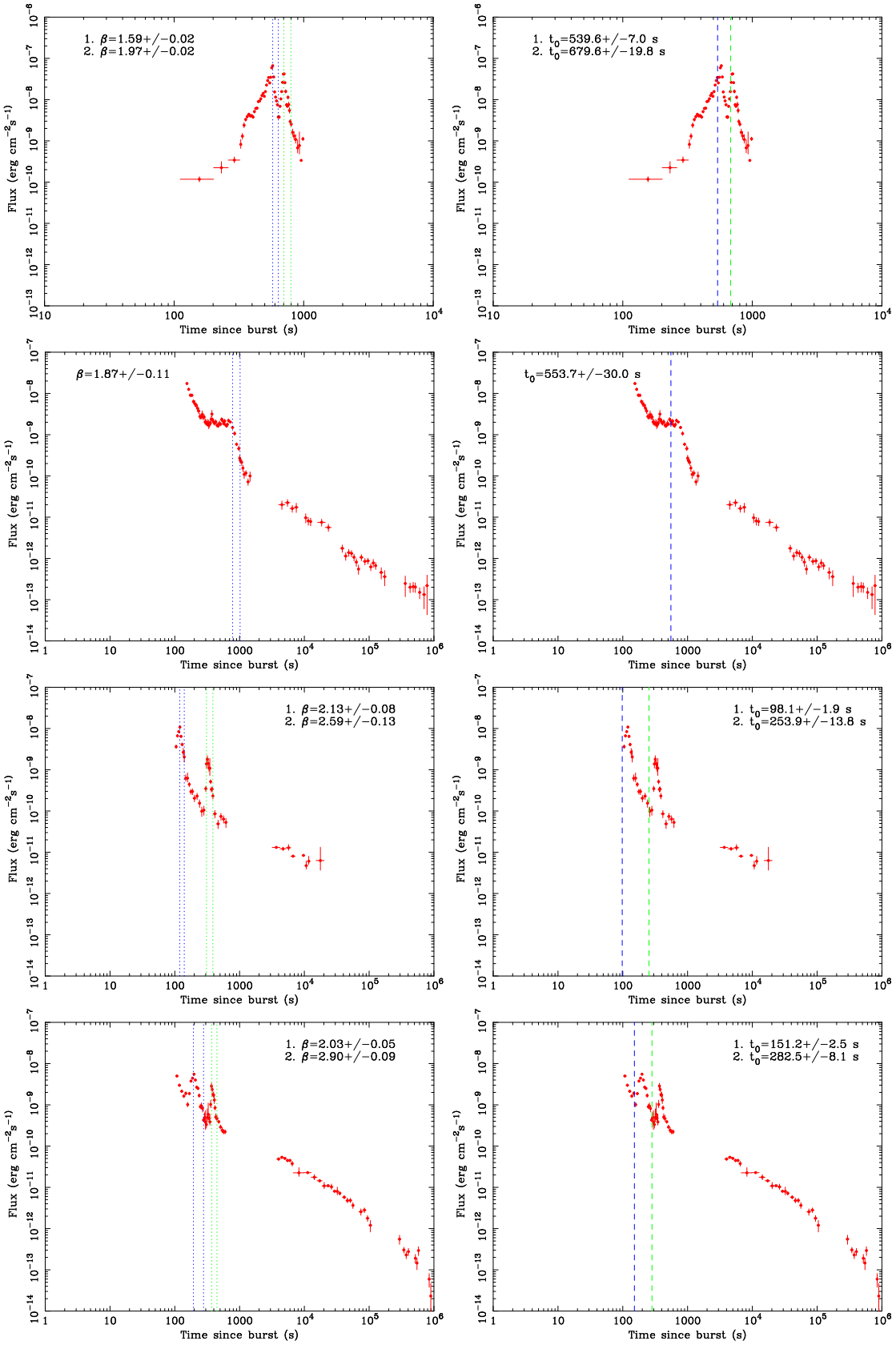

Figure J.5: XRT Light curves in 0.5-10 keV. *Left*: The vertical dotted lines represent the foreground region of the spectrum. *Right*: The vertical dotted lines mark the best-fit t0 values;GRB 060124, GRB 060202, GRB 060204B, GRB 060210

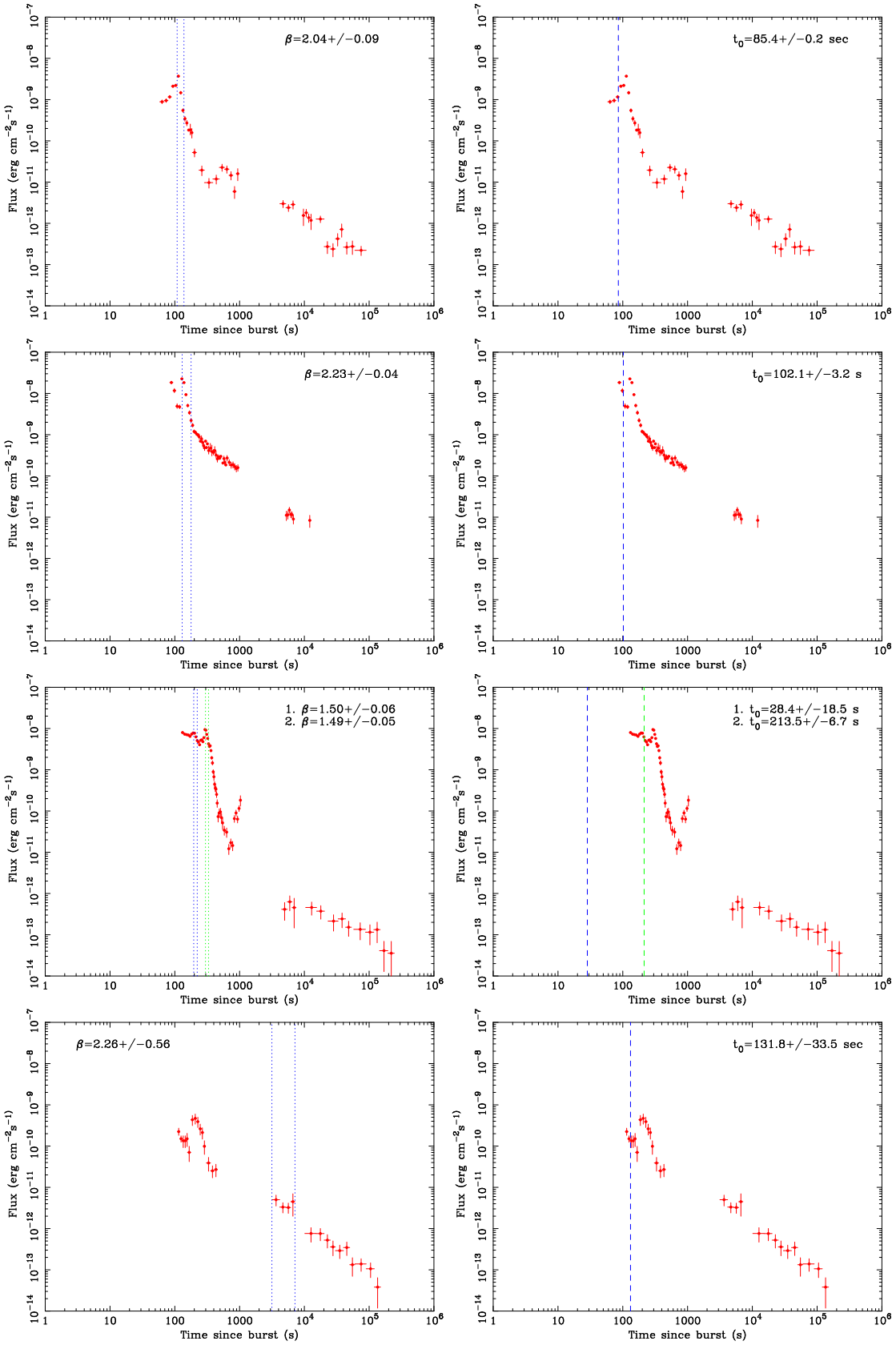

Figure J.6: XRT Light curves in 0.5-10 keV. *Left*: The vertical dotted lines represent the foreground region of the spectrum. *Right*: The vertical dotted lines mark the best-fit t0 values;GRB 060312, GRB 060418, GRB 060510B, GRB 060512

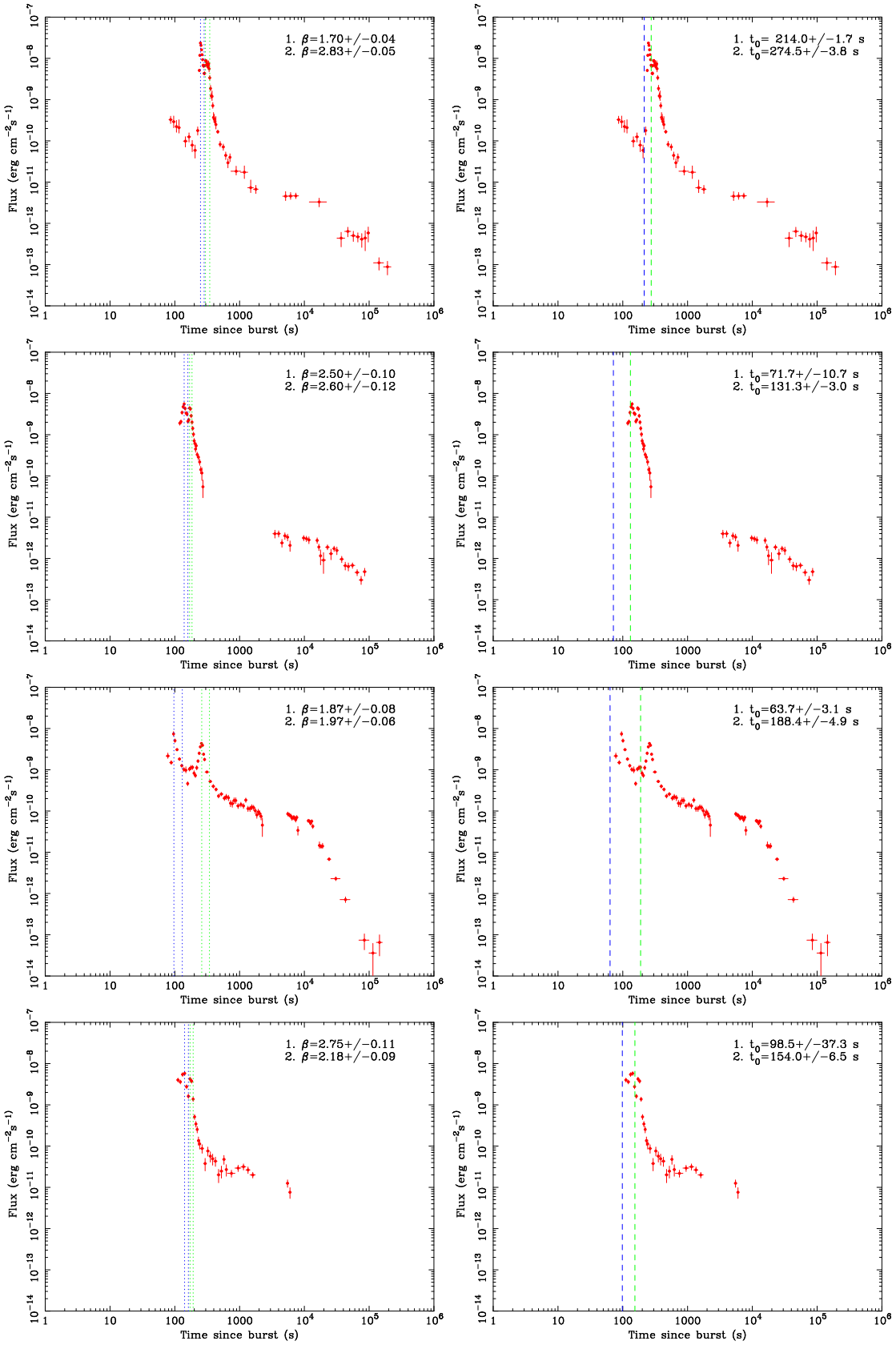

Figure J.7: XRT Light curves in 0.5-10 keV. *Left*: The vertical dotted lines represent the foreground region of the spectrum. *Right*: The vertical dotted lines mark the best-fit t0 values;GRB 060526, GRB 060604, GRB 060607, GRB 060714

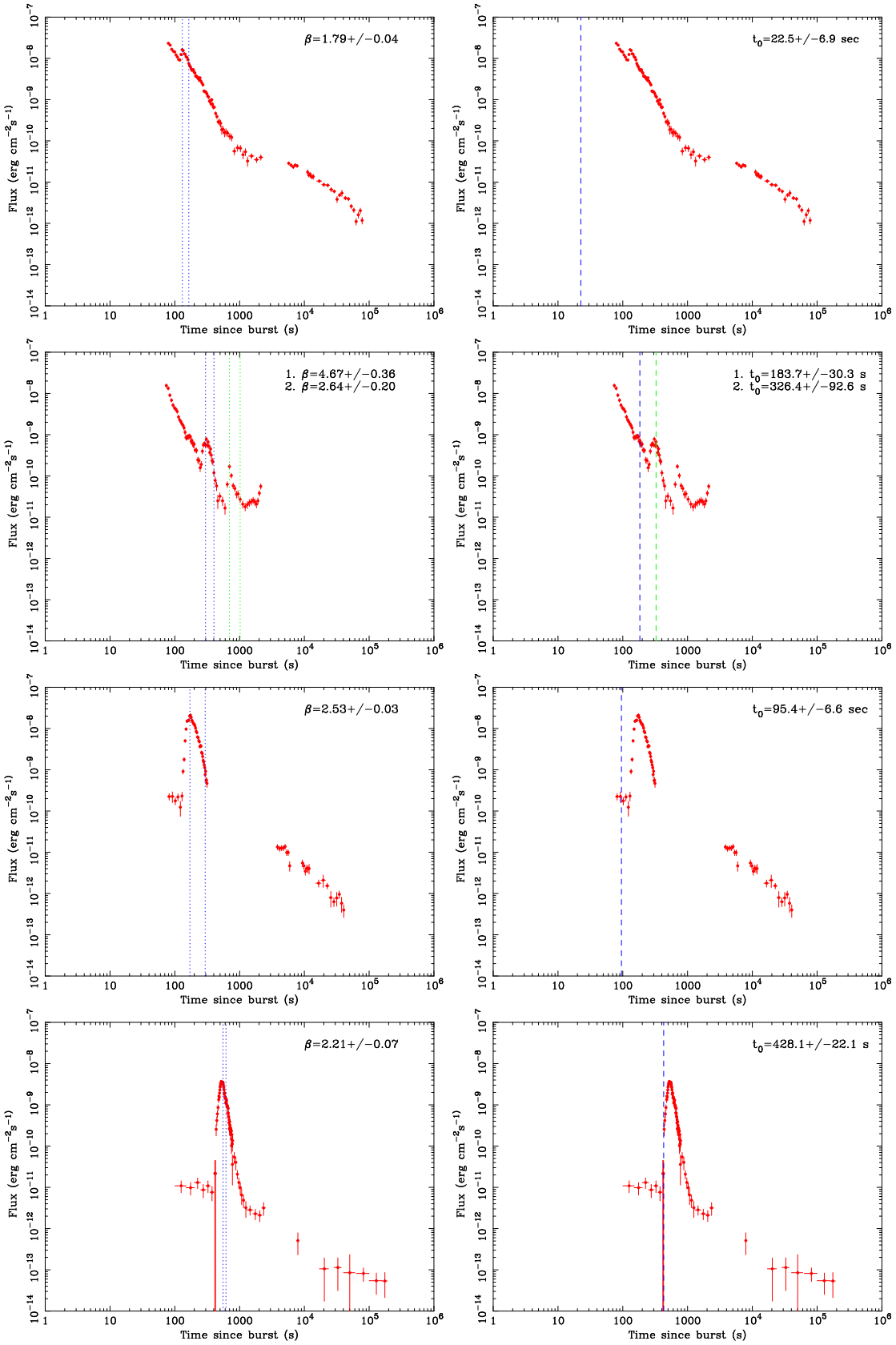

Figure J.8: XRT Light curves in 0.5-10 keV. *Left*: The vertical dotted lines represent the foreground region of the spectrum. *Right*: The vertical dotted lines mark the best-fit t0 values;GRB 060814, GRB 060904, GRB 060904B GRB 060929